Gamma-Ray Bursts

Contents

1 Topics

- GRB classification in different families with different progenitor systems.
- "Genuine short" GRBs: Possible identifications and selection effects
- The observed spectra of the P-GRBs
- GRB prompt emission spectra below 5 keV: challenges for future missions
- Interpretation of the ultra high energy emission from GRBs observed by Fermi, AGILE and MAGIC
- Analysis of different families of progenitors for GRBs with different energetics
- GRBs at redshift $z > 6$
- GRBs originating from a multiple collapse
- Prompt emission: the clumpiness of CBM
- Microphysical description of the interaction between the fireshell and the CBM
- Emission from newly born neutron stars, or "neo neutron stars" (νNS).
- Induced Gravitational Collapse process for GRBs associated with supernovae.
- Redshift estimators for GRBs with no measured redshift.
- Binary Driven Hypernovae (BdHNe) as progenitor of GRBs via Induced Gravitational Collapse.

- GRB light curves as composed of different episodes.
- "Cosmic Matrix" for GRBs.
- GRB X-Ray Flares and Gamma-Ray Flares.
- GRB afterglow theory consistent with the mildly relativistic velocities inferred from the observations.
- Extended thermal emission components in GRBs.
- GRBs from merging white dwarfs.
- "Inner engine" of GRB emission.
- Quantized emission in GRBs.

2 Participants

2.1 ICRANet participants

- David Arnett
- Carlo Luciano Bianco
- Massimo Della Valle
- Li Liang
- Rahim Moradi
- Jorge Armando Rueda Hernandez
- Remo Ruffini
- Narek Sahakyan
- Gregory Vereshchagin
- Yu Wang
- She-Sheng Xue

2.2 Past collaborators

- Andrey Baranov
- Maria Grazia Bernardini (OAB, Italy)
- Joao Braga (INPE, Brazil)
- Sabrina Casanova (MPIK, Germany)

- Letizia Caito
- Pascal Chardonnet (Université de Savoie, France)
- Guido Chincarini (Università di Milano "Bicocca", Italy)
- Demetrios Christodoulou (ETH Zurich, Switzerland)
- Alessandra Corsi (INAF-IASF Roma, Italy)
- Valeri Chechetkin
- Maria Giovanna Dainotti
- Thibault Damour (IHES, France)
- Maxime Enderli
- Walter Ferrara
- Federico Fraschetti (CEA Saclay, France)
- Roberto Guida
- Vahe Gurzadyan (Yerevan Physics Institute, Armenia)
- Wen-Biao Han
- Milos Kovacevic
- Massimiliano Lattanzi (Oxford Astrophysics, UK)
- Vincenzo Liccardo
- Hendrik Ludwig
- Marco Muccino
- Nino Panagia
- Barbara Patricelli (Pisa University, Italy)
- Elena Pian
- Giovanni Battista Pisani

- Giuliano Preparata (Università di Milano, Italy)
- Daria Primorac
- Jay D. Salmonson (Livermore Lab, USA)
- Vineeth Valsan
- Jim Wilson (Livermore Lab, USA)

2.3 Ongoing collaborations

- Alexey Aksenov (ITEP, Russia)
- Lorenzo Amati (INAF-IASF Bologna, Italy)
- Ulisses Barres de Almeida (CBPF, Brazil)
- Laura Marcela Becerra Bayona (Universidad Industrial de Santander, Colombia)
- Riccardo Belvedere (ICRANet-Rio, Brazil)
- Sandip Kumar Chakrabarti (S.N. Bose National Centre and Indian Centre for Space Physics, India)
- Christian Cherubini (Università Campus Biomedico, Italy)
- Alessandro Chieffi (INAF-IASF Roma, Italy)
- Stefano Covino (OAB, Italy)
- Gustavo de Barros (UFRJ, Brazil)
- Simonetta Filippi (Università Campus Biomedico, Italy)
- Filippo Frontera (Università di Ferrara, Italy)
- Chris Fryer (Los Alamos National Laboratories, USA).
- Dafne Guetta (OAR, Italy)
- Cristiano Guidorzi (OAB, Italy)

- Stanislav Kelner (MEPhI, Russia, and MPIK, Germany)
- Marco Limongi (OAR, Italy)
- Clovis Maia (University of Brasilia, Brazil)
- Vanessa Mangano (INAF-IASF Palermo, Italy)
- Marco Marongiu (INAF - Cagliari Observatory and University of Ferrara, Italy)
- Grant Mathews (University of Notre Dame, USA)
- Ana Virginia Penacchioni (INPE, Brazil)
- Luis Juracy Rangel Lemos (Fundação Universidade Federal do Tocantins, Brazil)
- Felix Ryde (KTH Royal Institute of Technology, Stockholm, Sweden)
- Soroush Shakeri (Isfahan University of Technology, Iran)
- Ivan Siutsou (ICRANet-Rio, Brazil)
- Bing Zhang (University of Nevada, USA)
- Susanna Vergani (Dunsink Observatory, Ireland)
- Francesco Vissani (INFN, Italy)
- Elena Zaninoni (ICRANet-Rio, Brazil)

2.4 Students

- Yerlan Aimuratov (IRAP PhD, Kazakhstan)
- Stefano Campion (IRAP PhD, Italy)
- Yen-Chen Chen (IRAP-PhD, China-Taiwan)
- Mile Karlika (IRAP PhD, Croatia)
- Ronaldo V. Lobato (IRAP-PhD, Brazil)

- J. David Melon Fuksman (IRAP PhD, Argentina)
- Jose Fernando Rodriguez Ruiz (IRAP PhD, Colombia)

3 Selected publications before 2005

3.1 Refereed journals

1. D. Christodoulou, R. Ruffini; "Reversible Transformations of a Charged Black Hole"; Physical Review D, 4, 3552 (1971).

   A formula is derived for the mass of a black hole as a function of its "irreducible mass", its angular momentum, and its charge. It is shown that 50% of the mass of an extreme charged black hole can be converted into energy as contrasted with 29% for an extreme rotating black hole.

2. T. Damour, R. Ruffini; "Quantum electrodynamical effects in Kerr-Newman geometries"; Physical Review Letters, 35, 463 (1975).

   Following the classical approach of Sauter, of Heisenberg and Euler and of Schwinger the process of vacuum polarization in the field of a "bare" Kerr-Newman geometry is studied. The value of the critical strength of the electromagnetic fields is given together with an analysis of the feedback of the discharge on the geometry. The relevance of this analysis for current astrophysical observations is mentioned.

3. G. Preparata, R. Ruffini, S.-S. Xue; "The dyadosphere of black holes and gamma-ray bursts"; Astronomy & Astrophysics, 338, L87 (1999).

   The "dyadosphere" has been defined as the region outside the horizon of a black hole endowed with an electromagnetic field (abbreviated to EMBH for "electromagnetic black hole") where the electromagnetic field exceeds the critical value, predicted by Heisenberg & Euler for $e^{\pm}$ pair production. In a very short time ($\sim O(\hbar/mc^2)$) a very large number of pairs is created there. We here give limits on the EMBH parameters leading to a Dyadosphere for $10M_{\odot}$ and $10^5M_{\odot}$ EMBH's, and give as well the pair densities as functions of the radial coordinate. We here assume that the pairs reach thermodynamic equilibrium with a photon gas and estimate the average energy per pair as a function of the EMBH mass. These data give the initial conditions for the analysis of an enormous pair-electromagnetic-pulse or "P.E.M. pulse" which naturally leads to relativistic expansion. Basic energy requirements for gamma ray bursts (GRB), including GRB971214 recently observed at z=3.4, can be accounted for by processes occurring in the dyadosphere. In this letter we do not address the problem of forming either the EMBH or the dyadosphere: we establish some inequalities which must be satisfied during their formation process.

4. R. Ruffini, J.D. Salmonson, J.R. Wilson, S.-S. Xue; "On the pair electromagnetic pulse of a black hole with electromagnetic structure"; Astronomy & Astrophysics, 350, 334 (1999).

   We study the relativistically expanding electron-positron pair plasma formed by the process of vacuum polarization around an electromagnetic black hole (EMBH). Such processes can occur for EMBH's with mass all the way up to $6 \times 10^5 M_\odot$. Beginning with a idealized model of a Reissner-Nordstrom EMBH with charge to mass ratio $\xi = 0.1$, numerical hydrodynamic calculations are made to model the expansion of the pair-electromagnetic pulse (PEM pulse) to the point that the system is transparent to photons. Three idealized special relativistic models have been compared and contrasted with the results of the numerically integrated general relativistic hydrodynamic equations. One of the three models has been validated: a PEM pulse of constant thickness in the laboratory frame is shown to be in excellent agreement with results of the general relativistic hydrodynamic code. It is remarkable that this precise model, starting from the fundamental parameters of the EMBH, leads uniquely to the explicit evaluation of the parameters of the PEM pulse, including the energy spectrum and the astrophysically unprecedented large Lorentz factors (up to 6×10^3 for a $10^3 M_\odot$ EMBH). The observed photon energy at the peak of the photon spectrum at the moment of photon decoupling is shown to range from 0.1 MeV to 4 MeV as a function of the EMBH mass. Correspondingly the total energy in photons is in the range of 10^{52} to 10^{54} ergs, consistent with observed gamma-ray bursts. In these computations we neglect the presence of baryonic matter which will be the subject of forthcoming publications.

5. R. Ruffini, J.D. Salmonson, J.R. Wilson, S.-S. Xue; "On the pair-electro magnetic pulse from an electromagnetic black hole surrounded by a baryonic remnant"; Astronomy & Astrophysics, 359, 855 (2000).

   The interaction of an expanding Pair-Electromagnetic pulse (PEM pulse) with a shell of baryonic matter surrounding a Black Hole with electromagnetic structure (EMBH) is analyzed for selected values of the baryonic mass at selected distances well outside the dyadosphere of an EMBH. The dyadosphere, the region in which a super critical field exists for the creation of e+e- pairs, is here considered in the special case of a Reissner-Nordstrom geometry. The interaction of the PEM pulse with the baryonic matter is described using a simplified model of a slab of constant thickness in the laboratory frame (constant-thickness approximation) as well as performing the integration of the general relativistic hydrodynamical equations. Te validation of the constant-thickness approximation, already presented in a previous paper Ruffini et al. (1999) for a PEM pulse in vacuum, is here generalized to the presence of baryonic matter. It is found that for a baryonic shell of mass-energy less than 1% of the total energy of the dyadosphere, the constant-thickness approximation is in excellent agreement with full general relativistic computations. The approximation breaks down for larger values of the baryonic shell mass, however such cases are of less interest for observed Gamma Ray Bursts (GRBs). On the basis of numerical computations of the slab model for PEM pulses, we describe (i) the properties of relativistic evolution of a PEM pulse colliding with a baryonic shell; (ii) the details of the expected emission energy and observed temperature of the associated GRBs for a given value of the EMBH mass; $10^3 M_\odot$, and for baryonic mass-energies in the range 10^{-8} to 10^{-2} the total energy of the dyadosphere.

6. C.L. Bianco, R. Ruffini, S.-S. Xue; "The elementary spike produced by a pure e+e- pair-electromagnetic pulse from a Black Hole: The PEM Pulse"; Astronomy & Astrophysics, 368, 377 (2001).

   In the framework of the model that uses black holes endowed with electromagnetic structure (EMBH) as the energy source, we study how an elementary spike appears to the detectors. We consider the simplest possible case of a pulse produced by a pure e^+e^- pair-electro-magnetic plasma, the PEM pulse, in the absence of any baryonic matter. The resulting time profiles show a *Fast-Rise-Exponential-Decay* shape, followed by a power-law tail. This is obtained without any special fitting procedure, but only by fixing the energetics of the process taking place in a given EMBH of selected mass, varying in the range from 10 to 10^3 $M_\odot$ and considering the relativistic effects to be expected in an electron-positron plasma gradually reaching transparency. Special attention is given to the contributions from all regimes with Lorentz γ factor varying from $\gamma = 1$ to $\gamma = 10^4$ in a few hundreds of the PEM pulse travel time. Although the main goal of this paper is to obtain the elementary spike intensity as a function of the arrival time, and its observed duration, some qualitative considerations are also presented regarding the expected spectrum and on its departure from the thermal one. The results of this paper will be comparable, when data will become available, with a subfamily of particularly short GRBs not followed by any afterglow. They can also be propedeutical to the study of longer bursts in presence of baryonic matter currently observed in GRBs.

7. R. Ruffini, C.L. Bianco, P. Chardonnet, F. Fraschetti, S.-S. Xue; "Relative spacetime transformations in Gamma-Ray Bursts"; The Astrophysical Journal, 555, L107 (2001).

   The GRB 991216 and its relevant data acquired from the BATSE experiment and RXTE and Chandra satellites are used as a prototypical case to test the theory linking the origin of gamma ray bursts (GRBs) to the process of vacuum polarization occurring during the formation phase of a black hole endowed with electromagnetic structure (EMBH). The relative space-time transformation paradigm (RSTT paradigm) is presented. It relates the observed signals of GRBs to their past light cones, defining the events on the worldline of the source essential for the interpretation of the data. Since GRBs present regimes with unprecedently large Lorentz γ factor, also sharply varying with time, particular attention is given to the constitutive equations relating the four time variables: the comoving time, the laboratory time, the arrival time at the detector, duly corrected by the cosmological effects. This paradigm is at the very foundation of any possible interpretation of the data of GRBs.

8. R. Ruffini, C.L. Bianco, P. Chardonnet, F. Fraschetti, S.-S. Xue; "On the interpretation of the burst structure of Gamma-Ray Bursts"; The Astrophysical Journal, 555, L113 (2001).

   Given the very accurate data from the BATSE experiment and RXTE and Chandra satellites, we use the GRB 991216 as a prototypical case to test the EMBH theory linking the origin of the energy of GRBs to the electromagnetic energy of black holes. The fit of the afterglow fixes the only two free parameters of the model and leads to a new paradigm for the interpretation of the burst structure, the IBS paradigm. It leads as well to a reconsideration of the relative roles of the afterglow and burst in GRBs by defining two new phases in this complex phenomenon: a) the injector phase, giving rise to the proper-GRB (P-GRB), and b) the beam-target phase, giving rise to the extended afterglow peak emission (E-APE) and to the afterglow. Such differentiation leads to a natural possible explanation of the bimodal distribution of GRBs observed by BATSE. The agreement with the observational data in regions extending from the horizon of the EMBH all the way out to the distant observer confirms the uniqueness of the model.

9. R. Ruffini, C.L. Bianco, P. Chardonnet, F. Fraschetti, S.-S. Xue; "On a possible Gamma-Ray Burst-Supernova time sequence"; The Astrophysical Journal, 555, L117 (2001).

   The data from the Chandra satellite on the iron emission lines in the afterglow of GRB 991216 are used to give further support for the EMBH theory, which links the origin of the energy of GRBs to the extractable energy of electromagnetic black holes (EMBHs), leading to an interpretation of the GRB-supernova correlation. Following the relative space-time transformation (RSTT) paradigm and the interpretation of the burst structure (IBS) paradigm, we introduce a paradigm for the correlation between GRBs and supernovae. The following sequence of events is shown as kinematically possible and consistent with the available data: a) the GRB-progenitor star P_1 first collapses to an EMBH, b) the proper GRB (P-GRB) and the peak of the afterglow (E-APE) propagate in interstellar space until the impact on a supernova-progenitor star P_2 at a distance $\leq 2.69 \times 10^{17}$ cm, and they induce the supernova explosion, c) the accelerated baryonic matter (ABM) pulse, originating the afterglow, reaches the supernova remnants 18.5 hours after the supernova explosion and gives rise to the iron emission lines. Some considerations on the dynamical implementation of the paradigm are presented. The concept of induced supernova explosion introduced here specifically for the GRB-supernova correlation may have more general application in relativistic astrophysics.

10. R. Ruffini, C.L. Bianco, P. Chardonnet, F. Fraschetti, S.-S. Xue; "On the physical processes which lie at the bases of time variability of GRBs"; Il Nuovo Cimento B, 116, 99 (2001).

    The relative-space-time-transformation (RSTT) paradigm and the interpretation of the burst-structure (IBS) paradigm are applied to probe the origin of the time variability of GRBs. Again GRB 991216 is used as a prototypical case, thanks to the precise data from the CGRO, RXTE and Chandra satellites. It is found that with the exception of the relatively inconspicuous but scientifically very important signal originating from the initial "proper gamma ray burst" (P-GRB), all the other spikes and time variabilities can be explained by the interaction of the accelerated-baryonic-matter pulse with inhomogeneities in the interstellar matter. This can be demonstrated by using the RSTT paradigm as well as the IBS paradigm, to trace a typical spike observed in arrival time back to the corresponding one in the laboratory time. Using these paradigms, the identification of the physical nature of the time variablity of the GRBs can be made most convincingly. It is made explicit the dependence of a) the intensities of the afterglow, b) the spikes amplitude and c) the actual time structure on the Lorentz gamma factor of the accelerated-baryonic-matter pulse. In principle it is possible to read off from the spike structure the detailed density contrast of the interstellar medium in the host galaxy, even at very high redshift.

11. R. Ruffini, C.L. Bianco, P. Chardonnet, F. Fraschetti, S.-S. Xue; "On the structures in the afterglow peak emission of gamma ray bursts"; The Astrophysical Journal, 581, L19 (2002).

    Using GRB 991216 as a prototype, it is shown that the intensity substructures observed in what is generally called the "prompt emission" in gamma ray bursts (GRBs) do originate in the collision between the accelerated baryonic matter (ABM) pulse with inhomogeneities in the interstellar medium (ISM). The initial phase of such process occurs at a Lorentz factor $\gamma \sim 310$. The crossing of ISM inhomogeneities of sizes $\Delta R \sim 10^{15}$ cm occurs in a detector arrival time interval of ~ 0.4 s implying an apparent superluminal behavior of $\sim 10^5 c$. The long lasting debate between the validity of the external shock model vs. the internal shock model for GRBs is solved in favor of the first.

12. R. Ruffini, C.L. Bianco, P. Chardonnet, F. Fraschetti, S.-S. Xue; "On the structure of the burst and afterglow of Gamma-Ray Bursts I: the radial approximation"; International Journal of Modern Physics D, 12, 173 (2003).

    We have recently proposed three paradigms for the theoretical interpretation of gamma-ray bursts (GRBs). (1) The relative space-time transformation (RSTT) paradigm emphasizes how the knowledge of the entire world-line of the source from the moment of gravitational collapse is a necessary condition in order to interpret GRB data. (2) The interpretation of the burst structure (IBS) paradigm differentiates in all GRBs between an injector phase and a beam-target phase. (3) The GRB-supernova time sequence (GSTS) paradigm introduces the concept of *induced supernova explosion* in the supernovae-GRB association. In the introduction the RSTT and IBS paradigms are enunciated and illustrated using our theory based on the vacuum polarization process occurring around an electromagnetic black hole (EMBH theory). The results are summarized using figures, diagrams and a complete table with the space-time grid, the fundamental parameters and the corresponding values of the Lorentz gamma factor for GRB 991216 used as a prototype. In the following sections the detailed treatment of the EMBH theory needed to understand the results of the three above letters is presented. We start from the considerations on the dyadosphere formation. We then review the basic hydrodynamic and rate equations, the equations leading to the relative space-time transformations as well as the adopted numerical integration techniques. We then illustrate the five fundamental eras of the EMBH theory: the self acceleration of the e^+e^- pair-electromagnetic plasma (PEM pulse), its interaction with the baryonic remnant of the progenitor star, the further self acceleration of the e^+e^- pair-electroma--gnetic radiation and baryon plasma (PEMB pulse). We then study the approach of the PEMB pulse to transparency, the emission of the proper GRB (P-GRB) and its relation to the "short GRBs". Particular attention is given to the free parameters of the theory and to the values of the thermodynamical quantities at transparency. Finally the three different regimes of the afterglow are described within the fully radiative and radial approximations: the ultrarelativistic, the relativistic and the nonrelativistic regimes. The best fit of the theory leads to an unequivocal identification of the "long GRBs" as extended emission occurring at the afterglow peak (E-APE). The relative intensities, the time separation and the hardness ratio of the P-GRB and the E-APE are used as distinctive observational test of the EMBH theory and the excellent agreement between our theoretical predictions and the observations are documented. The afterglow power-law indexes in the EMBH theory are compared and contrasted with the ones in the literature, and no beaming process is found for GRB 991216. Finally, some preliminary results relating the observed time variability of the E-APE to the inhomogeneities in the interstellar medium are presented, as well as some general considerations on the EMBH formation. The issue of the GSTS paradigm will be the object of a forthcoming publication and the relevance of the iron-lines observed in GRB 991216 is shortly reviewed. The general conclusions are then presented based on the three fundamental parameters of the EMBH theory: the dyadosphere energy, the baryonic mass of the remnant, the interstellar medium density. An in depth discussion and comparison of the EMBH theory with alternative theories is presented as well as indications of further developments beyond the radial approximation, which will be the subject of paper II in this series. Future needs for specific GRB observations are outlined.

13. R. Ruffini, C.L. Bianco, P. Chardonnet, F. Fraschetti, V. Gurzadyan, S.-S. Xue; "On the instantaneous spectrum of gamma ray bursts"; International Journal of Modern Physics D, 13, 843 (2004).

    A theoretical attempt to identify the physical process responsible for the afterglow emission of Gamma-Ray Bursts (GRBs) is presented, leading to the occurrence of thermal emission in the comoving frame of the shock wave giving rise to the bursts. The determination of the luminosities and spectra involves integration over an infinite number of Planckian spectra, weighted by appropriate relativistic transformations, each one corresponding to a different viewing angle in the past light cone of the observer. The relativistic transformations have been computed using the equations of motion of GRBs within our theory, giving special attention to the determination of the equitemporal surfaces. The only free parameter of the present theory is the "effective emitting area" in the shock wave front. A self consistent model for the observed hard-to-soft transition in GRBs is also presented. When applied to GRB 991216 a precise fit $\left(\chi^2 \simeq 1.078\right)$ of the observed luminosity in the 2–10 keV band is obtained. Similarly, detailed estimates of the observed luminosity in the 50–300 keV and in the 10–50 keV bands are obtained.

3.2 Conference proceedings

1. R. Ruffini; "Beyond the critical mass: The dyadosphere of black holes"; in "Black Holes and High Energy Astrophysics", H. sato, N. Sugiyama, Editors; p. 167; Universal Academy Press (Tokyo, Japan, 1998).

   The "dyadosphere" (from the Greek word "duas-duados" for pairs) is here defined as the region outside the horizon of a black hole endowed with an electromagnetic field (abbreviated to EMBH for "electromagnetic black hole") where the electromagnetic field exceeds the critical value, predicted by Heisenberg and Euler for e^+e^- pair production. In a very short time ($\sim O(\hbar/mc^2)$), a very large number of pairs is created there. I give limits on the EMBH parameters leading to a Dyadosphere for $10M_\odot$ and $10^5M_\odot$ EMBH's, and give as well the pair densities as functions of the radial coordinate. These data give the initial conditions for the analysis of an enormous pair-electromagnetic-pulse or "PEM-pulse" which naturally leads to relativistic expansion. Basic energy requirements for gamma ray bursts (GRB), including GRB971214 recently observed at $z = 3.4$, can be accounted for by processes occurring in the dyadosphere.

2. R. Ruffini, C.L. Bianco, P. Chardonnet, F. Fraschetti, L. Vitagliano, S.-S. Xue; "New perspectives in physics and astrophysics from the theoretical understanding of Gamma-Ray Bursts"; in "COSMOLOGY AND GRAVITATION: Xth Brazilian School of Cosmology and Gravitation; 25th Anniversary (1977-2002)", Proceedings of the Xth Brazilian School on Cosmology and Gravitation, Mangaratiba, Rio de Janeiro (Brazil), July - August 2002, M. Novello, S.E. Perez Bergliaffa, Editors; AIP Conference Proceedings, 668, 16 (2003).

   If due attention is given in formulating the basic equations for the Gamma-Ray Burst (GRB) phenomenon and in performing the corresponding quantitative analysis, GRBs open a main avenue of inquiring on totally new physical and astrophysical regimes. This program is very likely one of the greatest computational efforts in physics and astrophysics and cannot be actuated using shortcuts. A systematic approach is needed which has been highlighted in three basic new paradigms: the relative space-time transformation (RSTT) paradigm, the interpretation of the burst structure (IBS) paradigm, the GRB-supernova time sequence (GSTS) paradigm. From the point of view of fundamental physics new regimes are explored: (1) the process of energy extraction from black holes; (2) the quantum and general relativistic effects of matter-antimatter creation near the black hole horizon; (3) the physics of ultrarelativisitc shock waves with Lorentz gamma factor $\gamma > 100$. From the point of view of astronomy and astrophysics also new regimes are explored: (i) the occurrence of gravitational collapse to a black hole from a critical mass core of mass $M \gtrsim 10M_{\odot}$, which clearly differs from the values of the critical mass encountered in the study of stars "catalyzed at the endpoint of thermonuclear evolution" (white dwarfs and neutron stars); (ii) the extremely high efficiency of the spherical collapse to a black hole, where almost 99.99% of the core mass collapses leaving negligible remnant; (iii) the necessity of developing a fine tuning in the final phases of thermonuclear evolution of the stars, both for the star collapsing to the black hole and the surrounding ones, in order to explain the possible occurrence of the "induced gravitational collapse". New regimes are as well encountered from the point of view of nature of GRBs: (I) the basic structure of GRBs is uniquely composed by a proper-GRB (P-GRB) and the afterglow; (II) the long bursts are then simply explained as the peak of the afterglow (the E-APE) and their observed time variability is explained in terms of inhomogeneities in the interstellar medium (ISM); (III) the short bursts are identified with the P-GRBs and the crucial information on general relativistic and vacuum polarization effects are encoded in their spectra and intensity time variability. A new class of space missions to acquire information on such extreme new regimes are urgently needed.

3. R. Ruffini, C.L. Bianco, P. Chardonnet, F. Fraschetti, S.-S. Xue; "The EMBH Model in GRB 991216 and GRB 980425"; in Proceedings of "Third Rome Workshop on Gamma-Ray Burst in the Afterglow Era", 17-20 September 2002; M. Feroci, F. Frontera, N. Masetti, L. Piro, Editors; ASP Conference Series, 312, 349 (2004).

   This is a summary of the two talks presented at the Rome GRB meeting by C.L. Bianco and R. Ruffini. It is shown that by respecting the Relative Space-Time Transformation (RSTT) paradigm and the Interpretation of the Burst Structure (IBS) paradigm, important inferences are possible: a) in the new physics occurring in the energy sources of GRBs, b) on the structure of the bursts and c) on the composition of the interstellar matter surrounding the source.

4. M.G. Bernardini, C.L. Bianco, P. Chardonnet, F. Fraschetti, R. Ruffini, S.-S. Xue; "A New Astrophysical 'Triptych': GRB030329/SN2003dh/ URCA-2"; in "GAMMA-RAY BURSTS: 30 YEARS OF DISCOVERY", Proceedings of the Los Alamos "Gamma Ray Burst Symposium", Santa Fe, New Mexico, 8 – 12 September 2003, E.E. Fenimore, M. Galassi, Editors; AIP Conference Proceedings, 727, 312 (2004).

   We analyze the data of the Gamma-Ray Burst/Supernova GRB030329/ SN2003dh system obtained by HETE-2, R-XTE, XMM and VLT within our theory for GRB030329. By fitting the only three free parameters of the EMBH theory, we obtain the luminosity in fixed energy bands for the prompt emission and the afterglow. Since the Gamma-Ray Burst (GRB) analysis is consistent with a spherically symmetric expansion, the energy of GRB030329 is $E = 2.1 \times 10^{52}$ erg, namely $\sim 2 \times 10^3$ times larger than the Supernova energy. We conclude that either the GRB is triggering an induced-supernova event or both the GRB and the Supernova are triggered by the same relativistic process. In no way the GRB can be originated from the supernova. We also evidence that the XMM observations, much like in the system GRB980425/SN1998bw, are not part of the GRB afterglow, as interpreted in the literature, but are associated to the Supernova phenomenon. A dedicated campaign of observations is needed to confirm the nature of this XMM source as a newly born neutron star cooling by generalized URCA processes.

5. F. Fraschetti, M.G. Bernardini, C.L. Bianco, P. Chardonnet, R. Ruffini, S.-S. Xue; "The GRB980425-SN1998bw Association in the EMBH Model"; in "GAMMA-RAY BURSTS: 30 YEARS OF DISCOVERY", Proceedings of the Los Alamos "Gamma Ray Burst Symposium", Santa Fe, New Mexico, 8 – 12 September 2003, E.E. Fenimore, M. Galassi, Editors; AIP Conference Proceedings, 727, 424 (2004).

   Our GRB theory, previously developed using GRB 991216 as a prototype, is here applied to GRB 980425. We fit the luminosity observed in the 40–700 keV, 2–26 keV and 2–10 keV bands by the BeppoSAX satellite. In addition the supernova SN1998bw is the outcome of an "induced gravitational collapse" triggered by GRB 980425, in agreement with the GRB-Supernova Time Sequence (GSTS) paradigm. A further outcome of this astrophysically exceptional sequence of events is the formation of a young neutron star generated by the SN1998bw event. A coordinated observational activity is recommended to further enlighten the underlying scenario of this most unique astrophysical system.

6. A. Corsi, M.G. Bernardini, C.L. Bianco, P. Chardonnet, F. Fraschetti, R. Ruffini, S.-S. Xue; "GRB 970228 Within the EMBH Model"; in "GAMMA-RAY BURSTS: 30 YEARS OF DISCOVERY", Proceedings of the Los Alamos "Gamma Ray Burst Symposium", Santa Fe, New Mexico, 8 – 12 September 2003, E.E. Fenimore, M. Galassi, Editors; AIP Conference Proceedings, 727, 428 (2004).

   We consider the gamma-ray burst of 1997 February 28 (GRB 970228) within the ElectroMagnetic Black Hole (EMBH) model. We first determine the value of the two free parameters that characterize energetically the GRB phenomenon in the EMBH model, that is to say the dyadosphere energy, $E_{dya} = 5.1 \times 10^{52}$ ergs, and the baryonic remnant mass M_B in units of E_{dya}, $B = M_B c^2 / E_{dya} = 3.0 \times 10^{-3}$. Having in this way estimated the energy emitted during the beam-target phase, we evaluate the role of the InterStellar Medium (ISM) number density (n_{ISM}) and of the ratio $\mathcal{R}$ between the effective emitting area and the total surface area of the GRB source, in reproducing the observed profiles of the GRB 970228 prompt emission and X-ray (2-10 keV energy band) afterglow. The importance of the ISM distribution three-dimensional treatment around the central black hole is also stressed in this analysis.

4 Publications (2005–2022)

4.1 Refereed journals

1. R. Ruffini, C.L. Bianco, P. Chardonnet, F. Fraschetti, V. Gurzadyan, S.-S. Xue; "Emergence of a filamentary structure in the fireball from GRB spectra"; International Journal of Modern Physics D, 14, 97 (2005).

   It is shown that the concept of a fireball with a definite filamentary structure naturally emerges from the analysis of the spectra of Gamma-Ray Bursts (GRBs). These results, made possible by the recently obtained analytic expressions of the equitemporal surfaces in the GRB afterglow, depend crucially on the single parameter R describing the effective area of the fireball emitting the X-ray and gamma-ray radiation. The X-ray and gamma-ray components of the afterglow radiation are shown to have a thermal spectrum in the co-moving frame of the fireball and originate from a stable shock front described self-consistently by the Rankine-Hugoniot equations. Precise predictions are presented on a correlation between spectral changes and intensity variations in the prompt radiation verifiable, e.g., by the Swift and future missions. The highly variable optical and radio emission depends instead on the parameters of the surrounding medium. The GRB 991216 is used as a prototype for this model.

2. R. Ruffini, M.G. Bernardini, C.L. Bianco, P. Chardonnet, F. Fraschetti, V. Gurzadyan, M. Lattanzi, L. Vitagliano, S.-S. Xue; "Extracting energy from black holes: 'long' and 'short' GRBs and their astrophysical settings"; Il Nuovo Cimento C, 28, 589 (2005).

   The introduction of the three interpretational paradigms for Gamma-Ray Bursts (GRBs) and recent progress in understanding the X- and gamma-ray luminosity in the afterglow allow us to make assessments about the astrophysical settings of GRBs. In particular, we evidence the distinct possibility that some GRBs occur in a binary system. This subclass of GRBs manifests itself in a "tryptich": one component formed by the collapse of a massive star to a black hole, which originates the GRB; a second component by a supernova and a third one by a young neutron star born in the supernova event. Similarly, the understanding of the physics of quantum relativistic processes during the gravitational collapse makes possible precise predictions about the structure of short GRBs.

3. M.G. Bernardini, C.L. Bianco, P. Chardonnet, F. Fraschetti, R. Ruffini, S.-S. Xue; "Theoretical interpretation of luminosity and spectral properties of GRB 031203"; The Astrophysical Journal, 634, L29 (2005).

   The X-ray and gamma-ray observations of the source GRB 031203 by INTEGRAL are interpreted within our theoretical model. In addition to a complete spacetime parameterization of the GRB, we specifically assume that the afterglow emission originates from a thermal spectrum in the comoving frame of the expanding baryonic matter shell. By determining the two free parameters of the model and estimating the density and filamentary structure of the ISM, we reproduce the observed luminosity in the 20-200 keV energy band. As in previous sources, the prompt radiation is shown to coincide with the peak of the afterglow, and the luminosity substructure is shown to originate in the filamentary structure of the ISM. We predict a clear hard-to-soft behavior in the instantaneous spectra. The time-integrated spectrum over 20 s observed by INTEGRAL is well fitted. Despite the fact that this source has been considered "unusual", it appears to us to be a normal low-energy GRB.

4. R. Ruffini, M.G. Bernardini, C.L. Bianco, P. Chardonnet, F. Fraschetti, S.-S. Xue; Evidence for isotropic emission in GRB991216; Advances in Space Research, 38, 1291 (2006).

   The issue of the possible presence or absence of jets in GRBs is here re-examined for GRB991216. We compare and contrast our theoretically predicted afterglow luminosity in the 2–10 keV band for spherically symmetric versus jetted emission. At these wavelengths the jetted emission can be excluded and data analysis confirms spherical symmetry. These theoretical fits are expected to be improved by the forthcoming data of the Swift mission.

5. R. Ruffini, M.G. Bernardini, C.L. Bianco, P. Chardonnet, F. Fraschetti, R. Guida, S.-S. Xue; "GRB 050315: A step toward understanding the uniqueness of the overall GRB structure"; The Astrophysical Journal, 645, L109 (2006).

Using the Swift data of GRB 050315, we are making progress toward understanding the uniqueness of our theoretically predicted gamma-ray burst (GRB) structure, which is composed of a proper GRB (P-GRB), emitted at the transparency of an electron-positron plasma with suitable baryon loading, and an afterglow comprising the so-called prompt emission due to external shocks. Thanks to the Swift observations, the P-GRB is identified, and for the first time we can theoretically fit detailed light curves for selected energy bands on a continuous timescale ranging over 106 s. The theoretically predicted instantaneous spectral distribution over the entire afterglow is presented, confirming a clear hard-to-soft behavior encompassing, continuously, the "prompt emission" all the way to the latest phases of the afterglow.

6. C.L. Bianco, L. Caito, R. Ruffini; "Theoretical interpretation of GRB 011121"; Il Nuovo Cimento B, 121, 1441 (2006).

   GRB011121 is analyzed as a prototype to understand the "flares" recently observed by Swift in the afterglow of many GRB sources. Detailed theoretical computation of the GRB011121 light curves in selected energy bands are presented and compared and contrasted with observational BeppoSAX data.

7. R. Ruffini, M.G. Bernardini, C.L. Bianco, P. Chardonnet, F. Fraschetti, R. Guida, S.-S. Xue; "GRB 050315: A step toward the uniqueness of the overall GRB structure"; Il Nuovo Cimento B, 121, 1367 (2006).

   Using the *Swift* data of GRB 050315, we progress on the uniqueness of our theoretically predicted Gamma-Ray Burst (GRB) structure as composed by a proper-GRB (P-GRB), emitted at the transparency of an electron-positron plasma with suitable baryon loading, and an afterglow comprising the so called "prompt emission" as due to external shocks. Thanks to the *Swift* observations, we can theoretically fit detailed light curves for selected energy bands on a continuous time scale ranging over 10^6 seconds. The theoretically predicted instantaneous spectral distribution over the entire afterglow confirms a clear hard-to-soft behavior encompassing, continuously, the "prompt emission" all the way to the latest phases of the afterglow. Consequences of the instrumental threshold on the definition of "short" and "long" GRBs are discussed.

8. M.G. Bernardini, C.L. Bianco, L. Caito, P. Chardonnet, A. Corsi, M.G. Dainotti, F. Fraschetti, R. Guida, R. Ruffini, S.-S. Xue; GRB970228 as a prototype for short GRBs with afterglow; Il Nuovo Cimento B, 121, 1439 (2006).

GRB970228 is analyzed as a prototype to understand the relative role of short GRBs and their associated afterglows, recently observed by Swift and HETE-II. Detailed theoretical computation of the GRB970228 light curves in selected energy bands are presented and compared with observational BeppoSAX data.

9. M.G. Dainotti, M.G. Bernardini, C.L. Bianco, L. Caito, R. Guida, R. Ruffini; "GRB060218 and GRBs associated with Supernovae Ib/c"; Astronomy & Astrophysics, 471, L29 (2007).

   Context: The *Swift* satellite has given continuous data in the range 0.3–150 keV from 0 s to 10^6 s for GRB060218 associated with SN2006aj. This Gamma-Ray Burst (GRB) which has an unusually long duration ($T_{90} \sim 2100$ s) fulfills the Amati relation. These data offer the opportunity to probe theoretical models for GRBs connected with Supernovae (SNe).
   Aims: We plan to fit the complete γ- and X-ray light curves of this long duration GRB, including the prompt emission, in order to clarify the nature of the progenitors and the astrophysical scenario of the class of GRBs associated with SNe Ib/c.
   Methods: We apply our "fireshell" model based on the formation of a black hole, giving the relevant references. It is characterized by the precise equations of motion and equitemporal surfaces and by the role of thermal emission.
   Results: The initial total energy of the electron-positron plasma $E_{e^\pm}^{tot} = 2.32 \times 10^{50}$ erg has a particularly low value, similar to the other GRBs associated with SNe. For the first time, we observe a baryon loading $B = 10^{-2}$ which coincides with the upper limit for the dynamical stability of the fireshell. The effective CircumBurst Medium (CBM) density shows a radial dependence $n_{cbm} \propto r^{-\alpha}$ with $1.0 \lesssim \alpha \lesssim 1.7$ and monotonically decreases from 1 to 10^{-6} particles/cm^3. This behavior is interpreted as being due to a fragmentation in the fireshell. Analogies with the fragmented density and filling factor characterizing Novae are outlined. The fit presented is particularly significant in view of the complete data set available for GRB060218 and of the fact that it fulfills the Amati relation.
   Conclusions: We fit GRB060218, usually considered as an X-Ray Flash (XRF), as a "canonical GRB" within our theoretical model. The smallest possible black hole, formed by the gravitational collapse of a neutron star in a binary system, is consistent with the especially low energetics of the class of GRBs associated with SNe Ib/c. We provide the first evidence for a fragmentation in the fireshell. This fragmentation is crucial in explaining both the unusually large T_{90} and the consequently inferred abnormally low value of the CBM effective

density.

10. M.G. Bernardini, C.L. Bianco, L. Caito, M.G. Dainotti, R. Guida, R. Ruffini; "GRB970228 and a class of GRBs with an initial spikelike emission"; Astronomy & Astrophysics, 474, L13 (2007).

    Context: The discovery by *Swift* and HETE-2 of an afterglow emission associated possibly with short GRBs opened the new problematic of their nature and classification. This issue has been further enhanced by the observation of GRB060614 and by a new analysis of the BATSE catalog which led to the identification of a new class of GRBs with "an occasional softer extended emission lasting tenths of seconds after an initial spikelike emission".
    Aims: We plan a twofold task: a) to fit this new class of "hybrid" sources within our "canonical GRB" scenario, where all GRBs are generated by a "common engine" (i.e. the gravitational collapse to a black hole); b) to propose GRB970228 as the prototype of the above mentioned class, since it shares the same morphology and observational features.
    Methods: We analyze *Beppo*SAX data on GRB970228 within the "fireshell" model and we determine the parameters describing the source and the CircumBurst Medium (CBM) needed to reproduce its light curves in the 40–700 keV and 2–26 keV energy bands.
    Results: We find that GRB970228 is a "canonical GRB", like e.g. GRB050315, with the main peculiarity of a particularly low average density of the CBM $\langle n_{cbm} \rangle \sim 10^{-3}$ particles/cm^3. We also simulate the light curve corresponding to a rescaled CBM density profile with $\langle n_{cbm} \rangle = 1$ particle/cm^3. From such a comparison it follows that the total time-integrated luminosity is a faithful indicator of the nature of GRBs, contrary to the peak luminosity which is merely a function of the CBM density.
    Conclusions: We call attention on discriminating the short GRBs between the "genuine" and the "fake" ones. The "genuine" ones are intrinsically short, with baryon loading $B \lesssim 10^{-5}$, as stated in our original classification. The "fake" ones, characterized by an initial spikelike emission followed by an extended emission lasting tenths of seconds, have a baryon loading $10^{-4} \lesssim B \leq 10^{-2}$. They are observed as such only due to an underdense CBM consistent with a galactic halo environment which deflates the afterglow intensity.

11. R. Guida, M.G. Bernardini, C.L. Bianco, L. Caito, M.G. Dainotti, R. Ruffini; "The Amati relation in the "fireshell" model"; Astronomy & Astrophysics, 487, L37 (2008).

Context: The cosmological origin of gamma-ray bursts (GRBs) has been firmly established, with redshifts up to $z = 6.29$. They are possible candidates for use as "distance indicators" for testing cosmological models in a redshift range hardly achievable by other cosmological probes. Asserting the validity of the empirical relations among GRB observables is now crucial for their calibration.
Aims: Motivated by the relation proposed by Amati and collaborators, we look within the "fireshell" model for a relation between the peak energy E_p of the νF_ν total time-integrated spectrum of the afterglow and the total energy of the afterglow E_{aft}, which in our model encompasses and extends the prompt emission.
Methods: The fit within the fireshell model, as for the "canonical" GRB050315, uses the complete arrival time coverage given by the Swift satellite. It is performed simultaneously, self-consistently, and recursively in the four BAT energy bands (15–25 keV, 25–50 keV, 50–100 keV, and 100-150 keV), as well as in the XRT one (0.2–10 keV). It uniquely determines the two free parameters characterizing the GRB source, the total energy $E_{tot}^{e^\pm}$ of the $e^\pm$ plasma and its baryon loading B, as well as the effective CircumBurst Medium (CBM) distribution. We can then build two sets of "gedanken" GRBs varying the total energy of the electron-positron plasma $E_{tot}^{e^\pm}$ and keeping the same baryon loading B of GRB050315. The first set assumes the one obtained in the fit of GRB050315 for the effective CBM density. The second set assumes instead a constant CBM density equal to the average value of the GRB050315 prompt phase.
Results: For the first set of "gedanken" GRBs we find a relation $E_p \propto (E_{aft})^a$, with $a = 0.45 \pm 0.01$, whose slope strictly agrees with the Amati one. Such a relation, in the limit $B \to 10^{-2}$, coincides with the Amati one. Instead, no correlation is found in the second set of "gedanken" GRBs.
Conclusions: Our analysis excludes the proper GRB (P-GRB) from the prompt emission, extends all the way to the latest afterglow phases, and is independent of the assumed cosmological model, since all "gedanken" GRBs are at the same redshift. The Amati relation, on the other hand, includes the P-GRB, focuses only on the prompt emission, being therefore influenced by the instrumental threshold that fixes the end of the prompt emission, and depends on the assumed cosmology. This might explain the intrinsic scatter observed in the Amati relation.

12. L. Caito, M.G. Bernardini, C.L. Bianco, M.G. Dainotti, R. Guida, R. Ruffini; "GRB060614: a "fake" short GRB from a merging binary system"; Astronomy & Astrophysics, 489, 501 (2009).

Context: GRB060614 observations by VLT and by Swift have infringed the traditionally accepted gamma-ray burst (GRB) collapsar scenario that purports the origin of all long duration GRBs from supernovae (SN). GRB060614 is the first nearby long duration GRB clearly not associated with a bright Ib/c SN. Moreover, its duration ($T_{90} \sim 100$ s) makes it hardly classifiable as a short GRB. It presents strong similarities with GRB970228, the prototype of a new class of "fake" short GRBs that appear to originate from the coalescence of binary neutron stars or white dwarfs spiraled out into the galactic halo. *Aims*: Within the "canonical" GRB scenario based on the "fireshell" model, we test if GRB060614 can be a "fake" or "disguised" short GRB. We model the traditionally termed "prompt emission" and discriminate the signal originating from the gravitational collapse leading to the GRB from the process occurring in the circumburst medium (CBM). *Methods*: We fit GRB060614 light curves in Swift's BAT ($15 - 150$ keV) and XRT ($0.2 - 10$ keV) energy bands. Within the fireshell model, light curves are formed by two well defined and different components: the proper-GRB (P-GRB), emitted when the fireshell becomes transparent, and the extended afterglow, due to the interaction between the leftover accelerated baryonic and leptonic shell and the CBM. *Results*: We determine the two free parameters describing the GRB source within the fireshell model: the total $e^{\pm}$ plasma energy ($E_{tot}^{e^{\pm}} = 2.94 \times 10^{51}$erg) and baryon loading ($B = 2.8 \times 10^{-3}$). A small average CBM density $\sim 10^{-3}$ particles/cm^3 is inferred, typical of galactic halos. The first spikelike emission is identified with the P-GRB and the following prolonged emission with the extended afterglow peak. We obtain very good agreement in the BAT ($15 - 150$ keV) energy band, in what is traditionally called "prompt emission", and in the XRT ($0.2 - 10$ keV) one. *Conclusions*: The *anomalous* GRB060614 finds a natural interpretation within our canonical GRB scenario: it is a "disguised" short GRB. The total time-integrated extended afterglow luminosity is greater than the P-GRB one, but its peak luminosity is smaller since it is deflated by the peculiarly low average CBM density of galactic halos. This result points to an old binary system, likely formed by a white dwarf and a neutron star, as the progenitor of GRB060614 and well justifies the absence of an associated SN Ib/c. Particularly important for further studies of the final merging process are the temporal structures in the P-GRB down to 0.1 s.

13. M.G. Bernardini, C.L. Bianco, L. Caito, M.G. Dainotti, R. Guida, R. Ruffini; "GRB970228 in the "canonical GRB" scenario"; Journal of the Korean Physical Society, 56, 1575 (2010).

Within the "fireshell" model, we define a "canonical GRB" light curve with two sharply different components: the proper-GRB (P-GRB), emitted when the optically thick fireshell of an electron-positron plasma originating from the phenomenon reaches transparency, and the afterglow, emitted due to the collision between the remaining optically thin fireshell and the circumburst medium (CBM). On the basis of the recent understanding of GRB970228 as the prototype for a new class of GRBs with "an occasional softer extended emission lasting tenths of seconds after an initial spikelike emission", we outline our "canonical GRB" scenario, originating from the gravitational collapse to a black hole, with special emphasis on the discrimination between "genuine" and "fake" short GRBs. Furthermore, we investigate how the GRB970228 analysis provides a theoretical explanation for the apparent absence of such a correlation for the GRBs belonging to this new class.

14. L. Caito, M.G. Bernardini, C.L. Bianco, M.G. Dainotti, R. Guida, R. Ruffini; "GRB060614: a preliminary result"; Journal of the Korean Physical Society, 56, 1579 (2010).

    The explosion of GRB 060614 produced a deep break in the GRB scenario and opened new horizons of investigation because it can't be traced back to any traditional scheme of classification. In fact, it manifests peculiarities both of long bursts and of short bursts, and above all, it is the first case of a long-duration near GRB without any bright Ib/c associated Supernova. We will show that, in our canonical GRB scenario, this "anomalous" situation finds a natural interpretation and allows us to discuss a possible variation in the traditional classification scheme, introducing a distinction between "genuine" and "fake" short bursts.

15. M.G. Dainotti, M.G. Bernardini, C.L. Bianco, L. Caito, R. Guida, R. Ruffini; "The astrophysical trypthic: GRB, SN and URCA can be extended to GRB060218?"; Journal of the Korean Physical Society, 56, 1588 (2010).

    The *Swift* satellite has given continuous data in the range 0.3–150 keV from 0 s to 10^6 s for GRB060218 associated with SN2006aj. This GRB is the fourth GRB spectroscopically associated with SNe after the cases of GRB980425-SN1998bw, GRB031203-SN2003lw, GRB 030329-SN2003dh. It has an unusually long duration ($T_{90} \sim 2100$ s). These data offer the opportunity to probe theoretical models for Gamma-Ray Bursts (GRBs) connected with Supernovae (SNe). We plan to fit the complete γ- and X-ray light curves of this long duration GRB, including the prompt emission, in order to clarify the nature of the progenitors and the astrophysical scenario of the class of GRBs associated to SNe Ib/c. We apply our "fireshell" model based on the formation of a black hole, giving the relevant references. The initial total energy of the electron-positron plasma $E^{tot}_{e^{\pm}} = 2.32 \times 10^{50}$ erg has a particularly low value similarly to the other GRBs associated with SNe. For the first time we observe a baryon loading $B = 10^{-2}$ which coincides with the upper limit for the dynamical stability of the fireshell. The effective CircumBurst Medium (CBM) density shows a radial dependence $n_{cbm} \propto r^{-\alpha}$ with $1.0 \lesssim \alpha \lesssim 1.7$ and monotonically decreases from 1 to 10^{-6} particles/cm^3. Such a behavior is interpreted as due to a fragmentation in the fireshell. Such a fragmentation is crucial in explaining both the unusually large T_{90} and the consequently inferred abnormal low value of the CBM effective density. We fit GRB060218, usually considered as an X-Ray Flash (XRF), as a "canonical GRB" within our theoretical model. The smallest possible black hole, formed by the gravitational collapse of a neutron star in a binary system, is consistent with the especially low energetics of the class of GRBs associated with SNe Ib/c. We present the URCA process and the connection between the GRBs associated with SNe extended also to the case of GRB060218.

16. L. Izzo, M.G. Bernardini, C.L. Bianco, L. Caito, B. Patricelli, R. Ruffini; "GRB 090423 at Redshift 8.1: a Theoretical Interpretation"; Journal of the Korean Physical Society, 57, 551 (2010).

    GRB 090423 is the farthest gamma ray burst ever observed, with a redshift of about 8.1. We present within the fireshell scenario a complete analysis of this GRB. We model the prompt emission and the first rapid flux decay of the afterglow emission as being to the canonical emission of the interaction in the interval $0 \leq t \leq 440$ s by using accelerated baryonic matter with the circumburst medium. After the data reduction of the Swift data in the BAT (15 - 150 keV) and XRT (0.2 - 10 keV) energy bands, we interpret the light curves and the spectral distribution in the context of the fireshell scenario. We also confirm in this source the existence of a second component, a plateau phase, as being responsible for the late emission in the X-ray light curve. This extra component originates from the fact that the ejecta have a range of the bulk Lorentz Γ factor, which starts to interact each other ejecta at the start of the plateau phase.

17. L. Caito, L. Amati, M.G. Bernardini, C.L. Bianco, G. De Barros, L. Izzo, B. Patricelli, R. Ruffini; "GRB 071227: an additional case of a disguised

short burst"; Astronomy & Astrophysics, 521, A80 (2010).

Context: Observations of gamma-ray bursts (GRBs) have shown an hybridization between the two classes of long and short bursts. In the context of the fireshell model, the GRB light curves are formed by two different components: the *proper* GRB (P-GRB) and the extended afterglow. Their relative intensity is linked to the fireshell baryon loading B. The GRBs with P-GRB predominance are the short ones, the remainders are long. A new family of *disguised* short bursts has been identified: long bursts with a protracted low instantaneous luminosity due to a low density CircumBurst Medium (CBM). In the 15–150 keV energy band GRB 071227 exhibits a short duration (about 1.8s) spike-like emission followed by a very soft extended tail up to one hundred seconds after the trigger. It is a faint ($E_{iso} = 5.8 \times 10^{50}$) nearby GRB ($z = 0.383$) that does not have an associated type Ib/c bright supernova (SN). For these reasons, GRB 071227 has been classified as a short burst not fulfilling the Amati relation holding for long burst. *Aims:* We check the classification of GRB 071227 provided by the fireshell model. In particular, we test whether this burst is another example of a *disguised* short burst, after GRB 970228 and GRB 060614, and, for this reason, whether it fulfills the Amati relation. *Methods:* We simulate GRB 071227 light curves in the *Swift* BAT 15–50 keV bandpass and in the XRT (0.3–10 keV) energy band within the fireshell model. *Results:* We perform simulations of the tail in the 15–50 keV bandpass, as well as of the first part of the X-ray afterglow. This infers that: $E_{tot}^{e^\pm} = 5.04 \times 10^{51}$ erg, $B = 2.0 \times 10^{-4}$, $E_{P-GRB}/E_{aft} \sim 0.25$, and $\langle n_{cbm} \rangle = 3.33$ particles/cm^3. These values are consistent with those of "long duration" GRBs. We interpret the observed energy of the first hard emission by identifying it with the P-GRB emission. The remaining long soft tail indeed fulfills the Amati relation. *Conclusions:* Previously classified as a short burst, GRB 071227 on the basis of our analysis performed in the context of the fireshell scenario represents another example of a *disguised* short burst, after GRB 970228 and GRB 060614. Further confirmation of this result is that the soft tail of GRB 071227 fulfills the Amati relation.

18. M.G. Bernardini, C.L. Bianco, L. Caito, L. Izzo, B. Patricelli, R. Ruffini; "Analysis of GRB060607A within the fireshell model: prompt emission, X-ray flares and late afterglow phase"; Astronomy & Astrophysics, submitted to.

    Context: GRB060607A is a very distant ($z = 3.082$) and energetic event ($E_{iso} \sim 10^{53}$ erg). Its main peculiarity is that the peak of the near-infrared (NIR) afterglow has been observed with the REM robotic telescope. This NIR peak has been interpreted as the afterglow onset within the fireball forward shock model, and the initial Lorentz gamma factor of the emitting system has been inferred. *Aims*: We analyze GRB060607A within the fireshell model. We emphasize the central role of the prompt emission in determining the initial Lorentz gamma factor of the extended afterglow and we interpret the X-ray flares as produced by the interaction of the optically thin fireshell with overdense CircumBurst Medium (CBM) clumps. *Methods*: We deal only with the Swift BAT and XRT observations, that are the basic contribution to the GRB emission and that are neglected in the treatment adopted in the current literature. The numerical modeling of the fireshell dynamics allows to calculate all its characteristic quantities, in particular the exact value of the Lorentz gamma factor at the transparency. *Results*: We show that the theoretically computed prompt emission light curves are in good agreement with the observations in all the *Swift* BAT energy bands as well as the spectra integrated over different time intervals. The flares observed in the decaying phase of the X-ray afterglow are also reproduced by the same mechanism, but in a region in which the typical dimensions of the clumps are smaller than the visible area of the fireshell and most energy lies in the X-ray band due to the hard-to-soft evolution. *Conclusions*: We show that it is possible to obtain flares with $\Delta t/t$ compatible with the observations when the three-dimensional structure of the CBM clumps is duly taken into account. We stop our analysis at the beginning of the X-ray plateau phase, since we suppose this originates from the instabilities developed in the collision between different subshells within a structured fireshell.

19. G. de Barros, M. G. Bernardini, C.L. Bianco, L. Caito, L. Izzo, B. Patricelli, R. Ruffini; "On the nature of GRB 050509b: a disguised short GRB"; Astronomy & Astrophyscs, 529, A130 (2011)

    Context: GRB 050509b, detected by the *Swift* satellite, is the first case where an X-ray afterglow has been observed associated with a short gamma-ray burst (GRB). Within the fireshell model, the canonical GRB light curve presents two different components: the proper-GRB (P-GRB) and the extended afterglow. Their relative intensity is a function of the fireshell baryon loading parameter B and of the CircumBurst Medium (CBM) density (n_{CBM}). In particular, the traditionally called short GRBs can be either "genuine" short GRBs (with $B \lesssim 10^{-5}$, where the P-GRB is energetically predominant) or "disguised" short GRBs (with $B \gtrsim 3.0 \times 10^{-4}$ and $n_{CBM} \ll 1$, where the extended afterglow is energetically predominant). *Aims*: We verify whether GRB 050509b can be classified as a “genuine” short or a “disguised” short GRB, in the fireshell model. *Methods*: We investigate two alternative scenarios. In the first, we start from the assumption that this GRB is a “genuine” short burst. In the second attempt, we assume that this GRB is a “disguised” burst. *Results*: If GRB 050509b were a genuine short GRB, there should initially be very hard emission which is ruled out by the observations. The analysis that assumes that this is a disguised short GRB is compatible with the observations. The theoretical model predicts a value of the extended afterglow energy peak that is consistent with the Amati relation. *Conclusions*: GRB 050509b cannot be classified as a “genuine” short GRB. The observational data are consistent with a “disguised” short GRB classification, i.e., a long burst with a weak extended afterglow “deflated” by the low density of the CBM. We expect that all short GRBs with measured redshifts are disguised short GRBs because of a selection effect: if there is enough energy in the afterglow to measure the redshift, then the proper GRB must be less energetic than the afterglow. The Amati relation is found to be fulfilled only by the extended afterglow excluding the P-GRB.

20. L. Caito, M.G. Bernardini, C.L. Bianco, L. Izzo, B. Patricelli, R. Ruffini; “GRB 071227: another disguised short burst”; International Journal of Modern Physics D, 20, 1931 (2011).

    Observations of Gamma-ray Bursts (GRBs) put forward in the recent years have revealed, with increasing evidence, that the historical classification between long and short bursts has to be revised. Within the Fireshell scenario, both short and long bursts are canonical bursts, consisting of two different phases. First, a Proper-GRB (P-GRB), that is the emission of photons at the transparency of the fireshell. Then, the Extended Afterglow, multiwavelength emission due to the interacion of the baryonic remnants of the fireshell with the CircumBurst Medium (CBM). We discriminate between long and short bursts by the amount of energy stored in the first phase with respect to the second one. Within the Fireshell scenario, we have introduced a third intermediate class: the disguised GRBs. They appear like short bursts, because their morphology is characterized by a first, short, hard episode and a following deflated tail, but this last part — coincident with the peak of the afterglow — is energetically predominant. The origin of this peculiar kind of sources is inferred to a very low average density of the environment (of the order of 10^{-3}). After GRB 970228 and GRB 060614, we find in GRB 071227 a third example of disguised burst.

21. L. Izzo, M.G. Bernardini, C.L. Bianco, L. Caito, B. Patricelli, L.J. Rangel Lemos, R. Ruffini; "GRB 080916C and the high-energy emission in the fireshell scenario"; International Journal of Modern Physics D, 20, 1949 (2011).

    In this paper we discuss a possible explanation for the high energy emission (up to $\sim$ GeV) seen in GRB 080916C. We propose that the GeV emission is originated by the collision between relativistic baryons in the fireshell after the transparency and the nucleons located in molecular clouds near the burst site. This collision should give rise pion production, whose immediate decay provides high energy photons, neutrinos and leptons. Using a public code (SYBILL) we simulate these relativistic collisions in their simple form, so that we can draw our preliminar results in this paper. We will present moreover our hypothesis that the delayed onset of this emission identifies in a complete way the P-GRB emission.

22. B. Patricelli, M.G. Bernardini, C.L. Bianco, L. Caito, L. Izzo, R. Ruffini, G. Vereshchagin; "A new spectral energy distribution of photons in the fireshell model of GRBs"; International Journal of Modern Physics D, 20, 1983 (2011).

    The analysis of various Gamma-Ray Bursts (GRBs) having a low energetics (an isotropic energy $E_{iso} \lesssim 10^{53}$ ergs) within the fireshell model has shown how the $N(E)$ spectrum of their prompt emission can be reproduced in a satisfactory way by a convolution of thermal spectra. Nevertheless, from the study of very energetic bursts ($E_{iso} \lesssim 10^{54}$ ergs) such as, for example, GRB 080319B, some discrepancies between the numerical simulations and the observational data have been observed. We investigate a different spectrum of photons in the comoving frame of the fireshell in order to better reproduce the spectral properties of GRB prompt emission within the fireshell model. We introduce a phenomenologically modified thermal spectrum: a thermal spectrum characterized by a different asymptotic power-law index in the low energy region. Such an index depends on a free parameter α, so that the pure thermal spectrum corresponds to the case $\alpha = 0$. We test this spectrum by comparing the numerical simulations with the observed prompt emission spectra of various GRBs. From this analysis it has emerged that the observational data can be correctly reproduced by assuming a modified thermal spectrum with $\alpha = -1.8$.

23. A.V. Penacchioni, R. Ruffini, L. Izzo, M. Muccino, C.L. Bianco, L. Caito, B. Patricelli, L. Amati; "Evidence for a proto-black hole and a double

astrophysical component in GRB 101023"; Astronomy & Astrophysics, 538, A58 (2012).

Context: It has been recently shown that GRB 090618, observed by AGILE, Coronas Photon, Fermi, Konus, Suzaku and Swift, is composed of two very different components: episode 1, lasting 50 s, shows a thermal plus power-law spectrum with a characteristic temperature evolving in time as a power law; episode 2 (the remaining 100 s) is a canonical long GRB. We have associated episode 1 to the progenitor of a collapsing bare core leading to the formation of a black hole: what was defined as a "proto black hole". *Aims*: In precise analogy with GRB 090618 we aim to analyze the 89s of the emission of GRB 101023, observed by Fermi, Gemini, Konus and Swift, to see if there are two different episodes: the first one presenting a characteristic black-body temperature evolving in time as a broken power law, and the second one consistent with a canonical GRB. *Methods*: To obtain information on the spectra, we analyzed the data provided by the GBM detector onboard the Fermi satellite, and we used the heasoft package XSPEC and RMFIT to obtain their spectral distribution. We also used the numerical code GRBsim to simulate the emission in the context of the fireshell scenario for episode 2. *Results*: We confirm that the first episode can be well fit by a black body plus power-law spectral model. The temperature changes with time following a broken power law, and the photon index of the power-law component presents a soft-to-hard evolution. We estimate that the radius of this source increases with time with a velocity of $1.5 \times 10^4 km/s$. The second episode appears to be a canonical GRB. By using the Amati and the Atteia relations, we determined the cosmological redshift, $z \sim 0.9 \pm 0.084(stat.) \pm 0.2(sys.)$. The results of GRB 090618 are compared and contrasted with the results of GRB 101023. Particularly striking is the scaling law of the soft X-ray component of the afterglow. *Conclusions*: We identify GRB 090618 and GRB 101023 with a new family of GRBs related to a single core collapse and presenting two astrophysical components: a first one related to the proto-black hole prior to the process of gravitational collapse (episode 1), and a second one, which is the canonical GRB (episode 2) emitted during the formation of the black hole. For the first time we are witnessing the process of a black hole formation from the instants preceding the gravitational collapse up to the GRB emission. This analysis indicates progress towards developing a GRB distance indicator based on understanding the P-GRB and the prompt emission, as well as the soft X-ray behavior of the late afterglow.

24. R. Negreiros, R. Ruffini, C. L. Bianco, J. A. Rueda; "Cooling of young

neutron stars in GRB associated to supernovae"; Astronomy & Astrophysics, 540, A12 (2012).

Context: The traditional study of neutron star cooling has been generally applied to quite old objects such as the Crab Pulsar (957 years) or the central compact object in Cassiopeia A (330 years) with an observed surface temperature $\sim 10^6$ K. However, recent observations of the late ($t = 10^8$–10^9 s) emission of the supernovae (SNe) associated to GRBs (GRB-SN) show a distinctive emission in the X-ray regime consistent with temperatures $\sim 10^7$–10^8 K. Similar features have been also observed in two Type Ic SNe SN 2002ap and SN 1994I that are not associated to GRBs. *Aims*: We advance the possibility that the late X-ray emission observed in GRB-SN and in isolated SN is associated to a hot neutron star just formed in the SN event, here defined as a neo-neutron star. *Methods*: We discuss the thermal evolution of neo-neutron stars in the age regime that spans from ~ 1 minute (just after the proto-neutron star phase) all the way up to ages $<$ 10–100 yr. We examine critically the key factor governing the neo-neutron star cooling with special emphasis on the neutrino emission. We introduce a phenomenological heating source, as well as new boundary conditions, in order to mimic the high temperature of the atmosphere for young neutron stars. In this way we match the neo-neutron star luminosity to the observed late X-ray emission of the GRB-SN events: URCA-1 in GRB980425-SN1998bw, URCA-2 in GRB030329-SN2003dh, and URCA-3 in GRB031203-SN2003lw. *Results*: We identify the major role played by the neutrino emissivity in the thermal evolution of neo-neutron stars. By calibrating our additional heating source at early times to $\sim 10^{12}$–10^{15} erg/g/s, we find a striking agreement of the luminosity obtained from the cooling of a neo-neutron stars with the prolonged ($t = 10^8$–10^9 s) X-ray emission observed in GRB associated with SN. It is therefore appropriate a revision of the boundary conditions usually used in the thermal cooling theory of neutron stars, to match the proper conditions of the atmosphere at young ages. The traditional thermal processes taking place in the crust might be enhanced by the extreme high-temperature conditions of a neo-neutron star. Additional heating processes that are still not studied within this context, such as e^+e^- pair creation by overcritical fields, nuclear fusion, and fission energy release, might also take place under such conditions and deserve further analysis. *Conclusions*: Observation of GRB-SN has shown the possibility of witnessing the thermal evolution of neo-neutron stars. A new campaign of dedicated observations is recommended both of GRB-SN and of isolated Type Ic SN.

25. L. Izzo, R. Ruffini, A.V. Penacchioni, C.L. Bianco, L. Caito, S.K. Chakrabarti, J.A. Rueda, A. Nandi, B. Patricelli; "A double component in GRB 090618: a proto-black hole and a genuinely long gamma-ray burst"; Astronomy & Astrophysics, 543, A10 (2012).

    Context: The joint X-ray and gamma-ray observations of GRB 090618 by very many satellites offer an unprecedented possibility of testing crucial aspects of theoretical models. In particular, they allow us to test (a) in the process of gravitational collapse, the formation of an optically thick e+e.-baryon plasma self-accelerating to Lorentz factors in the range $200 < \Gamma < 3000$; (b) its transparency condition with the emission of a component of 10^{53-54} baryons in the TeV region and (c) the collision of these baryons with the circumburst medium (CBM) clouds, characterized by dimensions of 10^{15-16} cm. In addition, these observations offer the possibility of testing a new understanding of the thermal and power-law components in the early phase of this GRB. *Aims*: We test the fireshell model of GRBs in one of the closest ($z = 0.54$) and most energetic ($E_{iso} = 2.90 \times 10^{53}$ erg) GRBs, namely GRB 090618. It was observed at ideal conditions by several satellites, namely *Fermi*, *Swift*, Konus-WIND, AGILE, RT-2, and Suzaku, as well as from on-ground optical observatories. *Methods*: We analyzed the emission from GRB 090618 using several spectral models, with special attention to the thermal and power-law components. We determined the fundamental parameters of a canonical GRB within the context of the fireshell model, including the identification of the total energy of the e^+e^- plasma, E_{tot}^{e+e-}, the proper GRB (P-GRB), the baryon load, the density and structure of the CBM. *Results*: We find evidence of the existence of two different episodes in GRB 090618. The first episode lasts 50 s and is characterized by a spectrum consisting of a thermal component, which evolves between $kT = 54$ keV and $kT = 12$ keV, and a power law with an average index $\gamma = 1.75 \pm 0.04$. The second episode, which lasts for ~ 100 s, behaves as a canonical long GRB with a Lorentz gamma factor at transparency of $\Gamma = 495$, a temperature at transparency of 29.22 keV and with a characteristic size of the surrounding clouds of $R_{cl} \sim 10^{15-16}$ cm and masses of $\sim 10^{22-24}$ g. *Conclusions*: We support the recently proposed two-component nature of GRB 090618, namely, episode 1 and episode 2, with a specific theoretical analysis.We furthermore illustrate that episode 1 cannot be considered to be either a GRB or a part of a GRB event, but it appears to be related to the progenitor of the collapsing bare core, leading to the formation of the black hole, which we call a "proto-black hole". Thus, for the first time, we are witnessing the process of formation of a black hole from the phases just preceding the gravitational collapse all the way up to the GRB emission.

26. B. Patricelli, M.G. Bernardini, C.L. Bianco, L. Caito, G. De Barros, L. Izzo, R. Ruffini, G.V. Vereshchagin; "Analysis of GRB 080319B and GRB 050904 within the Fireshell Model: Evidence for a Broader Spectral Energy Distribution"; The Astrophysical Journal, 756, 16 (2012).

    The observation of GRB 080319B, with an isotropic energy $E_{iso} = 1.32 \times 10^{54}$ erg, and GRB 050904, with $E_{iso} = 1.04 \times 10^{54}$ erg, offers the possibility of studying the spectral properties of the prompt radiation of two of the most energetic Gamma Ray Bursts (GRBs). This allows us to probe the validity of the fireshell model for GRBs beyond 10^{54} erg, well outside the energy range where it has been successfully tested up to now (10^{49}–10^{53} erg). We find that in the low energy region, the prompt emission spectra observed by *Swift* BAT reveals more power than theoretically predicted. The opportunities offered by these observations to improve the fireshell model are outlined in this paper. One of the distinguishing features of the fireshell model is that it relates the observed GRB spectra to the spectrum in the comoving frame of the fireshell. Originally, a fully radiative condition and a comoving thermal spectrum were adopted. An additional power-law in the comoving thermal spectrum is required due to the discrepancy of the theoretical and observed light curves and spectra in the fireshell model for GRBs 080319B and 050904. A new phenomenological parameter α is correspondingly introduced in the model. We perform numerical simulations of the prompt emission in the *Swift* BAT bandpass by assuming different values of α within the fireshell model. We compare them with the GRB 080319B and GRB 050904 observed time-resolved spectra, as well as with their time-integrated spectra and light curves. Although GRB 080319B and GRB 050904 are at very different redshifts (z=0.937 and z=6.29 respectively), a value of $\alpha = -1.8$ leads for both of them to a good agreement between the numerical simulations and the observed BAT light curves, time-resolved and time-integrated spectra. Such a modified spectrum is also consistent with the observations of previously analyzed less energetic GRBs and reasons for this additional agreement are given. Perspectives for future low energy missions are outlined.

27. M. Muccino, R. Ruffini, C.L. Bianco, L. Izzo, A.V. Penacchioni; "GRB 090227B: The missing link between the genuine short and long GRBs"; The Astrophysical Journal, 763, 125 (2013).

The time-resolved spectral analysis of GRB 090227B, made possible by the *Fermi*-GBM data, allows to identify in this source the missing link between the genuine short and long GRBs. Within the Fireshell model of the Gamma-Ray Bursts (GRBs) we predict genuine short GRBs: bursts with the same inner engine of the long bursts but endowed with a severely low value of the Baryon load, $B \lesssim 5 \times 10^{-5}$. A first energetically predominant emission occurs at the transparency of the e^+e^- plasma, the Proper-GRB (P-GRB), followed by a softer emission, the extended afterglow. The typical separation between the two emissions is expected to be of the order of 10^{-3} – 10^{-2} s. We identify the P-GRB of GRB 090227B in the first 96 ms of emission, where a thermal component with the temperature $kT = (517 \pm 28)$ keV and a flux comparable with the non thermal part of the spectrum is observed. This non thermal component as well as the subsequent emission, where there is no evidence for a thermal spectrum, is identified with the extended afterglow. We deduce a theoretical cosmological redshift $z = 1.61 \pm 0.14$. We then derive the total energy $E^{tot}_{e^+e^-} = (2.83 \pm 0.15) \times 10^{53}$ ergs, the Baryon load $B = (4.13 \pm 0.05) \times 10^{-5}$, the Lorentz Γ factor at transparency $\Gamma_{tr} = (1.44 \pm 0.01) \times 10^4$, and the intrinsic duration $\Delta t' \sim 0.35$ s. We also determine the average density of the CircumBurst Medium (CBM), $\langle n_{CBM} \rangle = (1.90 \pm 0.20) \times 10^{-5}$ particles/cm^3. There is no evidence of beaming in the system. In view of the energetics and of the Baryon load of the source, as well as of the low interstellar medium and of the intrinsic time scale of the signal, we identify the GRB progenitor as a binary neutron star. From the recent progress in the theory of neutron stars, we obtain masses of the stars $m_1 = m_2 = 1.34 M_\odot$ and their corresponding radii $R_1 = R_2 = 12.24$ km and thickness of their crusts ~ 0.47 km, consistent with the above values of the Baryon load, of the energetics and of the time duration of the event.

28. A.V. Penacchioni, R. Ruffini, C.L. Bianco, L. Izzo, M. Muccino, G.B. Pisani, J.A. Rueda; "GRB 110709B in the induced gravitational collapse paradigm"; Astronomy & Astrophysics, 551, A133 (2013).

    Context: GRB 110709B is the first source for which *Swift* BAT triggered twice, with a time separation of ~ 10 minutes. The first emission (called here Episode 1) goes from 40 s before the first trigger up to 60 s after it. The second emission (hereafter Episode 2) goes from 35 s before the second trigger to 100 s after it. These features reproduce the ones of GRB 090618, which has been recently interpreted within the Induced Gravitational Collapse paradigm (IGC). In line with this paradigm we assume the progenitor to be a close binary system composed of a core of an evolved star and a Neutron Star (NS). The evolved star

explodes as a Supernova (SN) and ejects material that is partially accreted by the NS. We identify this process with Episode 1. The accretion process brings the NS over its critical mass, thus gravitationally collapsing to a BH. This process leads to the GRB emission, Episode 2. The double trigger has given for the first time the possibility to have a coverage of the X-ray emission observed by XRT both prior to and during the prompt phase of GRB 110709B. *Aims*: We analyze the spectra and time variability of Episode 1 and 2 and compute the relevant parameters of the binary progenitor, as well as the astrophysical parameters both in the SN and the GRB phase in the IGC paradigm. *Methods*: We perform a time-resolved spectral analysis of Episode 1 by fitting the spectrum with a blackbody (BB) plus a power-law (PL) spectral model. From the BB fluxes and temperatures of Episode 1 and the luminosity distance d_L, we evaluate the evolution with time of the radius of the BB emitter, associated here to the evolution of the SN ejecta. We analyze Episode 2 within the Fireshell model, identifying the Proper-GRB (P-GRB) and simulating the light curve and spectrum. We establish the redshift to be $z = 0.75$, following the phenomenological methods by Amati, by Yonetoku and by Grupe, and our analysis of the late X-ray afterglow. It is most remarkable that the determination of the cosmological redshift on the ground of the scaling of the late X-ray afterglow, already verified in GRB 090618 and GRB 101023, is again verified by this analysis. *Results*: We find for Episode 1 a temperature of the BB component that evolves with time following a broken PL, with the slope of the PL at early times $\alpha = 0$ (constant function) and the slope of the PL at late times $\beta = -4 \pm 2$. The break occurs at $t = 41.21$ s. The total energy of Episode 1 is $E^{(1)}_{iso} = 1.42 \times 10^{53}$ erg. The total energy of Episode 2 is $E^{(2)}_{iso} = 2.43 \times 10^{52}$ erg. We find at transparency a Lorentz factor $\Gamma \sim 1.73 \times 10^2$, laboratory radius of 6.04×10^{13} cm, P-GRB observed temperature $kT_{P-GRB} = 12.36$ keV, baryon load $B = 5.7 \times 10^{-3}$ and P-GRB energy of $E_{P-GRB} = 3.44 \times 10^{50}$ erg. We find a remarkable coincidence of the cosmological redshift by the scaling of the XRT data and with three other phenomenological methods. *Conclusions*: We interpret GRB 110709B as a member of the IGC sources, together with GRB 970828, GRB 090618 and GRB 101023. The existence of the XRT data during the prompt phase of the emission of GRB 110709B (Episode 2) offers an unprecedented tool for improving the diagnostic of GRBs emission.

29. G.B. Pisani, L. Izzo, R. Ruffini, C.L. Bianco, M. Muccino, A.V. Penacchioni, J.A. Rueda, Y. Wang; “Novel distance indicator for gamma-ray bursts associated with supernovae”; Astronomy & Astrophysics, 552,

L5 (2013).

Context: In recent years it has been proposed that the temporal coincidence of a Gamma Ray Burst (GRB) and a type Ib/c supernova (SN) can be explained by the concept of Induced Gravitational Collapse (IGC) of a Neutron Star (NS) to a Black Hole (BH) by accretion of matter ejected by a SN Ib/c. This scenario reveals a possible common behavior in the late time X-ray emission of this subclass of GRBs. *Aims*: We want to test if such a common behavior can actually be present in the sources belonging to this GRB sub-class and if this may lead to a redshift estimator for these sources. *Methods*: We build a sample of GRBs belonging to this sub-class, and we rescale the X-ray light curves of all of them both in time and in flux to a common cosmological redshift. *Results*: We found that the X-ray light curves of all the GRBs of the sample with a measured redshift present a common late time behavior when rescaled to a common redshift $z = 1$. We then use this result to estimate the redshift of the GRBs of the sample with no measured redshift. *Conclusions*: The common behavior in the late decay of the X-ray light curves of the GRBs of the sample points to a common physical mechanism in this particular phase of the GRB emission, possibly related to the SN process. This scenario may represent an invaluable tool to estimate the redshift of GRBs belonging to this sub-class of events. More GRBs are therefore needed in order to enlarge the subclass and to make more stringent constraints on the redshift estimates performed with this method for GRBs pertaining to this class.

30. C.L. Bianco, M. G. Bernardini, L. Caito, G. De Barros, L. Izzo, M. Muccino, B. Patricelli, A.V. Penacchioni, G.B. Pisani, R. Ruffini; "The canonical GRB scenario"; Il Nuovo Cimento C, 36 s01, 21 (2013).

    The canonical GRB scenario implied by the fireshell model is briefly summarized.

31. A.V. Penacchioni, R. Ruffini, L. Izzo, M. Muccino, C.L. Bianco, L. Caito, B. Patricelli; "Evidences for a double component in the emission of GRB 101023"; Il Nuovo Cimento C, 36 s01, 117 (2013).

    In this work we present the results of the analysis of GRB 101023 in the fireshell scenario. Its redshift is not known, so we attempted to infer it from the Amati Relation, obtaining $z = 0.9$. Its light curve presents a double emission, which makes it very similar to the already studied GRB 090618. We called each part Episode 1 and Episode 2. We performed a time-resolved spectral analysis with RMFIT using different spectral models, and fitted the light curve with a numerical code integrating the fireshell equations of motion. We used Fermi GBM data to build the light curve, in particular the second NaI detector, in the range (8.5–1000 keV). We considered different hypotheses regarding which part of the light curve could be the GRB and performed the analysis of all of them. We noticed a great variation of the temperature with time in the first episode, as well as almost no variation of the progenitor radius. We found that the first emission does not match the requirements for a GRB, while the second part perfectly agrees with being a canonical GRB, with a P-GRB lasting 4 s.

32. M. Muccino, R. Ruffini, C.L. Bianco, L. Izzo, A.V. Penacchioni, G.B. Pisani; "GRB 090510: A Disguised Short Gamma-Ray Burst with the Highest Lorentz Factor and Circumburst Medium"; The Astrophysical Journal, 772, 62 (2013).

    GRB 090510, observed both by Fermi and AGILE satellites, is the first bright short-hard Gamma-Ray Burst (GRB) with an emission from the keV up to the GeV energy range. Within the Fireshell model, we interpret the faint precursor in the light curve as the emission at the transparency of the expanding e^+e^- plasma: the Proper-GRB (P-GRB). From the observed isotropic energy we assume a total plasma energy $E^{tot}_{e^+e^-} = (1.10 \pm 0.06) \times 10^{53}$erg and derive a Baryon load $B = (1.45 \pm 0.28) \times 10^{-3}$ and a Lorentz factor at transparency $\Gamma_{tr} = (6.7 \pm 1.6) \times 10^2$. The main emission $\sim$ 0.4s after the initial spike is interpreted as the extended afterglow, due to the interaction of the ultrarelativistic baryons with the CircumBurst Medium (CBM). Using the condition of fully radiative regime, we infer a CBM average spherically symmetric density of $\langle n_{CBM} \rangle = (1.85 \pm 0.14) \times 10^3$ particles/cm^3, one of the highest found in the Fireshell model. The value of the filling factor, $1.5 \times 10^{-10} \leq \mathcal{R} \leq 3.8 \times 10^{-8}$, leads to the estimate of filaments with densities $n_{fil} = n_{CBM}/\mathcal{R} \approx (10^6 - 10^{14})$ particles/cm^3. The sub-MeV and the MeV emissions are well reproduced. When compared to the canonical GRBs with $\langle n_{CBM} \rangle \approx 1$ particles/cm^3 and to the disguised short GRBs with $\langle n_{CBM} \rangle \approx 10^{-3}$ particles/cm^3, the case of GRB 090510 leads to the existence of a new family of bursts exploding in an over-dense galactic region with $\langle n_{CBM} \rangle \approx 10^3$ particles/cm^3. The joint effect of the high Γ_{tr} and the high density compresses in time and "inflates" in intensity the extended afterglow, making it appear as a short burst, which we here define as "disguised short GRB by excess". The determination of the above parameters values may represent an important step towards the explanation of the GeV emission.

33. R. Ruffini, M. Muccino, C.L. Bianco, M. Enderli, L. Izzo, M. Kovacevic, A.V. Penacchioni, G.B. Pisani, J.A. Rueda, Y. Wang; "On Binary Driven Hypernovae and their nested late X-ray emission"; Astronomy & Astrophysics, 565, L10 (2014).

    Context: The induced gravitational collapse (IGC) paradigm addresses the very energetic (10^{52}–10^{54} erg) long gamma-ray bursts (GRBs) associated to supernovae (SNe). Unlike the traditional "collapsar" model, an evolved FeCO core with a companion neutron star (NS) in a tight binary system is considered as the progenitor. This special class of sources, here named "binary driven hypernovae" (BdHNe), presents a composite sequence composed of four different episodes with precise spectral and luminosity features.
    Aims: We first compare and contrast the steep decay, the plateau, and the power-law decay of the X-ray luminosities of three selected BdHNe (GRB 060729, GRB 061121, and GRB 130427A). Second, to explain the different sizes and Lorentz factors of the emitting regions of the four episodes, for definiteness, we use the most complete set of data of GRB 090618. Finally, we show the possible role of r-process, which originates in the binary system of the progenitor.
    Methods: We compare and contrast the late X-ray luminosity of the above three BdHNe. We examine correlations between the time at the starting point of the constant late power-law decay t_a^*, the average prompt luminosity $\langle L_{iso} \rangle$, and the luminosity at the end of the plateau L_a. We analyze a thermal emission ($\sim$ 0.97–0.29 keV), observed during the X-ray steep decay phase of GRB 090618.
    Results: The late X-ray luminosities of the three BdHNe, in the rest-frame energy band 0.3–10 keV, show a precisely constrained "nested" structure. In a space-time diagram, we illustrate the different sizes and Lorentz factors of the emitting regions of the three episodes. For GRB 090618, we infer an initial dimension of the thermal emitter of $\sim 7 \times 10^{12}$ cm, expanding at $\Gamma \approx 2$. We find tighter correlations than the Dainotti-Willingale ones.
    Conclusions: We confirm a constant slope power-law behavior for the late X-ray luminosity in the source rest frame, which may lead to a new distance indicator for BdHNe. These results, as well as the emitter size and Lorentz factor, appear to be inconsistent with the traditional afterglow model based on synchrotron emission from an ultra-relativistic ($\Gamma \sim 10^2$–10^3) collimated jet outflow. We argue, instead, for the possible role of r-process, originating in the binary system, to power the mildly relativistic X-ray source.

34. R. Ruffini, L. Izzo, M. Muccino, G.B. Pisani, J.A. Rueda, Y. Wang, C. Barbarino, C.L. Bianco, M. Enderli, M. Kovacevic; "Induced gravitational collapse at extreme cosmological distances: the case of GRB 090423"; Astronomy & Astrophysics, 569, A39 (2014).

    Context: The induced gravitational collapse (IGC) scenario has been introduced in order to explain the most energetic gamma ray bursts (GRBs), $E_{iso} = 10^{52} - 10^{54}$ erg, associated with type Ib/c supernovae (SNe). It has led to the concept of binary-driven hypernovae (BdHNe) originating in a tight binary system composed by a FeCO core on the verge of a SN explosion and a companion neutron star (NS). Their evolution is characterized by a rapid sequence of events: 1) The SN explodes, giving birth to a new NS (νNS). The accretion of SN ejecta onto the companion NS increases its mass up to the critical value; 2) The consequent gravitational collapse is triggered, leading to the formation of a black hole (BH) with GRB emission; 3) A novel feature responsible for the emission in the GeV, X-ray, and optical energy range occurs and is characterized by specific power-law behavior in their luminosity evolution and total spectrum; 4) The optical observations of the SN then occurs.
    Aims: We investigate whether GRB 090423, one of the farthest observed GRB at $z = 8.2$, is a member of the BdHN family.
    Methods: We compare and contrast the spectra, the luminosity evolution, and the detectability in the observations by *Swift* of GRB 090423 with the corresponding ones of the best known BdHN case, GRB 090618.
    Results: Identification of constant slope power-law behavior in the late X-ray emission of GRB 090423 and its overlapping with the corresponding one in GRB 090618, measured in a common rest frame, represents the main result of this article. This result represents a very significant step on the way to using the scaling law properties, proven in Episode 3 of this BdHN family, as a cosmological standard candle.
    Conclusions: Having identified GRB 090423 as a member of the BdHN family, we can conclude that SN events, leading to NS formation, can already occur already at $z = 8.2$, namely at 650 Myr after the Big Bang. It is then possible that these BdHNe originate stem from 40-60 $M_\odot$ binaries. They are probing the Population II stars after the completion and possible disappearance of Population III stars.

35. M. Muccino, C.L. Bianco, L. Izzo, Y. Wang, M. Enderli, M. Kovacevic, G.B. Pisani, A.V. Penacchioni, R. Ruffini; "The Genuine Short GRB 090227B and the Disguised by Excess GRB 090510"; Gravitation and

Cosmology, 20, 197 (2014).

GRB 090227B and GRB 090510, traditionally classified as short gamma-ray Bursts (GRBs), indeed originate from different systems. For GRB 090227B we inferred a total energy of the e^+e^- plasma $E^{tot}_{e^+e^-} = (2.83 \pm 0.15) \times 10^{53}$ erg, a baryon load of $B = (4.1 \pm 0.05) \times 10^{-5}$, and a CircumBurst Medium (CBM) average density $\langle n_{CBM} \rangle = (1.90 \pm 0.20) \times 10^{-5}$ cm^{-3}. From these results we have assumed the progenitor of this burst to be a symmetric neutron stars (NSs) merger with masses $m = 1.34 M_\odot$, radii $R = 12.24$ km. GRB 090510, instead, has $E^{tot}_{e^+e^-} = (1.10 \pm 0.06) \times 10^{53}$ erg, $B = (1.45 \pm 0.28) \times 10^{-3}$, implying a Lorentz factor at transparency of $\Gamma = (6.7 \pm 1.7) \times 10^2$, which are characteristic of the long GRB class, and a very high CBM density, $\langle n_{CBM} \rangle = (1.85 \pm 0.14) \times 10^3$ cm^{-3}. The joint effect of the high values of Γ and of $\langle n_{CBM} \rangle$ compresses in time and "inflates" in intensity in an extended afterglow, making appear GRB 090510 as a short burst, which we here define as "disguised short GRB by excess" occurring an overdense region with 10^3 cm^{-3}.

36. M. Muccino, C.L. Bianco, L. Izzo, Y. Wang, M. Enderli, G.B. Pisani, A.V. Penacchioni, R. Ruffini; "Two short bursts originating from different astrophysical systems: The genuine short GRB 090227B and the disguised short GRB 090510 by excess"; Journal of the Korean Physical Society, 65, 865 (2014).

GRB 090227B and GRB 090510 are two gamma-ray bursts (GRBs) traditionally classified as short bursts. The major outcome of our analysis is that they indeed originate from different systems. In the case of GRB 090227B, from the inferred values of the total energy of the e^+e^- plasma, $E^{tot}_{e^+e^-} = (2.83 \pm 0.15) \times 10^{53}$ erg, the engulfed baryonic mass M_B, expressed as $B = M_B c^2 / E^{tot}_{e^+e^-} = (4.1 \pm 0.05) \times 10^{-5}$, and the circumburst medium (CBM) average density, $\langle n_{CBM} \rangle = (1.90 \pm 0.20) \times 10^{-5}$ cm^{-3}, we have assumed the progenitor of this burst to be a symmetric neutron star (NS) merger with masses $m = 1.34 M_\odot$, radii $R = 12.24$ km, and crustal thicknesses of ~ 0.47 km. In the case of GRB 090510, we have derived the total plasma energy, $E^{tot}_{e^+e^-} = (1.10 \pm 0.06) \times 10^{53}$ erg, the Baryon load, $B = (1.45 \pm 0.28) \times 10^{-3}$, and the Lorentz factor at transparency, $\Gamma = (6.7 \pm 1.7) \times 10^2$, which are characteristic of the long GRB class, as well as a very high CBM density, $\langle n_{CBM} \rangle = (1.85 \pm 0.14) \times 10^3$ cm^{-3}. The joint effect of the high values of Γ and $\langle n_{CBM} \rangle$ compresses in time and "inflates" in intensity the extended afterglow, making GRB 090510 appear to be a short burst, which we here define as a "disguised short GRB by excess", occurring in an overdense region with 10^3 cm^{-3}.

37. R. Ruffini, Y. Wang, M. Kovacevic, C.L. Bianco, M. Enderli, M. Muccino, A.V. Penacchioni, G.B. Pisani, J. Rueda; "GRB 130427A and SN 2013cq: A Multi-wavelength Analysis of An Induced Gravitational Collapse Event"; The Astrophysical Journal, 798, 10 (2015).

    We have performed our data analysis of the observations by *Swift*, *NuStar* and *Fermi* satellites in order to probe the induced gravitational collapse (IGC) paradigm for GRBs associated with supernovae (SNe), in the "terra incognita" of GRB 130427A. We compare and contrast our data analysis with those in the literature. We have verified that the GRB 130427A conforms to the IGC paradigm by examining the power law behavior of the luminosity in the early 10^4 s of the XRT observations. This has led to the identification of the four different episodes of the "binary driven hypernovae" (BdHNe) and to the prediction, on May 2, 2013, of the occurrence of SN 2013cq, duly observed in the optical band on May 13, 2013. The exceptional quality of the data has allowed the identification of novel features in *Episode 3* including: a) the confirmation and the extension of the existence of the recently discovered "nested structure" in the late X-ray luminosity in GRB 130427A, as well as the identification of a spiky structure at 10^2 s in the cosmological rest-frame of the source; b) a power law emission of the GeV luminosity light curve and its onset at the end of *Episode 2*; c) different Lorentz Γ factors for the emitting regions of the X-ray and GeV emissions in this *Episode 3*. These results make it possible to test the details of the physical and astrophysical regimes at work in the BdHNe: 1) a newly born neutron star and the supernova ejecta, originating in *Episode 1*, 2) a newly formed black hole originating in *Episode 2*, and 3) the possible interaction among these components, observable in the standard features of *Episode 3*.

38. M. Muccino, R. Ruffini, C.L. Bianco, M. Enderli, M. Kovacevic, L. Izzo, A.V. Penacchioni, G.B. Pisani, J.A. Rueda, Y. Wang; "On binary driven hypernovae and their nested late X-ray emission"; Astronomy Reports, 59, 581 (2015).

    The induced gravitational collapse (IGC) paradigm addresses energetic (10^{52}–10^{54} erg), long gamma-ray bursts (GRBs) associated to supernovae (SNe) and proposes as their progenitors tight binary systems composed of an evolved FeCO core and a companion neutron star (NS). Their emission is characterized by four specific episodes: Episode 1, corresponding to the on-set of the FeCO

SN explosion and the accretion of the ejecta onto the companion NS; Episode 2, related the collapse of the companion NS to a black hole (BH) and to the emission of a long GRB; Episode 3, observed in X-rays and characterized by a steep decay, a plateau phase and a late power-law decay; Episode 4, corresponding to the optical SN emission due to the ^{56}Ni decay. We focus on Episode 3 and we show that, from the thermal component observed during the steep decay of the prototype GRB 090618, the emission region has a typical dimension of $\sim 10^{13}$ cm, which is inconsistent with the typical size of the emitting region of GRBs, e.g., $\sim 10^{16}$ cm. We propose, therefore, that the X-ray afterglow emission originates from a spherically symmetric SN ejecta expanding at $\Gamma \sim 2$ or, possibly, from the accretion onto the newly formed black hole, and we name these systems "binary driven hypernovae" (BdHNe). This interpretation is alternative to the traditional afterglow model based on the GRB synchrotron emission from a collimated jet outflow, expanding at ultra-relativistic Lorentz factor of $\Gamma \sim 10^2 - 10^3$ and originating from the collapse of a single object. We show then that the rest-frame energy band 0.3–10 keV X-ray luminosities of three selected BdHNe, GRB 060729, GRB 061121, and GRB 130427A, evidence a precisely constrained "nested" structure and satisfy precise scaling laws between the average prompt luminosity, $< L_{iso} >$, and the luminosity at the end of the plateau, L_a, as functions of the time at the end of the plateau. All these features extend the applicability of the "cosmic candle" nature of Episode 3. The relevance of r-process in fulfilling the demanding scaling laws and the nested structure are indicated.

39. R. Ruffini, J.A. Rueda, C. Barbarino, C. L. Bianco, H. Dereli, M. Enderli, L. Izzo, M. Muccino, A.V. Penacchioni, G.B. Pisani, Y. Wang; "Induced Gravitational Collapse in the BATSE era: the case of GRB 970828"; Astronomy Reports, 59, 626 (2015).

    Following the recently established "Binary-driven HyperNova" (BdHN) paradigm, we here interpret GRB 970828 in terms of the four episodes typical of such a model. The "Episode 1", up to 40 s after the trigger time t_0, with a time varying thermal emission and a total energy of $E_{iso,1st} = 2.60 \times 10^{53}$ erg, is interpreted as due to the onset of an hyper-critical accretion process onto a companion neutron star, triggered by the companion star, an FeCO core approaching a SN explosion. The "Episode 2", observed up t_0+90 s, is interpreted as a canonical gamma ray burst, with an energy of $E^{e^+e^-}_{tot} = 1.60 \times 10^{53}$ erg, a baryon load of $B = 7 \times 10^{-3}$ and a bulk Lorentz factor at transparency of $\Gamma = 142.5$. From this Episode 2, we infer that the GRB exploded in an environment with a large average particle density $\langle n \rangle \approx 10^3$ particles/cm^3 and dense clouds characterized by typical dimensions of $(4 \div 8) \times 10^{14}$ cm and $\delta n/n \sim 10$. The "Episode 3" is identified from t_0+90 s all the way up to 10^{5-6} s: despite the paucity of the early X-ray data, typical in the BATSE, pre-Swift era, we find extremely significant data points in the late X-ray afterglow emission of GRB 970828, which corresponds to the ones observed in all BdHNe sources. The "Episode 4", related to the Supernova emission, does not appear to be observable in this source, due to the presence of darkening from the large density of the GRB environment, also inferred from the analysis of the Episode 2.

40. Y. Wang, R. Ruffini, M. Kovacevic, C.L. Bianco, M. Enderli, M. Muccino, A.V. Penacchioni, G.B. Pisani, J.A. Rueda; "Predicting supernova associated to gamma-ray burst 130427a"; Astronomy Reports, 59, 667 (2015).

    Binary systems constituted by a neutron star and a massive star are not rare in the universe. The Induced Gravitational Gamma-ray Burst (IGC) paradigm interprets Gamma-ray bursts as the outcome of a neutron star that collapses into a black hole due to the accretion of the ejecta coming from its companion massive star that underwent a supernova event. GRB 130427A is one of the most luminous GRBs ever observed, of which isotropic energy exceeds 10^{54} erg. And it is within one of the few GRBs obtained optical, X-ray and GeV spectra simultaneously for hundreds of seconds, which provides an unique opportunity so far to understand the multi-wavelength observation within the IGC paradigm, our data analysis found low Lorentz factor blackbody emission in the Episode 3 and its X-ray light curve overlaps typical IGC Golden Sample, which comply to the IGC mechanisms. We consider these findings as clues of GRB 130427A belonging to the IGC GRBs. We predicted on GCN the emergence of a supernova on May 2, 2013, which was later successfully detected on May 13, 2013.

41. R. Ruffini, M. Muccino, M. Kovacevic, F.G. Oliveira, J.A. Rueda, C.L. Bianco, M. Enderli, A.V. Penacchioni, G.B. Pisani, Y. Wang, E. Zaninoni; "GRB 140619B: a short GRB from a binary neutron star merger leading to black hole formation"; The Astrophysical Journal, 808, 190 (2015).

    We show the existence of two families of short GRBs, both originating from the merger of binary neutron stars (NSs): family-1 with $E_{iso} < 10^{52}$ erg, leading to a massive NS as the merged core, and family-2 with $E_{iso} > 10^{52}$ erg, leading to a black hole (BH). Following the identification of the prototype

GRB 090227B, we present the details of a new example of family-2 short burst: GRB 140619B. From the spectral analysis of the early ~ 0.2 s, we infer an observed temperature $kT = (324 \pm 33)$ keV of the e^+e^--plasma at transparency (P-GRB), a theoretically derived redshift $z = 2.67 \pm 0.37$, a total burst energy $E^{tot}_{e^+e^-} = (6.03 \pm 0.79) \times 10^{52}$ erg, a rest-frame peak energy $E_{p,i} = 4.7$ MeV, and a baryon load $B = (5.52 \pm 0.73) \times 10^{-5}$. We also estimate the corresponding emission of gravitational waves. Two additional examples of family-2 short bursts are identified: GRB 081024B and GRB 090510, remarkable for its well determined cosmological distance. We show that marked differences exist in the nature of the afterglows of these two families of short bursts: family-2 bursts, leading to BH formation, consistently exhibit high energy emission following the P-GRB emission; family-1 bursts, leading to the formation of a massive NS, should never exhibit high energy emission. We also show that both the families fulfill an $E_{p,i}$–E_{iso} relation with slope $\gamma = 0.59 \pm 0.07$ and a normalization constant incompatible with the one for long GRBs. The observed rate of such family-2 events is $\rho_0 = \left(2.1^{+2.8}_{-1.4}\right) \times 10^{-4}\mathrm{Gpc}^{-3}\mathrm{yr}^{-1}$.

42. R. Ruffini, Y. Aimuratov, C.L. Bianco, M. Enderli, M. Kovacevic, R. Moradi, M. Muccino, A.V. Penacchioni, G.B. Pisani, J.A. Rueda, Y. Wang; "Induced gravitational collapse in FeCO Core-Neutron star binaries and Neutron star-Neutron star binary mergers"; International Journal of Modern Physics A, 30, 1545023 (2015).

    We review the recent progress in understanding the nature of gamma-ray bursts (GRBs). The occurrence of GRB is explained by the Induced Gravitational Collapse (IGC) in FeCO Core-Neutron star binaries and Neutron star-Neutron star binary mergers, both processes occur within binary system progenitors. Making use of this most unexpected new paradigm, with the fundamental implications by the neutron star (NS) critical mass, we find that different initial configurations of binary systems lead to different GRB families with specific new physical predictions confirmed by observations.

43. R. Ruffini, M. Muccino, Y. Aimuratov, C.L. Bianco, C. Cherubini, M. Enderli, M. Kovacevic, R. Moradi, A.V. Penacchioni, G.B. Pisani, J.A. Rueda, Y. Wang; "GRB 090510: A genuine short-GRB from a binary neutron star coalescing into a Kerr-Newman black hole"; The Astrophysical Journal, 831, 178 (2016).

    In a new classification of merging binary neutron stars (NSs) we separate short gamma-ray bursts (GRBs) in two sub-classes. The ones with $E_{\rm iso} \lesssim 10^{52}$ erg coalesce to form a massive NS and are indicated as short gamma-ray flashes (S-GRFs). The hardest, with $E_{\rm iso} \gtrsim 10^{52}$ erg, coalesce to form a black hole (BH) and are indicated as genuine short-GRBs (S-GRBs). Within the fireshell model, S-GRBs exhibit three different components: the P-GRB emission, observed at the transparency of a self-accelerating baryon-e^+e^- plasma; the prompt emission, originating from the interaction of the accelerated baryons with the circumburst medium; the high-energy (GeV) emission, observed after the P-GRB and indicating the formation of a BH. GRB 090510 gives the first evidence for the formation of a Kerr BH or, possibly, a Kerr-Newman BH. Its P-GRB spectrum can be fitted by a convolution of thermal spectra whose origin can be traced back to an axially symmetric dyadotorus. A large value of the angular momentum of the newborn BH is consistent with the large energetics of this S-GRB, which reach in the 1–10000 keV range $E_{\rm iso} = (3.95 \pm 0.21) \times 10^{52}$ erg and in the 0.1–100 GeV range $E_{\rm LAT} = (5.78 \pm 0.60) \times 10^{52}$ erg, the most energetic GeV emission ever observed in S-GRBs. The theoretical redshift $z_{\rm th} = 0.75 \pm 0.17$ that we derive from the fireshell theory is consistent with the spectroscopic measurement $z = 0.903 \pm 0.003$, showing the self-consistency of the theoretical approach. All S-GRBs exhibit GeV emission, when inside the *Fermi*-LAT field of view, unlike S-GRFs, which never evidence it. The GeV emission appears to be the discriminant for the formation of a BH in GRBs, confirmed by their observed overall energetics.

44. Ruffini, R.; Rueda, J. A.; Muccino, M.; Aimuratov, Y.; Becerra, L. M.; Bianco, C. L.; Kovacevic, M.; Moradi, R.; Oliveira, F. G.; Pisani, G. B.; Wang, Y.; On the classification of GRBs and their occurrence rates; The Astrophysical Journal, 832, 136 (2016).

    There is mounting evidence for the binary nature of the progenitors of gamma-ray bursts (GRBs). For a long GRB, the induced gravitational collapse (IGC) paradigm proposes as progenitor, or "in-state", a tight binary system composed of a carbon-oxygen core ($CO_{\rm core}$) undergoing a supernova (SN) explosion which triggers hypercritical accretion onto a neutron star (NS) companion. For a short GRB, a NS-NS merger is traditionally adopted as the progenitor. We divide long and short GRBs into two sub-classes, depending on whether or not a black hole (BH) is formed in the merger or in the hypercritical accretion process exceeding the NS critical mass. For long bursts, when no BH is formed we have the sub-class of X-ray flashes (XRFs), with isotropic energy $E_{iso} \lesssim 10^{52}$ erg and rest-frame spectral peak energy $E_{p,i} \lesssim 200$ keV. When a BH is formed we have the sub-class of binary-driven hypernovae (BdHNe), with $E_{iso} \gtrsim 10^{52}$ erg and $E_{p,i} \gtrsim 200$ keV. In analogy, short bursts are similarly divided into two sub-classes. When no BH is formed, short gamma-ray flashes (S-GRFs) occur, with $E_{iso} \lesssim 10^{52}$ erg and $E_{p,i} \lesssim 2$ MeV. When a BH is formed, the authentic short GRBs (S-GRBs) occur, with $E_{iso} \gtrsim 10^{52}$ erg and $E_{p,i} \gtrsim 2$ MeV. We give examples and observational signatures of these four sub-classes and their rate of occurrence. From their respective rates it is possible that "in-states" of S-GRFs and S-GRBs originate from the "out-states" of XRFs. We indicate two additional progenitor systems: white dwarf-NS and BH-NS. These systems have hybrid features between long and short bursts. In the case of S-GRBs and BdHNe evidence is given of the coincidence of the onset of the high energy GeV emission with the birth of a Kerr BH.

45. Becerra, L.; Bianco, C. L.; Fryer, C. L.; Rueda, J. A.; Ruffini, R.; On the induced gravitational collapse scenario of gamma-ray bursts associated with supernovae; The Astrophysical Journal, 833, 107 (2016).

    Following the induced gravitational collapse (IGC) paradigm of gamma-ray bursts (GRBs) associated with type Ib/c supernovae, we present numerical simulations of the explosion of a carbon-oxygen (CO) core in a binary system with a neutron-star (NS) companion. The supernova ejecta trigger a *hypercritical* accretion process onto the NS thanks to a copious neutrino emission and the trapping of photons within the accretion flow. We show that temperatures 1–10 MeV develop near the NS surface, hence electron-positron annihilation into neutrinos becomes the main cooling channel leading to accretion rates 10^{-9}–10^{-1} $M_\odot$ s^{-1} and neutrino luminosities 10^{43}–10^{52} erg s^{-1} (the shorter the orbital period the higher the accretion rate). We estimate the maximum orbital period, $P_{\rm max}$, as a function of the NS initial mass, up to which the NS companion can reach by hypercritical accretion the critical mass for gravitational collapse leading to black-hole (BH) formation. We then estimate the effects of the accreting and orbiting NS companion onto a novel geometry of the supernova ejecta density profile. We present the results of a 1.4×10^7 particle simulation which show that the NS induces accentuated asymmetries in the ejecta density around the orbital plane. We elaborate on the observables associated with the above features of the IGC process. We apply this framework to specific GRBs: we find that X-ray flashes (XRFs) and binary-driven hypernovae (BdHNe) are produced in binaries with $P > P_{\rm max}$ and $P < P_{\rm max}$, respectively. We analyze in detail the case of XRF 060218.

46. Pisani, G. B.; Ruffini, R.; Aimuratov, Y.; Bianco, C. L.; Kovacevic, M.;

Moradi, R.; Muccino, M.; Penacchioni, A. V.; Rueda, J. A.; Shakeri, S.; Wang, Y.; On the universal late X-ray emission of binary-driven hypernovae and its possible collimation; The Astrophysical Journal, 833, 159 (2016).

It has been previously discovered a universal power-law behaviour of the late X-ray emission (LXRE) of a "golden sample" (GS) of six long energetic GRBs, when observed in the rest-frame of the source. This remarkable feature, independent on the different isotropic energy (E_{iso}) of each GRB, has been used to estimate the cosmological redshift of some long GRBs. This analysis is here extended to a new class of 161 long GRBs, all with $E_{iso} > 10^{52}$ erg. These GRBs are indicated as binary-driven hypernovae (BdHNe) in view of their progenitors: a tight binary systems composed of a carbon-oxigen core (CO_{core}) and a neutron star (NS) undergoing an induced gravitational collapse (IGC) to a black hole (BH) triggered by the CO_{core} explosion as a supernova (SN). We confirm the universal behaviour of the LXRE for the "enlarged sample" (ES) of 161 BdHNe observed up to the end of 2015, assuming a double-cone emitting region. We obtain a distribution of half-opening angles peaking at $\theta = 17.62°$, with mean value 30.05°, and a standard deviation 19.65°. This, in turn, leads to the possible establishment of a new cosmological candle. Within the IGC model, such universal LXRE behaviour is only indirectly related to the GRB and originates from the SN ejecta, of a standard constant mass, being shocked by the GRB emission. The fulfillment of the universal relation in the LXRE and its independence of the prompt emission, further confirmed in this article, establishes a crucial test for any viable GRB model.

47. Y. Aimuratov, R. Ruffini, M. Muccino, C.L. Bianco, A.V. Penacchioni, G.B. Pisani, D. Primorac, J.A. Rueda, Y. Wang; GRB 081024B and GRB 140402A: Two Additional Short GRBs from Binary Neutron Star Mergers; The Astrophysical Journal, 844, 83 (2017).

Theoretical and observational evidences have been recently gained for a twofold classification of short bursts: 1) short gamma-ray flashes (S-GRFs), with isotropic energy $E_{iso} < 10^{52}$ erg and no BH formation, and 2) the authentic short gamma-ray bursts (S-GRBs), with isotropic energy $E_{iso} > 10^{52}$ erg evidencing a BH formation in the binary neutron star merging process. The signature for the BH formation consists in the on-set of the high energy (0.1–100 GeV) emission, coeval to the prompt emission, in all S-GRBs. No GeV emission is expected nor observed in the S-GRFs. In this paper we present two additional S-GRBs, GRB 081024B and GRB 140402A, following the already identified S-GRBs, i.e., GRB 090227B, GRB 090510 and GRB 140619B. We also return on the absence of the GeV emission of the S-GRB 090227B, at an angle of 71° from the *Fermi*-LAT boresight. All the correctly identified S-GRBs correlate to the high energy emission, implying no significant presence of beaming in the GeV emission. The existence of a common power-law behavior in the GeV luminosities, following the BH formation, when measured in the source rest-frame, points to a commonality in the mass and spin of the newly-formed BH in all S-GRBs.

48. J.A. Rueda, Y. Aimuratov, U. Barres de Almeida, L.M. Becerra, C.L. Bianco, C. Cherubini, S. Filippi, M. Karlica, M. Kovacevic, J.D. Melon Fuksman, R. Moradi, M. Muccino, A.V. Penacchioni, G.B. Pisani, D. Primorac, R. Ruffini, N. Sahakyan, S. Shakeri, Y. Wang; The binary systems associated with short and long gamma-ray bursts and their detectability; International Journal of Modern Physics D, 26, 1730016 (2017).

    Short and long-duration gamma-ray bursts (GRBs) have been recently subclassified into seven families according to the binary nature of their progenitors. For short GRBs, mergers of neutron star binaries (NS–NS) or neutron star-black hole binaries (NS-BH) are proposed. For long GRBs, the induced gravitational collapse (IGC) paradigm proposes a tight binary system composed of a carbon–oxygen core (COcore) and a NS companion. The explosion of the COcore as supernova (SN) triggers a hypercritical accretion process onto the NS companion which might reach the critical mass for the gravitational collapse to a BH. Thus, this process can lead either to a NS-BH or to NS–NS depending on whether or not the accretion is sufficient to induce the collapse of the NS into a BH. We shall discuss for the above compact object binaries: (1) the role of the NS structure and the equation-of-state on their final fate; (2) their occurrence rates as inferred from the X and gamma-ray observations; (3) the expected number of detections of their gravitational wave (GW) emission by the Advanced LIGO interferometer.

49. R. Ruffini, Y. Aimuratov, L.M. Becerra, C.L. Bianco, M. Karlica, M. Kovacevic, J.D. Melon Fuksman, R. Moradi, M. Muccino, A.V. Penacchioni, G.B. Pisani, D. Primorac, J.A. Rueda, S. Shakeri, G.V. Vereshchagin, Y. Wang, S.-S. Xue; The cosmic matrix in the 50th anniversary of relativistic astrophysics; International Journal of Modern Physics D, 26, 1730019 (2017).

Our concept of induced gravitational collapse (IGC paradigm) starting from a supernova occurring with a companion neutron star, has unlocked the understanding of seven different families of gamma ray bursts (GRBs), indicating a path for the formation of black holes in the universe. An authentic laboratory of relativistic astrophysics has been unveiled in which new paradigms have been introduced in order to advance knowledge of the most energetic, distant and complex systems in our universe. A novel cosmic matrix paradigm has been introduced at a relativistic cosmic level, which parallels the concept of an S-matrix introduced by Feynmann, Wheeler and Heisenberg in the quantum world of microphysics. Here the "in" states are represented by a neutron star and a supernova, while the "out" states, generated within less than a second, are a new neutron star and a black hole. This novel field of research needs very powerful technological observations in all wavelengths ranging from radio through optical, X-ray and gamma ray radiation all the way up to ultra-high-energy cosmic rays.

50. R. Ruffini, Y. Wang, Y. Aimuratov, U. Barres de Almeida, L.M. Becerra, C.L. Bianco, Y.C. Chen, M. Karlica, M. Kovacevic, L. Li, J.D. Melon Fuksman, R. Moradi, M. Muccino, A.V. Penacchioni, G.B. Pisani, D. Primorac, J.A. Rueda, S. Shakeri, G.V. Vereshchagin, S.-S. Xue; Early X-Ray Flares in GRBs; The Astrophysical Journal, 852, 53 (2018).

    We analyze the early X-ray flares in the GRB "flare-plateau-afterglow" (FPA) phase observed by Swift-XRT. The FPA occurs only in one of the seven GRB subclasses: the binary-driven hypernovae (BdHNe). This subclass consists of long GRBs with a carbon-oxygen core and a neutron star (NS) binary companion as progenitors. The hypercritical accretion of the supernova (SN) ejecta onto the NS can lead to the gravitational collapse of the NS into a black hole. Consequently, one can observe a GRB emission with isotropic energy $E_{iso} \gtrsim 10^{52}$ erg, as well as the associated GeV emission and the FPA phase. Previous work had shown that gamma-ray spikes in the prompt emission occur at $\sim 10^{15}$–10^{17} cm with Lorentz gamma factor $\Gamma \sim 10^2$–10^3. Using a novel data analysis we show that the time of occurrence, duration, luminosity and total energy of the X-ray flares correlate with E_{iso}. A crucial feature is the observation of thermal emission in the X-ray flares that we show occurs at radii $\sim 10^{12}$ cm with $\Gamma \lesssim 4$. These model independent observations cannot be explained by the "fireball" model, which postulates synchrotron and inverse Compton radiation from a single ultra relativistic jetted emission extending from the prompt to the late afterglow and GeV emission phases. We show that in BdHNe a collision between the GRB and the SN ejecta occurs at $\simeq 10^{10}$ cm reaching transparency at $\sim 10^{12}$ cm with $\Gamma \lesssim 4$. The agreement between the thermal emission observations and these theoretically derived values validates our model and opens the possibility of testing each BdHN episode with the corresponding Lorentz gamma factor.

51. R. Ruffini, J. Rodriguez, M. Muccino, J.A. Rueda, Y. Aimuratov, U. Barres de Almeida, L.M. Becerra, C.L. Bianco, C. Cherubini, S. Filippi, D. Gizzi, M. Kovacevic, R. Moradi, F.G. Oliveira, G.B. Pisani, Y. Wang; On the Rate and on the Gravitational Wave Emission of Short and Long GRBs; The Astrophysical Journal, 859, 30 (2018).

    On the ground of the large number of gamma-ray bursts (GRBs) detected with cosmological redshift, we classified GRBs in seven subclasses, all with binary progenitors which emit gravitational waves (GWs). Each binary is composed of combinations of carbon-oxygen cores (COcore), neutron stars (NSs), black holes (BHs), and white dwarfs (WDs). The long bursts, traditionally assumed to originate from a BH with an ultrarelativistic jetted emission, not emitting GWs, have been subclassified as (I) X-ray flashes (XRFs), (II) binary-driven hypernovae (BdHNe), and (III) BH-supernovae (BH-SNe). They are framed within the induced gravitational collapse paradigm with a progenitor COcore-NS/BH binary. The SN explosion of the COcore triggers an accretion process onto the NS/BH. If the accretion does not lead the NS to its critical mass, an XRF occurs, while when the BH is present or formed by accretion, a BdHN occurs. When the binaries are not disrupted, XRFs lead to NS-NS and BdHNe lead to NS-BH. The short bursts, originating in NS-NS, are subclassified as (IV) short gamma-ray flashes (S-GRFs) and (V) short GRBs (S-GRBs), the latter when a BH is formed. There are (VI) ultrashort GRBs (U-GRBs) and (VII) gamma-ray flashes (GRFs) formed in NS-BH and NS-WD, respectively. We use the occurrence rate and GW emission of these subclasses to assess their detectability by Advanced LIGO-Virgo, eLISA, and resonant bars. We discuss the consequences of our results in view of the announcement of the LIGO/Virgo Collaboration of the source GW 170817 as being originated by an NS-NS.

52. J.A. Rueda, R. Ruffini, Y. Wang, Y. Aimuratov, U. Barres de Almeida, C.L. Bianco, Y.-C. Chen, R.V. Lobato, C. Maia, D. Primorac, R. Moradi, J. Rodriguez; GRB 170817A-GW170817-AT 2017gfo and the observations of NS-NS, NS-WD and WD-WD mergers; Journal of Cosmology and Astroparticle Physics, 10, 006 (2018).

The LIGO-Virgo Collaboration has announced the detection of GW170817 and has associated it with GRB 170817A . These signals have been followed after 11 hours by the optical and infrared emission of AT 2017gfo. The origin of this complex phenomenon has been attributed to a neutron star-neutron star (NS-NS) merger. In order to probe this association we confront our current understanding of the gravitational waves and associated electromagnetic radiation with four observed GRBs originating in binaries composed of different combinations NSs and white dwarfs (WDs). We consider 1) GRB 090510 the prototype of NS-NS merger leading to a black hole (BH); 2) GRB 130603B the prototype of a NS-NS merger leading to massive NS (MNS) with an associated kilonova; 3) GRB 060614 the prototype of a NS-WD merger leading to a MNS with an associated kilonova candidate; 4) GRB 170817A the prototype of a WD-WD merger leading to massive WD with an associated AT 2017gfo-like emission. None of these systems support the above mentioned association. The clear association between GRB 170817A and AT 2017gfo has led to introduce a new model based on a new subfamily of GRBs originating from WD-WD mergers. We show how this novel model is in agreement with the exceptional observations in the optical, infrared, X- and gamma-rays of GRB 170817A-AT 2017gfo.

53. R. Ruffini, M. Karlica, N. Sahakyan, J.A. Rueda, Y. Wang, G.W. Mathews, C.L. Bianco, M. Muccino; A GRB Afterglow Model Consistent with Hypernova Observations; The Astrophysical Journal, 869, 101 (2018).

We describe the afterglows of the long gamma-ray-burst (GRB) 130427A within the context of a binary-driven hypernova. The afterglows originate from the interaction between a newly born neutron star (νNS), created by an Ic supernova (SN), and a mildly relativistic ejecta of a hypernova (HN). Such an HN in turn results from the impact of the GRB on the original SN Ic. The mildly relativistic expansion velocity of the afterglow ($\Gamma \sim 3$) is determined, using our model-independent approach, from the thermal emission between 196 and 461 s. The power law in the optical and X-ray bands of the afterglow is shown to arise from the synchrotron emission of relativistic electrons in the expanding magnetized HN ejecta. Two components contribute to the injected energy: the kinetic energy of the mildly relativistic expanding HN and the rotational energy of the fast-rotating highly magnetized ?NS. We reproduce the afterglow in all wavelengths from the optical (10^{14} Hz) to the X-ray band (10^{19} Hz) over times from 604 s to 5.18×10^6 s relative to the Fermi-GBM trigger. Initially, the emission is dominated by the loss of kinetic energy of the HN component.

After 10^5 s the emission is dominated by the loss of rotational energy of the νNS, for which we adopt an initial rotation period of 2 ms and a dipole plus quadrupole magnetic field of $\lesssim 7 \times 10^{12}$ G or $\sim 10^{14}$ G. This scenario with a progenitor composed of a COcore and an NS companion differs from the traditional ultra-relativistic-jetted treatments of the afterglows originating from a single black hole.

54. R. Ruffini, L.M. Becerra, C.L. Bianco, Y.-C. Chen, M. Karlica, M. Kovacevic, J.D. Melon Fuksman, R. Moradi, M. Muccino, G.B. Pisani, D. Primorac, J.A. Rueda, G.V. Vereshchagin, Y. Wang, S.-S. Xue; On the ultra-relativistic Prompt Emission (UPE), the Hard and Soft X-ray Flares, and the extended thermal emission (ETE) in GRB 151027A; The Astrophysical Journal, 869, 151 (2018).

    We analyze GRB 151027A within the binary-driven hypernova approach, with a progenitor of a carbon–oxygen core on the verge of a supernova (SN) explosion and a binary companion neutron star (NS). The hypercritical accretion of the SN ejecta onto the NS leads to its gravitational collapse into a black hole (BH), to the emission of the gamma-ray burst (GRB), and to a copious e+e- plasma. The impact of this e+e- plasma on the SN ejecta explains the early soft X-ray flare observed in long GRBs. Here, we apply this approach to the ultra-relativistic prompt emission (UPE) and to the hard X-ray flares. We use GRB 151027A as a prototype. From the time-integrated and the time-resolved analysis, we identify a double component in the UPE and confirm its ultra-relativistic nature. We confirm the mildly relativistic nature of the soft X-ray flare, of the hard X-ray flare, and of the extended thermal emission (ETE). We show that the ETE identifies the transition from an SN to a hypernova (HN). We then address the theoretical justification of these observations by integrating the hydrodynamical propagation equations of the e+e- into the SN ejecta, with the latter independently obtained from 3D smoothed particle hydrodynamics simulations. We conclude that the UPE, the hard X-ray flare, and the soft X-ray flare do not form a causally connected sequence. Within our model, they are the manifestation of the same physical process of the BH formation as seen through different viewing angles, implied by the morphology and the ~ 300 s rotation period of the HN ejecta.

55. R. Moradi, R. Ruffini, C.L. Bianco, Y.-C. Chen, M. Karlica, J.D. Melon Fuksman, D. Primorac, J.A. Rueda, S. Shakeri, Y. Wang, S.-S. Xue; Relativistic Behavior and Equitemporal Surfaces in Ultra-Relativistic Prompt

Emission Phase of Gamma-Ray Bursts; Astronomy Reports, 62, 905 (2018).

In this work we study a role of baryon load and interstellar medium density to explain the nature of peaks in the ultra-relativistic prompt emission (UPE) phase of Gamma-ray Bursts (GRBs). We study the behavior of their Γ Lorenz factor fromthe moment of transparency all the way up to interstellar medium. We finally study the characteristic of equitemporal surfaces in the UPE phase.

56. D. Primorac, M. Muccino, R. Moradi, Y. Wang, J.D. Melon Fuksman, R. Ruffini, C.L. Bianco, J.A. Rueda; Structure of the Prompt Emission of GRB 151027A Within the Fireshell Model; Astronomy Reports, 62, 933 (2018).

    Long gamma-ray burst GRB 151027A was observed by all three detectors onboard the Swift spacecraft, and many more, including MAXI, Konus-Wind and Fermi GBM/LAT instruments. This revealed a complex structure of the prompt and afterglow emission, consisting of a double-peak gammaray prompt with a quiescent period and a HRF/SXF within the X-ray afterglow, together with multiple BB components seen within the time-resolved spectral analysis. These features, within the fireshell model, are interpreted as the manifestation of the same physical process viewed at different angles with respect to the HN ejecta. Here we present the time-resolved and time-integrated spectral analysis used to determine the energy of the e-e+ plasma E_{tot} and the baryon load B. These quantities describe the dynamics of the fireshell up to the transparency point. We proceed with the light-curve simulation from which CBM density values and its inhomogeneities are deduced. We also investigate the properties of GRB 140206A, whose prompt emission exhibits a similar structure.

57. Y. Wang, J.A. Rueda, R. Ruffini, C.L. Bianco, L.M. Becerra, L. Li, M. Karlica; Two Predictions of Supernova: GRB 130427A/SN 2013cq and GRB 180728A/SN 2018fip; The Astrophysical Journal, 874, 39 (2019).

    On 2018 July 28, GRB 180728A triggered *Swift* satellites and, soon after the determination of the redshift, we identified this source as a type II binary-driven hypernova (BdHN II) in our model. Consequently, we predicted the appearance time of its associated supernova (SN), which was later confirmed as SN 2018fip. A BdHN II originates in a binary composed of a carbon-oxygen core (CO_{core}) undergoing SN, and the SN ejecta hypercritically accrete onto a companion neutron star (NS). From the time of the SN shock breakout to the time when the hypercritical accretion starts, we infer the binary separation

$\simeq 3 \times 10^{10}$ cm. The accretion explains the prompt emission of isotropic energy $\simeq 3 \times 10^{51}$ erg, lasting ~ 10 s, and the accompanying observed blackbody emission from a thermal convective instability bubble. The new neutron star (νNS) originating from the SN powers the late afterglow from which a νNS initial spin of 2.5 ms is inferred. We compare GRB 180728A with GRB 130427A, a type I binary-driven hypernova (BdHN I) with isotropic energy $> 10^{54}$ erg. For GRB 130427A we have inferred an initially closer binary separation of $\simeq 10^{10}$ cm, implying a higher accretion rate leading to the collapse of the NS companion with consequent black hole formation, and a faster, 1 ms spinning νNS. In both cases, the optical spectra of the SNe are similar, and not correlated to the energy of the gamma-ray burst. We present three-dimensional smoothed-particle-hydrodynamic simulations and visualisations of the BdHNe I and II.

58. J.A. Rueda, R. Ruffini, Y. Wang, C.L. Bianco, J.M. Blanco-Iglesias, M. Karlica, P. Lorén-Aguilar, R. Moradi, N. Sahakyan; Electromagnetic emission of white dwarf binary mergers; Journal of Cosmology and Astroparticle Physics, 03, 044 (2019).

    It has been recently proposed that the ejected matter from white dwarf (WD) binary mergers can produce transient, optical and infrared emission similar to the "kilonovae" of neutron star (NS) binary mergers. To confirm this we calculate the electromagnetic emission from WD-WD mergers and compare with kilonova observations. We simulate WD-WD mergers leading to a massive, fast rotating, highly magnetized WD with an adapted version of the smoothed-particle-hydrodynamics (SPH) code Phantom. We thus obtain initial conditions for the ejecta such as escape velocity, mass and initial position and distribution. The subsequent thermal and dynamical evolution of the ejecta is obtained by integrating the energy-conservation equation accounting for expansion cooling and a heating source given by the fallback accretion onto the newly-formed WD and its magneto-dipole radiation. We show that magnetospheric processes in the merger can lead to a prompt, short gamma-ray emission of up to $\approx 10^{46}$ erg in a timescale of 0.1–1 s. The bulk of the ejecta initially expands non-relativistically with velocity 0.01 c and then it accelerates to 0.1 c due to the injection of fallback accretion energy. The ejecta become transparent at optical wavelengths around ~ 7 days post-merger with a luminosity 10^{41}–10^{42} erg s^{-1}. The X-ray emission from the fallback accretion becomes visible around $\sim$ 150–200 day post-merger with a luminosity of 10^{39} erg s^{-1}. We also predict the post-merger time at which the central WD should appear as a pulsar depending on the value of the magnetic field and rotation period.

59. J.A. Rueda, R. Ruffini, Y. Wang; Induced Gravitational Collapse, Binary-Driven Hypernovae, Long Gramma-ray Bursts and Their Connection with Short Gamma-ray Bursts; Universe, 5, 110 (2019).

There is increasing observational evidence that short and long Gamma-ray bursts (GRBs) originate in different subclasses, each one with specific energy release, spectra, duration, etc, and all of them with binary progenitors. The binary components involve carbon-oxygen cores (CO_{core}), neutron stars (NSs), black holes (BHs), and white dwarfs (WDs). We review here the salient features of the specific class of binary-driven hypernovae (BdHNe) within the induced gravitational collapse (IGC) scenario for the explanation of the long GRBs. The progenitor is a CO_{core}-NS binary. The supernova (SN) explosion of the CO_{core}, producing at its center a new NS (νNS), triggers onto the NS companion a hypercritical, i.e., highly super-Eddington accretion process, accompanied by a copious emission of neutrinos. By accretion the NS can become either a more massive NS or reach the critical mass for gravitational collapse with consequent formation of a BH. We summarize the results on this topic from the first analytic estimates in 2012 all the way up to the most recent three-dimensional (3D) smoothed-particle-hydrodynamics (SPH) numerical simulations in 2018. Thanks to these results it is by now clear that long GRBs are richer and more complex systems than thought before. The SN explosion and its hypercritical accretion onto the NS explain the X-ray precursor. The feedback of the NS accretion, the NS collapse and the BH formation produce asymmetries in the SN ejecta, implying the necessity of a 3D analysis for GRBs. The newborn BH, the surrounding matter and the magnetic field inherited from the NS, comprises the *inner engine* from which the GRB electron-positron (e^+e^-) plasma and the high-energy emission are initiated. The impact of the e^+e^- on the asymmetric ejecta transforms the SN into a hypernova (HN). The dynamics of the plasma in the asymmetric ejecta leads to signatures depending on the viewing angle. This explains the ultrarelativistic prompt emission in the MeV domain and the mildly-relativistic flares in the early afterglow in the X-ray domain. The feedback of the νNS pulsar-like emission on the HN explains the X-ray late afterglow and its power-law regime. All of the above is in contrast with a simple GRB model attempting to explain the entire GRB with the kinetic energy of an ultrarelativistic jet extending through all of the above GRB phases, as traditionally proposed in the "collapsar-fireball" model. In addition, BdHNe in their different flavors lead to νNS-NS or νNS-BH binaries. The gravitational wave emission drives these binaries to merge producing short GRBs. It is thus established a previously unthought interconnection between long and short GRBs and their occurrence rates. This needs to be accounted for in the cosmological evolution of binaries within population synthesis models for the formation of compact-object binaries.

60. R. Ruffini, J.D. Melon Fuksman, G.V. Vereshchagin; On the role of a cavity in the hypernova ejecta of GRB 190114C; The Astrophysical Journal, 883, 191 (2019).

    Within the binary-driven hypernova I (BdHN I) scenario, the gamma-ray burst GRB190114C originates in a binary system composed of a massive carbon-oxygen core (CO_{core}), and a binary neutron star (NS) companion. As the CO_{core} undergoes a supernova explosion with the creation of a new neutron star (νNS), hypercritical accretion occurs onto the companion binary neutron star until it exceeds the critical mass for gravitational collapse. The formation of a black hole (BH) captures 10^{57} baryons by enclosing them within its horizon, and thus a cavity of approximately 10^{11} cm is formed around it with initial density 10^{-7} g/cm^3. A further depletion of baryons in the cavity originates from the expansion of the electron-positron-photon ($e^+e^-\gamma$) plasma formed at the collapse, reaching a density of 10^{-14} g/cm^3 by the end of the interaction. It is demonstrated here using an analytical model complemented by a hydrodynamical numerical simulation that part of the $e^+e^-\gamma$ plasma is reflected off the walls of the cavity. The consequent outflow and its observed properties are shown to coincide with the featureless emission occurring in a time interval of duration t_{rf}, measured in the rest frame of the source, between 11 and 20 s of the GBM observation. Moreover, similar features of the GRB light curve were previously observed in GRB 090926A and GRB 130427A, all belonging to the BdHN I class. This interpretation supports the general conceptual framework presented in R. Ruffini et al. and guarantees that a low baryon density is reached in the cavity, a necessary condition for the operation of the "*inner engine*" of the GRB presented in an accompanying article.

61. R. Ruffini, R. Moradi, J.A. Rueda, L.M. Becerra, C.L. Bianco, C. Cherubini, S. Filippi, Y.C. Chen, M. Karlica, N. Sahakyan, Y. Wang, S.-S. Xue; On the GeV Emission of the Type I BdHN GRB 130427A; The Astrophysical Journal, 886, 82 (2019).

    We propose that the *inner engine* of a type I binary-driven hypernova (BdHN) is composed of a Kerr black hole (BH) in a non-stationary state, embedded in a uniform magnetic field B_0 aligned with the BH rotation axis, and surrounded by an ionized plasma of extremely low density of 10^{-14} g cm^{-3}. Using GRB 130427A as a prototype we show that this *inner engine* acts in a sequence of *elementary impulses*. Electrons are accelerated to ultra-relativistic energy near the BH horizon and, propagating along the polar axis, $\theta = 0$, they can reach energies of $\sim 10^{18}$ eV, and partially contribute to ultra-high energy cosmic rays (UHECRs). When propagating with $\theta \neq 0$ through the magnetic field B_0 they give origin by synchrotron emission to GeV and TeV radiation. The mass of BH, $M = 2.3 M_{\odot}$, its spin, $\alpha = 0.47$, and the value of magnetic field $B_0 = 3.48 \times 10^{10}$ G, are determined self-consistently in order to fulfill the energetic and the transparency requirement. The repetition time of each elementary impulse of energy $\mathcal{E} \sim 10^{37}$ erg, is $\sim 10^{-14}$ s at the beginning of the process, then slowly increasing with time evolution. In principle, this "*inner engine*" can operate in a GRB for thousands of years. By scaling the BH mass and the magnetic field the same "*inner engine*" can describe active galactic nuclei (AGN).

62. L. Li; Thermal Components in Gamma-ray Bursts. II. Constraining the Hybrid Jet Model; The Astrophysical Journal, 894, 100 (2020).

    In explaining the physical origin of the jet composition of gamma-ray bursts (GRBs), a more general picture, i.e. the hybrid jet model (which introduced another magnetization parameter σ_0 on the basis of the traditional fireball model), has been well studied in Gao & Zhang. However, it still has not yet been applied to a large GRB sample. Here, we first employ the "top-down" approach of Gao & Zhang to diagnose the photosphere properties at the central engine to see how the hybrid model can account for the observed data as well, through applying a *Fermi* GRB sample (eight bursts) with the detected photosphere component, as presented in Li (our Paper I). We infer all physical parameters of a hybrid problem with three typical values of the radius of the jet base (r_0 = 10^7, 10^8, and 10^9 cm). We find that the dimensionless entropy for all the bursts shows $\eta \gg 1$ while the derived (1+σ_0) for five bursts (GRB 081224, GRB 110721A, GRB 090719, GRB 100707, and GRB 100724) is larger than unity, indicating that in addition to a hot fireball component, another cold Poynting-flux component may also play an important role. Our analysis also shows that in a few time bins for all r_0 in GRB 081224 and GRB 110721A, the magnetization parameter at $\sim 10^{15}$cm (1+σ_{r15}) is greater than unity, which implies that internal-collision-induced magnetic reconnection and turbulence may be the mechanism to power the nonthermal emission, rather than internal shocks. We conclude that the majority of bursts (probably all) can be well explained by the hybrid jet problem.

63. J.A. Rueda, R. Ruffini, M. Karlica, R. Moradi, Y. Wang; Magnetic fields and afterglows of bdhne: inferences from grb 130427a, grb 160509a, grb 160625b, grb 180728a, and grb 190114c; The Astrophysical Journal, 893, 148 (2020).

    GRB 190114C is the first binary-driven hypernova (BdHN) fully observed from the initial supernova appearance to the final emergence of the optical SN signal. It offers an unprecedented testing ground for the BdHN theory and it is here determined and further extended to additional gamma-ray bursts (GRBs). BdHNe comprise two subclasses of long GRBs with progenitors a binary system composed of a carbon-oxygen star (CO_{core}) and a neutron star (NS) companion. The CO_{core} explodes as a SN leaving at its center a newborn NS (νNS). The SN ejecta hypercritically accretes both on the νNS and the NS companion. BdHNe I are the tightest binaries where the accretion leads the companion NS to gravitational collapse into a black hole (BH). In BdHN II the accretion onto the NS is lower, so there is no BH formation. We observe the same structure of the afterglow for GRB 190114C and other selected examples of BdHNe I (GRB 130427A, GRB 160509A, GRB 160625B) and for BdHN II (GRB 180728A). In all the cases the explanation of the afterglow is reached via the synchrotron emission powered by the νNS: their magnetic fields structures and their spin are determined. For BdHNe I, we discuss the properties of the magnetic field embedding the newborn BH, inherited from the collapsed NS and amplified during the gravitational collapse process, and surrounded by the SN ejecta.

64. J.A. Rueda, R. Ruffini; The blackholic quantum; European Physical Journal C, 80, 300 (2020).

    We show that the high-energy emission of GRBs originates in the *inner engine*: a Kerr black hole (BH) surrounded by matter and a magnetic field B_0. It radiates a sequence of discrete events of particle acceleration, each of energy $\mathcal{E} = \hbar\,\Omega_{\rm eff}$, the *blackholic quantum*, where $\Omega_{\rm eff} = 4(m_{\rm Pl}/m_n)^8 (c\,a/G\,M)(B_0^2/\rho_{\rm Pl})\Omega_+$. Here M, $a = J/M$, $\Omega_+ = c^2\partial M/\partial J = (c^2/G)\,a/(2Mr_+)$ and r_+ are the BH mass, angular momentum per unit mass, angular velocity and horizon; m_n is the neutron mass, $m_{\rm Pl}$, $\lambda_{\rm Pl} = \hbar/(m_{\rm Pl}c)$ and $\rho_{\rm Pl} = m_{\rm Pl}c^2/\lambda_{\rm Pl}^3$, are the Planck mass, length and energy density. Here and in the following use CGS-Gaussian units. The timescale of each process is $\tau_{\rm el} \sim \Omega_+^{-1}$, along the rotation axis, while it is much shorter off-axis owing to energy losses such as synchrotron radiation. We show an analogy with the Zeeman and Stark effects, properly scaled from microphysics to macrophysics, that allows us to define the *BH magneton*,

$\mu_{\rm BH} = (m_{\rm Pl}/m_n)^4 (c\,a/G\,M) e\,\hbar/(Mc)$. We give quantitative estimates for GRB 130427A adopting $M = 2.3\ M_\odot$, $c\,a/(G\,M) = 0.47$ and $B_0 = 3.5 \times 10^{10}$ G. Each emitted *quantum*, $\mathcal{E} \sim 10^{37}$ erg, extracts only 10^{-16} times the BH rotational energy, guaranteeing that the process can be repeated for thousands of years. The *inner engine* can also work in AGN as we here exemplified for the supermassive BH at the center of M87.

65. B. Zhang, Y. Wang, L. Li; Dissecting the Energy Budget of a Gamma-Ray Burst Fireball; The Astrophysical Journal Letters, 909, L3 (2021)

66. L. Li, B. Zhang; Testing the High-latitude Curvature Effect of Gamma-Ray Bursts with Fermi Data: Evidence of Bulk Acceleration in Prompt Emission; The Astrophysical Journal Supplement Series, 253, 43 (2021)

67. L. Li, F. Ryde, A. Pe'er, H.-F. Yu, Z. Acuner; The Astrophysical Journal Supplement Series; 254, 35 (2021)

68. Y. Wang; Do All Long-duration Gamma-Ray Bursts Emit GeV Photons?; The Astrophysical Journal, 913, 86 (2021)

69. L. Li; Searching for Observational Evidence for Binary Star Systems in Gamma-ray Bursts; Astronomy Reports, 65, 973 (2021)

70. Y. Wang; Gamma-Ray Burst from Binary Star: Neutron Star and Carbon–Oxygen Core; Astronomy Reports, 65, 1077 (2021)

71. R. Ruffini; Discovery of the Moment of Formation of the Black Hole in GRB 190114C; Astronomy Reports, 65, 1030 (2021)

72. R. Ruffini, R. Moradi, J.A. Rueda, L. Li, N. Sahakyan, Y.-C. Chen, Y. Wang, Y. Aimuratov, L. Becerra, C.L. Bianco, C. Cherubini, S. Filippi, M. Karlica, G.J. Mathews, M. Muccino, G.B. Pisani, S.-S. Xue; The morphology of the X-ray afterglows and of the jetted GeV emission in long GRBs; Monthly Notices of the Royal Astronomical Society, 504, 5301 (2021)

73. R. Moradi, J.?A. Rueda, R. Ruffini, Liang Li, C.?L. Bianco, S. Campion, C. Cherubini, S. Filippi, Y. Wang, and S.?S. Xue; Nature of the ultrarelativistic prompt emission phase of GRB 190114C; Phys. Rev. D, 104, 063043 (2021)

74. R. Moradi, J.A. Rueda, R. Ruffini and Y. Wang; The newborn black hole in GRB 191014C proves that it is alive; Astronomy & Astrophysics, 649, A75 (2021)

75. Xu, Fan, Geng, Jin-Jun, Wang, Xu, Li, Liang, Huang, Yong-Feng, "Is the birth of PSR J0538+2817 accompanied by a gamma-ray burst?"; Monthly Notices of the Royal Astronomical Society, 509, 4916 (2022)

76. Li, Liang; "Standard GRB Spectral Models "Misused"?"; The Astrophysical Journal, 941, 27 (2022)

77. Marongiu, M.; Guidorzi, C., Stratta, G., Gomboc, A., Jordana-Mitjans, N., Dichiara, S., Kobayashi, S., Kopa?, D., Mundell, C. G.; "Radio data challenge the broadband modelling of GRB 160131A afterglow"; Astronomy & Astrophysics, 658, A11 (2022)

4.2 Conference proceedings

1. R. Ruffini, M.G. Bernardini, C.L. Bianco, P. Chardonnet, F. Fraschetti, V. Gurzadyan, L. Vitagliano, S.-S. Xue; "The Blackholic energy: long and short Gamma-Ray Bursts (New perspectives in physics and astrophysics from the theoretical understanding of Gamma-Ray Bursts, II)"; in Proceedings of the XIth Brazilian School on Cosmology and Gravitation, Mangaratiba, Rio de Janeiro (Brazil), July – August 2004, M. Novello, S.E. Perez Bergliaffa, Editors; AIP Conference Proceedings, 782, 42 (2005).

   We outline the confluence of three novel theoretical fields in our modeling of Gamma-Ray Bursts (GRBs): 1) the ultrarelativistic regime of a shock front expanding with a Lorentz gamma factor ~ 300; 2) the quantum vacuum polarization process leading to an electron-positron plasma originating the shock front; and 3) the general relativistic process of energy extraction from a black hole originating the vacuum polarization process. There are two different classes of GRBs: the long GRBs and the short GRBs. We here address the issue of the long GRBs. The theoretical understanding of the long GRBs has led to the detailed description of their luminosities in fixed energy bands, of their spectral features and made also possible to probe the astrophysical scenario in which they originate. We are specially interested, in this report, to a subclass of long GRBs which appear to be accompanied by a supernova explosion. We are considering two specific examples: GRB980425/SN1998bw and GRB030329/SN2003dh. While these supernovae appear to have a standard energetics of 10^{49} ergs, the GRBs are highly variable and can have energetics $10^4 - 10^5$ times larger than the ones of the supernovae. Moreover, many long GRBs occurs without the presence of a supernova. It is concluded that in no way a GRB can originate from a supernova. The precise theoretical understanding of the GRB luminosity we present evidence, in both these systems, the existence of an independent component in the X-ray emission, usually interpreted in the current literature as part of the GRB afterglow. This component has been observed by Chandra and XMM to have a strong decay on scale of months. We have named here these two sources respectively URCA-1 and URCA-2, in honor of the work that George Gamow and Mario Shoenberg did in 1939 in this town of Urca identifying the basic mechanism, the Urca processes, leading to the process of gravitational collapse and the formation of a neutron star and a supernova. The further hypothesis is considered to relate this X-ray source to a neutron star, newly born in the Supernova. This hypothesis should be submitted to further theoretical and observational investigation. Some theoretical developments to clarify the astrophysical origin of this new scenario are outlined. We turn then to the theoretical developments in the short GRBs: we first report some progress in the understanding the dynamical phase of collapse, the mass-energy formula and the extraction of blackholic energy which have been motivated by the analysis of the short GRBs. In this context progress has also been accomplished on establishing an absolute lower limit to the irreducible mass of the black hole as well as on some critical considerations about the relations of general relativity and the second law of thermodynamics. We recall how this last issue has been one of the most debated in theoretical physics in the past thirty years due to the work of Bekenstein and Hawking. Following these conceptual progresses we analyze the vacuum polarization process around an overcritical collapsing shell. We evidence the existence of a separatrix and a dyadosphere trapping surface in the dynamics of the electron-positron plasma generated during the process of gravitational collapse. We then analyze, using recent progress in the solution of the Vlasov-Boltzmann-Maxwell system, the oscillation regime in the created electron-positron plasma and their rapid convergence to a thermalized spectrum. We conclude by making precise predictions for the spectra, the energy fluxes and characteristic time-scales of the radiation for short-bursts. If the precise luminosity variation and spectral hardening of the radiation we have predicted will be confirmed by observations of short-bursts, these systems will play a major role as standard candles in cosmology. These considerations will also be relevant for the analysis of the long-bursts when the baryonic matter contribution will be taken into account.

2. R. Ruffini, M.G. Bernardini, C.L. Bianco, P. Chardonnet, F. Fraschetti, V. Gurzadyan, L. Vitagliano, S.-S. Xue; "Black hole physics and astrophysics: The GRB-Supernova connection and URCA-1 – URCA-2"; in Proceedings of the Tenth Marcel Grossmann Meeting on General Relativity, Rio de Janeiro, Brazil, July 2003, M. Novello, S.E. Perez-Bergliaffa, Editors; p. 369; World Scientific, (Singapore, 2006).

   We outline the confluence of three novel theoretical fields in our modeling of Gamma-Ray Bursts (GRBs): 1) the ultrarelativistic regime of a shock front expanding with a Lorentz gamma factor ~ 300; 2) the quantum vacuum polarization process leading to an electron-positron plasma originating the shock front; and 3) the general relativistic process of energy extraction from a black hole originating the vacuum polarization process. There are two different classes of GRBs: the long GRBs and the short GRBs. We here address the issue of the long GRBs. The theoretical understanding of the long GRBs has led to the detailed description of their luminosities in fixed energy bands, of their spectral features and made also possible to probe the astrophysical scenario in which they originate. We are specially interested, in this report, to a subclass of long GRBs which appear to be accompanied by a supernova explosion. We are considering two specific examples: GRB980425/SN1998bw and GRB030329/SN2003dh. While these supernovae appear to have a standard energetics of 10^{49} ergs, the GRBs are highly variable and can have energetics 10^4 – 10^5 times larger than the ones of the supernovae. Moreover, many long GRBs occurs without the presence of a supernova. It is concluded that in no way a GRB can originate from a supernova. The precise theoretical understanding of the GRB luminosity we present evidence, in both these systems, the existence of an independent component in the X-ray emission, usually interpreted in the current literature as part of the GRB afterglow. This component has been observed by Chandra and XMM to have a strong decay on scale of months. We have named here these two sources respectively URCA-1 and URCA-2, in honor of the work that George Gamow and Mario Shoenberg did in 1939 in this town of Urca identifying the basic mechanism, the Urca processes, leading to the process of gravitational collapse and the formation of a neutron star and a supernova. The further hypothesis is considered to relate this X-ray source to a neutron star, newly born in the Supernova. This hypothesis should be submitted to further theoretical and observational investigation. Some theoretical developments to clarify the astrophysical origin of this new scenario are outlined.

3. M.G. Bernardini, C.L. Bianco, P. Chardonnet, F. Fraschetti, R. Ruffini, S.-S. Xue; "General features of GRB 030329 in the EMBH model"; in Proceedings of the Tenth Marcel Grossmann Meeting on General Relativity, Rio de Janeiro, Brazil, July 2003, M. Novello, S.E. Perez-Bergliaffa, Editors; p. 2459; World Scientific, (Singapore, 2006).

   GRB 030329 is considered within the EMBH model. We determine the three free parameters and deduce its luminosity in given energy bands comparing it with the observations. The observed substructures are compared with the predictions of the model: by applying the result that substructures observed in the extended afterglow peak emission (E-APE) do indeed originate in the collision of the accelerated baryonic matter (ABM) pulse with the inhomogeneities in the interstellar medium around the black-hole, masks of density inhomogeneities are considered in order to reproduce the observed temporal substructures. The induced supernova concept is applied to this system and the general consequences that we are witnessing are the formation of a cosmological thriptych of a black hole originating the GRB 030329, the supernova SN2003dh and a young neutron star. Analogies to the system GRB 980425–SN1998bw are outlined.

4. R. Ruffini, M.G. Bernardini, C.L. Bianco, P. Chardonnet, A. Corsi, F. Fraschetti, S.-S. Xue; "GRB 970228 and its associated Supernova in the EMBH model"; in Proceedings of the Tenth Marcel Grossmann Meeting on General Relativity, Rio de Janeiro, Brazil, July 2003, M. Novello, S.E. Perez-Bergliaffa, Editors; p. 2465; World Scientific, (Singapore, 2006).

   The γ-ray burst of 1997 February 28 is analyzed within the Electromagnetic Black Hole model. We first estimate the value of the total energy deposited in the dyadosphere, E_{dya}, and the amount of baryonic matter left over by the EMBH progenitor star, $B = M_B c^2 / E_{dya}$. We then consider the role of the interstellar medium number density n_{ISM} and of the ratio R between the effective emitting area and the total surface area of the γ-ray burst source, in reproducing the prompt emission and the X-ray afterglow of this burst. Some considerations are also done concerning the possibility of explaining, within the theory, the observed evidence for a supernova in the optical afterglow.

5. F. Fraschetti, M.G. Bernardini, C.L. Bianco, P. Chardonnet, R. Ruffini, S.-S. Xue; "Inferences on the ISM structure around GRB980425 and GRB980425-SN1998bw association in the EMBH Model"; in Proceedings of the Tenth Marcel Grossmann Meeting on General Relativity, Rio de Janeiro, Brazil, July 2003, M. Novello, S.E. Perez-Bergliaffa, Editors; p. 2451; World Scientific, (Singapore, 2006).

   We determine the four free parameters within the EMBH model for GRB 980425 and deduce its luminosity in given energy bands, its spectra and its time variability in the prompt radiation. We compute the basic kinematical parameters of GRB 980425. In the extended afterglow peak emission the Lorentz γ factor is lower than the critical value 150 which has been found in Ruffini et al. (2002) to be necessary in order to perform the tomography of the ISM surrounding the GRB as suggested by Dermer & Mitman (1999). The detailed structure of the density inhomogeneities as well as the effects of radial apparent superluminal effects are evaluated within the EMBH model. Under the assumption that the energy distribution of emitted radiation is thermal in the comoving frame, time integrated spectra of EMBH model for prompt emission are computed. The induced supernova concept is applied to this system and general consequences on the astrophysical and cosmological scenario are derived.

6. R. Ruffini, M.G. Bernardini, C.L. Bianco, P. Chardonnet, F. Fraschetti, R. Guida, S.-S. Xue; "GRB 050315: A step in the proof of the uniqueness of the overall GRB structure"; in "GAMMA-RAY BURSTS IN THE SWIFT ERA: Sixteenth Maryland Astrophysics Conference", Washington, DC, USA, November 29th – December 2nd 2005, Stephen S. Holt, Neil Gehrels, John A. Nousek, Editors; AIP Conference Proceedings, 836, 103 (2006).

   Using the Swift data of GRB 050315, we progress in proving the uniqueness of our theoretically predicted Gamma-Ray Burst (GRB) structure as composed by a proper-GRB, emitted at the transparency of an electron-positron plasma with suitable baryon loading, and an afterglow comprising the "prompt radiation" as due to external shocks. Detailed light curves for selected energy bands are theoretically fitted in the entire temporal region of the Swift observations ranging over 10^6 seconds.

7. R. Ruffini, M.G. Bernardini, C.L. Bianco, P. Chardonnet, F. Fraschetti, S.-S. Xue; "Theoretical Interpretation of GRB 031203 and URCA-3"; in

"Relativistic Astrophysics and Cosmology - Einstein's Legacy", B. Aschenbach, V. Burwitz, G. Hasinger, B. Leibundgut, Editors; Springer-Verlag (2007).

8. R. Ruffini, M.G. Bernardini, C.L. Bianco, L. Caito, P. Chardonnet, M.G. Dainotti, F. Fraschetti, R. Guida, M. Rotondo, G. Vereshchagin, L. Vita--gliano, S.-S. Xue; "The Blackholic energy and the canonical Gamma-Ray Burst"; in Proceedings of the XIIth Brazilian School on Cosmology and Gravitation, Mangaratiba, Rio de Janeiro (Brazil), September 2006, M. Novello, S.E. Perez Bergliaffa, Editors; AIP Conference Proceedings, 910, 55 (2007).

   Gamma-Ray Bursts (GRBs) represent very likely "the" most extensive computational, theoretical and observational effort ever carried out successfully in physics and astrophysics. The extensive campaign of observation from space based X-ray and γ-ray observatory, such as the *Vela*, CGRO, BeppoSAX, HETE-II, INTEGRAL, *Swift*, R-XTE, *Chandra*, XMM satellites, have been matched by complementary observations in the radio wavelength (e.g. by the VLA) and in the optical band (e.g. by VLT, Keck, ROSAT). The net result is unprecedented accuracy in the received data allowing the determination of the energetics, the time variability and the spectral properties of these GRB sources. The very fortunate situation occurs that these data can be confronted with a mature theoretical development. Theoretical interpretation of the above data allows progress in three different frontiers of knowledge: **a)** the ultrarelativistic regimes of a macroscopic source moving at Lorentz gamma factors up to ~ 400; **b)** the occurrence of vacuum polarization process verifying some of the yet untested regimes of ultrarelativistic quantum field theories; and **c)** the first evidence for extracting, during the process of gravitational collapse leading to the formation of a black hole, amounts of energies up to 10^{55} ergs of blackholic energy — a new form of energy in physics and astrophysics. We outline how this progress leads to the confirmation of three interpretation paradigms for GRBs proposed in July 2001. Thanks mainly to the observations by *Swift* and the optical observations by VLT, the outcome of this analysis points to the existence of a "canonical" GRB, originating from a variety of different initial astrophysical scenarios. The communality of these GRBs appears to be that they all are emitted in the process of formation of a black hole with a negligible value of its angular momentum. The following sequence of events appears to be canonical: the vacuum polarization process in the dyadosphere with the creation of the optically thick self accelerating electron-positron plasma; the engulfment of baryonic mass during the plasma expansion; adiabatic expansion of the optically thick "fireshell" of electron-positron-baryon plasma up to the transparency; the interaction of the accelerated baryonic matter with the interstellar medium (ISM). This leads to the canonical GRB composed of a proper GRB (P-GRB), emitted at the moment of transparency, followed by an extended afterglow. The sole parameters in this scenario are the total energy of the dyadosphere E_{dya}, the fireshell baryon loading M_B defined by the dimensionless parameter $B \equiv M_B c^2 / E_{dya}$, and the ISM filamentary distribution around the source. In the limit $B \to 0$ the total energy is radiated in the P-GRB with a vanishing contribution in the afterglow. In this limit, the canonical GRBs explain as well the short GRBs. In these lecture notes we systematically outline the main results of our model comparing and contrasting them with the ones in the current literature. In both cases, we have limited ourselves to review already published results in refereed publications. We emphasize as well the role of GRBs in testing yet unexplored grounds in the foundations of general relativity and relativistic field theories.

9. R. Ruffini, M.G. Bernardini, C.L. Bianco, L. Caito, P. Chardonnet, M.G. Dainotti, F. Fraschetti, R. Guida, G. Vereshchagin, S.-S. Xue; "The role of GRB 031203 in clarifying the astrophysical GRB scenario"; in Proceedings of the 6^{th} Integral Workshop - The Obscured Universe, Moscow, (Russia), July 2006, S. Grebenev, R. Sunyaev, C. Winkler, A. Parmar, L. Ouwehand, Editors; ESA Special Publication, SP-622, 561 (2007).

   The luminosity and the spectral distribution of the afterglow of GRB 031203 have been presented within our theoretical framework, which envisages the GRB structure as composed by a proper-GRB, emitted at the transparency of an electron-positron plasma with suitable baryon loading, and an afterglow comprising the "prompt emission" as due to external shocks. In addition to the GRB emission, there appears to be a prolonged soft X-Ray emission lasting for 10^6–10^7 seconds followed by an exponential decay. This additional source has been called by us URCA-3. It is urgent to establish if this component is related to the GRB or to the Supernova (SN). In this second case, there are two possibilities: either the interaction of the SN ejecta with the interstellar medium or, possibly, the cooling of a young neutron star formed in the SN 2003lw process. The analogies and the differences between this triptych GRB 031203 / SN 2003lw / URCA-3 and the corresponding ones GRB 980425 / SN 1998bw / URCA-1 and GRB 030329 / SN 2003dh / URCA-2, as well as GRB 060218 / SN 2006aj are discussed.

10. M.G. Bernardini, C.L. Bianco, L. Caito, M.G. Dainotti, R. Guida, R. Ruffini; "GRB970228 and the class of GRBs with an initial spikelike emission: do they follow the Amati relation?"; in Relativistic Astrophysics – Proceedings of the 4^{th} Italian-Sino Workshop, Pescara (Italy), July 2007, C.L. Bianco, S.-S. Xue, Editors; AIP Conference Proceedings, 966, 7 (2008).

    On the basis of the recent understanding of GRB050315 and GRB060218, we return to GRB970228, the first Gamma-Ray Burst (GRB) with detected afterglow. We proposed it as the prototype for a new class of GRBs with "an occasional softer extended emission lasting tenths of seconds after an initial spikelike emission". Detailed theoretical computation of the GRB970228 light curves in selected energy bands for the prompt emission are presented and compared with observational *Beppo*SAX data. From our analysis we conclude that GRB970228 and likely the ones of the above mentioned new class of GRBs are "canonical GRBs" have only one peculiarity: they exploded in a galactic environment, possibly the halo, with a very low value of CBM density. Here we investigate how GRB970228 unveils another peculiarity of this class of GRBs: they do not fulfill the "Amati relation". We provide a theoretical explanation within the fireshell model for the apparent absence of such correlation for the GRBs belonging to this new class.

11. C.L. Bianco, M.G. Bernardini, L. Caito, M.G. Dainotti, R. Guida, R. Ruffini; "The "Fireshell" Model and the "Canonical" GRB Scenario; in Relativistic Astrophysics – Proceedings of the 4^{th} Italian-Sino Workshop, Pescara (Italy), July 2007, C.L. Bianco, S.-S. Xue, Editors; AIP Conference Proceedings, 966, 12 (2008).

    In the "fireshell" model we define a "canonical GRB" light curve with two sharply different components: the Proper-GRB (P-GRB), emitted when the optically thick fireshell of electron-positron plasma originating the phenomenon reaches transparency, and the afterglow, emitted due to the collision between the remaining optically thin fireshell and the CircumBurst Medium (CBM). We outline our "canonical GRB" scenario, originating from the gravitational collapse to a black hole, with a special emphasis on the discrimination between "genuine" and "fake" short GRBs.

12. L. Caito, M.G. Bernardini, C.L. Bianco, M.G. Dainotti, R. Guida, R. Ruffini; "GRB 060614: A Progress Report"; in Relativistic Astrophysics – Proceedings of the 4^{th} Italian-Sino Workshop, Pescara (Italy), July 2007, C.L. Bianco, S.-S. Xue, Editors; AIP Conference Proceedings, 966, 16 (2008).

The explosion of GRB 060614, detected by the Swift satellite, produced a deep break in the GRB scenario opening new horizons of investigation, because it can't be traced back to any traditional scheme of classification. In fact, it manifests peculiarities both of long bursts and of short bursts. Above all, it is the first case of long duration near GRB without any bright Ib/c associated Supernova. We will show that, in our canonical GRB scenario, this "anomalous" situation finds a natural interpretation and allows us to discuss a possible variation to the traditional classification scheme, introducing the distinction between "genuine" and "fake" short bursts.

13. M.G. Dainotti, M.G. Bernardini, C.L. Bianco, L. Caito, R. Guida, R. Ruffini; "GRB 060218 and the Binaries as Progenitors of GRB-SN Systems"; in Relativistic Astrophysics – Proceedings of the 4^{th} Italian-Sino Workshop, Pescara (Italy), July 2007, C.L. Bianco, S.-S. Xue, Editors; AIP Conference Proceedings, 966, 25 (2008).

    We study the Gamma-Ray Burst (GRB) 060218: a particularly close source at $z = 0.033$ with an extremely long duration, namely $T_{90} \sim 2000$ s, related to SN 2006aj. This source appears to be a very soft burst, with a peak in the spectrum at 4.9 keV, therefore interpreted as an X-Ray Flash (XRF). It fullfills the Amati relation. I present the fitting procedure, which is time consuming. In order to show its sensitivity I also present two examples of fits with the same value of B and different value of $E^{tot}_{e^\pm}$. We fit the X- and γ-ray observations by *Swift* of GRB 060218 in the 0.1–150 keV energy band during the entire time of observations from 0 all the way to 10^6 s within a unified theoretical model. The free parameters of our theory are only three, namely the total energy $E^{tot}_{e\pm}$ of the $e^\pm$ plasma, its baryon loading $B \equiv M_B c^2/E^{tot}_{e\pm}$, as well as the CircumBurst Medium (CBM) distribution. We justify the extremely long duration of this GRB by a total energy $E^{tot}_{e\pm} = 2.32 \times 10^{50}$ erg, a very high value of the baryon loading $B = 1.0 \times 10^{-2}$ and the effective CircumBurst Medium (CBM) density which shows a radial dependence $n_{cbm} \propto r^{-\alpha}$ with $1.0 \leq \alpha \leq 1.7$ and monotonically decreases from 1 to 10^{-6} particles/cm^3. We recall that this value of the B parameter is the highest among the sources we have analyzed and it is very close to its absolute upper limit expected. By our fit we show that there is no basic differences between XRFs and more general GRBs. They all originate from the collapse process to a black hole and their difference is due to the variability of the three basic parameters within the range of full applicability of the theory. We also think that the smallest possible black hole, formed by the gravitational collapse of a neutron star in a binary system, is consistent with the especially low energetics of the class of GRBs associated with SNe Ib/c.

14. R. Guida, M.G. Bernardini, C.L. Bianco, L. Caito, M.G. Dainotti, R. Ruffini; "The Amati Relation within the Fireshell Model"; in Relativistic Astrophysics – Proceedings of the 4^{th} Italian-Sino Workshop, Pescara (Italy), July 2007, C.L. Bianco, S.-S. Xue, Editors; AIP Conference Proceedings, 966, 46 (2008).

    In this work we show the existence of a spectral-energy correlation within our "fireshell" model for GRBs. The free parameters of the model are the total energy $E_{tot}^{e\pm}$ of the $e^{\pm}$ plasma and its baryon loading $B \equiv M_B c^2/E_{tot}^{e\pm}$, characterizing the source, and the parameters describing the effective CircumBurst medium (CBM) distribution, namely its particle number density ρ and its effective emitting area R. We build a sample of pseudo-GRBs, i.e. a set of theoretically simulated light curves, varying the total energy of the electron-positron plasma $E_{tot}^{e\pm}$ and keeping the same baryon loading; the parametrization used to describe the distribution of the CircumBurst medium is the same as well for all the pseudo-GRBs. The values of these parameters (B, ρ and R) used in this work are equal to the ones assumed to fit GRB050315, a *Swift* burst representing a good example of what in the literature has been addressed as "canonical light curve". For each GRB of the sample we calculate the νF_ν spectrum integrating the theoretically computed light curve over the total time, namely from our T_0, the end of the Proper-GRB (P-GRB), up to the end of our afterglow phase, when the fireshell Lorentz gamma factor is close to unity; we exclude the P-GRB from this spectral computation because, following our "canonical" GRB scenario, this component of the GRB emission is physically different from the other component, that is our afterglow component, so one should take care in no mixing them. We find that the maximum of this spectrum, that is the observed peak energy $E_{p,tot}$, correlates with the initial electron-positron plasma energy $E_{tot}^{e\pm}$ in a way very similar to the Amati one: $E_{p,tot} \propto (E_{tot}^{e\pm})^{0.5}$.

15. R. Guida, M.G. Bernardini, C.L. Bianco, L. Caito, M.G. Dainotti, R. Ruffini; "Theoretical interpretation of the Amati relation within the fireshell model"; in GAMMA-RAY BURSTS 2007: Proceedings of the Santa Fe Conference, Santa Fe (NM, USA), November 2007, M. Galassi, D. Palmer, E. Fenimore, Editors; AIP Conference Proceedings, 1000, 60 (2008).

    We discuss within our theoretical "fireshell" model for Gamma-Ray Bursts (GRBs) the theoretical interpretation of the phenomenological correlation between the isotropic-equivalent radiated energy of the prompt emission E_{iso} and the cosmological rest-frame νF_ν spectrum peak energy E_p observed by Amati and collaborators. Possible reasons for some of the outliers of this relation are given.

16. L. Caito, M.G. Bernardini, C.L. Bianco, M.G. Dainotti, R. Guida, R. Ruffini; "GRB 060614: a Fake Short Gamma-Ray Burst"; in GAMMA-RAY BURSTS 2007: Proceedings of the Santa Fe Conference, Santa Fe (NM, USA), November 2007, M. Galassi, D. Palmer, E. Fenimore, Editors; AIP Conference Proceedings, 1000, 301 (2008).

    The explosion of GRB 060614 produced a deep break in the GRB scenario and opened new horizons of investigation because it can't be traced back to any traditional scheme of classification. In fact, it manifests peculiarities both of long bursts and of short bursts and, above all, it is the first case of long duration near GRB without any bright Ib/c associated Supernova. We will show that, in our canonical GRB scenario, this "anomalous" situation finds a natural interpretation and allows us to discuss a possible variation to the traditional classification scheme, introducing the distinction between "genuine" and "fake" short bursts.

17. C.L. Bianco, M.G. Bernardini, L. Caito, M.G. Dainotti, R. Guida, R. Ruffini; "Short and canonical GRBs"; in GAMMA-RAY BURSTS 2007: Proceedings of the Santa Fe Conference, Santa Fe (NM, USA), November 2007, M. Galassi, D. Palmer, E. Fenimore, Editors; AIP Conference Proceedings, 1000, 305 (2008).

    Within the "fireshell" model for the Gamma-Ray Bursts (GRBs) we define a "canonical GRB" light curve with two sharply different components: the Proper-GRB (P-GRB), emitted when the optically thick fireshell of electron-positron plasma originating the phenomenon reaches transparency, and the afterglow, emitted due to the collision between the remaining optically thin fireshell and the CircumBurst Medium (CBM). We outline our "canonical GRB" scenario, with a special emphasis on the discrimination between "genuine" and "fake" short GRBs.

18. C.L. Bianco, M.G. Bernardini, L. Caito, M.G. Dainotti, R. Guida, R. Ruffini, G. Vereshchagin, S.-S. Xue; "The Equations of motion of the "fireshell""; in OBSERVATIONAL EVIDENCE FOR BLACK HOLES IN THE UNIVERSE: Proceedings of the 2nd Kolkata Conference, Kolkata (India),

February 2008, S.K. Chakrabarti, A.S. Majumdar, Editors; AIP Conference Proceedings, 1053, 259 (2008).

The Fireshell originating a Gamma-Ray Burst (GRB) encompasses an optically thick regime followed by an optically thin one. In the first one the fireshell self-accelerates from a Lorentz gamma factor equal to 1 all the way to 200-300. The physics of this system is based on the continuous annihilation of electron-positron pairs in an optically thick e^+e^- plasma with a small baryon loading. In the following regime, the optically thin fireshell, composed by the baryons left over after the transparency point, ballistically expands into the Circum-Burst Medium (CBM). The dynamics of the fireshell during both regimes will be analyzed. In particular we will re-examine the validity of the constant-index power-law relation between the fireshell Lorentz gamma factor and its radial coordinate, usually adopted in the current literature on the grounds of an "ultrarelativistic" approximation. Such expressions are found to be mathematically correct but only approximately valid in a very limited range of the physical and astrophysical parameters and in an asymptotic regime which is reached only for a very short time, if any.

19. M.G. Bernardini, C.L. Bianco, L. Caito, M.G. Dainotti, R. Guida, R. Ruffini; "The "Canonical" GRBs within the fireshell model"; in OBSERVATIONAL EVIDENCE FOR BLACK HOLES IN THE UNIVERSE: Proceedings of the 2nd Kolkata Conference, Kolkata (India), February 2008, S.K. Chakrabarti, A.S. Majumdar, Editors; AIP Conference Proceedings, 1053, 267 (2008).

    Within the fireshell model we define a "canonical" GRB light curve with two sharply different components: the Proper-GRB (P-GRB), emitted when the optically thick fireshell of electron-positron plasma originating the phenomenon reaches transparency, and the afterglow, emitted due to the collision between the remaining optically thin fireshell and the CircumBurst Medium (CBM). On the basis of the recent understanding of GRB970228 as the prototype for a new class of GRBs with "an occasional softer extended emission lasting tenths of seconds after an initial spikelike emission" we outline our "canonical" GRB scenario, originating from the gravitational collapse to a black hole, with a special emphasis on the discrimination between short GRBs and the ones appearing as such due to their peculiar astrophysical setting.

20. M.G. Dainotti, M.G. Bernardini, C.L. Bianco, L. Caito, R. Guida, R. Ruffini; "GRB 060218: the density mask and its peculiarity compared to the other sources"; in OBSERVATIONAL EVIDENCE FOR BLACK HOLES

IN THE UNIVERSE: Proceedings of the 2^{nd} Kolkata Conference, Kolkata (India), February 2008, S.K. Chakrabarti, A.S. Majumdar, Editors; AIP Conference Proceedings, 1053, 283 (2008).

The Swift satellite has given continuous data in the range 0.3–150 keV from 0 s to 106 s for GRB060218 associated with SN2006aj. It has an unusually long duration ($T_{90} \sim 2100$ s). We plan to fit the complete γ- and X-ray light curves of this long duration GRB, including the prompt emission and we give peculiar attention to the afterglow lightcurve in order to better constrain the density mask. We apply our "fireshell" model based on the formation of a black hole, giving the relevant references. The initial total energy of the electron-positron plasma $E^{tot}_{e^{\pm}} == 2.32 \times 10^{50}$ erg has a particularly low value similarly to the other GRBs associated with SNe. For the first time we observe a baryon loading $B = 10^{-2}$ which coincides with the upper limit for the dynamical stability of the fireshell. The effective CircumBurst Medium (CBM) density shows a radial dependence $n_{cbm} \propto r^{-a}$ with $1.0 \leq a \leq 1.7$ and monotonically decreases from 1 to 10^{-6} particles/cm^3. Such a behavior is interpreted as due to a fragmentation in the fireshell. Such a fragmentation is crucial in explaining both the unusually large T_{90} and the consequently inferred abnormal low value of the CBM effective density. We present the comparison between the density mask of this source and the ones of a normal GRB 050315 and a fake short, GRB 970228, making some assumptions on the CBM behaviour in the surrounding of the Black hole.

21. L. Caito, M.G. Bernardini, C.L. Bianco, M.G. Dainotti, R. Guida, R. Ruffini; "GRB 060614 in the canonical fireshell model"; in OBSERVATIONAL EVIDENCE FOR BLACK HOLES IN THE UNIVERSE: Proceedings of the 2^{nd} Kolkata Conference, Kolkata (India), February 2008, S.K. Chakrabarti, A.S. Majumdar, Editors; AIP Conference Proceedings, 1053, 291 (2008).

Gamma-Ray Burst (GRB) 060614 is the first nearby long duration GRB clearly not associated to any bright Ib/c Supernova. The explosion of this burst undermines one of the fundamental assumptions of the standard scenario and opens new horizons and hints of investigation. GRB 060614, hardly classifiable as a short GRB, is not either a "typical" long GRB since it occurs in a low star forming region. Moreover, it presents deep similarities with GRB 970228, which is the prototype of the "fake" short bursts, or better canonical GRBs disguised as short ones. Within the "fireshell" model, we test if this "anomalous" source can be a disguised short GRB.

22. L.J. Rangel Lemos, S. Casanova, R. Ruffini, S.S. Xue; "Fermi's approach to the study of pp interactions"; in OBSERVATIONAL EVIDENCE FOR BLACK HOLES IN THE UNIVERSE: Proceedings of the 2^{nd} Kolkata Conference, Kolkata (India), February 2008, S.K. Chakrabarti, A.S. Majumdar, Editors; AIP Conference Proceedings, 1053, 275 (2008).

    The physics of hadronic interactions found much difficulties for explain the experimental data. In this work we study the approach of Fermi (1950) about the multiplicity of pions emitted in pp interactions and in follow we compare with the modern approach

23. R. Ruffini, A.G. Aksenov, M.G. Bernardini, C.L. Bianco, L. Caito, M.G. Dainotti, G. De Barros, R. Guida, G.V. Vereshchagin, S.-S. Xue; "The canonical Gamma-Ray Bursts and their 'precursors"'; in 2008 NANJING GAMMA-RAY BURST CONFERENCE, Proceedings of the 2008 Nanjing Gamma-Ray Burst Conference, Nanjing (China), June 2008, Y.-F. Huang, Z.-G. Dai, B. Zhang, Editors; AIP Conference Proceedings, 1065, 219 (2008).

    The fireshell model for Gamma-Ray Bursts (GRBs) naturally leads to a canonical GRB composed of a proper-GRB (P-GRB) and an afterglow. P-GRBs, introduced by us in 2001, are sometimes considered "precursors" of the main GRB event in the current literature. We show in this paper how the fireshell model leads to the understanding of the structure of GRBs, with precise estimates of the time sequence and intensities of the P-GRB and the of the afterglow. It leads as well to a natural classification of the canonical GRBs which overcomes the traditional one in short and long GRBs.

24. M.G. Bernardini, C.L. Bianco, L. Caito, M.G. Dainotti, R. Guida, R. Ruffini; "Preliminary analysis of GRB060607A within the fireshell model"; in 2008 NANJING GAMMA-RAY BURST CONFERENCE; Proceedings of the 2008 Nanjing Gamma-Ray Burst Conference, Nanjing (China), June 2008, Y.-F. Huang, Z.-G. Dai, B. Zhang, Editors; AIP Conference Proceedings, 1065, 227 (2008).

    GRB060607A is a very distant ($z = 3.082$) and energetic event ($E_{iso} \sim 10^{53}$ erg). Its main peculiarity is that the peak of the near-infrared afterglow has been observed with the REM robotic telescope, allowing to infer the initial Lorentz gamma factor of the emitting system. We present a preliminary analysis of the spectra and light curves of GRB060607A prompt emission within the fireshell model. We show that the N(E) spectrum of the prompt emission, whose behavior is usually described as "simple power-law", can also be fitted in a satisfactory way by a convolution of thermal spectra as predicted by the model we applied. The theoretical time-integrated spectrum of the prompt emission as well as the light curves in the BAT and XRT energy band are in good agreement with the observations, enforcing the plausibility of our approach. Furthermore, the initial value of Lorentz gamma factor we predict is compatible with the one deduced from the REM observations.

25. C.L. Bianco, M.G. Bernardini, L. Caito, M.G. Dainotti, R. Guida, R. Ruffini; "The "fireshell" model and the "canonical GRB" scenario"; in 2008 NANJING GAMMA-RAY BURST CONFERENCE; Proceedings of the 2008 Nanjing Gamma-Ray Burst Conference, Nanjing (China), June 2008, Y.-F. Huang, Z.-G. Dai, B. Zhang, Editors; AIP Conference Proceedings, 1065, 223 (2008).

    The Swift observation of GRB 060614, as well as the catalog analysis by Norris & Bonnell (2006), opened the door "on a new Gamma-Ray Bursts (GRBs) classification scheme that straddles both long and short bursts" (Gehrels et al. 2006). Within the "fireshell" model for the Gamma-Ray Bursts (GRBs) we define a "canonical GRB" light curve with two sharply different components: the Proper-GRB (P-GRB), emitted when the optically thick fireshell of electron-positron plasma originating the phenomenon reaches transparency, and the afterglow, emitted due to the collision between the remaining optically thin fireshell and the CircumBurst Medium (CBM). We here outline our "canonical GRB" scenario, which implies three different GRB classes: the "genuine" short GRBs, the "fake" or "disguised" short GRBs and the other (so-called "long") GRBs. We also outline some implications for the theoretical interpretation of the Amati relation.

26. G. De Barros, M.G. Bernardini, C.L. Bianco, L. Caito, M.G. Dainotti, R. Guida, R. Ruffini; "Is GRB 050509b a "genuine" short GRB?"; in 2008 NANJING GAMMA-RAY BURST CONFERENCE; Proceedings of the 2008 Nanjing Gamma-Ray Burst Conference, Nanjing (China), June 2008, Y.-F. Huang, Z.-G. Dai, B. Zhang, Editors; AIP Conference Proceedings, 1065, 231 (2008).

    Within our "fireshell" model we introduced a "canonical" GRB scenario which differentiates physically the "proper GRB" (P-GRB) emission when photons decouple, and the afterglow emission due to interaction of the accelerated baryons with the CircumBurst Medium (CBM). The ratio between energetics of the two components is ruled by the baryon loading of the fireshell. We here analyse the possibility that GRB050509b is the first case of a "genuine" short GRB the ones with smaller baryon loading. In such a case, the GRB050509b "prompt emission" would be dominated by the "proper GRB" and, moreover, the P-GRB total energy would be greater than the afterglow one. Our fit of the afterglow data and of the P-GRB energetics indicates that this source present the smallest baryon loading we ever encountered so far, being on the order of 10^{-4}.

27. G. De Barros, A.G. Aksenov, C.L. Bianco, R. Ruffini, G.V. Vereshchagin; "Fireshell versus Fireball scenarios"; in 2008 NANJING GAMMA-RAY BURST CONFERENCE; Proceedings of the 2008 Nanjing Gamma-Ray Burst Conference, Nanjing (China), June 2008, Y.-F. Huang, Z.-G. Dai, B. Zhang, Editors; AIP Conference Proceedings, 1065, 234 (2008).

    We revisit Cavallo and Rees classification based on the analysis of initial conditions in electron-positron-photon plasma which appears suddenly around compact astrophysical objects and gives origin to GRBs. These initial conditions were recently studied in [1,2] by numerical integration of relativistic Boltzmann equations with collision integrals, including binary and triple interactions between particles. The main conclusion is that the pair plasma in GRB sources quickly reaches thermal equilibrium well before its expansion starts. In light of this work we comment on each of the four scenarios proposed by Cavallo and Rees and discuss their applicability to describe evolution of GRB sources.

28. M.G. Bernardini, C.L. Bianco, L. Caito, M.G. Dainotti, R. Guida, R. Ruffini; "GRB970228 as a prototype for the class of GRBs with an initial spikelike emission"; in Proceedings of the Eleventh Marcel Grossmann Meeting on General Relativity, Berlin, Germany, July 2006, H. Kleinert, R.T. Jantzen, Editors; World Scientific, (Singapore, 2008).

    We interpret GRB970228 prompt emission within our "canonical" GRB scenario, identifying the initial spikelike emission with the Proper-GRB (P-GRB) and the following bumps with the afterglow peak emission. Furthermore, we emphasize the necessity to consider the "canonical" GRB as a whole due to the highly non-linear nature of the model we applied.

29. M.G. Bernardini, C.L. Bianco, L. Caito, M.G. Dainotti, R. Guida, R. Ruffini;

"GRB980425 and the puzzling URCA1 emission"; in Proceedings of the Eleventh Marcel Grossmann Meeting on General Relativity, Berlin, Germany, July 2006, H. Kleinert, R.T. Jantzen, Editors; World Scientific, (Singapore, 2008).

We applied our "fireshell" model to GRB980425 observational data, reproducing very satisfactory its prompt emission. We use the results of our analysis to provide a possible interpretation for the X-ray emission of the source S1. The effect on the GRB analysis of the lack of data in the pre-Swift observations is also outlined.

30. C.L. Bianco, M.G. Bernardini, L. Caito, P. Chardonnet, M.G. Dainotti, F. Fraschetti, R. Guida, R. Ruffini, S.-S. Xue; "Theoretical interpretation of 'long' and 'short' GRBs"; in Proceedings of the Eleventh Marcel Grossmann Meeting on General Relativity, Berlin, Germany, July 2006, H. Kleinert, R.T. Jantzen, Editors; World Scientific, (Singapore, 2008).

    Within the "fireshell" model we define a "canonical GRB" light curve with two sharply different components: the Proper-GRB (P-GRB), emitted when the optically thick fireshell of electron-positron plasma originating the phenomenon reaches transparency, and the afterglow, emitted due to the collision between the remaining optically thin fireshell and the CircumBurst Medium (CBM). We here present the consequences of such a scenario on the theoretical interpretation of the nature of "long" and "short" GRBs.

31. C.L. Bianco, M.G. Bernardini, P. Chardonnet, F. Fraschetti, R. Ruffini, S.-S. Xue; "Theoretical interpretation of luminosity and spectral properties of GRB 031203"; in Proceedings of the Eleventh Marcel Grossmann Meeting on General Relativity, Berlin, Germany, July 2006, H. Kleinert, R.T. Jantzen, Editors; World Scientific, (Singapore, 2008).

    We show how an emission endowed with an instantaneous thermal spectrum in the co-moving frame of the expanding fireshell can reproduce the time-integrated GRB observed non-thermal spectrum. An explicit example in the case of GRB 031203 is presented.

32. C.L. Bianco, R. Ruffini; "The 'Fireshell' model in the Swift era"; in Proceedings of the Eleventh Marcel Grossmann Meeting on General Relativity, Berlin, Germany, July 2006, H. Kleinert, R.T. Jantzen, Editors; World Scientific, (Singapore, 2008).

We here re-examine the validity of the constant-index power-law relation between the fireshell Lorentz gamma factor and its radial coordinate, usually adopted in the current Gamma-Ray Burst (GRB) literature on the grounds of an "ultrarelativistic" approximation. Such expressions are found to be mathematically correct but only approximately valid in a very limited range of the physical and astrophysical parameters and in an asymptotic regime which is reached only for a very short time, if any.

33. L. Caito, M.G. Bernardini, C.L. Bianco, M.G. Dainotti, R. Guida, R. Ruffini; "Theoretical interpretation of GRB011121"; in Proceedings of the Eleventh Marcel Grossmann Meeting on General Relativity, Berlin, Germany, July 2006, H. Kleinert, R.T. Jantzen, Editors; World Scientific, (Singapore, 2008).

    GRB 011121, detected by the BeppoSAX satellite, is studied as a prototype to understand the presence of flares observed by Swift in the afterglow of many GRB sources. Detailed theoretical analysis of the GRB 011121 light curves in selected energy bands are presented and compared with observational data. An interpretation of the flare of this source is provided by the introduction of the three-dimensional structure of the CircumBurst Medium(CBM).

34. M.G. Dainotti, M.G. Bernardini, C.L. Bianco, L. Caito, R. Guida, R. Ruffini; "On GRB 060218 and the GRBs related to Supernovae Ib/c"; in Proceedings of the Eleventh Marcel Grossmann Meeting on General Relativity, Berlin, Germany, July 2006, H. Kleinert, R.T. Jantzen, Editors; World Scientific, (Singapore, 2008).

    We study the Gamma-Ray Burst (GRB) 060218: a particularly close source at $z = 0.033$ with an extremely long duration, namely $T_{90} \sim 2000$ s, related to SN 2006aj. This source appears to be a very soft burst, with a peak in the spectrum at 4.9 keV, therefore interpreted as an X-Ray Flash (XRF) and it obeys to the Amati relation. We fit the X- and γ-ray observations by Swift of GRB 060218 in the 0.1–150 keV energy band during the entire time of observations from 0 all the way to 106 s within a unified theoretical model. The details of our theoretical analysis have been recently published in a series of articles. The free parameters of the theory are only three, namely the total energy $E^{tot}_{e\pm}$ of the $e^{\pm}$ plasma, its baryon loading $B = M_B c^2 / E^{tot}_{e\pm}$, as well as the CircumBurst Medium (CBM) distribution. We fit the entire light curve, including the prompt emission as an essential part of the afterglow. We recall that this value of the B parameter is the highest among the sources we have analyzed and it is very close to its absolute upper limit expected. We successfully make definite predictions about the spectral distribution in the early part of the light curve, exactly we derive the instantaneous photon number spectrum N(E) and we show that although the spectrum in the co-moving frame of the expanding pulse is thermal, the shape of the final spectrum in the laboratory frame is clearly non thermal. In fact each single instantaneous spectrum is the result of an integration of thousands of thermal spectra over the corresponding EQuiTemporal Surfaces (EQTS). By our fit we show that there is no basic differences between XRFs and more general GRBs. They all originate from the collapse process to a black hole and their difference is due to the variability of the three basic parameters within the range of full applicability of the theory.

35. R. Guida, M.G. Bernardini, C.L. Bianco, L. Caito, M.G. Dainotti, R. Ruffini; "Theoretical interpretation of GRB060124"; in Proceedings of the Eleventh Marcel Grossmann Meeting on General Relativity, Berlin, Germany, July 2006, H. Kleinert, R.T. Jantzen, Editors; World Scientific, (Singapore, 2008).

    We show the preliminary results of the application of our "fireshell" model to GRB060124. This source is very peculiar because it is the first event for which both the prompt and the afterglow emission were observed simultaneously by the three Swift instruments: BAT (15 - 350 keV), XRT (0,2 - 10 keV) and UVOT (170 - 650 nm), due to the presence of a precursor $\sim$ 570 s before the main burst. We analyze GRB060124 within our "canonical" GRB scenario, identifying the precursor with the P-GRB and the prompt emission with the afterglow peak emission. In this way we reproduce correctly the energetics of both these two components. We reproduce also the observed time delay between the precursor (P-GRB) and the main burst. The effect of such a time delay in our model will be discussed.

36. R. Ruffini, M.G. Bernardini, C.L. Bianco, L. Caito, P. Chardonnet, C. Cherubini, M.G. Dainotti, F. fraschetti, A. Geralico, R. Guida, B. Patricelli, M. Rotondo, J. Rueda Hernandez, G. Vereshchagin, S.-S. Xue; "Gamma-Ray Bursts"; in Proceedings of the Eleventh Marcel Grossmann Meeting on General Relativity, Berlin, Germany, July 2006, H. Kleinert, R.T. Jantzen, Editors; World Scientific, (Singapore, 2008).

    We show by example how the uncoding of Gamma-Ray Bursts (GRBs) offers unprecedented possibilities to foster new knowledge in fundamental physics and in astrophysics. After recalling some of the classic work on vacuum polarization in uniform electric fields by Klein, Sauter, Heisenberg, Euler and Schwinger, we summarize some of the efforts to observe these effects in heavy ions and high energy ion collisions. We then turn to the theory of vacuum polarization around a Kerr-Newman black hole, leading to the extraction of the blackholic energy, to the concept of dyadosphere and dyadotorus, and to the creation of an electron-positron-photon plasma. We then present a new theoretical approach encompassing the physics of neutron stars and heavy nuclei. It is shown that configurations of nuclear matter in bulk with global charge neutrality can exist on macroscopic scales and with electric fields close to the critical value near their surfaces. These configurations may represent an initial condition for the process of gravitational collapse, leading to the creation of an electron-positron-photon plasma: the basic self-accelerating system explaining both the energetics and the high energy Lorentz factor observed in GRBs. We then turn to recall the two basic interpretational paradigms of our GRB model: 1) the Relative Space-Time Transformation (RSTT) paradigm and 2) the Interpretation of the Burst Structure (IBS) paradigm. These paradigms lead to a "canonical" GRB light curve formed from two different components: a Proper-GRB (P-GRB) and an extended afterglow comprising a raising part, a peak, and a decaying tail. When the P-GRB is energetically predominant we have a "genuine" short GRB, while when the afterglow is energetically predominant we have a so-called long GRB or a "fake" short GRB. We compare and contrast the description of the relativistic expansion of the electron-positron plasma within our approach and within the other ones in the current literature. We then turn to the special role of the baryon loading in discriminating between "genuine" short and long or "fake" short GRBs and to the special role of GRB 991216 to illustrate for the first time the "canonical" GRB bolometric light curve. We then propose a spectral analysis of GRBs, and proceed to some applications: GRB 031203, the first spectral analysis, GRB 050315, the first complete light curve fitting, GRB 060218, the first evidence for a critical value of the baryon loading, GRB 970228, the appearance of "fake" short GRBs. We finally turn to the GRB-Supernova Time Sequence (GSTS) paradigm: the concept of induced gravitational collapse. We illustrate this paradigm by the systems GRB 980425 / SN 1998bw, GRB 030329 / SN 2003dh, GRB 031203 / SN 2003lw, GRB 060218 / SN 2006aj, and we present the enigma of the URCA sources. We then present some general conclusions.

37. R. Ruffini, A.G. Aksenov, M.G. Bernardini, C.L. Bianco, L. Caito, M.G.

Dainotti, G. De Barros, R. Guida, G. Vereshchagin, S.-S. Xue; "The canonical Gamma-Ray Bursts: long, 'fake'-'disguised' and 'genuine' short bursts; in PROBING STELLAR POPULATIONS OUT TO THE DISTANT UNIVERSE: CEFALU 2008, Proceedings of the International Conference; Cefalù (Italy), September 2008, G. Giobbi, A. Tornambe, G. Raimondo, M. Limongi, L. A. Antonelli, N. Menci, E. Brocato, Editors; AIP Conference Proceedings, 1111, 325 (2009).

The Gamma-Ray Bursts (GRBs) offer the unprecedented opportunity to observe for the first time the blackholic energy extracted by the vacuum polarization during the process of gravitational collapse to a black hole leading to the formation of an electron-positron plasma. The uniqueness of the Kerr-Newman black hole implies that very different processes originating from the gravitational collapse a) of a single star in a binary system induced by the companion, or b) of two neutron stars, or c) of a neutron star and a white dwarf, do lead to the same structure for the observed GRB. The recent progress of the numerical integration of the relativistic Boltzmann equations with collision integrals including 2-body and 3-body interactions between the particles offer a powerful conceptual tool in order to differentiate the traditional "fireball" picture, an expanding hot cavity considered by Cavallo and Rees, as opposed to the "fireshell" model, composed of an internally cold shell of relativistically expanding electron-positron-baryon plasma. The analysis of the fireshell naturally leads to a canonical GRB composed of a proper-GRB and an extended afterglow. By recalling the three interpretational paradigms for GRBs we show how the fireshell model leads to an understanding of the GRB structure and to an alternative classification of short and long GRBs.

38. M.G. Bernardini, M.G. Dainotti, C.L. Bianco, L. Caito, R. Guida, R. Ruffini; "Prompt emission and X-ray flares: the case of GRB 060607 A"; in PROBING STELLAR POPULATIONS OUT TO THE DISTANT UNIVERSE: CEFALU 2008, Proceedings of the International Conference; Cefalù (Italy), September 2008, G. Giobbi, A. Tornambe, G. Raimondo, M. Limongi, L. A. Antonelli, N. Menci, E. Brocato, Editors; AIP Conference Proceedings, 1111, 383 (2009).

GRB 060607A is a very distant and energetic event. Its main peculiarity is that the peak of the near-infrared (NIR) afterglow has been observed with the REM robotic telescope, allowing to estimate the initial Lorentz gamma factor within the fireball forward shock model. We analyze GRB 060607A within the fireshell model. The initial Lorentz gamma factor of the fireshell can be obtained adopting the exact solutions of its equations of motion, dealing only with the BAT and XRT observations, that are the basic contribution to the afterglow emission, up to a distance from the progenitor $r \sim 10^{18}$ cm. According to the "canonical GRB" scenario we interpret the whole prompt emission as the peak of the afterglow emission, and we show that the observed temporal variability of the prompt emission can be produced by the interaction of the fireshell with overdense CircumBurst Medium (CBM) clumps. This is indeed the case also of the X-ray flares which are present in the early phases of the afterglow light curve.

39. C.L. Bianco, M.G. Bernardini, L. Caito, M.G. Dainotti, R. Guida, R. Ruffini; "The 'fireshell' model and the 'canonical GRB' scenario. Implications for the Amati relation"; in PROBING STELLAR POPULATIONS OUT TO THE DISTANT UNIVERSE: CEFALU 2008, Proceedings of the International Conference; Cefalù (Italy), September 2008, G. Giobbi, A. Tornambe, G. Raimondo, M. Limongi, L. A. Antonelli, N. Menci, E. Brocato, Editors; AIP Conference Proceedings, 1111, 587 (2009).

    Within the "fireshell" model for GRBs we define a "canonical GRB" light curve with two sharply different components: the Proper-GRB (P-GRB), emitted when the optically thick fireshell reaches transparency, and the extended afterglow, emitted due to the collision between the remaining optically thin fireshell and the CircumBurst Medium (CBM). We here outline our "canonical GRB" scenario, which implies three different GRB classes: the "genuine" short GRBs, the "fake" or "disguised" short GRBs and the other (so-called "long") GRBs. We will also outline the corresponding implications for the Amati relation, which are opening its use for cosmology.

40. R. Ruffini, A.G. Aksenov, M.G. Bernardini, C.L. Bianco, L. Caito, P. Chardonnet, M.G. Dainotti, G. De Barros, R. Guida, L. Izzo, B. Patricelli, L.J. Rangel Lemos, M. Rotondo, J.A. Rueda Hernandez, G. Vereshchagin, S.-S. Xue; "The Blackholic energy and the canonical Gamma-Ray Burst IV: the 'long', 'genuine short' and 'fake – disguised short' GRBs"; in Proceedings of the XIIIth Brazilian School on Cosmology and Gravitation, Mangaratiba, Rio de Janeiro (Brazil), July-August 2008, M. Novello, S.E. Perez Bergliaffa, Editors; AIP Conference Proceedings, 1132, 199 (2009).

    We report some recent developments in the understanding of GRBs based on the theoretical framework of the "fireshell" model, already presented in the last three editions of the "Brazilian School of Cosmology and Gravitation". After recalling the basic features of the "fireshell model", we emphasize the following novel results: 1) the interpretation of the X-ray flares in GRB afterglows as due to the interaction of the optically thin fireshell with isolated clouds in the CircumBurst Medium (CBM); 2) an interpretation as "fake - disguised" short GRBs of the GRBs belonging to the class identified by Norris & Bonnell; we present two prototypes, GRB 970228 and GRB 060614; both these cases are consistent with an origin from the final coalescence of a binary system in the halo of their host galaxies with particularly low CBM density $n_{cbm} \sim 10^{-3}$ particles/cm^3; 3) the first attempt to study a genuine short GRB with the analysis of GRB 050509B, that reveals indeed still an open question; 4) the interpretation of the GRB-SN association in the case of GRB 060218 via the "induced gravitational collapse" process; 5) a first attempt to understand the nature of the "Amati relation", a phenomenological correlation between the isotropic-equivalent radiated energy of the prompt emission E_{iso} with the cosmological rest-frame νF_ν spectrum peak energy $E_{p,i}$. In addition, recent progress on the thermalization of the electron-positron plasma close to their formation phase, as well as the structure of the electrodynamics of Kerr-Newman Black Holes are presented. An outlook for possible explanation of high-energy phenomena in GRBs to be expected from the AGILE and the Fermi satellites are discussed. As an example of high energy process, the work by Enrico Fermi dealing with ultrarelativistic collisions is examined. It is clear that all the GRB physics points to the existence of overcritical electrodynamical fields. In this sense we present some progresses on a unified approach to heavy nuclei and neutron stars cores, which leads to the existence of overcritical fields under the neutron star crust.

41. A.G. Aksenov, M.G. Bernardini, C.L. Bianco, L. Caito, C. Cherubini, G. De Barros, A. Geralico, L. Izzo, F.A. Massucci, B. Patricelli, M. Rotondo, J.A. Rueda Hernandez, R. Ruffini, G. Vereshchagin, S.-S. Xue; "The fireshell model for Gamma-Ray Bursts"; in The Shocking Universe, Proceedings of the conference held in Venice (Italy), September 2009, G. Chincarini, P. D'Avanzo, R. Margutti, R. Salvaterra, Editors; SIF Conference Proceedings, 102, 451 (2010).

The fireshell model for GRBs is briefly outlined, and the currently ongoing developments are summarized.

42. M.G. Bernardini, C.L. Bianco, L. Caito, L. Izzo, B. Patricelli, R. Ruffini; "The end of the prompt emission within the fireshell model"; in The Shocking Universe, Proceedings of the conference held in Venice (Italy), September 2009, G. Chincarini, P. D'Avanzo, R. Margutti, R. Salvaterra, Editors; SIF Conference Proceedings, 102, 489 (2010)

    The shallow decay emission, revealed by the Swift satellite in the X-ray afterglow of a good sample of bursts, is a puzzle. Within the fireshell model it has been recently proposed an alternative explanation: if we assume that after the prompt phase the system has a range of Lorentz factors, the plateau phase is simply the product of the injection of slower material into the fireshell. This injection produces a modification both in the dynamics of the fireshell and in the spectrum of the emitted radiation. We postulate that this spread in the fireshell Lorentz factor occurs when the fireshell becomes transparent and do not depend on a prolonged activity of the central engine. The aim of this paper is to characterize dynamically the system in order to understand the nature of that material.

43. L. Izzo, M.G. Bernardini, C.L. Bianco, L. Caito, B. Patricelli, R. Ruffini; "GRB 090423 in the fireshell scenario"; in The Shocking Universe, Proceedings of the conference held in Venice (Italy), September 2009, G. Chincarini, P. D'Avanzo, R. Margutti, R. Salvaterra, Editors; SIF Conference Proceedings, 102, 537 (2010).

44. B. Patricelli, M.G. Bernardini, C.L. Bianco, L. Caito, L. Izzo, R. Ruffini, G. Vereshchagin; "A new spectral energy distribution of photons in the fireshell model of GRBs"; in The Shocking Universe, Proceedings of the conference held in Venice (Italy), September 2009, G. Chincarini, P. D'Avanzo, R. Margutti, R. Salvaterra, Editors; SIF Conference Proceedings, 102, 559 (2010).

    The fireshell model of Gamma Ray Bursts (GRBs) postulates that the emission process is thermal in the comoving frame of the fireshell, but this is just a first approximation. We investigate a different spectrum of photons in the comoving frame in order to better reproduce the observed spectral properties of GRB prompt emission. We introduce a modified thermal spectrum whose low energy slope depends on an index α, left as a free parameter. We test it by comparing the numerical simulations with observed BAT spectra integrated over different intervals of time. We find that the observational data can be correctly reproduced by assuming $\alpha = -1.8$.

45. C.L. Bianco, M.G. Bernardini, L. Caito, G. De Barros, L. Izzo, B. Patricelli, R. Ruffini; "Disguised Short Bursts and the Amati Relation"; in Deciphering the ancient universe with Gamma-Ray Bursts, Proceedings of the conference held in Kyoto (Japan), April 2010, N. Kawai, S. Nagataki, Editors; AIP Conference Proceedings, 1279, 299 (2010).

    The class of "Disguised short" GRBs implied by the fireshell scenario is presented, with special emphasis on the implications for the Amati relation.

46. L. Izzo, M.G. Bernardini, C.L. Bianco, L. Caito, B. Patricelli, L.J. Rangel Lemos, R. Ruffini; "On GRB 080916C and GRB 090902B observed by the Fermi satellite"; in Deciphering the ancient universe with Gamma-Ray Bursts, Proceedings of the conference held in Kyoto (Japan), April 2010, N. Kawai, S. Nagataki, Editors; AIP Conference Proceedings, 1279, 343 (2010).

    We propose a possible explanation, in the context of the Fireshell scenario, for the high-energy emission observed in GRB 080916C and GRB 090902B. The physical process underlying this emission consists mainly in the interaction of the baryon in the Fireshell with some high-density region around the burst site. Moreover we associate the observed delay of the onset of the high-energy emission as due to the P-GRB emission.

47. B. Patricelli, M.G. Bernardini, C.L. Bianco, L. Caito, G. De Barros, L. Izzo, R. Ruffini; "Black Holes in Gamma Ray Bursts"; in Deciphering the ancient universe with Gamma-Ray Bursts, Proceedings of the conference held in Kyoto (Japan), April 2010, N. Kawai, S. Nagataki, Editors; AIP Conference Proceedings, 1279, 406 (2010).

    Within the fireshell model, Gamma Ray Bursts (GRBs) originate from an optically thick $e^{\pm}$ plasma created by vacuum polarization process during the formation of a Black Hole (BH). Here we briefly recall the basic features of this model, then we show how it is possible to interpret GRB observational properties within it. In particular we present, as a specific example, the analysis of GRB 050904 observations of the prompt emission light curve and spectrum in the Swift BAT energy band (15-150 keV).

48. M.G. Bernardini, C.L. Bianco, L. Caito, M.G. Dainotti, R. Guida, R. Ruffini; "The GRB classification within the "fireshell" model: short, long and "fake" short GRBs"; in Proceedings of the 3rd Stueckelberg Workshop on Relativistic Field Theories, Pescara, Italy, July 2008, N. Carlevaro,

R. Ruffini, G.V. Vereshchagin, Editors; Cambridge Scientific Publishers, (UK, 2011).

49. C.L. Bianco, M.G. Bernardini, L. Caito, M.G. Dainotti, R. Guida, R. Ruffini, G.V. Vereshchagin, S.-S. Xue; "Equations of motion of the "fireshell""; in Proceedings of the 3rd Stueckelberg Workshop on Relativistic Field Theories, Pescara, Italy, July 2008, N. Carlevaro, R. Ruffini, G.V. Vereshchagin, Editors; Cambridge Scientific Publishers, (UK, 2011).

50. L. Caito, M.G. Bernardini, C.L. Bianco, M.G. Dainotti, R. Guida, R. Ruffini; "GRB 060614: another example of "fake" short burst from a merging binary system"; in Proceedings of the 3rd Stueckelberg Workshop on Relativistic Field Theories, Pescara, Italy, July 2008, N. Carlevaro, R. Ruffini, G.V. Vereshchagin, Editors; Cambridge Scientific Publishers, (UK, 2011).

51. G. De Barros, M.G. Bernardini, C.L. Bianco, L. Caito, R. Guida, R. Ruffini; "Analysis of GRB 050509b"; in Proceedings of the 3rd Stueckelberg Workshop on Relativistic Field Theories, Pescara, Italy, July 2008, N. Carlevaro, R. Ruffini, G.V. Vereshchagin, Editors; Cambridge Scientific Publishers, (UK, 2011).

52. R. Ruffini, L. Izzo, A.V. Penacchioni, C.L. Bianco, L. Caito, S.K. Chakrabarti, A. Nandi; "GRB 090618: a possible case of multiple GRB?"; in Proceedings of the 25th Texas Symposium on Relativistic Astrophysics, held in Heidelberg (Germany), December 2010, F.M. Rieger, C. van Eldik, W. Hofmann, Editors; PoS(Texas2010), 101.

53. L.J. Rangel Lemos, C.L. Bianco, H.J. Mosquera Cuesta, J.A. Rueda, R. Ruffini; "Luminosity function of BATSE GRBs dominated by extended afterglow"; in Proceedings of the 25th Texas Symposium on Relativistic Astrophysics, held in Heidelberg (Germany), December 2010, F.M. Rieger, C. van Eldik, W. Hofmann, Editors; PoS(Texas2010), 204.

54. R. Ruffini, A.G. Aksenov, M.G. Bernardini, C.L. Bianco, L. Caito, P. Chardonnet, M.G. Dainotti, G. De Barros, R. Guida, L. Izzo, B. Patricelli, L.J. Rangel Lemos, M. Rotondo, J.A. Rueda Hernandez, G. Vereshchagin, She-Sheng Xue; "Black Holes Energetics and GRBs"; in The Sun, the Stars, the Universe and General Relativity: Proceedings of Sobral

2009; S.E. Perez Bergliaffa, M. Novello , R. Ruffini, Editors; Cambridge Scientific Publishers (UK, 2011).

55. C.L. Bianco, L. Amati, M.G. Bernardini, L. Caito, G. De Barros, L. Izzo, B. Patricelli, R. Ruffini; "The class of 'disguised' short GRBs and its implications for the Amati relation"; in GRBs as probes - from the progenitors environment to the high redshift Universe, Proceedings of the conference held in Como (Italy), May 2011, S. Campana, P. D'Avanzo, A. Melandri, Editors; Mem. S.A.It. Suppl., 21, 139 (2012).

56. A.V. Penacchioni, R. Ruffini, L. Izzo, M. Muccino, C.L. Bianco, L. Caito, B. Patricelli; "Evidences for a double component in the emission of GRB 101023"; in GRBs as probes - from the progenitors environment to the high redshift Universe, Proceedings of the conference held in Como (Italy), May 2011, S. Campana, P. D'Avanzo, A. Melandri, Editors; Mem. S.A.It. Suppl., 21, 230 (2012).

57. M.G. Bernardini, C.L. Bianco, L. Caito, L. Izzo, B. Patricelli, R. Ruffini; "The X-Ray Flares of GRB 060607A within the Fireshell Model"; in Proceedings of the Twelfth Marcel Grossmann Meeting on General Relativity, Paris, France, July 2009, T. Damour, R.T. Jantzen, R. Ruffini, Editors; World Scientific, (Singapore, 2012).

58. L. Izzo, M.G. Bernardini, C.L. Bianco, L. Caito, B. Patricelli, R. Ruffini; "GRB 090423 in the Fireshell Scenario: A Canonical GRB at Redshift 8.2"; in Proceedings of the Twelfth Marcel Grossmann Meeting on General Relativity, Paris, France, July 2009, T. Damour, R.T. Jantzen, R. Ruffini, Editors; World Scientific, (Singapore, 2012).

59. B. Patricelli, M.G. Bernardini, C.L. Bianco, L. Caito, L. Izzo, R. Ruffini, G.V. Vereshchagin; "A New Spectral Energy Distribution of Photons in the Fireshell Model of GRBs"; in Proceedings of the Twelfth Marcel Grossmann Meeting on General Relativity, Paris, France, July 2009, T. Damour, R.T. Jantzen, R. Ruffini, Editors; World Scientific, (Singapore, 2012).

60. C.L. Bianco, M.G. Bernardini, L. Caito, G. De Barros, L. Izzo, M. Muccino, B. Patricelli, A.V. Penacchioni, G.B. Pisani, R. Ruffini; "Needs for a new GRB classification following the fireshell model: "genuine short", "disguised short" and "long" GRBs"; in Proceedings of the Gamma-Ray

Bursts 2012 Conference, held in Munich (Germany), May 2012, A. Rau, J. Greiner, Editors; PoS(GRB 2012), 043.

61. A.V. Penacchioni, G.B. Pisani, R. Ruffini, C.L. Bianco, L. Izzo, M. Muccino; "The proto-black hole concept in GRB 101023 and its possible extension to GRB 110709B"; in Proceedings of the Gamma-Ray Bursts 2012 Conference, held in Munich (Germany), May 2012, A. Rau, J. Greiner, Editors; PoS(GRB 2012), 042.

62. B. Patricelli, M.G. Bernardini, C.L. Bianco, L. Caito, L. Izzo, R. Ruffini; "GRB 050904: The study of a high redshift GRB within the Fireshell Model"; in Proceedings of the Twelfth Marcel Grossmann Meeting on General Relativity, Paris, France, July 2009, T. Damour, R.T. Jantzen, R. Ruffini, Editors; World Scientific, (Singapore, 2012).

63. L. Izzo, G.B. Pisani, M. Muccino, J.A. Rueda, Y.Wang, C.L. Bianco, A.V. Penacchioni, R. Ruffini; "A common behavior in the late X-ray afterglow of energetic GRB-SN systems"; EAS Publications Series, Volume 61, 595-597 (2013).

64. R. Ruffini; "Black Holes, Supernovae and Gamma Ray Bursts"; in Proceedings of the Thirteenth Marcel Grossmann Meeting on General Relativity, Stockholm, Sweden, July 2012, R.T. Jantzen, K. Rosquist, R. Ruffini, Editors; World Scientific, (Singapore, 2015).

65. M. Muccino, R. Ruffini, C.L. Bianco, L. Izzo, A.V. Penacchioni, G.B. Pisani; "GRB 090227B: The missing link between the genuine short and long GRBs"; in Proceedings of the Thirteenth Marcel Grossmann Meeting on General Relativity, Stockholm, Sweden, July 2012, R.T. Jantzen, K. Rosquist, R. Ruffini, Editors; World Scientific, (Singapore, 2015).

66. A.V. Penacchioni, R. Ruffini, C.L. Bianco, L. Izzo, M. Muccino, G.B. Pisani, J.A. Rueda; "The family of the Induced Gravitational Collapse scenario: The case of GRB 110709B"; in Proceedings of the Thirteenth Marcel Grossmann Meeting on General Relativity, Stockholm, Sweden, July 2012, R.T. Jantzen, K. Rosquist, R. Ruffini, Editors; World Scientific, (Singapore, 2015).

67. A.V. Penacchioni, R. Ruffini, C.L. Bianco, L. Izzo, M. Muccino, G.B. Pisani; "GRB 111228, analysis within the Induced Gravitational Collapse scenario and association with a supernova"; in Proceedings of

the Thirteenth Marcel Grossmann Meeting on General Relativity, Stockholm, Sweden, July 2012, R.T. Jantzen, K. Rosquist, R. Ruffini, Editors; World Scientific, (Singapore, 2015).

68. G.B. Pisani, L. Izzo, R. Ruffini, C.L. Bianco, M. Muccino, A.V. Penacchioni, J.A. Rueda, Y. Wang; "On a novel distance indicator for Gamma-Ray Bursts associated with supernovae"; in Proceedings of the Thirteenth Marcel Grossmann Meeting on General Relativity, Stockholm, Sweden, July 2012, R.T. Jantzen, K. Rosquist, R. Ruffini, Editors; World Scientific, (Singapore, 2015).

69. M. Muccino, R. Ruffini, C.L. Bianco, L. Izzo, A.V. Penacchioni, G.B. Pisani; "GRB 090510, explosion of a GRB in the highest circumburst medium even inferred: a disguised short GRB"; in Proceedings of the Thirteenth Marcel Grossmann Meeting on General Relativity, Stockholm, Sweden, July 2012, R.T. Jantzen, K. Rosquist, R. Ruffini, Editors; World Scientific, (Singapore, 2015).

70. L. Izzo, G.B. Pisani, M. Muccino, R. Ruffini, C.L. Bianco, M. Enderli, Y. Wang; "Hints for a physically based GRB distance indicator"; in Proceedings of the Thirteenth Marcel Grossmann Meeting on General Relativity, Stockholm, Sweden, July 2012, R.T. Jantzen, K. Rosquist, R. Ruffini, Editors; World Scientific, (Singapore, 2015).

71. R. Ruffini, Y. Aimuratov, V. Belinski, C.L. Bianco, M. Enderli, L. Izzo, M. Kovacevic, G.J. Mathews, R. Moradi, M. Muccino, A.V. Penacchioni, G.B. Pisani, J.A. Rueda, G.V. Vereshchagin, Y. Wang, S.-S. Xue; Cosmic matrix in the jubilee of relativistic astrophysics; in THE SECOND ICRANET CÉSAR LATTES MEETING: Supernovae, Neutron Stars and Black Holes, Proceedings of the conference held in Rio de Janeiro – Niterói – João Pessoa – Recife – Fortaleza (Brazil), 13-22 April 2015, U. Barres de Almeida, P. Chardonnet, R. Picanco Negreiros, J. Rueda, R. Ruffini, G. Vereshchagin, C. Zen Vasconcellos, Editors; AIP Conference Proceedings, 1693, 020001 (2015).

72. L. Becerra, C.L. Bianco, F. Cipolletta, M. Enderli, C.L. Fryer, L. Izzo, M. Kovacevic, R. Camargo Rodrigues de Lima, M. Muccino, F.G. de Oliveira, A.V. Penacchioni, G.B. Pisani, J.A. Rueda, R. Ruffini, Y. Wang, E. Zaninoni; Black holes, neutron stars and supernovae within the induced gravitational collapse paradigm for GRBs; in THE SECOND ICRANET

CÉSAR LATTES MEETING: Supernovae, Neutron Stars and Black Holes, Proceedings of the conference held in Rio de Janeiro – Niterói – João Pessoa – Recife – Fortaleza (Brazil), 13-22 April 2015, U. Barres de Almeida, P. Chardonnet, R. Picanco Negreiros, J. Rueda, R. Ruffini, G. Vereshchagin, C. Zen Vasconcellos, Editors; AIP Conference Proceedings, 1693, 020002 (2015).

73. L.J. Rangel Lemos, C.L. Bianco, R. Ruffini; Applying the luminosity function statistics in the fireshell model; in THE SECOND ICRANET CÉSAR LATTES MEETING: Supernovae, Neutron Stars and Black Holes, Proceedings of the conference held in Rio de Janeiro – Niterói – João Pessoa – Recife – Fortaleza (Brazil), 13-22 April 2015, U. Barres de Almeida, P. Chardonnet, R. Picanco Negreiros, J. Rueda, R. Ruffini, G. Vereshchagin, C. Zen Vasconcellos, Editors; AIP Conference Proceedings, 1693, 070004 (2015).

74. J.A. Rueda, R. Ruffini, J.F. Rodriguez, M. Muccino, Y. Aimuratov, U. Barres de Almeida, L.M. Becerra, C.L. Bianco, C. Cherubini, S. Filippi, M. Kovacevic, R. Moradi, G.B. Pisani, Y. Wang; The binary progenitors of short and long GRBs and their gravitational-wave emission; EPJ Web of Conferences, 168, 01006 (2018).

75. M. Muccino, R. Ruffini, Y. Aimuratov, L.M. Becerra, C.L. Bianco, M. Karlika, M. Kovacevic, J.D. Melon Fuksman, R. Moradi, A.V. Penacchioni, G.B. Pisani, D. Primorac, J.A. Rueda, S. Shakeri, G.V. Vereshchagin, S.-S. Xue, Y. Wang; What can we learn from GRBs?; EPJ Web of Conferences, 168, 01015 (2018).

76. L.M. Becerra, C.L. Bianco, C. Fryer, J.A. Rueda, R. Ruffini; On the Induced Gravitational Collapse; EPJ Web of Conferences, 168, 02005 (2018).

77. G.B. Pisani, R. Ruffini, Y. Aimuratov, C.L. Bianco, M. Karlika, M. Kovacevic, R. Moradi, M. Muccino, A.V. Penacchioni, D. Primorac, J.A. Rueda, Y. Wang; The first ICRANet catalog of Binary-Driven Hypernovae; EPJ Web of Conferences, 168, 04002 (2018).

78. D. Primorac, R. Ruffini, G.B. Pisani, Y. Aimuratov, C.L. Bianco, M. Karlika, J.D. Melon Fuksman, R. Moradi, M. Muccino, A.V. Penacchioni, J.A. Rueda, Y. Wang; GRB 110731A within the IGC paradgm; EPJ Web of Conferences, 168, 04008 (2018).

79. J.D. Melon Fuksman, L.M. Becerra, C.L. Bianco, M. Karlika, M. Kovacevic, R. Moradi, M. Muccino, G.B. Pisani, D. Primorac, J.A. Rueda, R. Ruffini, G.V. Vereshchagin, Y. Wang; Evolution of an electron-positron plasma produced by induced gravitational collapse in binary-driven hypernovae; EPJ Web of Conferences, 168, 04009 (2018).

Is the Birth of PSR J0538+2817 Accompanied by a Gamma-ray Burst?

Fan Xu,[1] Jin-Jun Geng,[2] Xu Wang,[1] Liang Li[3] and Yong-Feng Huang[1,4]⋆
[1]School of Astronomy and Space Science, Nanjing University, Nanjing 210023, People's Republic of China
[2]Purple Mountain Observatory, Chinese Academy of Sciences, Nanjing 210023, People's Republic of China
[3]ICRANet, Piazza della Repubblica 10, I-65122 Pescara, Italy
[4]Key Laboratory of Modern Astronomy and Astrophysics (Nanjing University), Ministry of Education, People's Republic of China

Accepted 2021 November 15. Received 2021 November 09; in original form 2021 September 23

ABSTRACT

Recently, the Five-hundred-meter Aperture Spherical radio Telescope (FAST) measured the three-dimensional velocity of PSR J0538+2817 with respect to its associated supernova remnant S147 and found a possible spin-velocity alignment for this pulsar. Here we show that the high velocity and the spin-velocity alignment of this pulsar can be explained by the so-called electromagnetic rocket mechanism. In this framework, the pulsar is kicked in the direction of the spin axis, which naturally explains the spin-velocity alignment. We scrutinize the evolution of the pulsar and show that the kick process can create a highly relativistic jet at the opposite direction of the kick velocity. The lifetime and energetics of the jet is estimated. It is argued that the jet can generate a gamma-ray burst (GRB). The long term dynamical evolution of the jet is calculated. It is found that the shock radius of the jet should expand to about 32 pc at present, which is well consistent with the observed radius of the supernova remnant S147 (32.1 ± 4.8 pc). Additionally, our calculations indicate that the current velocity of the GRB remnant should be about 440 km s^{-1}, which is also roughly consistent with the observed blast wave velocity of the remnant of S147 (500 km s^{-1}).

Key words: gamma-ray bursts – stars: neutron – pulsars: general – stars: magnetars

1 INTRODUCTION

It is well known that many pulsars possess large velocities compared with main sequence stars. Previous statistical study of young pulsars has shown an average three-dimensional (3D) velocity of about 400 km s^{-1} at birth (Hobbs et al. 2005). Some of the fastest ones can even reach ~ 1000 km s^{-1}. The origin of the high-velocity pulsars is still under debate. A natural requirement is some kind of asymmetry during the supernova (SN) explosion that creates a kick to the pulsar. It has been suggested that an anisotropic mass ejection or neutrino ejection could be responsible for the pulsar kick (Sagert & Schaffner-Bielich 2008; Janka 2017). Meanwhile, the electromagnetic rocket mechanism is also a promising model to explain the high-velocity pulsars (Harrison & Tademaru 1975; Lai et al. 2001; Huang et al. 2003). In this framework, the young pulsar is supposed to have an off-centered dipolar magnetic field. The asymmetry in the magnetic field will lead to extra radiation in the direction of the spin axis and give the pulsar a recoil velocity. The electromagnetic rocket process may last for a relatively long time (Janka et al. 2021). However, the timescale could also be as short as ~ 50 s if the pulsar has a large magnetic field and a small initial period, namely a millisecond magnetar (Huang et al. 2003).

Recently, Yao et al. (2021) reported the evidence for 3D spin-velocity alignment of PSR J0538+2817. They adopted a scintillation method to get the radial velocity of this pulsar by using observations made with the Five-hundred-meter Aperture Spherical Radio Telescope (FAST). Combining the pulsar observations of Chatterjee et al. (2009), they derived the inclination angle between the 3D pulsar velocity and the line of sight as $\zeta_v = 110^{\circ}{}^{+16^{\circ}}_{-29^{\circ}}$ and the overall 3D speed as 407^{+79}_{-57} km s^{-1}. Using the polarization fitting method, they further obtained the inclination angle of the pulsar spin axis with respect to the line of sight as $\zeta_{pol} = 118^{\circ}.5 \pm 6.3^{\circ}$. They argued that PSR J0538+2817 is the first pulsar that directly shows a 3D spin-velocity alignment. It is worth noting that the spin-velocity alignment has previously been hinted in the Crab and Vela pulsars, but observations only limit their alignments in the two-dimensional (2D) plane (Lai et al. 2001; Johnston et al. 2005).

The 3D spin-velocity alignment is not easy to be explained by current simulations of supernova explosions which mainly focus on anisotropic mass ejection or neutrino ejection (Janka 2017; Müller et al. 2019). Recently, Janka et al. (2021) described a subtle scenario to explain the alignment, considering the asymmetric mass ejection in the supernova explosion. In all previous hydro-dynamical supernova simulations, the effect of accretion by the neutron star is generally omitted. In their new scenario, the newly-born neutron star obtains a high-velocity through the anisotropic supernova explosion in the first few seconds and runs away from the explosion center. Then the spin direction of this neutron star would later be affected by the fallback materials mainly from the direction of neutron star motion, which may potentially lead to some kinds of spin-velocity alignment. However, even in their simulations, a satisfactory alignment could be obtained only in some rare cases. On the other hand, we note that the spin-velocity alignment is a natural result in the framework of the electromagnetic rocket scenario (Harrison & Tademaru 1975). Thus we will mainly focus on this mechanism in our study.

Gamma-ray Bursts (GRBs) are explosions with an extremely high

⋆ E-mail: hyf@nju.edu.cn

energy release. It is generally believed that long GRBs lasting for tens of seconds are associated with core collapse of massive stars (Woosley 1993; Iwamoto et al. 1998). Meanwhile, short GRBs lasting for less than ~ 2 s are deemed to be related to the mergers of two compact stars (Eichler et al. 1989; Abbott et al. 2017). In the former scenario, the core collapse of massive stars often leaves a remnant of a black hole or a millisecond magnetar to act as the central engine of GRBs. However, as suggested by Dar & Plaga (1999), GRBs might also come from pulsar kicks. This model interestingly connects high-speed pulsars with GRBs. Later, Huang et al. (2003) examined the kick process and studied the properties of the resultant GRBs in details. Here, we go further to argue that the observed spin-velocity alignment of PSR J0538+2817 indicates that the birth of this pulsar may be associated with a long GRB.

This paper is organized as follows. In Section 2, we briefly introduce the observed features of PSR J0538+2817 and its associated supernova remnant (SNR) S147. Section 3 describes the GRB model in detail. We calculate the dynamics and compare our results with the observational data in Section 4. The possible decay of the magnetic field and the spin evolution of the pulsar is studied in Section 5. Finally, our conclusions and brief discussion are presented in Section 6.

2 PSR J0538+2817 AND S147

PSR J0538+2817 was first discovered by Anderson et al. (1996) with the Arecibo radio telescope. This pulsar is thought to be associated with SNR S147. It has a short period of 143.16 ms with a period derivative of 3.67×10^{-15} s s^{-1} (Anderson et al. 1996; Kramer et al. 2003). Considering a simple magnetic dipole radiation, its characteristic age should be approximately 600 kyr. As for the distance, both parallax distance and the dispersion measure (DM) distance suggest that it is about 1.3 kpc away from us (Kramer et al. 2003; Chatterjee et al. 2009). The proper motion precisely measured by the Very Long Baseline Array (VLBA) of $\mu_\alpha = -23.57 \pm 0.1$ mas yr^{-1} and $\mu_\delta = 52.87 \pm 0.1$ mas yr^{-1} suggests a transverse velocity of 357^{+59}_{-43} km s^{-1} (Chatterjee et al. 2009). After converting it to the local standard of rest (LSR), the proper motion becomes $\mu_\alpha = -24.4 \pm 0.1$ mas yr^{-1} and $\mu_\delta = 57.2 \pm 0.1$ mas yr^{-1} (Dinçel et al. 2015). Then, assuming a distance of 1.33 ± 0.19 kpc, the transverse velocity in the LSR is 391 ± 56 km s^{-1} (Yao et al. 2021). From the transverse velocity and the conjecture of its association with S147, its kinematic age can be derived as 34.8±0.4 kyr (Yao et al. 2021). We summarize the observed and derived parameters of PSR J0538+2817 in Table 1 for reference.

The kinematic age derived above is very different from the characteristic age of PSR J0538+2817. It indicates that the characteristic age may have been overestimated. Such an overestimation is not rare for pulsars and it may be caused by a variety of factors. For example, the magnetic field of pulsars may vary or decay on a long timescale (Guseinov et al. 2004). Another possibility is that the pulsar may have a large initial period. However, in the case of PSR J0538+2817, the initial period should be as long as $P_0 = 139$ ms to make the two ages compatible (Kramer et al. 2003). Such a long initial period is rare for young pulsars. In fact, it is widely believed that pulsars should be born with a millisecond initial period. In this study, we argue that PSR J0538+2817 should be a millisecond magnetar at birth. It will be shown below that the observed high speed and the spin-velocity alignment can all be naturally explained in this circumstance. The inconsistency between the kinematic age and the characteristic age is then attributed to a significant decay of the dipolar magnetic field due to fallback accretion, which will be discussed in detail in Section 5.

As for the SNR of S147, although an early estimation gave a large age of about 100 kyr (Kirshner & Arnold 1979), it is often thought to have a smaller age of about 30 kyr, similar to the kinematic age of PSR J0538+2817 (Katsuta et al. 2012). Despite of its old age, this SNR still shows long delicate filaments in optical band with a nearly spherical shape (Dinçel et al. 2015). However, other than considering it as a perfect spherical shape, some authors argued that there exists an "ear" morphology in this SNR (Grichener & Soker 2017; Bear & Soker 2018), but note that the "ear" is not right on the opposite direction of the pulsar velocity (Bear & Soker 2018; Soker 2021). More interestingly, from the H_α image of S147 presented by Gvaramadze (2006), the filamentary structure seems to be more concentrated in the south-east, opposite to the direction of the pulsar proper motion. The distance of this remnant is estimated to be approximately 1.3 kpc, consistent with that of PSR J0538+2817 (Dinçel et al. 2015; Yao et al. 2021). Sofue et al. (1980) presented a 5 GHz map of S147 and measured its angular radius as $\theta_s = 83' \pm 3'$, which corresponds to a size of $R_s = 32.1 \pm 4.8$ pc at a distance of 1.33 ± 0.19 kpc (Yao et al. 2021).

The possible spin-velocity alignment of PSR J0538+2817 was previously proposed by Romani & Ng (2003). With the help of Chandra X-ray Observatory (CXO) imaging, they found that this pulsar might be surrounded by a faint pulsar wind nebula (PWN). Assuming that the elongated structure is an equatorial torus, they argued that the pulsar spin and velocity are aligned. This alignment was later supported by several other papers (Ng et al. 2007; Johnston et al. 2007), but only in the 2-dimensional plane. Recently, Yao et al. (2021) confirmed this alignment in the 3D space. They analyzed the scintillation arcs of PSR J0538+2817 based on the dynamic spectra obtained with FAST. Assuming that this pulsar is associated with S147 and that S147 has a spherical structure, they speculated that the pulsar-scattering screen is located at the SNR shell and determined the location of this pulsar in the 3D space. Then, considering the pulsar's kinematic age, they derived the 3D velocity of the pulsar as 407^{+79}_{-57} km s^{-1} and the corresponding 3D inclination angle as $\zeta_v = 110^{\circ}{}^{+16^{\circ}}_{-29^{\circ}}$. Also, they fitted the FAST polarization data with the rotating vector model (RVM) (Johnston et al. 2005) and got the inclination angle of the spin axis with respect to the line of sight as $\zeta_{pol} = 118^{\circ}.5 \pm 6.3^{\circ}$. These data strongly support the idea that the spin and velocity of PSR J0538+2817 are aligned.

3 GRB CONNECTED WITH THE BIRTH OF PSR J0538+2817

We argue that PSR J0538+2817 is born as a millisecond magnetar. At its birth, the electromagnetic rocket mechanism can satisfactorily explain the high kick speed and the spin-velocity alignment. In this framework, the kick of the pulsar should be accompanied by a relativistic jet moving in the opposite direction of the pulsar velocity. The jet will possess enough energy to power a long GRB. A schematic illustration of our scenario is shown in Figure 1. Here we describe the scenario in detail and confront our model with the various observational data.

3.1 Kick velocity and kick timescale

A pulsar with an off-centered dipolar magnetic field will lose energy asymmetrically, which would in return exert a recoil force on the pulsar (Harrison & Tademaru 1975). The force is parallel to the

Table 1. Parameters of PSR J0538+2817

Observed parameters	Value	Ref.[a]	Derived parameters	Value	Ref.
R.A. (J2000)	$05^{h}\ 38^{m}\ 25^{s}.0623$	2	Characteristic age (kyr)	600	4
Dec. (J2000)	$28^{\circ}\ 17'\ 09''.1$	2	Kinematic age (kyr)	34.8 ± 0.4	4
Period, P (ms)	143.157776645(2)	1	DM distance, $D_{\rm DM}$ (kpc)	1.2	3
First derivative, $\dot{P}$ ($\times10^{-15}$)	3.6681(1)	1	Parallax distance, D_{π} (kpc)	$1.30^{+0.22}_{-0.16}$	3
Dispersion measure (pc cm^{-3})	39.57	3	Transverse velocity, $V_{\perp}$ (km s^{-1})	357^{+59}_{-43}	3
μ_{α} (mas yr^{-1})	$-23.57^{+0.10}_{-0.10}$	3	3D velocity, $V_{\rm 3D}$ (km s^{-1})	407^{+79}_{-57}	4
μ_{δ} (mas yr^{-1})	$52.87^{+0.09}_{-0.10}$	3	Magnetic field (G)	7×10^{11}	1
π (mas)	$0.72^{+0.12}_{-0.09}$	3	Spin-down luminosity (erg s^{-1})	5×10^{34}	1

[a] List of references: 1 - Anderson et al. (1996); 2 - Kramer et al. (2003); 3 - Chatterjee et al. (2009); 4 - Yao et al. (2021)

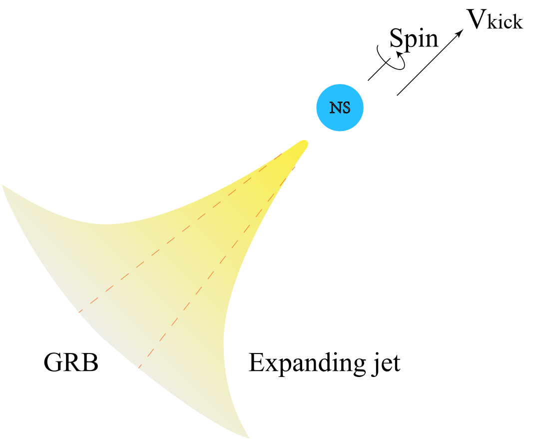

Figure 1. Schematic illustration of our scenario. The pulsar is born as a millisecond magnetar and gains a large kick velocity through the electromagnetic rocket process which lasts for approximately 180 s. Meanwhile, a highly beamed ultra-relativistic outflow is launched opposite to the kick direction, which will be powerful enough to generate a GRB. After producing the GRB, the jet continues to move outward, expanding laterally at the same time. After about 34.8 kyr, the radius of the jet increases to ~ 32 pc, which is consistent with the observed radius of SNR S147 (32.1 ± 4.8 pc).

spin axis when averaged over a period. Therefore, the pulsar would acquire a kick velocity aligned to the spin axis.

The kick speed $V_{\rm kick}$ depends on the exact configuration of the off-centered dipolar magnetic field. Here we consider a relatively simple case that the dipole is displaced by a distance of s with respect to the rotation axis. We further assume that the dipole has a zero radial magnetic momentum of $\mu_{\rho}=0$ to simplify the derivation and calculation. As for the tangential momentum, we take $\mu_z=1.5\mu_{\phi}$, which means the two tangential magnetic components are almost in equipartition. We will see below that this value will lead to a satisfactory result for both the kick speed and the timescale of the kick process. Under this configuration, the acquired kick velocity can be approximately derived as

$$V_{\rm kick}\simeq 445\,(\frac{R}{12\ {\rm km}})^{2}(\frac{P_0}{1\ {\rm ms}})^{-3}(\frac{s}{7\ {\rm km}})(\frac{\mu_z/\mu_{\phi}}{1.5}) \times\left[1-(\frac{P_1}{P_0})^{-3}\right]\ {\rm km\ s}^{-1}, \quad (1)$$

where $R_{\rm NS}$ is the radius of the pulsar, P_0 and P_1 are the initial period and the final period after the kick process respectively. This equation is somewhat similar to Equation 4 of Lai et al. (2001), but note the slight difference in the adopted configuration of the magnetic field.

Here, we consider a neutron star with a typical mass and radius of $M_{\rm NS}=1.4M_{\odot}$, $R_{\rm NS}=12$ km (Most et al. 2018; Abbott et al. 2018; Miller et al. 2019). Meanwhile, the spin period of the new born neutron star is taken as $P_0=1$ ms, which can be easily acquired after the contraction of the original proto-neutron star (Wheeler et al. 2000). As for the displacement of the dipole with respect to the rotation axis, Lai et al. (2001) assumed a distance of $s=10$ km for their neutron star with radius of 10 km. In this study, we consider a more moderate value of $s=7$ km. Under our configuration, the natal kick velocity can be larger than ~ 400 km s^{-1} as shown in Equation 1.

During the kick process, the pulsar will lose energy and will correspondingly spin down (Harrison & Tademaru 1975). As a result, its spin period will evolve with time as

$$P(t)\simeq P_0\left[2.0\times10^{-2}\ {\rm s}^{-1}\,(\frac{{\rm P}_0}{1\ {\rm ms}})^{-2}(\frac{{\rm R}_{\rm NS}}{12\ {\rm km}})^{4}(\frac{\mu_z/\mu_{\phi}}{1.5})^{-2} \times(\frac{B_0}{7\times10^{15}\ {\rm G}})^{2}\,t+1\right]^{\frac{1}{2}}, \quad (2)$$

where B_0 is the surface magnetic field of the pulsar. Here we take the magnetic field as several times 10^{15} G in our modeling, which is quite typical for a newborn millisecond neutron star to act as the central engine of GRB (Wheeler et al. 2000; Metzger et al. 2011; Janka 2012; Kumar & Zhang 2015).

From Equations 1 and 2, we see that the velocity acquired by the pulsar is a function of t. Taking $V_{\rm kick}\sim 400$ km s^{-1} as a target speed, we find that the kick process will last for a timescale of $\tau\sim 180$ s. After the kick process, the spin period decreases to $P_1=2.15$ ms according to Equation 2.

3.2 Energetics of the GRB

Accompanying the kick, a jet will be launched due to the momentum conservation. The momentum of the jet can be calculated as $p_{\rm flow}=M_{\rm NS}V_{\rm kick}$. In the electromagnetic rocket mechanism, very few baryons will be included in the jet, so that the outflow should be highly relativistic. Taking $V_{\rm kick}\sim 400$ km s^{-1}, the total energy of the relativistic jet ($E_{\rm flow}$) can be derived as (Dar & Plaga 1999; Huang et al. 2003)

$$E_{\rm flow}=p_{\rm flow}c=3.3\times10^{51}\ {\rm erg} \times(\frac{M_{\rm NS}}{1.4\ M_{\odot}})(\frac{V_{\rm kick}}{400\ {\rm km\ s}^{-1}}), \quad (3)$$

where c is the speed of light. Note that this pulsar is a millisecond magnetar at birth and the total energy of the jet should be smaller than the initial spin energy of the magnetar. Considering a typical moment of inertia of $I = 10^{45}$ g cm^2, the spin energy is

$$E_{\rm spin} = \frac{1}{2}I(\frac{2\pi}{P_0})^2 \approx 2\times 10^{52}(\frac{I}{10^{45}\ {\rm g\ cm^2}})(\frac{P_0}{1\ {\rm ms}})^{-2}\ {\rm erg}. \quad (4)$$

From the calculations in the above subsection, we get the terminal spin period after the kick process as $P_1 = 2.15$ ms. It corresponds to a spin energy of $E'_{\rm spin} = 4.3\times 10^{51}$ erg. Therefore, the spin energy loss is $\sim 1.57\times 10^{52}$ erg. We see that this energy is large enough to energize the jet, thus the above kick process is basically self-consistent.

If observed on-axis, the jet will show up as a GRB. Usually only a portion of the kinetic energy will be emitted as γ-rays during the main burst phase. Designating the efficiency of γ-ray emission as ε and the half opening angle of the jet as θ, then the isotropic energy of the GRB is

$$E_{\rm iso} = \frac{2\varepsilon E_{\rm flow}}{1-\cos\theta} \approx 4\varepsilon M_{\rm NS}V_{\rm NS}c\theta^{-2} = 1.3\times 10^{53}\ {\rm erg}$$
$$\times(\frac{\varepsilon}{0.1})(\frac{\theta}{0.1})^{-2}(\frac{M_{\rm NS}}{1.4\ M_\odot})(\frac{V_{\rm NS}}{400\ {\rm km\ s^{-1}}}). \quad (5)$$

We see that for typical parameters of $\varepsilon = 0.1$ and $\theta = 0.1$, the isotropic energy of the GRB can be as high as $\sim 10^{53}$ erg. In our scenario, since the kick process lasts for $\tau \sim 180$ s, the GRB should correspondingly be a long one.

4 DYNAMICS OF THE REMNANT

The kick process and the accompanied GRB occurred about 34.8 kyr ago. After producing the γ-ray burst, the jet interacted with the circum-burst interstellar medium and got decelerated. It would expand laterally as well. Now we calculate the long-term dynamical evolution of the outflow and compare the results with the observational data of the remnant S147.

The dynamical evolution of relativistic outflows that produce GRBs has been extensively studied by many authors. Following the generic dynamical equation proposed by Huang et al. (1999), many other authors have studied some subtle effects such as the role played by the pressure of the shocked material (van Eerten et al. 2010; Pe'er 2012). Xu & Huang (2010) investigated the evolution of a ring-shaped jet. Lamb et al. (2018) studied the jet-cocoon interaction. Geng et al. (2013, 2016) discussed the effect of a delayed energy injection. Zouaoui & Mebarki (2019) examined the compatibility of the generic dynamical equation with the Sedov solution in the non-relativistic phase. Jets propagating through a density-jump medium (Geng et al. 2014) or a stratified circumstellar medium (Fraija et al. 2021) are also studied in detail. Very recently, magnetized GRB shocks have been further discussed by Chen & Liu (2021).

The case studied here is relatively simple. We only need to consider an adiabatic jet interacting with a homogeneous interstellar medium (ISM). Following Huang et al., the dynamics of the jet can be described by the following four equations (Huang et al. 1999, 2000a,b),

$$\frac{dR}{dt} = \beta c\gamma(\gamma+\sqrt{\gamma^2-1}), \quad (6)$$
$$\frac{dm}{dR} = 2\pi R^2(1-\cos\theta)nm_{\rm p}, \quad (7)$$
$$\frac{d\theta}{dt} = \frac{c_{\rm s}(\gamma+\sqrt{\gamma^2-1})}{R}, \quad (8)$$
$$\frac{d\gamma}{dm} = -\frac{\gamma^2-1}{M_{\rm ej}+\varepsilon_{\rm r}m+2(1-\varepsilon_{\rm r})\gamma m}. \quad (9)$$

Here, R is the radius of the shock in the GRB rest frame, m is the swept-up ISM mass, γ is the Lorentz factor of the outflow and $\beta = \sqrt{\gamma^2-1}/\gamma$, t is the observer's time, n is the number density of the surrounding ISM, $m_{\rm p}$ is the proton mass, c_s is the comoving sound speed, and $\varepsilon_{\rm r}$ is the radiative efficiency.

We have calculated the long-term evolution of the jet numerically. The relevant parameters are taken as follows. Following our model described in Section 3, the total energy of the jet is $E_{\rm flow} = 3.3\times 10^{51}$ erg. The mass of ejecta is set as $M_{\rm ej} = 1.2\times 10^{-6}M_\odot$, so that the initial Lorentz factor takes a typical value of $\gamma_0 = 150$ ($E_{\rm flow} = \gamma_0 M_{\rm ej}c^2$). The initial half opening angle of the jet is assumed as $\theta_0 = 0.1$. Considering that S147 is in a low-density area (Katsuta et al. 2012), we take the number density as $n = 0.1$ cm^{-3}. The numerical result for the evolution of the shock radius is shown in Figure 2. We find that the shock radius of the jet is about 32.04 pc at present, which agrees well with the measured radius of S147 (32.1 ± 4.8 pc, at a distance of 1.33 kpc). Figure 3 illustrates the evolution of the shock velocity. S147 is currently in the Sedov-Taylor phase. Katsuta et al. (2012) have estimated its blast wave velocity as 500 km s^{-1}. As shown in Figure 3, our result indicates an expansion velocity of about 440 km s^{-1} for the remnant today. It is also well consistent with the estimation made by Katsuta et al. (2012). In Figure 4, we plot the evolution of the half opening angle of the jet. We see that the outflow is expected to expand to an angle of 2.67 rad currently. It means that the jet has been be widely diffused after propagating for a long time.

A supernova, when associated with a GRB, could be very energetic and is usually called a hypernova. Some of the most powerful hypernovae can even have an isotropic energy up to 10^{52} erg (Prentice et al. 2018). Interestingly, the kinetic energy of the remnant associated with PSR J0538+2817 (i.e. SNR S147), has been estimated as (1–3) $\times 10^{51}$ erg (Katsuta et al. 2012). We argue that the remnant should actually be a mixture of the supernova remnant and the highly diffused GRB jet. According to our modeling, the GRB jet initially had an intrinsic kinetic energy of 3.3×10^{51} erg (see Equation 3). In the prompt GRB phase, it might lose a significant portion of its energy (typically $\sim$ 10% – 50%). Then, in the early afterglow stage (being highly radiative), it would further lose some energy due to radiation loss. When it finally became adiabatic, the kinetic energy is expected to be comparable to that of the isotropic supernova remnant. From Figure 4, we see that the jet has expanded to an angle of 2.67 rad today ($t = 34.8$ kyr). On the other hand, although the supernova remnant itself (which is non-relativistic) was initially much slower and was left behind, it would finally catch up with the GRB remnant because it was much more massive and thus decelerated more slowly. As a result, SNR S147 should in fact be a mixture of the supernova remnant and the GRB outflow. Since the GRB outflow has expanded to a wide range of $\theta = 2.67$, the mixing of the two components should be complete so that the original GRB jet could no longer be discerned. Anyway, it is interesting to note that the southeastern portion of SNR S147, which is opposite to the direction of the pulsar motion, is obviously brighter than the northwest section. It clearly supports the existence of a one-sided jet.

5 MAGNETIC FIELD DECAY AND PERIOD EVOLUTION

In our scenario, the initial magnetic field strength of the pulsar is $B_0 = 7\times 10^{15}$ G. However, the current surface field inferred from the period derivative is around 7×10^{11} G. It indicates that PSR J0538+2817 may have experienced a significant magnetic field decay.

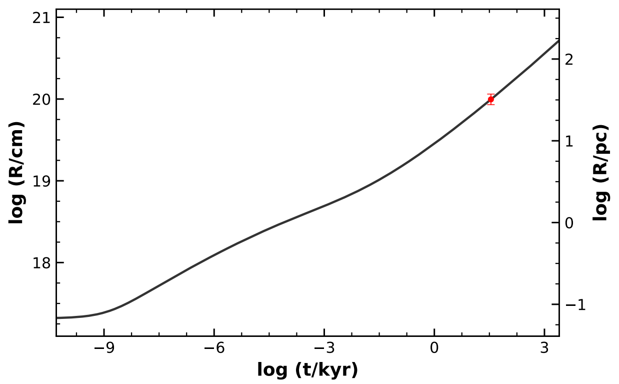

Figure 2. Long-term evolution of the shock radius after the jet produced the GRB. The observational data point represents the measured radius of S147 at present, which is 32.1 ± 4.8 pc (Yao et al. 2021). The calculated shock radius is 32.04 pc after 34.8 kyr, which is well consistent with the observations.

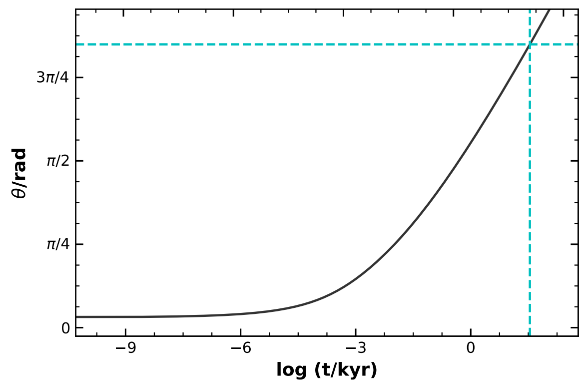

Figure 4. Long-term evolution of the half opening angle of the jet. The dashed lines show the current half opening angle, which is 2.67 rad.

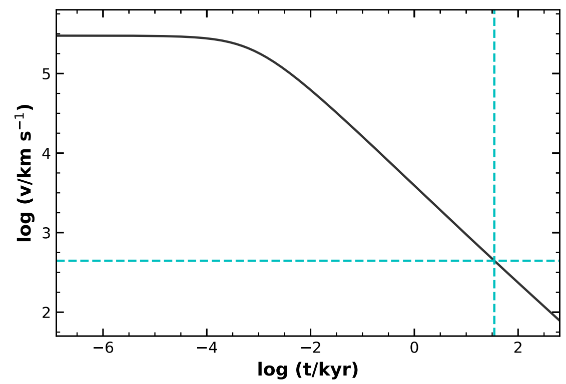

Figure 3. Long-term evolution of the shock velocity after the jet produced the GRB. The dashed lines mark the shock velocity at present, which is 440 km s^{-1}. It is consistent with the speed of ~ 500 km s^{-1} estimated from observations by Katsuta et al. (2012).

Magnetic field decay has been frequently inferred from pulsar observations. A possible recent example is the famous binary neutron star merger event of GW170817. Most people believe that the remnant should be a short-lived neutron star that collapsed into a black hole in a few seconds (Shibata et al. 2017; Margalit & Metzger 2017; Ruiz et al. 2018). However, Yu et al. (2018) argued that the remnant could be a long-lived massive neutron star (Yu et al. 2018). According to their estimates, the remnant neutron star should have an initial surface magnetic field of $10^{14} - 10^{15}$ G. But constraints from the data of later kilonova observations suggest that the field was only in a range of $10^{11} - 10^{12}$ G several thousands of seconds after the gravitational wave event. Some unknown mechanisms thus might have acted to significantly reduce the magnetic field (Yu et al. 2018).

How the magnetic field of neutron stars decays is still under debate. For isolated pulsars, maybe the most probable mechanism should involve Ohmic dissipation or Hall drift (Pons & Geppert 2007). However, this is not an effective process and the dissipation timescale is usually as long as $\sim 10^4 - 10^6$ yr (Pons & Geppert 2007). Another possibility is that the pulsar accretes matter which buries the magnetic field to make it decrease (Fu & Li 2013; Yu et al. 2018). The accreted matter can either be from a companion star or from the fallback materials.

Here, for PSR J0538+2817, we adopt the latter mechanism and consider the fallback accretion. An empirical relationship between the magnetic field and the accreted mass (ΔM) can be written as (Shibazaki et al. 1989; Fu & Li 2013),

$$B = \frac{B_0}{1 + \Delta M / 10^{-5} M_\odot}, \tag{10}$$

where B_0 is the initial magnetic field. For the magnetic field to decrease from $B_0 = 7 \times 10^{15}$ G to the currently observed value of $B = 7 \times 10^{11}$ G, the total accreted matter should be $\Delta M \sim 10^{-1} M_\odot$. Very recently, a detailed numerical simulation on the fallback accretion process has been conducted by Janka et al. (2021). It is revealed that a fallback mass of $\Delta M \sim 10^{-1} M_\odot$ is quite typical in the process (Janka et al. 2021). Additionally, the accretion timescale is generally in the range of 10^3 — 10^5 s.

The decay of the magnetic field will have a significant influence on the spin-down of the pulsar. From the calculations in Section 3.1, we have argued that PSR J0538+2817 should have a small initial period of $P_0 \sim 1$ ms (see Equation 1). Then it experienced an electromagnetic kick process that lasted for about $\tau \sim 180$ s. After the kick process, the spin period decreased to about $P_1 = 2.15$ ms (see Equation 2). Later, the pulsar would spin down through normal dipolar emission mechanism. At this stage, if the pulsar had a constant magnetic field of 7×10^{15} G, then the spin period would increase to about 370 ms in less than 1×10^6 s. However, as argued above, the magnetic field actually decayed significantly on a timescale of $\sim 10^3 - 10^5$ s due to the fallback accretion. Since the spin-down rate is proportional to the square of the surface magnetic field, the spin period will increase much slower. It would finally reach the observed period of 143 ms after 34.8 kyr. However, the detailed spin down process with a decreasing magnetic field is quite complicated and is beyond the scope of this study.

6 CONCLUSIONS AND DISCUSSION

An interesting spin-velocity alignment was recently reported for the high speed pulsar PSR J0538+2817 (Yao et al. 2021). We argue that this pulsar was initially born as a millisecond magnetar with a strong but asymmetrical magnetic field. The high kick speed and the spin-velocity alignment can be explained in the frame work of the electromagnetic rocket mechanism (Harrison & Tademaru 1975; Lai et al. 2001; Huang et al. 2003). It is suggested that the pulsar natal kick is accompanied by an ultra-relativistic jet in the opposite direction, which can essentially give birth to a long GRB. The long-term dynamical evolution of the jet is calculated. It is found that the shock radius of the jet should be 32.04 pc at present, which is well consistent with the observed radius of SNR S147 (32.1 ± 4.8 pc) (Yao et al. 2021). Our calculations indicate that the current shock velocity should be about 440 km s^{-1}. It also agrees well with the estimated speed of ~ 500 km s^{-1} by Katsuta et al. (2012).

Gamma-ray bursts may occur in binary systems (Zou et al. 2021). It is interesting to note that an OB runaway star, i.e. HD 37424, has been identified by Dinçel et al. (2015) to be inside SNR S147. They argued that the OB star is an interacting binary companion of the progenitor of PSR J0538+2817. The OB star may affect the evolution of the progenitor and cause a small spin-velocity misalignment ($5-10^{\circ}$) due to the break-up of a pre-supernova binary system (Yao et al. 2021). However, it will have little impact on the relativistic jet in our model.

In our framework, an off-centered dipolar magnetic field is needed for PSR J0538+2817. Usually the magnetic field of pulsars is thought to be of a simple dipolar configuration which is not off-centered. However, note that the realistic situation might be much more complicated. For example, it has been suggested that the most rapidly rotating neutron stars may have more complex surface magnetic configuration (Ruderman et al. 1998). Meanwhile, recently Miller et al. (2019) studied PSR J0030+0451 and provided interesting constraints on its surface magnetic field from the hot spot observations. They used the observational data from the Neutron Star Interior Composition Explorer (*NICER*) and discerned three hot spots on the surface of the compact star. They argued that these hot spots strongly indicate that the pulsar has an offset dipolar magnetic field or even a multi-pole field. Therefore, for PSR J0538+2817, we believe that the existence of an off-centered magnetic field could not be expelled. In fact, the bulk magnetic field configuration of pulsars is closely connected with their internal structure. However, our knowledge about the interiors of neutron stars is still quite poor. For example, these so called "neutron stars" might even be strange quark stars (Geng et al. 2021). We hope that the unprecedented high accuracy observations of *NICER* on pulsars would help clarify the fascinating enigmas of neutron stars.

It has been shown that the kick process of PSR J0538+2817 might be accompanied by a GRB that happened in our own Galaxy about 34.8 kyr ago. The filamentary structure of SNR S147 seems to be more concentrated in the south-east, opposite to the kick direction. This may support our model, in which a jet producing the GRB was launched toward the opposite direction of the kick. However, it is not clear whether this GRB pointed toward us or not. If it did point toward us, it would impose a huge effect to the Earth. Interestingly, in a recent study, Wang et al. (2017) measured the ^{14}C abundance of an ancient buried tree. They found rapid increases of ^{14}C in the tree rings between BC 3372 and BC 3371. They suggested that it may be associated with the ancient supernova that create the Vela pulsar. The GRB considered here happened about 34.8 kyr ago and is ~ 1.3 kpc away from us. It took about 4.2 kyr for the γ-rays to arrive at our planet. So, if the GRB pointed toward us, there may be some geological records on the Earth about 30,600 yr ago. Therefore, similar to Wang et al.'s case, we propose that people could also try to search for possible clues connected to the birth of PSR J0538+2817 through geological surveys.

Observationally, the GRB rate is only $\sim 0.2\%$ of the SN rate (Woosley & Bloom 2006). Meanwhile, high-velocity neutron stars are quite common, and the average velocity of pulsars is about 400 km s^{-1} at birth (Hobbs et al. 2005). One may worry that there would be too many GRBs according to our modeling. The contradiction can be relieved by considering the following requirements. First, not all high-speed pulsars are accompanied by an ultra-relativistic outflow. Some of them may acquire the high speed via other mechanisms. Second, the pulsar needs to be a millisecond one, together with a very strong magnetic field. Thirdly, even if the pulsar is accompanied by an ultra-relativistic outflow, the outflow may do not point toward us so that no GRB would be observed due to the beaming effect. Let us first consider normal bipolar jets with a half opening angle of 0.1 rad. Then the probability that these GRBs point toward us is only $\sim 0.5\%$. However, in our model, the jet is single-sided, so the fraction will further decrease by two fold to $\sim 0.25\%$. Synthesizing all the above ingredients, we believe that only a small fraction of the observed GRBs would be produced in this way.

ACKNOWLEDGEMENTS

We would like to thank the anonymous referee for helpful suggestions that lead to an overall improvement of this study. This work is supported by National SKA Program of China No. 2020SKA0120300, by the National Natural Science Foundation of China (Grant Nos. 11873030, 12041306, U1938201, 11903019, 11833003), and by the science research grants from the China Manned Space Project with NO. CMS-CSST-2021-B11.

DATA AVAILABILITY

The data underlying this article will be shared on reasonable request to the corresponding author.

REFERENCES

Abbott B. P., et al., 2017, ApJ, 848, L13
Abbott B. P., et al., 2018, Phys. Rev. Lett., 121, 161101
Anderson S. B., Cadwell B. J., Jacoby B. A., Wolszczan A., Foster R. S., Kramer M., 1996, ApJ, 468, L55
Bear E., Soker N., 2018, ApJ, 855, 82
Chatterjee S., et al., 2009, ApJ, 698, 250
Chen Q., Liu X.-W., 2021, MNRAS, 504, 1759
Dar A., Plaga R., 1999, A&A, 349, 259
Dinçel B., Neuhäuser R., Yerli S. K., Ankay A., Tetzlaff N., Torres G., Mugrauer M., 2015, MNRAS, 448, 3196
Eichler D., Livio M., Piran T., Schramm D. N., 1989, Nature, 340, 126
Fraija N., Kamenetskaia B. B., Dainotti M. G., Duran R. B., Gálvan Gámez A., Dichiara S., Caligula do E. S. Pedreira A. C., 2021, ApJ, 907, 78
Fu L., Li X.-D., 2013, ApJ, 775, 124
Geng J. J., Wu X. F., Huang Y. F., Yu Y. B., 2013, ApJ, 779, 28
Geng J. J., Wu X. F., Li L., Huang Y. F., Dai Z. G., 2014, ApJ, 792, 31
Geng J. J., Wu X. F., Huang Y. F., Li L., Dai Z. G., 2016, ApJ, 825, 107
Geng J., Li B., Huang Y., 2021, The Innovation, 2, 100152
Granot J., Guetta D., Gill R., 2017, ApJ, 850, L24
Grichener A., Soker N., 2017, MNRAS, 468, 1226

Guseinov O. H., Ankay A., Tagieva S. O., 2004, International Journal of Modern Physics D, 13, 1805
Gvaramadze V. V., 2006, A&A, 454, 239
Harrison E. R., Tademaru E., 1975, ApJ, 201, 447
Hobbs G., Lorimer D. R., Lyne A. G., Kramer M., 2005, MNRAS, 360, 974
Huang Y. F., Dai Z. G., Lu T., 1999, MNRAS, 309, 513
Huang Y. F., Dai Z. G., Lu T., 2000a, MNRAS, 316, 943
Huang Y. F., Gou L. J., Dai Z. G., Lu T., 2000b, ApJ, 543, 90
Huang Y. F., Dai Z. G., Lu T., Cheng K. S., Wu X. F., 2003, ApJ, 594, 919
Iwamoto K., et al., 1998, Nature, 395, 672
Janka H.-T., 2012, Annual Review of Nuclear and Particle Science, 62, 407
Janka H.-T., 2017, ApJ, 837, 84
Janka H. T., Wongwathanarat A., Kramer M., 2021, arXiv e-prints, p. arXiv:2104.07493
Johnston S., Hobbs G., Vigeland S., Kramer M., Weisberg J. M., Lyne A. G., 2005, MNRAS, 364, 1397
Johnston S., Kramer M., Karastergiou A., Hobbs G., Ord S., Wallman J., 2007, MNRAS, 381, 1625
Katsuta J., et al., 2012, ApJ, 752, 135
Kirshner R. P., Arnold C. N., 1979, ApJ, 229, 147
Kramer M., Lyne A. G., Hobbs G., Löhmer O., Carr P., Jordan C., Wolszczan A., 2003, ApJ, 593, L31
Kumar P., Zhang B., 2015, Phys. Rep., 561, 1
Lai D., Chernoff D. F., Cordes J. M., 2001, ApJ, 549, 1111
Lamb G. P., Mandel I., Resmi L., 2018, MNRAS, 481, 2581
Margalit B., Metzger B. D., 2017, ApJ, 850, L19
Metzger B. D., Giannios D., Thompson T. A., Bucciantini N., Quataert E., 2011, MNRAS, 413, 2031
Miller M. C., et al., 2019, ApJ, 887, L24
Most E. R., Weih L. R., Rezzolla L., Schaffner-Bielich J., 2018, Phys. Rev. Lett., 120, 261103
Müller B., et al., 2019, MNRAS, 484, 3307
Ng C. Y., Romani R. W., Brisken W. F., Chatterjee S., Kramer M., 2007, ApJ, 654, 487
Pe'er A., 2012, ApJ, 752, L8
Pons J. A., Geppert U., 2007, A&A, 470, 303
Prentice S. J., et al., 2018, MNRAS, 478, 4162
Romani R. W., Ng C. Y., 2003, ApJ, 585, L41
Ruderman M., Zhu T., Chen K., 1998, ApJ, 492, 267
Ruiz M., Shapiro S. L., Tsokaros A., 2018, Phys. Rev. D, 97, 021501
Sagert I., Schaffner-Bielich J., 2008, A&A, 489, 281
Shibata M., Fujibayashi S., Hotokezaka K., Kiuchi K., Kyutoku K., Sekiguchi Y., Tanaka M., 2017, Phys. Rev. D, 96, 123012
Shibazaki N., Murakami T., Shaham J., Nomoto K., 1989, Nature, 342, 656
Sofue Y., Furst E., Hirth W., 1980, PASJ, 32, 1
Soker N., 2021, arXiv e-prints, p. arXiv:2109.10230
Wang F. Y., Yu H., Zou Y. C., Dai Z. G., Cheng K. S., 2017, Nature Communications, 8, 1487
Wheeler J. C., Yi I., Höflich P., Wang L., 2000, ApJ, 537, 810
Woosley S. E., 1993, ApJ, 405, 273
Woosley S. E., Bloom J. S., 2006, ARA&A, 44, 507
Xu M., Huang Y. F., 2010, A&A, 523, A5
Yao J., et al., 2021, Nature Astronomy, 5, 788
Yu Y.-W., Liu L.-D., Dai Z.-G., 2018, ApJ, 861, 114
Zou Z.-C., Zhang B.-B., Huang Y.-F., Zhao X.-H., 2021, ApJ, 921, 2
Zouaoui E., Mebarki N., 2019, arXiv e-prints, p. arXiv:1911.07350
van Eerten H. J., Leventis K., Meliani Z., Wijers R. A. M. J., Keppens R., 2010, MNRAS, 403, 300

This paper has been typeset from a TEX/LATEX file prepared by the author.

The Astrophysical Journal, 941:27 (13pp), 2022 December 10 https://doi.org/10.3847/1538-4357/ac3d89

Standard GRB Spectral Models "Misused"?

Liang Li
ICRANet, Piazza della Repubblica 10, I-65122 Pescara, Italy; liang.li@icranet.org
INAF–Osservatorio Astronomico d'Abruzzo, Via Mentore Maggini snc, I-64100, Teramo, Italy
ICRA, Dipartimento di Fisica, Università di Roma 'La Sapienza', Piazzale Aldo Moro 5, I-00185 Roma, Italy
Received 2021 April 30; revised 2021 October 11; accepted 2021 November 11; published 2022 December 9

Abstract

The standard model characterizing the gamma-ray burst (GRB) spectrum invokes a four-parameter empirical function, the so-called the BAND model. An alternative model named cutoff power law (COMP) implements a power law with an exponential cutoff. These functions achieve almost equally good fits on observed spectra, and are adopted in nearly all of the GRB literature. Here, we reanalyze the sample defined in Li et al. (39 bursts including 944 spectra). We classify the spectra by two methods: (1) checking their corner–corner plots of the posteriors to determine well-constrained β (BAND-better) and unconstrained β (COMP-better) categories; and (2) defining the four groups by difference of the deviance information criterion (DIC). We find inconsistent peaks of the parameter distributions between the BAND-better spectra ($\alpha = -0.64 \pm 0.28$ and $\log_{10}(E_{\rm p}) = \log_{10}(191) \pm 0.41$) and the COMP-better spectra ($\alpha = -0.96 \pm 0.33$ and $\log_{10}(E_{\rm p}) = \log_{10}(249) \pm 0.40$). With the *statistically preferred* model and vice versa the *misused* model defined based on DIC statistics, we also find that the fitted parameters obtained by the *misused* model (COMP) significantly deviate from those obtained by the statistically preferred model (BAND). This means that if a spectrum is statistically preferred, described as the BAND, applying COMP to derive the spectral parameters will prominently deviate from their intrinsic shape, therefore affecting the physical interpretation. Our analysis indicates that the *better* or statistically preferred model should be duly examined during GRB spectral analysis. In addition, the β distribution exhibits a bimodal structure containing the BAND-better and COMP-better spectra, respectively, implying that BAND and COMP both may have physical origin.

Unified Astronomy Thesaurus concepts: Gamma-ray bursts (629); Relativistic jets (1390); Astronomy data analysis (1858)

1. Introduction

The standard approach to characterize the observational gamma-ray burst (GRB) spectral properties invokes a four-parameter empirical function known as the BAND model (Band et al. 1993). The photon number spectrum of BAND is defined as

$$f_{\rm BAND}(E) = A\begin{cases} \left(\frac{E}{E_{\rm piv}}\right)^{\alpha}\exp\left(-\frac{E}{E_0}\right), & E < (\alpha-\beta)E_0 \\ \left[\frac{(\alpha-\beta)E_0}{E_{\rm piv}}\right]^{(\alpha-\beta)}\exp \\ \times(\beta-\alpha)\left(\frac{E}{E_{\rm piv}}\right)^{\beta}, & E \geqslant (\alpha-\beta)E_0, \end{cases} \tag{1}$$

where A is the normalization factor in units of ph cm^{-2} keV^{-1} s^{-1}, $E_{\rm piv}$ is the pivot energy always fixed at 100 keV, E_0 is the break energy correlated with the peak energy of νF_ν spectrum (assuming $\beta < -2$) by $E_{\rm p} = (2+\alpha)E_0$, α and β are the low-energy and high-energy asymptotic power-law photon indices, respectively. The spectral indices (α and β) and the peak energy[1] ($E_{\rm p}$) are typically distributed around $\alpha = -0.8$ (below the break energy), $\beta = -2.5$ (above the break energy), and $E_{\rm p} = 210$ keV, respectively.

An alternative empirical approach involves a simpler function called the cutoff power-law (COMP, aka the Comptonized model) model. This approach is valid when the power-law index β is poorly constrained (having fairly large absolute values and large uncertainties; see, e.g., Figure 1). The COMP function is recovered from the BAND function as β tends to $-\infty$. The COMP function is given by

$$f_{\rm COMP}(E) = A\left(\frac{E}{E_{\rm piv}}\right)^{\alpha}\exp(-\frac{E}{E_c}), \tag{2}$$

where the peak energy $E_{\rm p}$ of the νF_ν spectrum is related to the E_c–$E_{\rm p} = (2+\alpha)E_c$.

The physical origins of these empirical functions, however, have yet to be identified, although they have been the most widely used to fit GRB spectra. Neither BAND nor COMP functions correspond to an explicit emission mechanism. Whether these models are due to thermal or nonthermal emission is highly debated, depending on the slope values of their spectral parameters. Physically, the leading mechanisms for interpreting GRB prompt emission invoke either nonthermal photons originating from synchrotron emission (or inverse Compton scattering) (e.g., Meszaros et al. 1994; Rees & Meszaros 1994; Zhang & Yan 2011; Geng et al. 2018; Meng et al. 2018, 2019; Li et al. 2019) or

[1] The peak energy also represents the energy at which most of the energy of the selected spectrum (time-resolved analysis) or the entire burst (time-integrated analysis) is released.

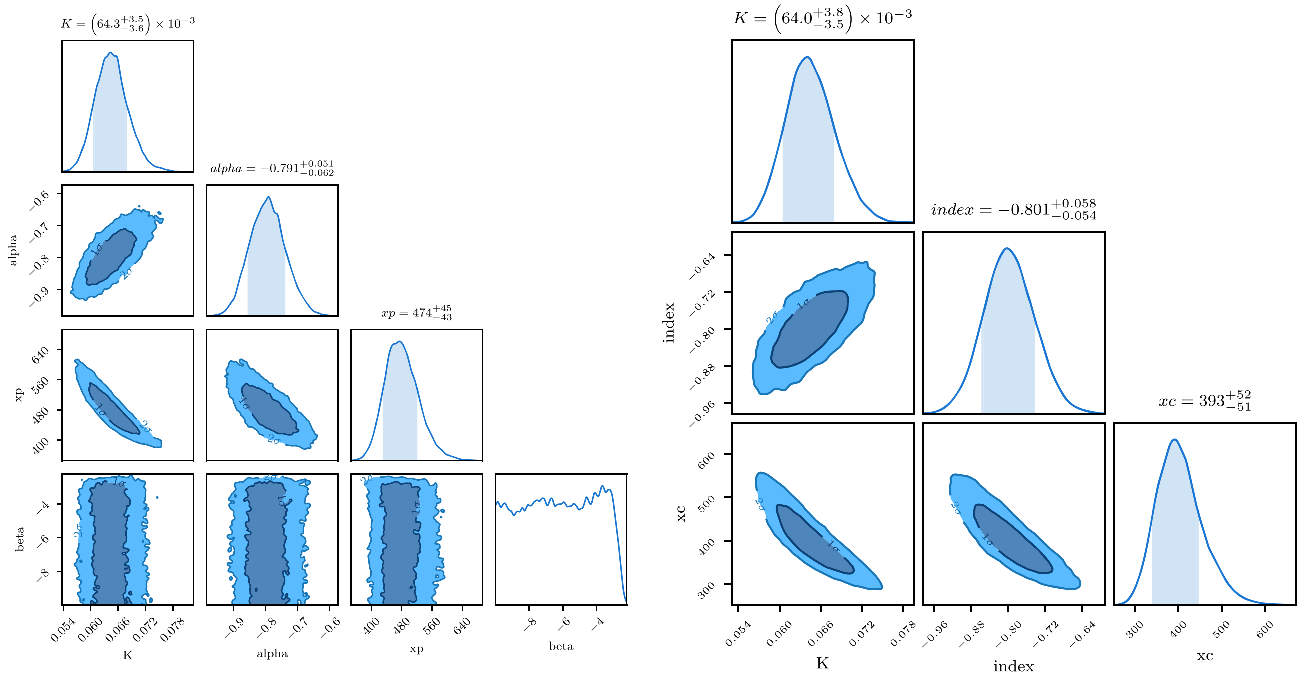

Figure 1. Bayesian MCMC spectral fits to the data in one time bin (between 24.215 and 25.597 s) of GRB 171227 comparing the BAND with COMP models. The left panel shows the BAND fit to the data with a well-constrained β while the right panel displays the COMP fit to the same data. The plots shows a COMP-preferred spectrum, with ΔDIC = 1.7.

Comptonized quasi-thermal photons associated with photosphere emission (e.g., Thompson 1994; Pe'er et al. 2007; Ryde et al. 2010; Ruffini et al. 2013; Li 2019a, 2019b, 2020; Xue 2021). The fast-cooling ($\alpha = -3/2$) and slow-cooling ($\alpha = -2/3$, so-called the *line of death* of synchrotron emission, Preece et al. 1998) synchrotron emission predicts two different values of α, whereas photosphere models predict much harder values of α (e.g., above $\alpha = -2/3$). For instance, Acuner et al. (2020) argued that the spectra that prefer the photospheric model all have low-energy power-law indices $\alpha \sim > -0.5$, as long as the data has a high significance. Therefore, applying these empirical models to the GRB spectral analysis plays an important role in identifying the GRB radiation mechanism, and investigation of spectral parameters, and therefore, will shed light on our understanding of GRB physics (e.g., Dai et al. 2006; Kaneko et al. 2006; Zhang et al. 2006; Gruber et al. 2014; Yu et al. 2016; Ruffini et al. 2018; Li 2019a, 2019b; Li et al. 2019; Li & Zhang 2021; Moradi et al. 2021; Xue 2021, and references therein).

In general, we can apply either time-integrated or time-resolved spectral analysis to study the spectral properties of a GRB. Several spectral catalogs of GRBs exist in the literature based on either the time-integrated analysis (e.g., Goldstein et al. 2012; Gruber et al. 2014) or the time-resolved analysis (e.g., Yu et al. 2016; Li et al. 2021). The time-integrated spectrum represents the average spectral properties since the entire period of emission is treated as a single time bin. However, GRB prompt emission is well known to have strong spectral evolution (e.g., Kaneko et al. 2006; Yu et al. 2019; Li et al. 2021, and references therein), which requires the more detailed time-resolved spectral analysis (treating the whole period of emission as multiple timing bins, and spectral analysis is therefore performed on each timing event individually, e.g., Yu et al. 2016, 2019; Li et al. 2021).

Several early GRB spectral catalogs make use of the frequentist approach (e.g., Kaneko et al. 2006). In recent years, a fully Bayesian analysis method has been increasingly developed. For example, time-resolved spectral catalogs based on such a fully Bayesian analysis method for single-pulse bursts (Yu et al. 2019) and multipulse bursts (Li et al. 2021) have been created. In the Bayesian analysis, Bayesian inference is used to account for relevant prior information and the resulting posterior probability distributions of parameters are obtained by the Markov Chain Monte Carlo (MCMC) iterations.

Phenomenologically, the BAND-like spectrum with well-constrained model parameters is typically observed in the time-integrated spectral analysis, while the simpler COMP-like spectrum is commonly observed in the time-resolved spectral analysis. This is because time-resolved spectral properties typically do not have good high-energy photon statistics, and therefore, the high-energy spectral index β for time-resolved spectra usually cannot be well evaluated due to the small number of photons available.

It is important to stress that the difference in fitting by BAND or COMP functions is not fully examined when performing the time-resolved analysis of large samples (e.g., Kaneko et al. 2006; Goldstein et al. 2012; Yu et al. 2019; Li et al. 2021). Moreover, in some articles COMP is applied throughout without a comparison with other models since the COMP is usually preferred for the majority of the time-resolved spectra. We have doubts about the statistical conclusions and the physical implications generated from possible *misused* model. Therefore, we dedicate this article to examining the deviation of spectral fittings between BAND and COMP. We wish to answer the question: Is the impact on parameters significant if misusing a model? Do BAND and COMP both have physical backgrounds? Here we reanalyze the sample (39 bursts including 944 spectra) defined in Li et al. (2021) to examine the spectral properties statistically of these two standard spectral models.

This paper is organized as follows. The methods are presented in Section 2. The detailed results are summarized in Section 3. The discussion and conclusion are presented in Sections 4 and 5, respectively. The convention $Q = 10^x Q_x$ is adopted in cgs units throughout the paper. The standard ΛCDM cosmology with the parameters $H_0 = 67.4$ km s^{-1} Mpc^{-1}, $\Omega_M = 0.315$, and $\Omega_\Lambda = 0.685$ are adopted (Planck Collaboration et al. 2020).

2. Methodology

2.1. Sample Revisited

The Gamma-ray Burst Monitor (GBM; 8 keV–40 MeV, Meegan et al. 2009), and the Large Area Telescope (LAT; 20 MeV–300 GeV, Atwood et al. 2009), are the two instruments on board Fermi providing unprecedented spectral coverage for seven orders of magnitude in energy. Fermi-GBM, together with Fermi-LAT, has been triggered by more than 2000 bursts since its launch in 2008. Here, we revisit the sample defined in Li et al. (2021). The sample is collected from the Fermi-GBM burst catalog published at HEASARC,[2] and it focuses on well-separated multipulse GBM-detected bursts. It consists of 39 bursts, 117 pulses, and 1228 spectra. There are two reasons that we included the sample in this task. First, all the spectra in the sample were selected to have a high statistical significance in order to allow us to perform a detailed time-resolved spectral analysis and ensure that the spectral fits are well determined, this is the key point. Second, the prompt-emission light curves of GRBs typically exhibit irregular, multipulse temporal profiles.

The sample selection in Li et al. (2021) includes the following main steps: (1) The first is to visually inspect the light curves for each burst that was observed by Fermi-GBM during its first 11 yr of mission (more than 2000 bursts), and about 120 bursts that have well-separated multipulse features are roughly identified; (2) The second is to capture the variations of the time-tagged events light curve and divide the light curve into time segments by following the Bayesian blocks (BBlocks; Scargle et al. 2013) algorithm, and the significance (S; Vianello et al. 2018) for each time bin was also calculated; (3). The third is to select at least two pulses in each burst whose individual pulse light curve has at least four time bins with high significance ($S \geqslant 20$);[3] hence, the final sample was defined (39 bursts, 103 pulses, and 944 spectra); (4). The final goal is to obtain the best spectral parameters by adopting a fully Bayesian analysis using the MCMC method and performing both the BAND and COMP functions to fit all the spectra, respectively. For information on the data procedure, including the burst, detector, source, and background selections, light-curve binning method, sample definition, and Bayesian and MCMC spectral fitting approaches; please refer to Li et al. (2021), Li (2019a), Li & Zhang (2021) for more details.

2.2. High-energy Power-law β and the Better Models

In reality, for a given spectrum, in order to determine which one (BAND or COMP) is *better*, one needs to check whether a well-constrained β can be determined. If β is not well constrained in some cases, there are two possibilities. First, lack of photons in the analyzed bins (e.g., $S < 20$), so that the spectral fit cannot be well determined. Second, the number of photons in the analyzed bins is sufficient (e.g., $S \geqslant 20$), but the model that better characterizes the spectral shape is indeed the COMP. Our sample defined in Li et al. (2021) with $S \geqslant 20$ rules out the first possibility. We therefore inspected all the posteriors of the BAND spectra to check their β indices. If a well-constrained β is clearly identified by a certain spectrum, the BAND model is considered as better, otherwise the COMP model is better. Under these criteria, all the spectra can be identified into two categories:

1. BAND-better spectra: All the spectra selected in this category are identified with a well-constrained β, indicating that the BAND model is indeed better. It contains 35% of the total number of spectra.
2. COMP-better spectra: All the spectra in this category are identified with an unconstrained β, implying that the COMP model is better. This is 65% of the total number of spectra.

In Figure 1, the left panel shows two-dimensional corner-corner plots of the spectral parameters using the Bayesian MCMC method used to perform the BAND fit. The spectral data is obtained from one time bin (between 24.215 and 25.597 s) from GRB 171227, and an unconstrained β is clearly identified from the posterior density map. While that of the COMP fit for the same spectral data is displayed in the right panel of Figure 1. For comparison, we also present the same plots using another time bin (between 24.215 and 25.597 s) from GRB 171227 in Figure 2, where a well-constrained β is clearly identified in the BAND fit.

In total, the fractions of the constrained-β and unconstrained-β spectra are 35% and 65%, respectively. This suggests that the majority of the spectra (two-thirds) can indeed be better fitted by the COMP, confirming the previous similar findings (Yu et al. 2019; Li et al. 2021).

2.3. Statistically Preferred Models Determined by Information Criteria

In practice, a more common approach for model comparison is by using information criteria, such as Akaike information criteria, Bayesian information criteria, and the deviance information criterion (DIC). The Bayesian analysis and MCMC method are fully applied in this work, the DIC (Spiegelhalter et al. 2002; Moreno et al. 2013) is computed to compare models, it is defined as $\mathrm{DIC} = -2\log[p(\mathrm{data}\,|\hat{\theta})] + 2p_{\mathrm{DIC}}$, where $\hat{\theta}$ is the posterior mean of the parameters, and p_{DIC} is a term to penalize the more complex model for overfitting (Gelman et al. 2014). The values of the difference between the BAND's and the COMP's, defined as $\Delta\mathrm{DIC} = \mathrm{DIC}_{\mathrm{BAND}} - \mathrm{DIC}_{\mathrm{COMP}}$, can be used to indicate the preferred one. For each individual spectrum, a negative DIC value indicates that the observational data favors a BAND-like spectrum. All of the spectra can be separated into the following groups using different threshold levels based on DIC statistics for Bayesian models (e.g.,

[2] https://heasarc.gsfc.nasa.gov/W3Browse/fermi/fermigbrst.html

[3] Although the BBlocks method can better capture the intrinsic variation of light curve (e.g., Li et al. 2021), the time bins created by such a method usually have varied signal-to-noise ratios. This means that we cannot ensure that there are enough photons in each time bin in order to establish a reliably spectral fit. In order to ensure that the spectral fits can be well determined, a relatively high statistical significance for each selected time bin is needed. On the other hand, the threshold levels of statistical significance required by different spectral models may also be different. Practically, more complicated models (with more free parameters) require more signal photons in order to establish a reliable fit result. Therefore, a threshold level of $S \geqslant 20$ is typically used for the BAND model while $S \geqslant 15$ for the COMP model since the BAND model (A, α, β, E_{p}) has one more free parameter than the COMP model (A, α, E_{c}). The sample defined in Li et al. (2021) adopted $S \geqslant 20$ to select the time bins, which is enough to study both two models.

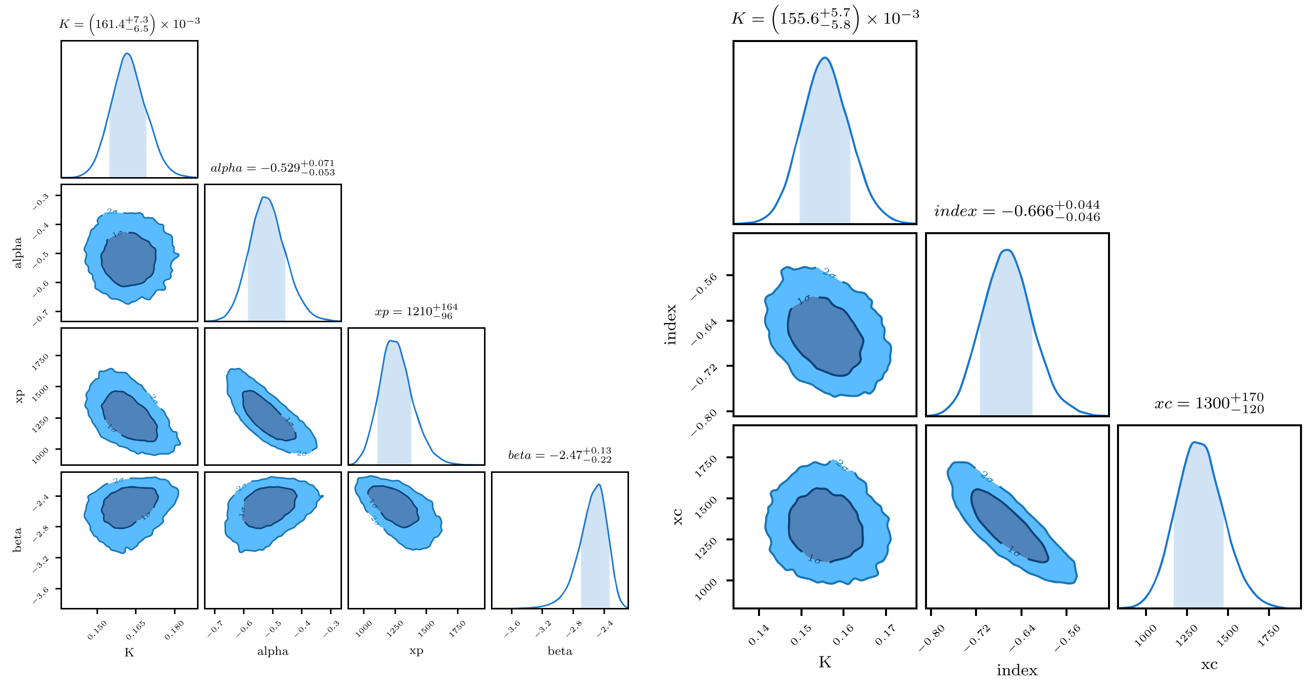

Figure 2. Same as Figure 1 but for another time bin (between 17.648 and 17.820 s) of GRB 171227. The left panel shows the BAND fit to the data with a well-constrained β while the right panel displays the COMP fit to the same data. The plots shows a BAND-preferred spectrum, with ΔDIC = -24.8.

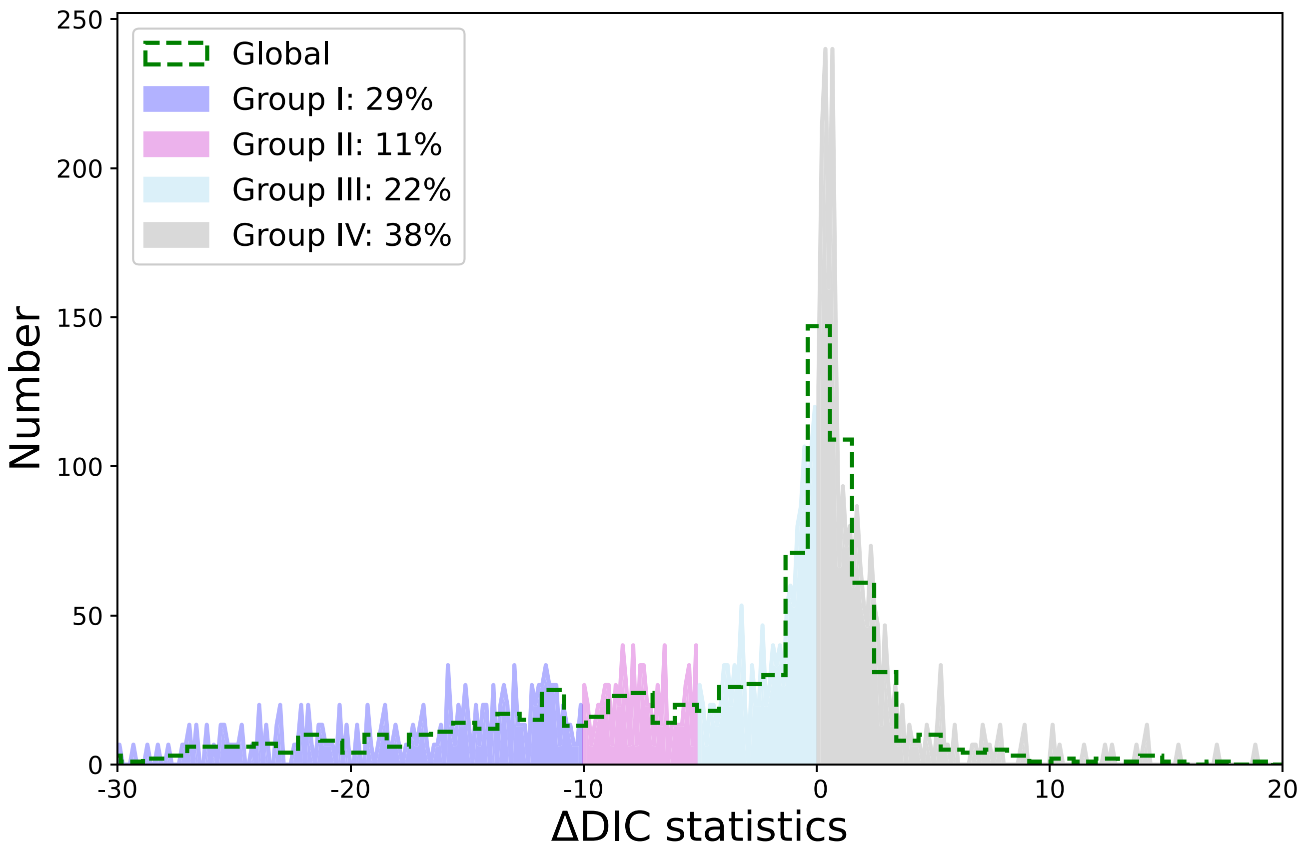

Figure 3. Distribution of ΔDIC. The different groups are overlaid by different colors: Group I (blue), Group II (magenta), Group III (sky blue), and Group IV (gray). While the global distribution is shown by the green curve.

Gelman et al. 2014; Pooley & Marion 2018), in which the BAND-preferred or COMP-preferred spectra could also be determined and gathered.

1. Group I: ΔDIC $< = -10$. BAND model is *statistically preferred*. This group contains 29% of the spectra, as shown in Figure 3.

2. Group II: $-10 < \Delta\mathrm{DIC} <= -5$. BAND model is still statistically preferred, but is not as strong as Group I. This group contains 11% of the spectra (Figure 3).
3. Group III: $-5 < \Delta\mathrm{DIC} <= 0$. COMP model is statistically preferred. This group contains 22% of the spectra (Figure 3).
4. Group IV: $\Delta\mathrm{DIC} > 0$. COMP model is statistically preferred, and is stronger than Group III. This group contains 38% of the spectra (Figure 3).

Based on the BAND-better and COMP-better spectra defined in Section 2.2, we then check the fractions of the spectra with or without a constrained β for each DIC-defined group. Groupwise, the corresponding fractions are [93%, 7%], [58%, 42%], [5%, 95%], and [1%, 99%] for Group I, Group II, Group III, and Group IV, respectively. In Group I, we find that for almost all the spectra (up to ∼93%) a well-constrained β can be clearly identified. However, there are very few spectra showing a well-constrained β both Group III and Group IV. These results suggest that BAND-like spectra dominate Group I while COMP-like spectra dominate Group III and Group IV. Interestingly, we also find that in Group-II both BAND-like (58%) and COMP-like (42%) spectra are almost identical. The results also suggest that our two methods of classifying GRBs are consistent, but one needs to consider a relatively large DIC value (e.g., −5 is good and −10 is perfect, these values are in agreement with previous works (Acuner et al. 2020; Li et al. 2021).

3. Results

Before we move forward, a few remarks need to be made here. First, we focus on the two most widely used models for GRB spectra (BAND and COMP), and we miss several other models (e.g., power-law model, smooth broken power-law model, and the BETA model) that were used in the previous catalogs (e.g., Kaneko et al. 2006). In some cases, these models should be able to fit the spectra better than the BAND or COMP that we used in this task. For instance, if a break's energy lies outside the detector passband, or the source photon signal beyond the break energy is weak enough so that the break energy cannot be well determined. In such cases, the simpler power-law model (see one recent work, Tang et al. 2021, for instance) is superior to the other, more complicated models (having more parameters). As such, the models we used would be the better ones that characterize GRB intrinsic spectra, rather than the *best* ones. Second, our analysis is based on a sample of well-separated multipulse GBM-detected bursts and a criterion of statistical significance $S > 20$ was used to select the bright spectra for each individual burst. These may be causing some bias in our analysis results. Lastly, compared to previous catalogs (e.g., Kaneko et al. 2006; Yu et al. 2016) that used the χ^2 method to statistically compare the models and determine the best-fit model for each individual spectrum, our analysis is based on a fully Bayesian analysis approach using the MCMC method and we used the information criteria to compare the models. Unlike the χ^2 method involving a different degree of freedom in different models and resulting in the comparison not being straightforwardly performed, the information criteria (e.g., DIC statistics) that we used in this task may easily offer a straightforward comparison among different models because penalty factors for overfitting of more complex models have also been taken into account. Based on such a Bayesian analysis and MCMC spectral fit method, we may also be able to select the better models more straightforward by inspecting their posterior distributions from MCMC sampling, as compared to some previous studies that invoke a more complicated selection method to determine their *good* class of parameters (e.g., Kaneko et al. 2006; Yu et al. 2016).

3.1. Statistically Preferred Model Misused

In this task, our primary interest is to assess the effect of misuse of the models on fitting results. For instance, for a given spectrum that can be better (or statistically preferred) described by the BAND model, are the spectral parameters obtained from the simpler COMP model still consistent with that from the BAND model? To better address this question, we define (1) the *BAND-to-BAND* case (Column 6 in Table 1): a statistically preferred BAND model is used for a given category (defined in Section 2.2) or group (defined in Section 2.3); (2) the *COMP-to-COMP* case: a statistically preferred COMP model is used. Alternatively, if a statistically preferred model is not being used, in contrast, the model used is a *statistically undesirable* one. This may involve the better model being misused. We therefore also define (3) the *BAND-to-COMP* case: a statistically preferred model is BAND but COMP is misused, this invokes the case of underfitting; (4) the *COMP-to-BAND* case: a statistically preferred model is COMP but BAND is misused, this invokes the case of overfitting.

We then investigate these misused cases using the following two typical examples, as shown in Figure 4. In the left panel of Figure 4, we present the spectral fit to a time bin (between 86.338 and 86.877 s in GRB 120728) using both BAND and COMP models. This spectrum can be statistically preferred fitted by the COMP model, confirmed by the DIC statistics with a value of $\Delta\mathrm{DIC} = 1.2$. The spectral parameters obtained by the COMP fit are $\alpha = -0.26^{+0.23}_{-0.23}$, and $E_\mathrm{p} = 74^{+16}_{-16}$ and obtained by the BAND fit are $\alpha = -0.17^{+0.25}_{-0.27}$, $\beta = -6.46^{+2.38}_{-2.38}$, and $E_\mathrm{p} = 71^{+6}_{-5}$. These results suggest that the fitted spectral parameters (α and E_p) between the COMP-to-BAND case all seem to agree. In the right panel of Figure 4, we present the spectral fit to another time bin (between 69.274 and 71.015 s in GRB 120728). The BAND model is the statistically preferred one that describes the spectral shape, which is also confirmed by the DIC statistics with a value of $\Delta\mathrm{DIC} = -123.8$. For comparison, we also fit the spectral data using the COMP model. For the BAND model: $\alpha = 0.09^{+0.12}_{-0.12}$, $\beta = -2.52^{+0.06}_{-0.06}$, and $E_\mathrm{p} = 76^{+4}_{-4}$. For the COMP model: $\alpha = {}^{-}0.61^{+0.05}_{-0.05}$, and $E_\mathrm{p} = 109^{+7}_{-7}$. We find a remarkable discrepancy in the spectral parameters between the BAND-to-COMP case (the COMP model with softer α values and higher E_p, as compared with the BAND model). This is due to compensating for the lack of a high-energy spectral component in the model resulting in the underfitting.

We also test the misuse of models by fitting the simulated spectra, which are generated by the GBM Data Tools.[4] For the source spectra, we take the functional modeling of the BAND and set the initial model parameters of $A = 0.03$, $\alpha = -0.55$, $E_\mathrm{p} = 500$, and $\beta = -2.5$, and those of the COMP with $A = 0.03$, $\alpha = -0.55$, and $E_\mathrm{c} = 500$. For the background spectrum, we generate it using a phenomenological method that first to fit the

[4] https://fermi.gsfc.nasa.gov/ssc/data/analysis/rmfit/gbm_data_tools/gdt-docs/

Table 1
Results of the Average and Deviation Values of the Parameter Distribution

Spectra (Categorized) (1)	Classified by (2)	Model (Preferred) (3)	Model (Used) (4)	Model (Identified) (5)	Model (Defined) (6)	Spectra (Number) (7)	α (8)	β (9)	$E_{\rm p}$ (keV) (10)
Overall	⋯	⋯	BAND	⋯	⋯	944	-0.82 ± 0.34	⋯	$\log_{10}(213) \pm 0.41$
Overall	⋯	⋯	COMP	⋯	⋯	944	-0.91 ± 0.33	⋯	$\log_{10}(239) \pm 0.40$
BAND preferred	Well-constrained β	BAND	BAND	Better	BAND-to-BAND	327	-0.64 ± 0.28	-2.53 ± 0.39	$\log_{10}(191) \pm 0.41$
COMP preferred	Unconstrained β	COMP	COMP	Better	COMP-to-COMP	617	-0.96 ± 0.33	⋯	$\log_{10}(249) \pm 0.40$
BAND preferred	Well-constrained β	BAND	COMP	Misused	BAND-to-COMP	327	-0.82 ± 0.29	⋯	$\log_{10}(252) \pm 0.38$
COMP preferred	Unconstrained β	COMP	BAND	Misused	COMP-to-BAND	617	-0.91 ± 0.31	-5.57 ± 0.90	$\log_{10}(225) \pm 0.42$
Group I	ΔDIC $<= -10$	BAND	BAND	Statistically preferred	BAND-to-BAND	272	-0.64 ± 0.35	-2.26 ± 0.50	$\log_{10}(188) \pm 0.39$
Group I	ΔDIC $<= -10$	BAND	COMP	Misused	BAND-to-COMP	272	-0.83 ± 0.33	⋯	$\log_{10}(251) \pm 0.33$
Group II	$-10 < \Delta$DIC $<= -5$	BAND	BAND	Statistically preferred	BAND-to-BAND	106	-0.74 ± 0.24	-3.23 ± 0.74	$\log_{10}(177) \pm 0.37$
Group II	$-10 < \Delta$DIC $<= -5$	BAND	COMP	Misused	BAND-to-COMP	106	-0.89 ± 0.25	⋯	$\log_{10}(232) \pm 0.40$
Group III	$-5 < \Delta$DIC $<= 0$	COMP	BAND	Misused	COMP-to-BAND	208	-0.84 ± 0.31	-5.01 ± 0.89	$\log_{10}(253) \pm 0.38$
Group III	$-5 < \Delta$DIC $<= 0$	COMP	COMP	Statistically preferred	COMP-to-COMP	208	-0.90 ± 0.32	⋯	$\log_{10}(283) \pm 0.36$
Group IV	ΔDIC > 0	COMP	BAND	Misused	COMP-to-BAND	358	-0.94 ± 0.31	-6.10 ± 0.45	$\log_{10}(206) \pm 0.42$
Group IV	ΔDIC > 0	COMP	COMP	Statistically preferred	COMP-to-COMP	358	-0.98 ± 0.31	⋯	$\log_{10}(222) \pm 0.40$

Column (1) lists the spectral categories and groups, Column (2) lists our criteria to select better or statistically preferred spectra, Columns (3)–(6) list the preferred model, the used model, and the identified model (better, statistically preferred, or misused), and the defined model for each category and group, Column (7) lists the number of the spectra, and Columns (8)–(10) list the average and its deviation (1σ) for the spectral parameters. Note that the global properties of these spectral parameters are displayed in the top panel of this table (see also in Table A1 of Li et al. 2021).

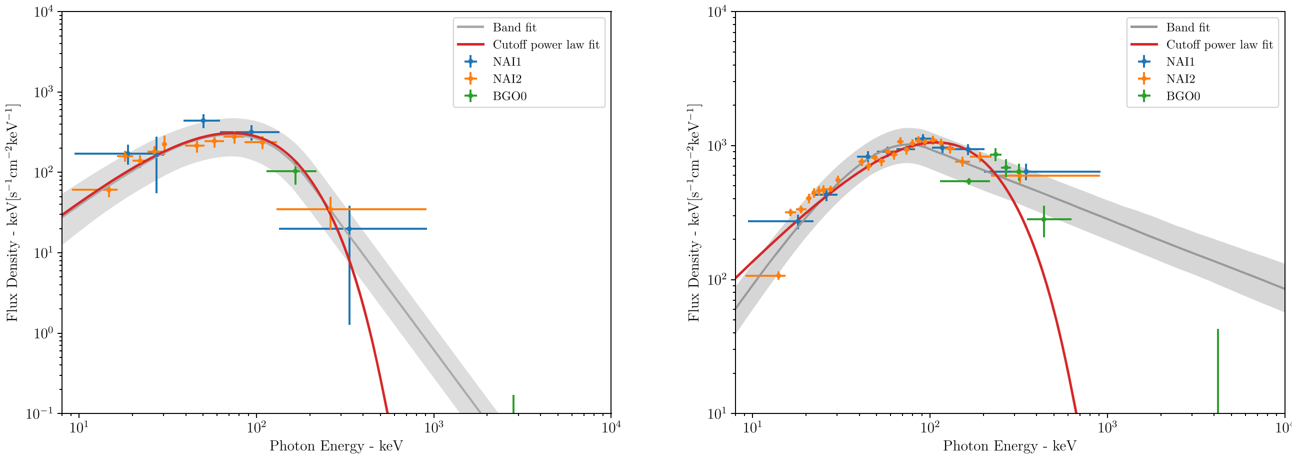

Figure 4. Comparison of the fitting of the same spectral data using BAND and COMP models. Left panel: COMP is the statistically preferred model for the time interval between 86.338 and 86.877 s of GRB 120728. Right panel: BAND is the statistically preferred model for the time interval between 69.274 and 71.015 s of GRB 120728.

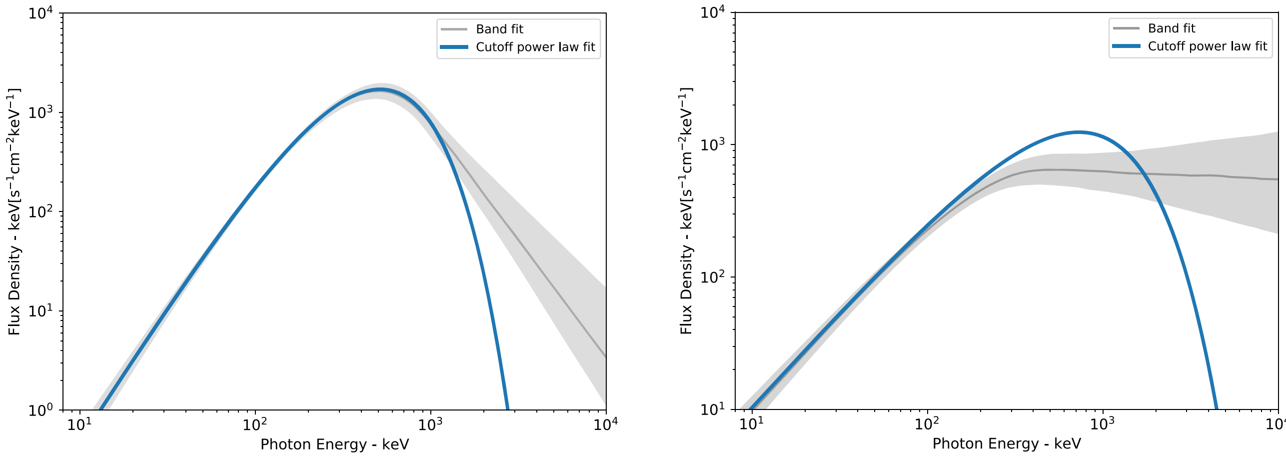

Figure 5. Same as Figure 4 but for the simulated spectra. The left panel is the fittings for the simulated COMP-like spectrum while the right panel is the fittings for the simulated BAND-like spectrum.

background of GRB 210518A[5] then to simulate the background spectrum from the fitted parameters. The response matrix is taken from the first 10 s of GRB 210518A.

The simulated COMP-like spectrum fitted using BAND and COMP gives rise to a differential value of ΔDIC $= 0.4$ (see the left panel of Figure 5). A small difference in DIC statistics suggests that adding a high-energy component to such a COMP-like spectrum does not significantly improve the fit. Whereas the simulated BAND-like spectrum results in large DIC statistics (ΔDIC$= -38.6$) improvements (see the right panel of Figure 5), indicating a statistically significant high-energy power-law component. These simulated results are consistent with the findings using true spectral fittings as described above.

3.2. Comparisons of Parameter Distribution for β-statistic-based Categories

With the categories defined in Section 2.2, we present the distributions of the spectral parameters that are used to compare the BAND-preferred spectra and COMP-preferred spectra in Figure 6. The average values and the corresponding standard deviation obtained from the best Gaussian fits for parameter distributions are summarized in Table 1, including α (BAND and COMP), β (BAND only), and $E_{\rm p}$ (BAND and COMP).

Before comparing the fitted parameters of BAND and COMP with different categories and groups, we caution that the low-energy spectral indices α obtained from BAND and COMP are asymptotic values rather than actual slopes, and therefore cannot be directly compared. In order to minimize the discrepancy, an effective $\alpha_{\rm eff}$, computed at 25 keV (the BATSE[6] detector lower limit), was introduced by Preece et al. (1998). In the GBM observations, the lower limit of the detector is at 8 keV, which is much smaller than the BATSE, and the difference between the asymptotic values and the actual slopes can be negligible (Figure 7). The fit values of α, therefore, can be directly used for our further analyses.

For α distribution (the right panel of Figure 6), we find the BAND-better spectra and COMP-better spectra showing inconsistent peaks. The best fit gives $\alpha^{\rm BAND} = -0.64 \pm 0.28$ for the BAND-better spectra and $\alpha^{\rm COMP} = -0.96 \pm 0.33$ for

[5] This burst is randomly selected, and its background is adopted, not the burst signal.

[6] The Burst and Transient Source Experiment on board the Compton Gamma-Ray Observatory (CGRO).

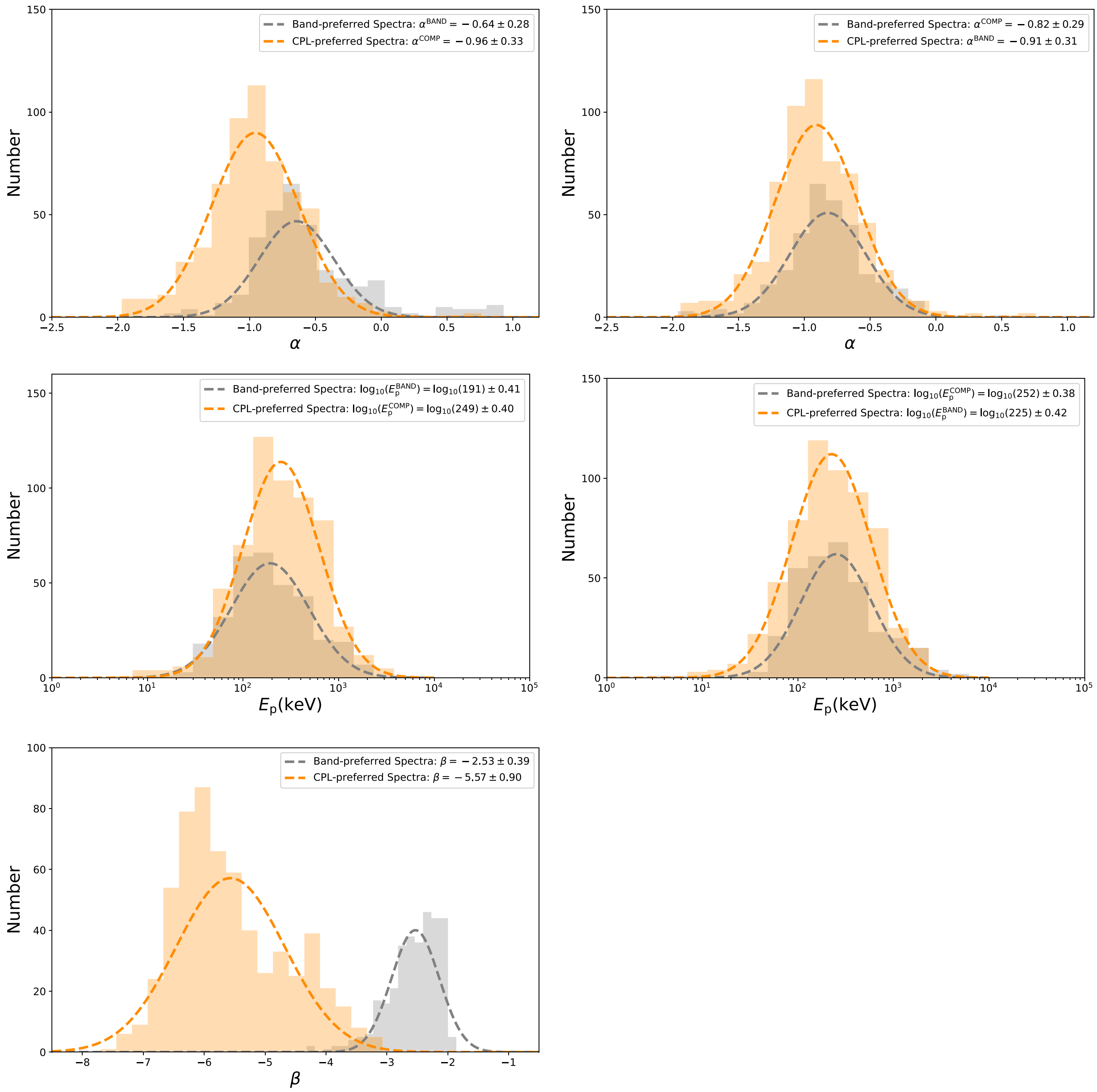

Figure 6. Distributions of α (upper panels), E_p (middle panels), and β (lower panel). All are based on statistical significance $S \geqslant 20$ (944 spectra). The spectra separated by the better models via to check their posterior plots. For each spectral parameter, the left panel shows the model preferred cases while the right panel displays the model misused cases. The BAND-preferred spectra is indicated by gray color while those of the COMP-preferred spectra reindicated by orange color.

the COMP-better spectra, with a difference between α of the BAND fits and the COMP fits of $\Delta\alpha = 0.32$, where $\Delta\alpha$ is defined as $\Delta\alpha = \alpha^{BAND} - \alpha^{COMP}$.

While if the BAND-better spectra are misused by the COMP fit, one has $\alpha^{COMP} = -0.82 \pm 0.29$, with a value of $\Delta\alpha$ of 0.18. Likewise, if the COMP-better spectra are misused by the BAND fit, one has $\alpha^{BAND} = -0.91 \pm 0.31$, with a value of $\Delta\alpha$ of 0.05. Based on these results, several interesting results can be drawn: (1) a significantly statistical difference of the spectral parameters between BAND-better spectra and COMP-better spectra is found; (2) the deviation (the COMP model with higher E_p and softer α indices than the BAND model) between the BAND-to-COMP case is much more significant than the COMP-to-BAND case. Similar results can also be found in the E_p distribution (see the middle panels of Figure 6 and Column 9 in Table 1).

We use the Kolmogorov–Smirnov (K-S) test to assess whether the distributions change between the two distinct categories. The chance probability, P, determined by the K-S test, leads to a value of $P_{K\text{-}S}(\alpha^{BAND}, \alpha^{COMP}) < 10^{-4}$ for the α distributions and of $P_{K-S}(E_p^{BAND}, E_p^{COMP}) = 1.06 \times 10^{-4}$ for the E_p distributions between the BAND-better spectra and the COMP-better spectra, indicating that these distributions are indeed different from one another.

With separated well-constrained and unconstrained β categories, the β distributions show a single peak for each

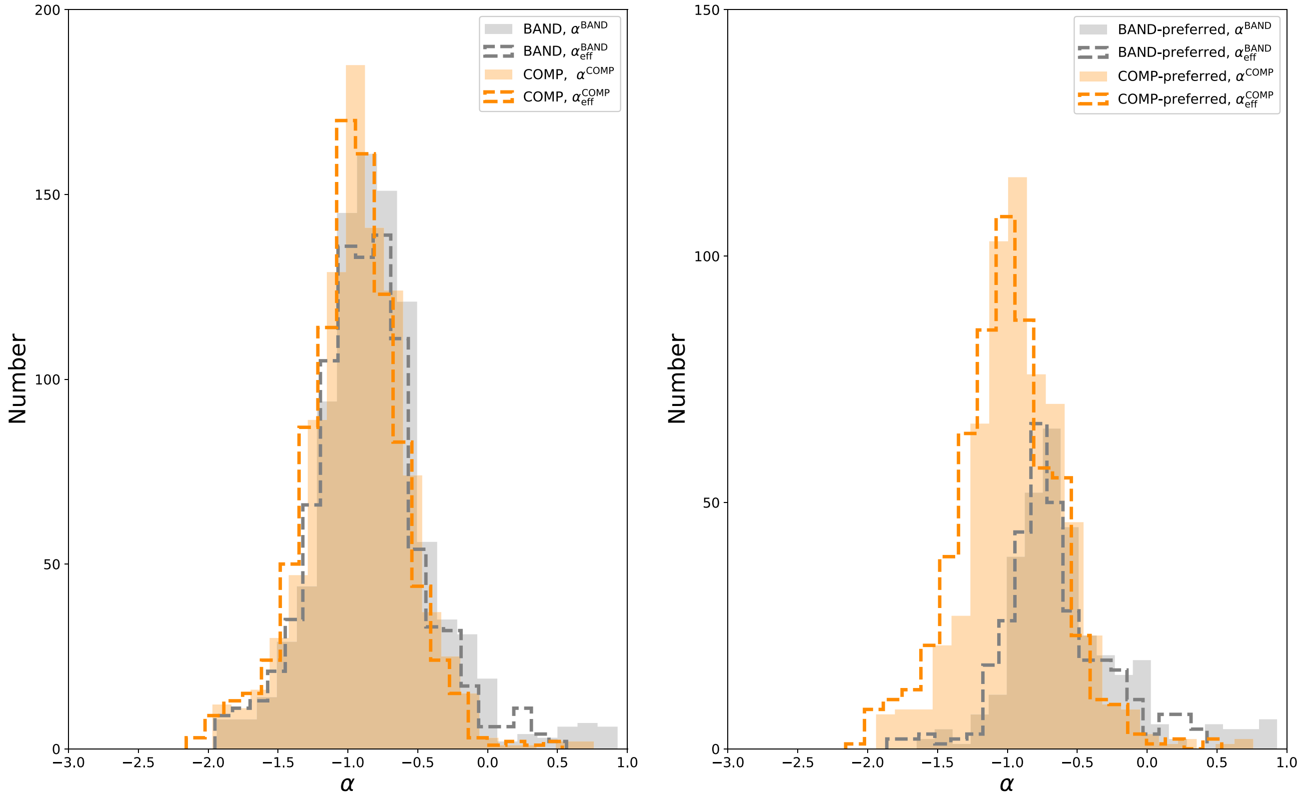

Figure 7. Distributions of fitted values of α obtained from the BAND and COMP as compared to their effective values α_{eff}, computed at 8 keV using the Equation (2) in Preece et al. (1998). Left panel: for the global spectra. Right panel: for the β-based spectra.

category, with the best fits giving $\beta = -2.53 \pm 0.39$ for well-constrained β categories and $\beta = -5.57 \pm 0.90$ for unconstrained β category, respectively (the lower panel of Figure 6 and Column 8 in Table 1).

3.3. Comparisons of Parameter Distribution for DIC-statistic-based Groups

We present the distributions of ΔDIC in Figure 3. We find that Group I, Group II, Group III, and Group IV can account for 29%, 11%, 22%, and 38% of the total number of the spectra, respectively. Based on these DIC-statistic-based groups, we then present the parameter distributions (α, E_p, and β) by comparing BAND and COMP (Figure 8) group-wisely. The parameter distributions obtained from the BAND model with the best Gaussian fit are shown by gray lines and those from the COMP model are shown by orange lines.

For α distribution (see the left panel of Figure 8 and Column 7 in Table 1), we find that α indices obtained from BAND are significantly harder than those obtained from COMP in each group.[7] More interestingly, such a statistically significant difference in parameters tends to be weaker during the transition from Group I (minimum-ΔDIC) to Group IV (maximum-ΔDIC).

Physically, we could diagnose the underlying physical mechanism through the distributions of α indices. This is because different theoretical models predict different distributions of α. The photosphere emission models usually associate with α indices while the synchrotron emission models typically relate to softer α indices. As pointed out by some previous works (e.g., Preece et al. 1998; Acuner et al. 2020), the low-energy index α is a good estimator for which model is preferred by the data. For example, the synchrotron emission explains the spectral indices with a limit, known as the line of death, $\alpha = -2/3$ (Preece et al. 1998). Acuner et al. (2020) argued that the spectra that prefer the photospheric model all have low-energy power-law indices $\alpha \gtrsim -0.5$. In Figure 8, the line of death of the synchrotron emission is indicated by the green lines for each group. As a result, we find that the fraction of the spectra with α beyond the synchrotron limit obtained from the BAND model is apparently greater than those obtained from the COMP model. Moreover, these fractions decrease for subsequent DIC-based groups. Groupwise, the corresponding fractions [BAND, COMP] are [49%, 25%], [34%, 25%], [30%, 25%], and [19%, 17%] for Group I, Group II, Group III, and Group IV, respectively. We also notice that the distribution of α has a smooth and well-defined Gaussian shape of at the line of death, challenging the existence of the line of death.

For E_p distributions (the middle panel of Figure 8 and Column 9 in Table 1), unlike α distribution, we do not find a strong trend among the groups. Interestingly, the statistical significant difference in parameters tends to be weaker for subsequent DIC-based groups, resembling the finding in the α distribution.

We present the groupwise β distributions in the right panel of Figure 8. Using the same data, Li et al. (2021) found a similar bimodal distribution based on the better model determined for each individual pulse, with the harder peak at ~ -2.3 and the softer peak at ~ -6.1. The results indicate that

[7] Following the traditional classification, the *hard* spectra are denoted as large values of both α and E_p, while the *soft* spectra are denoted as low values of α and E_p.

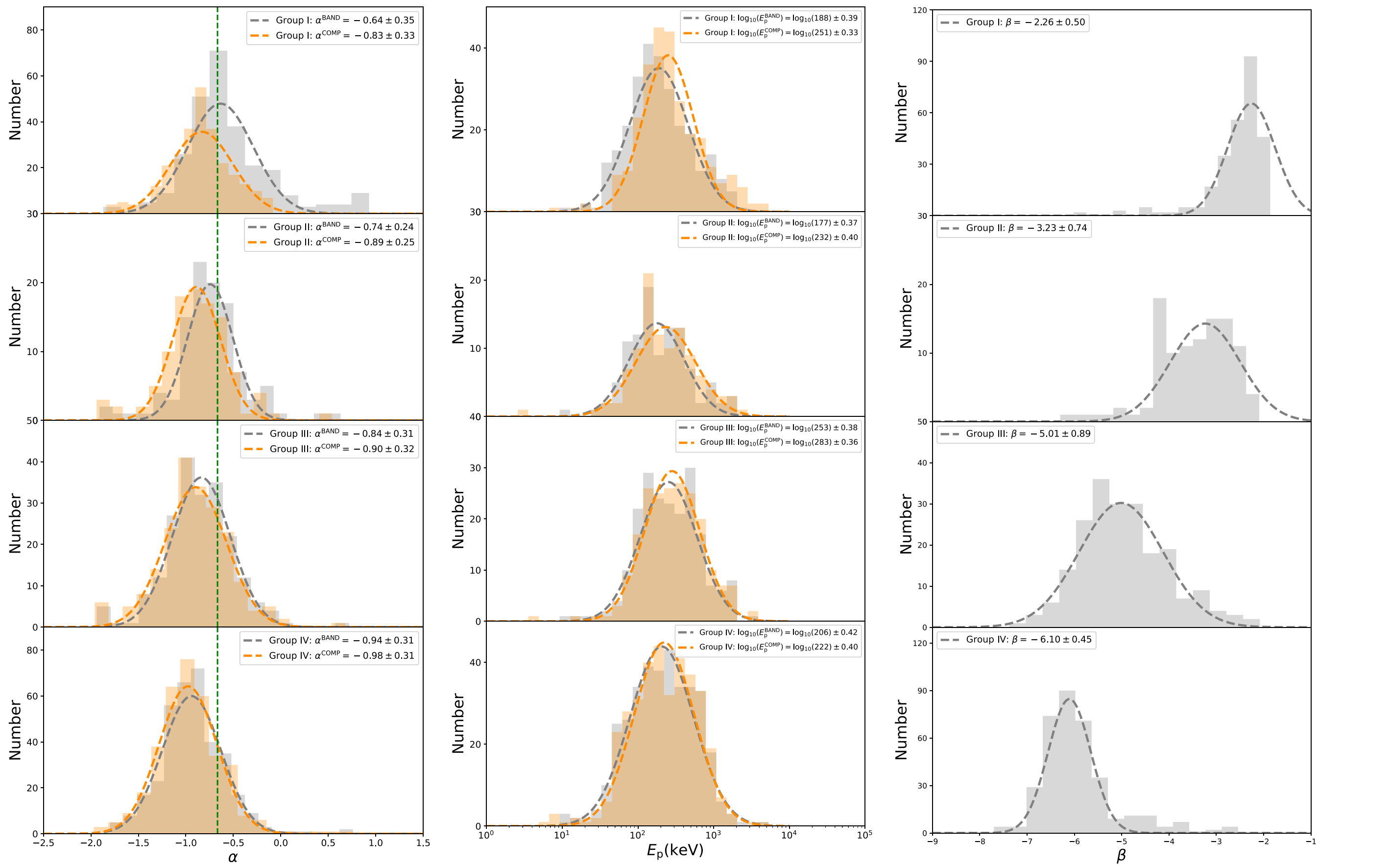

Figure 8. Same as Figure 6 but for the spectra grouped based on DIC statistic. The green line indicated the line of death for the synchrotron emission ($\alpha = -2/3$).

the BAND-better and COMP-better spectra should be mixed to compose the distributions, and the harder peak should be contributed by the BAND-better spectra while the softer peak should be contributed by the COMP-better spectra.

Separated by the DIC statistics, we group the spectra into four groups as defined in Section 2.3. Interestingly, we find that all of the groups show a single peak, but the peak is clearly shifted from Group I to Group IV with a hard-to-soft trend. The hardest peak is at ~ -2.3 found in the Group I (minimum-ΔDIC) (Figure 8). This value is the same as the harder peak of the bimodal distribution found in the pulse-wise categories (Li et al. 2021), implying that the peak is dominated by the BAND-like spectra. Likewise, the softest peak is at ~ -6.1 (Figure 8), which is found in Group IV (maximum-ΔDIC). This value is the same as the softer peak of the bimodal distribution found in Li et al. (2021), suggesting the peak is dominated by the COMP-like spectra. However, the peak (Figure 8) for Group II is $\beta = -3.23 \pm 0.74$ while that for Group III is $\beta = -5.01 \pm 0.89$, suggesting a mix of BAND-like and COMP-like spectra.

3.4. Comparisons of Parameter Relations

In GRB physics, the study of parameter correlations is an open question, and it plays an important role in understanding the underlying physical processes and radiation mechanisms (e.g., Amati et al. 2002; Geng & Huang 2013; Srinivasaragavan et al. 2020; Li et al. 2021, and references therein).

We first compare the same spectral parameters between two models by plotting $\alpha^{\rm COMP}$–$\alpha^{\rm BAND}$ (the left panels of Figure 9), $E_{\rm p}^{\rm COMP}$–$E_{\rm p}^{\rm BAND}$ (the middle panels of Figure 9), and $F_{\rm p}^{\rm COMP}$–$F_{\rm p}^{\rm BAND}$ (the right panels of Figure 9). We find that the α indices obtained from the BAND model are systematically harder than the ones obtained from the COMP model, particularly in the BAND-better spectra. However, this trend is weaker in the BAND-wise spectra as compared to the COMP-wise spectra, which is consistent with the finding based on parameter distributions as discussed in Section 3.3. Similar results are also found in the $E_{\rm p}^{\rm COMP}$–$E_{\rm p}^{\rm BAND}$ plot. An interesting result is found in the $F_{\rm p}^{\rm COMP}$–$F_{\rm p}^{\rm BAND}$ plot, where the energy flux obtained from BAND and COMP is similar, crossing different categories and groups.

It is even more interesting to see how these parameter relations are affected by the misused models. Based on the categories defined in Section 2.2, we therefore investigate the following pair parameter relations comparing BAND with COMP: ($\log F$, α), ($\log F$, $\log E_{\rm p}$), (α, $\log E_{\rm p}$). For each individual parameter relation, in order to ensure that the majority of spectra are BAND-like, we select three typical bursts (GRB 140206B for the F–α relation; GRB 130306B for the F–$E_{\rm p}$ relation; and GRB 120827 for the α–$E_{\rm p}$ relation), where the vast majority of spectra in these bursts satisfy ΔDIC < -10 (seven out of 10 from GRB 140206B, 13 out of 16 from GRB 130306B, and 30 out of 36 from GRB 120827). We use the following function to fit the data: $F = F_0\, e^{k_1 \alpha}$ for the F–α plot; $F = F_0\, E_{\rm p}^{k_2}$ for the F–$E_{\rm p}$ plot; and $\alpha = k_3 \ln(E_{\rm p}/E_0) + \alpha_0$ for the α–$E_{\rm p}$ plane. The time-resolved F–α relation (e.g., Ryde et al. 2019; Li et al. 2021), F–$E_{\rm p}$

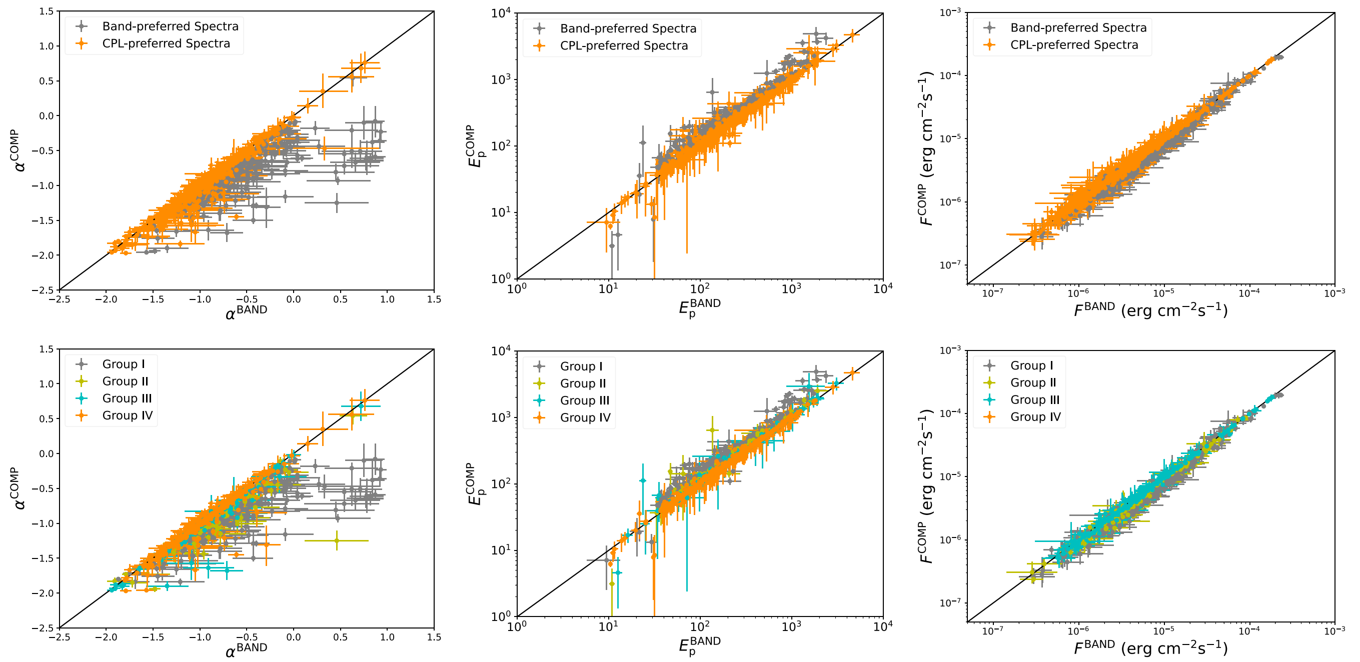

Figure 9. Comparison of the same spectral parameters between BAND and COMP: the $\alpha^{\rm BAND}$–$\alpha^{\rm COMP}$ (left panel), $E_{\rm p}^{\rm BAND}$–$E_{\rm p}^{\rm COMP}$ (middle panel), and $F^{\rm BAND}$–$F^{\rm COMP}$ (right panel) plottings. Upper panels: for the β-based categories. Lower panels: for the DIC-based groups.

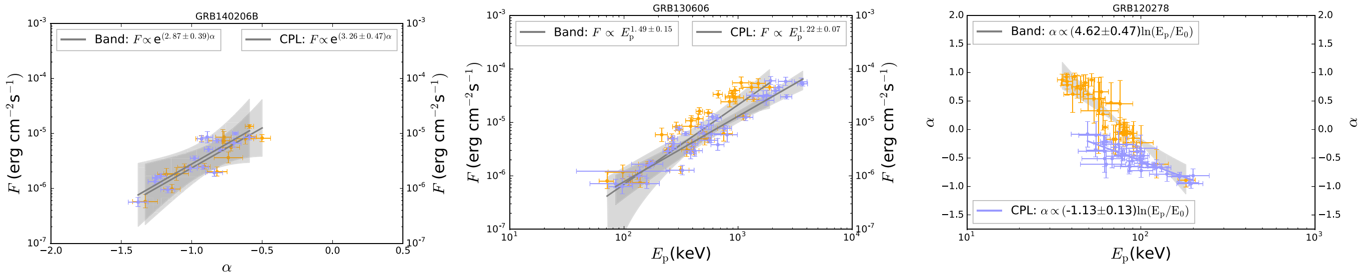

Figure 10. The parameter relation of the F–α (left panel), F–$E_{\rm p}$ (middle panel), and α–$E_{\rm p}$ (right panel), as well as the best-fit relations with the 2σ error region.

relation (Golenetskii et al. 1983), and α–$E_{\rm p}$ relation (e.g., Li et al. 2021) are presented in the left, middle, and right panels of Figure 10, respectively. The results of our linear regression analysis for these parameter relations comparing BAND with COMP are reported in Table 2. We find that $k_1^{\rm BAND} \sim 2.87 \pm 0.39$ is significantly shallower than $k_1^{\rm CPL} \sim 3.26 \pm 0.47$, whereas $k_2^{\rm BAND} \sim 1.49 \pm 0.15$ is clearly steeper than $k_2^{\rm CPL} \sim 1.22 \pm 0.07$, and likewise, $k_3^{\rm BAND} \sim -4.62 \pm 0.47$ is apparently steeper than $k_3^{\rm CPL} \sim -1.14 \pm 0.13$.

4. Discussion

BAND function and COMP are preferred respectively by a given group of GRBs, so a question is raised as to whether these two empirical functions have different physical origins? Or, is COMP just an approximation of BAND as demonstrated in Figure 4 when $\beta \ll 0$? We may find some clues in Figure 6, of which the histogram of β does not form the shape of the unimodal distribution; instead, it displays a clear bimodal structure which peaks at $\beta \simeq -2.5$ and $\beta \simeq -6$ respectively. Moreover, the two modes are separated at $\beta \simeq -3.5$, and each one is almost independently contributed by COMP-preferred spectra or BAND-preferred spectra. This separation is hardly due to that COMP is preferred by noisy data, because first the separation is distinct, and second all the spectra have $S > 20$, which is high enough to ensure data quality.[8] Figure 6 also exhibits the histograms of α and $E_{\rm p}$, for which the distributions of COMP and BAND preferred GRBs differ from each other, though not as distinguishable as the distribution of β. This statistical result infers that BAND and COMP may have different physical origins. One may propose that there exist two different mechanisms of prompt emission. One produces spectra consists of many power laws, e.g., synchrotron emission of charged particles accelerated by kinetic shock waves (e.g., Sari et al. 1998); the other produces spectra of a power law with an exponential tail, e.g., the convolution of blackbody spectra in photospheres, the cut of the highest temperature corresponds to the exponential tail (e.g., Ryde et al. 2010).

5. Conclusions

In this paper, we have revisited the catalog of the time-resolved spectrum of the multipulse Fermi-GBM bursts defined in Li et al. (2021). We used two methods to determine the

[8] We also tested the spectra with $S > 50$, the bimodal structure of β distribution clearly exists as well.

Table 2
Results of Our Linear Regression Analysis for Parameter Relations

Relation	Model	Expression	N	R	p
F–α	BAND	$F/(\mathrm{erg\ cm^{-2}\ s^{-1}}) = (9.61 \pm 0.42)e^{(2.87\pm0.39)\,\alpha}$	10	0.86	$<10^{-4}$
F–α	COMP	$F/(\mathrm{erg\ cm^{-2}\ s^{-1}}) = (9.40 \pm 0.49)e^{(3.26\pm0.47)\,\alpha}$	10	0.82	$<10^{-4}$
F–E_p	BAND	$F/(\mathrm{erg\ cm^{-2}\ s^{-1}}) = (9.23 \pm 1.06)\mathrm{e}{-6} \times (E_p/\mathrm{keV})^{(1.49\pm0.15)}$	16	0.88	$<10^{-4}$
F–E_p	COMP	$F/(\mathrm{erg\ cm^{-2}\ s^{-1}}) = (1.19 \pm 0.08)\mathrm{e}{-5} \times (E_p/\mathrm{keV})^{(1.22\pm0.07)}$	16	0.92	$<10^{-4}$
α–E_p	BAND	$\alpha = (-4.62 \pm 0.47)\ln(E_p/E_0) + (4.90 \pm 0.47) \times (E_p/\mathrm{keV})$	36	−0.91	$<10^{-4}$
α–E_p	COMP	$\alpha = (-1.14 \pm 0.13)\ln(E_p/E_0) + (1.72 \pm 0.26) \times (E_p/\mathrm{keV})$	36	−0.79	$<10^{-4}$

better (or statistically preferred) spectra between two standard empirical spectral functions: BAND and COMP. First, we grouped the spectra into the well-constrained β (BAND-better) and unconstrained β (COMP-better) categories by checking their two-dimensional corner-corner plots of the posteriors for each Bayesian MCMC spectral fit. Second, we also separated the spectra into four groups based on the DIC statistics: Group I with ΔDIC < -10 strongly suggests that BAND spectra are statistically preferred; Group II with $-10 < \Delta$DIC < -5 indicates that BAND spectra are still statistically preferred, but not as strong as Group I; Group III with $-5 < \Delta$DIC < 0, indicating COMP spectra are statistically preferred; and Group IV with ΔDIC > 0 significantly indicates that the COMP spectra are statistically preferred.

With these categories and groups defended, we therefore compared the spectral properties obtained by both BAND and COMP functions, including their spectral distributions, spectral relations, and spectral evolution.

In the categories defined by identifying well-constrained β and unconstrained β, we found inconsistent peaks of the parameter distributions (both α and E_p) showing between the BAND-better and COMP-better spectra.

These results were also independently confirmed by an analysis based on the DIC statistics. Moreover, such a statistical difference in parameters tends to be weaker when transitioning from Group I (minimum-ΔDIC) to Group IV (maximum-ΔDIC). The BAND-β distributions show a single peak for all the DIC-statistic-based groups, and the peaks obtained from the Group I and Group IV samples are the same as the harder and softer peaks found in Li et al. (2021), suggesting that these peaks are more likely dominated by the BAND-like spectra and COMP-like spectra, respectively.

We also discussed the effect of the misused model on the results for each category and group. We found that the apparent deviation from the parameters is found between the BAND-to-COMP cases, while the parameters between the COMP-to-BAND cases all seem to agree.

As a self-consistency test, we also compare the same spectral parameters between the BAND-better and COMP-better categories and among the DIC-statistic-based groups by investigating the α^{COMP}–α^{BAND}, E_p^{COMP}–E_p^{BAND}, and F_p^{COMP}–F_p^{BAND} plotting. The greater dispersion for data points is still found between the BAND-to-COMP cases. We further investigated the F–α, F−E_p, and α–E_p relations for such the misused case using three example cases. The obtained power-law index (slope) between the misused model (COMP) and the better model (BAND) are significantly different. The index (k^{COMP}) derived from the misused model is shallower (F–E_p relation and α–E_p relation) and steeper (F–α relation) than that (k^{BAND}) derived from the better model.

We also discussed the bimodal distribution of β, which indicates that BAND and COMP may have different physical origins.

In conclusion, our analysis suggests that the choice between BAND and COMP spectral model for the GRB spectral analysis should be made with caution. The fit from the misused model deviates from the real spectral shape and then may lead to incorrect physical interpretation.

L.L. thanks the anonymous referee for valuable comments and suggestions. L.L. also thanks Felix Ryde, M.G. Dainotti, Gregory Vereshchagin, Remo Ruffini, and ICRANet members for many discussions on GRB physics and phenomena. L.L. particularly thanks Yu Wang for many useful discussions that greatly improved the paper. This research has made use of the High Energy Astrophysics Science Archive Research Center (HEASARC) Online Service at the NASA/Goddard Space Flight Center (GSFC).

ORCID iDs

Liang Li https://orcid.org/0000-0002-1343-3089

References

Acuner, Z., Ryde, F., Pe'er, A., Mortlock, D., & Ahlgren, B. 2020, ApJ, 893, 128
Amati, L., Frontera, F., Tavani, M., et al. 2002, A&A, 390, 81
Atwood, W. B., Abdo, A. A., Ackermann, M., et al. 2009, ApJ, 697, 1071
Band, D., Matteson, J., Ford, L., et al. 1993, ApJ, 413, 281
Dai, Z. G., Wang, X. Y., Wu, X. F., & Zhang, B. 2006, Sci, 311, 1127
Gelman, A., Hwang, J., & Vehtari, A. 2014, Stat. Comput., 24, 997
Geng, J. J., & Huang, Y. F. 2013, ApJ, 764, 75
Geng, J.-J., Huang, Y.-F., Wu, X.-F., Zhang, B., & Zong, H.-S. 2018, ApJS, 234, 3
Goldstein, A., Burgess, J. M., Preece, R. D., et al. 2012, ApJS, 199, 19
Golenetskii, S. V., Mazets, E. P., Aptekar, R. L., & Ilinskii, V. N. 1983, Natur, 306, 451
Gruber, D., Goldstein, A., Weller von Ahlefeld, V., et al. 2014, ApJS, 211, 12
Kaneko, Y., Preece, R. D., Briggs, M. S., et al. 2006, ApJS, 166, 298
Li, L. 2019a, ApJS, 242, 16
Li, L. 2019b, ApJS, 245, 7
Li, L. 2020, ApJ, 894, 100
Li, L., Geng, J.-J., Meng, Y.-Z., et al. 2019, ApJ, 884, 109
Li, L., Ryde, F., Pe'er, A., Yu, H.-F., & Acuner, Z. 2021, ApJS, 254, 35
Li, L., & Zhang, B. 2021, ApJS, 253, 43
Meegan, C., Lichti, G., Bhat, P. N., et al. 2009, ApJ, 702, 791
Meng, Y.-Z., Geng, J.-J., Zhang, B.-B., et al. 2018, ApJ, 860, 72
Meng, Y.-Z., Liu, L.-D., Wei, J.-J., Wu, X.-F., & Zhang, B.-B. 2019, ApJ, 882, 26
Meszaros, P., Rees, M. J., & Papathanassiou, H. 1994, ApJ, 432, 181
Moradi, R., Li, L., Rueda, J. A., et al. 2021, arXiv:2103.09158
Moreno, E., Vazquez-Polo, F. J., & Robert, C. P. 2013, arXiv:1310.2905
Pe'er, A., Ryde, F., Wijers, R. A. M. J., Mészáros, P., & Rees, M. J. 2007, ApJL, 664, L1
Planck Collaboration, Aghanim, N., Akrami, Y., et al. 2020, A&A, 641, A6
Pooley, C., & Marion, G. 2018, RSOS, 5, 171519
Preece, R. D., Briggs, M. S., Mallozzi, R. S., et al. 1998, ApJL, 506, L23

Rees, M. J., & Meszaros, P. 1994, ApJL, 430, L93
Ruffini, R., Siutsou, I. A., & Vereshchagin, G. V. 2013, ApJ, 772, 11
Ruffini, R., Wang, Y., Aimuratov, Y., et al. 2018, ApJ, 852, 53
Ryde, F., Axelsson, M., Zhang, B. B., et al. 2010, ApJL, 709, L172
Ryde, F., Yu, H.-F., Dereli-Bégué, H., et al. 2019, MNRAS, 484, 1912
Sari, R., Piran, T., & Narayan, R. 1998, ApJL, 497, L17
Scargle, J. D., Norris, J. P., Jackson, B., & Chiang, J. 2013, ApJ, 764, 167
Spiegelhalter, D. J., Best, N. G., Carlin, B. P., & Van Der Linde, A. 2002, J. R. Stat. Soc. B, 64, 583
Srinivasaragavan, G. P., Dainotti, M. G., Fraija, N., et al. 2020, ApJ, 903, 18
Tang, Q.-W., Wang, K., Li, L., & Liu, R.-Y. 2021, ApJ, 922, 255
Thompson, C. 1994, MNRAS, 270, 480
Vianello, G., Gill, R., Granot, J., et al. 2018, ApJ, 864, 163
Xue, S.-S. 2021, JCAP, 2021, 044
Yu, H.-F., Dereli-Bégué, H., & Ryde, F. 2019, ApJ, 886, 20
Yu, H.-F., Preece, R. D., Greiner, J., et al. 2016, A&A, 588, A135
Zhang, B., Fan, Y. Z., Dyks, J., et al. 2006, ApJ, 642, 354
Zhang, B., & Yan, H. 2011, ApJ, 726, 90

A&A 658, A11 (2022)
https://doi.org/10.1051/0004-6361/202140403

Astronomy & Astrophysics

Radio data challenge the broadband modelling of GRB 160131A afterglow

M. Marongiu[1,2,3], C. Guidorzi[2,4,5], G. Stratta[6], A. Gomboc[7], N. Jordana-Mitjans[8], S. Dichiara[9,10,11], S. Kobayashi[12], D. Kopač[13], and C. G. Mundell[8]

[1] INAF – Osservatorio Astronomico di Cagliari, Via della Scienza 5, 09047 Selargius, Italy
e-mail: marco.marongiu@inaf.it
[2] Department of Physics and Earth Science, University of Ferrara, Via Saragat 1, 44122 Ferrara, Italy
[3] ICRANet, Piazzale della Repubblica 10, 65122 Pescara, Italy
[4] INFN – Sezione di Ferrara, Via Saragat 1, 44122 Ferrara, Italy
[5] INAF – Osservatorio di Astrofisica e Scienza dello Spazio di Bologna, Via Piero Gobetti 101, 40129 Bologna, Italy
[6] INAF – Istituto di Astrofisica e Planetologia Spaziali, Via Fosso del Cavaliere 100, 00133 Rome, Italy
[7] Center for Astrophysics and Cosmology, University of Nova Gorica, Vipavska 13, 5000 Nova Gorica, Slovenia
[8] Department of Physics, University of Bath, Claverton Down, Bath BA2 7AY, UK
[9] Department of Astronomy, University of Maryland, College Park, MD 20742–4111, USA
[10] Astrophysics Science Division, NASA Goddard Space Flight Center, 8800 Greenbelt Rd, Greenbelt, MD 20771, USA
[11] Department of Astronomy and Astrophysics, The Pennsylvania State University, 525 Davey Lab, University Park, PA 16802, USA
[12] Astrophysics Research Institute, Liverpool John Moores University, IC2, Liverpool Science Park, 146 Brownlow Hill, Liverpool L3 5RF, UK
[13] Faculty of Mathematics and Physics, University of Ljubljana, Jadranska 19, Ljubljana 1000, Slovenia

Received 22 January 2021 / Accepted 28 October 2021

ABSTRACT

Context. Gamma-ray burst (GRB) afterglows originate from the interaction between the relativistic ejecta and the surrounding medium. Consequently, their properties depend on several aspects: radiation mechanisms, relativistic shock micro-physics, circumburst environment, and the structure and geometry of the relativistic jet. While the standard afterglow model accounts for the overall spectral and temporal evolution for a number of GRBs, its validity limits emerge when the data set is particularly rich and constraining, especially in the radio band.
Aims. We aimed to model the afterglow of the long GRB 160131A (redshift $z = 0.972$), for which we collected a rich, broadband, and accurate data set, spanning from 6×10^8 Hz to 7×10^{17} Hz in frequency, and from 330 s to 160 days post-burst in time.
Methods. We modelled the spectral and temporal evolution of this GRB afterglow through two approaches: (1) the adoption of empirical functions to model an optical/X-ray data set, later assessing their compatibility with the radio domain; and (2) the inclusion of the entire multi-frequency data set simultaneously through the Python package named SAGA (Software for AfterGlow Analysis), to obtain an exhaustive and self-consistent description of the micro-physics, geometry, and dynamics of the afterglow.
Results. From deep broadband analysis (from radio to X-ray frequencies) of the afterglow light curves, GRB 160131A outflow shows evidence of jetted emission. Moreover, we observe dust extinction in the optical spectra, and energy injection in the optical/X-ray data. Finally, radio spectra are characterised by several peaks that could be due to either interstellar scintillation (ISS) effects or a multi-component structure.
Conclusions. The inclusion of radio data in the broadband set of GRB 160131A makes a self-consistent modelling barely attainable within the standard model of GRB afterglows.

Key words. radiation mechanisms: non-thermal – gamma-ray burst: individual: GRB160131A – methods: data analysis

1. Introduction

Gamma-ray bursts (GRBs) consist in short and intense pulses of gamma-ray radiation originating from either core collapsing massive stars (e.g. Woosley & Bloom 2006) or binary neutron star (BNS) mergers (e.g. Abbott et al. 2017). These sources can launch relativistic jets with opening angles of a few degrees. According to the standard model (e.g. Rees & Meszaros 1992; Meszaros & Rees 1997; Panaitescu et al. 1998), GRB afterglow emission takes place when the outflow from the GRB central engine impacts on the circumburst medium (CBM), resulting mainly in synchrotron radiation (for a review see e.g. Piran 2004; Mészáros 2006; Gao et al. 2013a). The long-lasting afterglow emission can be detected days to months after the burst, and spans a broad range of electromagnetic spectrum (from gamma-ray to radio domain). It originates in two shock regions: a forward shock (FS) that propagates in the CBM (e.g. Granot & Sari 2002, hereafter GS02), and a reverse shock (RS) that propagates back into the flow itself and radiates at lower frequencies (e.g. Mészáros & Rees 1999; Kobayashi & Sari 2000; Kobayashi & Zhang 2007; Gao & Mészáros 2015).

GRB afterglows encode a wealth of information on (1) the radiation mechanism, in particular the possible presence of large-scale magnetic fields ploughing the ejecta, which is still one of the main open questions in this area of research (e.g. Jordana-Mitjans et al. 2020); (2) relativistic shock micro-physics; (3) energetics; and (4) jet geometry. All these issues can be addressed effectively and uniquely through observations at lower frequencies, especially in the radio band. Observations of radio afterglows are key to elucidating the GRB physics (e.g. Mundell et al. 2007), especially for the understanding of the RS component, which is directly linked to the nature of the outflow and, consequently, to the progenitor itself (e.g. Kopač et al. 2015). On the other hand, the detection of radio afterglows has proven challenging with current radio telescopes (e.g. Chandra & Frail 2012) – especially in single-dish mode (Marongiu et al. 2020) – mainly because of their milliJansky (mJy) and sub-mJy nature. Radio/mm follow-up campaigns in interferometric mode have improved the observational coverage of the lower part of the emission spectrum (e.g. Laskar et al. 2013, 2015, 2018a, 2019a) through increasingly sensitive facilities – such as the upgraded Giant Metre-wave Radio Telescope (GMRT, Swarup 1990; Kapahi & Ananthakrishnan 1995; Gupta et al. 2017)[1], the *Karl G. Jansky* Very Large Array (VLA, Thompson et al. 1980)[2], the Arcminute Microkelvin Imager Large Array (AMI-LA, Zwart et al. 2008)[3], and the NOrthern Extended Millimeter Array (NOEMA, Chenu et al. 2016)[4].

In addition to synchrotron radiation, the emission of GRB afterglows can be modelled via other radiation mechanisms (e.g. inverse Compton at high energies; Magic & Acciari 2019; Zhang et al. 2020). Additionally, the jet collimation, energy injection, dust extinction, and radio interstellar scintillation can further shape the observed afterglow. Well-sampled GRB afterglows in time and frequency domains are usually modelled with fine-tuning of the standard model, from radio to gamma-ray frequencies (e.g. Frail et al. 2006; Laskar et al. 2014; Perley et al. 2014), but especially ranging between the optical and gamma-ray domains (e.g. Lazzati 2002; Heyl & Perna 2003; Jakobsson et al. 2005; Gendre et al. 2006; Castro-Tirado et al. 2007; Starling et al. 2009; Zauderer et al. 2013; van der Horst et al. 2015). Sometimes, additions to the fine-tuning of the model lack a broadband consistency check, suggesting that available broadband data (from radio to gamma-ray frequencies) could not be completely explained within the standard model (e.g. Klotz et al. 2008; Gendre et al. 2010); in this context, modelling and simulation of GRB afterglow evolution is a particularly challenging problem (e.g. Granot 2007; van Eerten 2018), especially when radio observations are included in the analysis (e.g. Frail et al. 2000a,b, 2003; Corsi et al. 2005; Gendre et al. 2010; Resmi et al. 2012; Horesh et al. 2015). In the radio domain, there are other physical components that usually dominate the total emission, such as the RS (e.g. Sari & Piran 1999; Kobayashi & Zhang 2003; Laskar et al. 2013, 2016a, 2019b; Cucchiara et al. 2015; Veres et al. 2015; Alexander et al. 2017), rebrightenings due to refreshed shocks, and flares caused by central-engine activity (e.g. Björnsson & Fransson 2004; Zhang et al. 2006; Melandri et al. 2010; Chincarini et al. 2010; Margutti et al. 2010b).

Ongoing technological evolution has led to the development of several computational packages to model GRB afterglows (e.g. Rhoads 1999; Kobayashi et al. 1999; Daigne & Mochkovitch 2000; Kumar & Granot 2003; Cannizzo et al. 2004; Zhang & MacFadyen 2009; van Eerten et al. 2010a, 2012; Wygoda et al. 2011; De Colle et al. 2012; Granot & Piran 2012; Laskar et al. 2013; Leventis et al. 2013; Rhodes et al. 2020; Aksulu et al. 2020; Ryan et al. 2020; Ayache et al. 2022), but to date there is no computational tool that is able to fully describe the complex landscape of the GRB afterglows. The richness of the data set collected for GRB 160131A, in both time (from 430 s to ~163 d) and frequency (from 6×10^8 to 7×10^{17} Hz), makes it an ideal test bed for the standard GRB afterglow model.

This paper is organised as follows. Observations are reported in Sect. 2, and the modelling of broadband data is described in Sect. 3. After the presentation of our results in Sect. 4, we discuss them in Sect. 5, and finally we give our conclusions in Sect. 6.

In this paper, we assume ΛCDM cosmological parameters of $\Omega_m = 0.32$, $\Omega_\Lambda = 0.68$, and $H_0 = 67$ km s^{-1} Mpc^{-1} (Planck Collaboration VI 2020). We adopt the convention $F_\nu \propto t^\alpha \nu^\beta$ as adopted by GS02, where α and β indicate the temporal decay index and the spectral index, respectively; we report the uncertainties at a 1σ confidence level unless stated otherwise.

2. Observations and data reduction

GRB 160131A was discovered by the *Neil Gehrels Swift* Observatory (Gehrels et al. 2004) on January 16 at 08:20:31 UT, 2016 (Page & Barthelmy 2016). Discovered at redshift $z = 0.972$ (Malesani et al. 2016; de Ugarte Postigo et al. 2016a), this very long GRB with $T_{90} = 325 \pm 72$ s (Cummings et al. 2016) has an isotropic-equivalent $E_{\gamma,\mathrm{iso}} = (8.3 \pm 0.7) \times 10^{53}$ erg in the 0.02−15 MeV range (Tsvetkova et al. 2016). Prompt gamma-ray polarimetric measurements in the 100−300 keV band indicated that GRB 160131A is possibly highly polarised (94 ± 33%, although the confidence level is $<3\sigma$, Chattopadhyay et al. 2019): this suggests that the GRB is due to synchrotron emission within a time-independent, ordered magnetic field (Nakar et al. 2003; Granot & Königl 2003; Waxman 2003), with an initial bulk Lorentz factor of $\Gamma_0 = 460 \pm 50$ and jet half-opening angle of $\theta_j = 3^{+3}_{-1.8}$ degrees, calculated from the jet breaks observed in *Swift*/XRT X-ray light curves[5] (Sari 1999; Frail et al. 2001). This constraint on θ_j corresponds to a beaming-corrected isotropic energy in the γ-ray band of $E_\gamma = E_{\gamma,iso}(1 - \cos\theta_j) = 6.0^{1.8}_{-0.5} \times 10^{51}$ erg (Chattopadhyay et al. 2019). The study of the inhomogeneities in the optical light curves of GRB afterglows of Mazaeva et al. (2018) shows that the early ($\lesssim$0.5 d) optical afterglow of GRB 160131A is characterised by a broken power law with small-scale deviations (wiggles), followed a steep decay, suggestive of a jet break at $t_j = 1.2 \pm 0.3$ d.

2.1. X-ray observations with Swift/XRT

Swift/XRT observed the region of GRB 160131A in window timing (WT) mode from 60 to 595 s and in photon counting (PC) from 3820 s to 9 d after the BAT trigger and found a bright, uncatalogued X-ray source located at $\alpha = 5^{\mathrm{h}}12^{\mathrm{m}}40.31^{\mathrm{s}}$, $\delta = -7°02'59''.4$ (J2000), with an uncertainty of 1.4 arcsec (radius, 90% containment)[6]. We obtained the observed 0.3–10 keV light curve from the Leicester University repository[7], based on the time-averaged spectrum with a count-to-flux conversion factor of 3.55×10^{-11} erg cm^{-2} count^{-1} (observed flux), and binned it by imposing a minimum significance of 3σ per bin. The lack of evidence for a significant spectral evolution in the PC data justifies the adoption of a constant count-to-flux ratio. We extracted the

[1] http://www.gmrt.ncra.tifr.res.in/
[2] https://science.nrao.edu/facilities/vla
[3] https://www.astro.phy.cam.ac.uk/research/research-projects/AMI
[4] http://iram-institute.org/EN/noema-project.php
[5] http://www.swift.ac.uk/xrt_curves/
[6] https://www.swift.ac.uk/xrt_positions/00672236/
[7] https://www.swift.ac.uk/xrt_curves/00672236/

time-averaged spectrum (4.0–131 ks) using the Leicester web interface (Evans et al. 2009) based on HEASOFT (v6.22). We then grouped energy channels with the GRPPHA tool so as to ensure at least 20 counts per bin. The spectrum is well modelled by a highly absorbed power law using the XSPEC model TBABS * ZTBABS * POWERLAW, where the Galactic term was fixed to $N_{H,\rm gal} = 1.15 \times 10^{21}$ cm^{-2} corresponding to the GRB direction (Willingale et al. 2013)[8] and the redshift was fixed to $z = 0.972$. The best-fit photon index was $\Gamma_X = 2.04 \pm 0.06$ and the source-frame (intrinsic) hydrogen column $N_{H,\rm int} = (5.0\pm0.1)\times10^{21}$ cm^{-2} (χ^2/d.o.f. = 171/178). We determined the instantaneous reference epoch for the XRT spectrum as follows: we preliminarily noticed that the light curve in the interested time interval can be modelled with a simple power law $\propto t^{-\alpha_x}$ with $\alpha_x \simeq 1.2$. Given that the observational coverage within this time window is reasonably uniform, the reference time t_x was found by demanding that the instantaneous flux at t_x be equal to the observed time-averaged one between $t_1 = 4$ and $t_2 = 131$ ks:

$$t_x \;=\; \Big[\frac{1}{\alpha_x - 1}\,\Big(\frac{t_1^{1-\alpha_x} - t_2^{1-\alpha_x}}{t_2 - t_1}\Big)\Big]^{-1/\alpha_x} \;=\; 33\ \text{ks}\,. \tag{1}$$

We followed a similar line of reasoning to find the reference energy for the 0.3–10 keV average flux density light curve: using the two energy boundaries, $E_1 = 0.3$ and $E_2 = 10$ keV, and the power-law index $\Gamma_X = 2.04$, we calculated the energy E_x at which the flux density is equal to the corresponding average flux density, finding $E_x = 2.75$ keV (6.65×10^{17} Hz). This value is hereafter used as the reference energy for the average flux density light curve. We list the full table of X-ray data in Table A.1.

2.2. UVOIR observations

The *Swift*/XRT UltraViolet and Optical Telescope (UVOT; Roming et al. 2005) observed the region of GRB 160131A from 78 s to ∼ 6 d and found a source located at $\alpha = 5^{\rm h}12^{\rm m}40.34^{\rm s}$, $\delta = -7°02'59''.1$, with an uncertainty of 0.61 arcsec (radius, 90% containment). This position is 7.5 arcsec from the centre of the XRT error circle. We analysed the UV band data using HEASOFT (v. 6.22)[9], the dedicated software package for optical/X-ray astronomical spectral, timing, and imaging data analysis. In particular, data were analysed for the six filters, *v, b, u, w1, w2* and *m2*, for which we extracted aperture photometry using a source region radius of 5″, following the prescriptions by Brown et al. (2009) and Breeveld et al. (2011). Flux measurements with $S/N < 3\sigma$ were replaced with the corresponding 3σ upper limits.

In the optical and near-infrared bands, GRB 160131A was first observed in the Pan-STARRS *g', r', i', z', Y* filters with the 2m Faulkes Telescope North (FTN; Guidorzi et al. 2016) soon followed by the 2m Faulkes Telescope South (FTS) and a 1m unit in Siding Springs, all of which are operated by Las Cumbres Observatory Global Network (LCOGT; Brown et al. 2013), starting from ∼74 minutes to 6.6 days (under proposal ARI2015A-001, PI: Kobayashi). We used the Spectral Camera (FOV 10.5′ × 10.5′, resolution of 0.304″ pixel^{-1}) for the 2m units, and the Sinistro Camera (FOV 26.5′ × 26.5′, resolution of 0.467″ pixel^{-1}) for the 1m unit. Individual exposures vary from a minimum of 30 s up to 120 s. Bias and flat-field corrections were applied using the specific LCOGT pipeline (Brown et al. 2013). From February 3 to 6, 2016, we also used the 2m Liverpool Telescope (LT; Steele et al. 2004; Guidorzi et al. 2006) at the Observatorio del Roque de Los Muchachos (Canary Islands) and observed with the IO:O Camera (FOV 10′ × 10′, with a 2×2 binning, which corresponds to a resolution of 0.30″ pixel^{-1}) within the AB r' and i' filters. Bias and flat-field corrections were automatically applied using the LT pipeline.

The afterglow magnitudes were obtained through PSF-fitting photometry after calibrating the zero-points with a dozen nearby Pan-STARRS catalogue stars[10] using the mean PSF AB magnitudes for the corresponding filters (Tonry et al. 2012). Filter-dependent systematic errors due to the zero-point scatter of the calibrating stars were added to the statistical uncertainties of magnitudes, with the following average values in magnitude units: 0.02, 0.01, 0.04, 0.02, and 0.02 for the *g', r', i', z'*, and *Y* filters, respectively. The obtained calibrated magnitudes were corrected for the Galactic extinction along the line of sight of $E_{\rm B-V} = 0.09$ mag[11] (Schlafly & Finkbeiner 2011), and converted to flux densities (Fukugita et al. 1996). The full table of UVOIR data is available in Table A.2.

2.3. Radio/mm observations

Followup observations with the VLA were carried out from February 1 to May 27, 2016, from ∼1 to ∼117 d post explosion (Laskar et al. 2016b; Laskar 2016) under large Proposal VLA/15A-235 (PI: Berger)[12]. Data were taken in five spectral windows at *C*-band (with baseband central frequency of 6 GHz), *X*-band (10 GHz), *Ku*-band (15 GHz), *K*-band (22.25 GHz), and *Ka*-band (33.25 GHz), with a nominal bandwidth of ∼0.4 GHz. 3C48 and J0522+0113 were used as flux/bandpass and phase/amplitude calibrators, respectively. To eventually observe multi-component behaviour in radio data, we split each radio band into eight parts, from 4.6 to 37.4 GHz, resulting in ∼300 VLA flux densities. The Common Astronomy Software Application (CASA, v. 5.1.1-4, McMullin et al. 2007)[13] was used to calibrate, flag, and image the data. Images were formed from the visibility data using the CLEAN algorithm (Högbom 1974). The image size was set to (240×240) pixels, the pixel size was determined as one-fifth of the nominal beam width and the images were cleaned using natural weighting. We also considered six observations (mainly upper limits) from GMRT (Chandra & Nayana 2016a,b), AMI-LA (Mooley et al. 2016), and NOEMA (de Ugarte Postigo et al. 2016b). The upper limits on the flux densities were calculated at a 3σ confidence level. All the 300 radio/mm flux densities are reported in Table A.3.

3. Data modelling

We analyse the broadband observations in the context of synchrotron emission arising from relativistic shocks, following the standard afterglow model described by GS02. The observed spectral energy distribution (SED) of each synchrotron component is described by three break frequencies (the characteristic frequency, ν_m, the cooling frequency, $\nu_{\rm c}$, and the self-absorption frequency, $\nu_{\rm sa}$), and the flux density normalisation,

[8] Derived using https://www.swift.ac.uk/analysis/nhtot/, taking the value $N_{H,\rm tot}$.
[9] https://heasarc.gsfc.nasa.gov/lheasoft/download.html
[10] https://panstarrs.stsci.edu/
[11] We assumed the following extinctions in mag units: $A_{m2} = 0.90$, $A_{w2} = 0.79$, $A_{w1} = 0.64$, $A_u = 0.47$, $A_b = 0.39$, $A_v = 0.30$, $A_{g'} = 0.36$, $A_{r'} = 0.25$, $A_{i'} = 0.18$ mag, $A_{z'} = 0.14$, and $A_Y = 0.12$.
[12] https://science.nrao.edu/science/science-program/large-proposals
[13] https://casa.nrao.edu/

$F_{\nu,m}$. Depending on the order of ν_m and ν_c, the synchrotron spectrum falls into two broad categories: fast-cooling regime ($\nu_m > \nu_c$), where all the less energetic electrons cool rapidly, and slow-cooling ($\nu_m < \nu_c$) regime, where only the most energetic electrons cool rapidly (e.g. GS02, Sari et al. 1998; Gao et al. 2013a). The prompt phase of GRBs is expected to be in the fast-cooling regime (Piran 1999), whereas the transition to the slow-cooling regime is expected to take place during the early stages of the afterglow (Meszaros & Rees 1997; Waxman 1997, GS02). During the afterglow phase, $\nu_{\rm sa}$ is usually the smallest among the three frequencies. When $\nu_{\rm sa} > \nu_c$, the electron energy distribution may be significantly modified, resulting in inaccurate analytical models (Gao et al. 2013a).

The richness of our broadband data set allows us to use a modelling strategy that combines two approaches to model the GRB afterglow emission: an empirical approach (Sect. 3.1), and a physical approach (Sect. 3.2). In the empirical approach, we modelled SEDs (for each observing epoch) and light curves (for each observing frequency) with simple empirical functions; later, we analysed the best-fit results comparing them with the standard afterglow model (described by GS02), and the jet emission (e.g. Panaitescu et al. 1998; Rhoads 1999; Sari et al. 1999; Panaitescu & Kumar 2002; Sari 2006; Granot 2007). This approach allows us to constrain the behaviour of the GRB afterglow emission – in terms of the main observational features (breaking frequencies and possible jet break time) and the kind of CBM (ISM-like vs. wind-like) – and then to apply the physical approach, where we modelled the data set of the GRB afterglow emission through a sophisticated, fully self-consistent modelling code developed in Python, called SAGA (Software for AfterGlow Analysis), which is briefly described in Sect. 3.2.

3.1. Empirical approach

We start by adopting empirical functions for both SEDs and light curves in the optical/X-ray domain (Sect. 4.2). Analysis of the radio data set (Sect. 4.3) allows us to better constrain the information inferred from the optical/X-ray analysis. We assumed three kind of empirical functions, reported here for completeness:

– Single power law (SPL):

$$F_x = F_0\left(\frac{x}{x_0}\right)^{\gamma}, \tag{2}$$

where F_0 is the flux density at the reference parameter x ($x \equiv \nu$ with $x_0 \equiv \nu_0 = 1$ GHz for SEDs, and $x \equiv t$ with $x_0 \equiv t_0 = 1$ d for the light curves). The slope index is γ, which corresponds to the spectral index β for SEDs and the decay index α for the light curves.

– Broken power-law (BPL):

$$F_{x,1b} = \begin{cases} F_b\left[\frac{1}{2}\left(\frac{x}{x_{b,1}}\right)^{-s\gamma_1} + \frac{1}{2}\left(\frac{x}{x_{b,1}}\right)^{-s\gamma_2}\right]^{-1/s} & \gamma_1 \geq \gamma_2 \\ F_b\left[\frac{1}{2}\left(\frac{x}{x_{b,1}}\right)^{s\gamma_1} + \frac{1}{2}\left(\frac{x}{x_{b,1}}\right)^{s\gamma_2}\right]^{1/s} & \gamma_1 < \gamma_2, \end{cases} \tag{3}$$

where $F_{b,1}$ is the flux density at the reference break parameter $x_{b,1}$, corresponding to the break frequency ν_b for SEDs and the break time t_b for the light curves, s is the sharpness factor (we fixed $s = 5$), and γ_1 and γ_2 are the slope indices before and after x_b, corresponding to the spectral index β for SEDs and the decay index α for the light curves.

– Double broken power-law (DBPL):

$$F_{x,2b} = \begin{cases} F_{x,1b} \times \left[1 + \left(\frac{x}{x_{b,2}}\right)^{w(\gamma_2-\gamma_3)}\right]^{-1/w} & \gamma_2 \geq \gamma_3 \\ F_{x,1b} \times \left[1 + \left(\frac{x}{x_{b,2}}\right)^{w(\gamma_3-\gamma_2)}\right]^{1/w} & \gamma_3 < \gamma_2, \end{cases} \tag{4}$$

where s and w are the sharpness factors (we fixed $s = w = 5$); γ_1, γ_2, and γ_3 are the slope indices among the break parameters $x_{b,1}$ and $x_{b,2}$, corresponding to the spectral index β for SEDs and the decay index α for the light curves.

3.2. Physical approach with SAGA

Once we estimated the main observational features of the GRB afterglow, we modelled the data through SAGA. Built adopting Bayesian statistics (e.g. Sharma 2017; Marquette 2018), our code joins other pre-existing fitting tools in the literature (e.g. Kobayashi et al. 1999; Daigne & Mochkovitch 2000; Cannizzo et al. 2004; Zhang & MacFadyen 2009; van Eerten et al. 2010a; Wygoda et al. 2011; De Colle et al. 2012; Laskar et al. 2013; Leventis et al. 2013; Rhodes et al. 2020; Aksulu et al. 2020; Ryan et al. 2020; Ayache et al. 2022) and provides an independent check, emphasising the broadband study of GRB afterglows over the last two decades. SAGA performs a simultaneous broadband data analysis –from radio to gamma-rays frequencies– in a single iteration through a new approach that consists in the manipulation of all the data, both at each observing epoch $t_{\rm obs}$ and observing frequency $\nu_{\rm obs}$, considering the different radiation processes and other aspects that are briefly described in this section. This approach allows us to simultaneously estimate the micro-physics parameters of the afterglow and other physical information (the complete parameter space is listed in Table 1).

SAGA models the data using the smoothly connected power-law synchrotron spectra for the FS (GS02, and the references therein), computing the break frequencies and normalisations as a function of the shock micro-physics parameters: the kinetic energy of the explosion ($E_{K,\rm iso}$), the CBM density (n_0 for ISM-like CBM; the normalised mass-loss rate A_* for wind-like CBM), the power-law index of the electron energy distribution (p), the fractions of the blastwave energy delivered to relativistic electrons ($\epsilon_{\rm e}$), and magnetic fields ($\epsilon_{\rm B}$). In addition to this standard model, SAGA considers the inverse Compton (IC) radiation process by computing the Compton y-parameter from the FS parameters, thereby scaling the spectral break frequencies and flux densities of the synchrotron spectrum by the appropriate powers of $1 + y$ (Sari & Esin 2001; Zhang et al. 2007; Laskar et al. 2014, GS02); if $y < 1$, the IC regime can be neglected, otherwise a high-energy component (of the order of 10 MeV) appears in the spectrum and the cooling timescale is shortened by a factor y (Sari & Esin 2001; Piran 2004).

Moreover, SAGA assumes the following:

The uniform jet regime (e.g. Granot 2007; Zhang 2019)[14]. This is based on purely geometrical or dynamical effects, and assumes a simplified conical jet blastwave with a half opening angle θ_j and blastwave Lorentz factor Γ, where only the emission inside the $1/\Gamma$ cone is detectable due to relativistic beaming. During the deceleration phase, Γ decreases gradually until $1/\Gamma > \theta_j$

[14] This jet regime is simpler than structured jet model, that assumes an angular distribution in energy and Lorentz factor, based on special relativistic hydrodynamics (e.g. De Colle et al. 2012; Granot et al. 2018; Coughlin & Begelman 2020), and other more complex regimes (e.g. Huang et al. 2004; Peng et al. 2005; Wu et al. 2005; Granot et al. 2018).

Table 1. Free parameter space available for the SAGA analysis, with relative range of definition.

Parameter	Unit	Description	Parameter space
p	–	Power-law index of the electron energy distribution	1.5 – 3.5
ϵ_e	–	Fraction of the blastwave energy delivered to relativistic electrons	0 – 1/3
ϵ_B	–	Fraction of the blastwave energy delivered to magnetic fields	0 – 1/3
$E_{K,\mathrm{iso},52}$	10^{52} erg	Kinetic energy of the explosion (in units of 10^{52} erg)	10^{-2} – 10^3
n_0	cm^{-3}	Density for ISM-like CBM	10^{-3} – 10^2
A_*	5×10^{11} g cm^{-1}	Parameter connected with the wind-like density CBM	10^{-3} – 10^2
A_V	mag	Extinction in the host galaxy	0 – 10
t_j	d	Jet break time	According to the case
$t_{ei,1}$	d	Start time of the first injection	According to the case
$t_{ei,2}$	d	Start time of the second injection	According to the case
m	–	Injection index	0 – 3 (ISM), 0 – 1 (wind)
m_2	–	Injection index (in case of two bumps during the energy injection regime)	0 – 3 (ISM), 0 – 1 (wind)

– for an observer in the line-of-sight of the jet – followed by an achromatic break in the light curve, at the jet break time t_j, measured both for ISM-like and wind-like CBM (see Waxman 1997; Rhoads 1999; Sari et al. 1999; Chevalier & Li 2000; Wang et al. 2018). The light curve steepening can arise from two effects: the pure edge effect (e.g. Panaitescu et al. 1998; Granot 2007) and the sideways expansion effect (e.g. Rhoads 1999; Sari et al. 1999). In the pure edge effect, the blastwave dynamics does not change during the jet break transition, and hence the deceleration rate/dynamics of the jet (such as the breaking frequencies) is the same with the spherical blastwave. On the other hand, the sideways expansion effect of a conical jet implies that the conical jet exponentially decelerates; this feature translates to a change of the evolution of both the spectral break frequencies and flux densities at t_j. SAGA considers the uniform jet regime based on selection by the user (before launching the analysis) between the pure edge effect and the sideways expansion, through the modification of the evolution of the spectral break frequencies and flux densities at t_j (Sari et al. 1999; Panaitescu & Kumar 2002; Sari 2006; Granot 2007, GS02), smoothing over the transition with a fixed smoothing parameter (s = 5, Granot et al. 2001).

The effect of non-relativistic/Newtonian (NR) ejecta (e.g. Wijers et al. 1997; Zhang 2019). This is reached at the transition times t_{NR} (Waxman 1997 for ISM-like CBM, and Chevalier & Li 2000 for wind-like CBM) when the relativistic blastwave, decelerated by the interaction with the CBM, is characterised by a bulk Lorentz factor $\gamma < \sqrt{2}$. Usually, this regime takes place on timescales of months or years (e.g. Livio & Waxman 2000; Zhang & MacFadyen 2009), when the electrons should be in the slow-cooling scenario ($\nu_m < \nu_c$). SAGA accounts for the NR regime modifying the evolution of the spectral break frequencies and flux densities at t_{NR} (Frail et al. 2000a; van Eerten et al. 2010b; Leventis et al. 2012), smoothing over the transition with a fixed smoothing parameter (s = 5, Granot et al. 2001).

The energy injection into the blastwave shock (e.g. Zhang & Mészáros 2002; Granot & Kumar 2006; Gao et al. 2013b). This is observed as one (or more) plateau or flattening in the light curves of GRB afterglows (e.g. Nousek et al. 2006; Liang et al. 2007; Margutti et al. 2010a; Hascoët et al. 2012). In general, the blastwave is fed by a long-lasting Poynting-flux-dominated wind defined by the power-law decay $L(t) = L_0\left(\frac{t}{t_0}\right)^{-q}$, where t is the central engine time (corresponding to the observer time of GRB afterglow), L_0 is the luminosity at the reference time t_0, and $q \geq 0$[15]; this corresponds to the temporal evolution of the blastwave energy $E \propto t^{1-q} = t^m$, where $m = 1 - q$ is the 'injection index'. In the absence of energy injection, the standard hydrodynamic evolution requires that $m = 0$, $s = 1$, or $q = 1$ in the above expressions (e.g. Gao et al. 2013a). SAGA accounts for the fact that energy injection continuously adjusts the content –in the time interval where this phenomenon takes place (between $t_{ei,i}$ and $t_{ei,f}$)– of the kinetic energy in the standard afterglow regime ($E_{k,\mathrm{iso}}(t)$, e.g. GS02) according to broken power-law functions described in Laskar et al. 2015.

The interstellar scintillation effect (ISS). This is caused by inhomogeneities in the electron density distribution in the Milky Way along the GRB line of sight, which are observable through variations in measured flux density of the source at low frequencies ($\lesssim$10 GHz) of radio domain (Rickett 1990; Goodman 1997; Walker 1998; Frail et al. 1997, 2000a; Goodman & Narayan 2006; Granot & van der Horst 2014; Misra et al. 2021); SAGA accounts for the ISS effect following the prescription described in Goodman & Narayan (2006) and Laskar et al. (2014, hereafter L14) to compute the modulation index m_{scint} (defined as the rms of the fractional flux density variation) and the model-predicted flux density F_{model} in the expected ISS contribution.

The dust extinction in the host galaxy along the sightline. This is achieved by adopting the extinction curves of Pei (1992), modelled using Milky Way (MW), or the dust models for the Small and Large Magellan Clouds (SMC and LMC, respectively), to determine the extinction A_V, measured in the V band.

The UV absorption by neutral hydrogen (from $z \gtrsim 1$). sAGa uses a sight-line-averaged model for the optical depth of the intergalactic medium (IGM) as described by Madau (1995) to compute the IGM transmission as a function of wavelength at the redshift of the GRB.

The photoelectric absorption for X-ray data. This is achieved through the related hydrogen-equivalent column density N_{H} (in units of 10^{22} cm^{-2}), obtained by a polynomial fit of the effective absorption cross-section per hydrogen atom as a function of energy in the 0.03–10 keV range assuming a given abundance pattern (Morrison & McCammon 1983).

[15] The same approach is sometimes based on $L(t) = L_0(t/t_0)^q$ and $q \leq 0$ (e.g. Misra et al. 2007; Marshall et al. 2011; van Eerten 2014; Laskar et al. 2015).

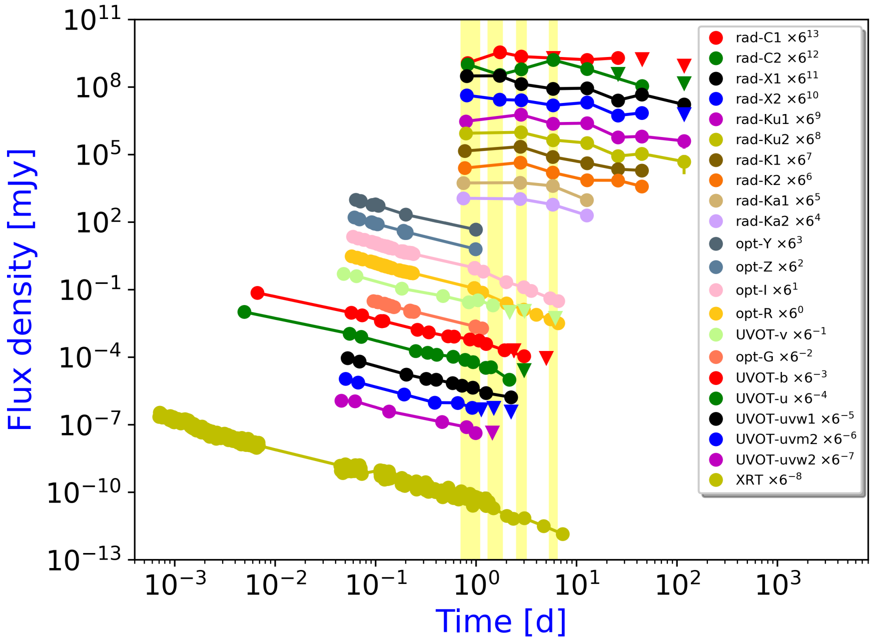

Fig. 1. GRB 160131A light curves from radio to X-rays. Yellow shaded areas show the time intervals (centred to 0.8 d, 1.7 d, 2.7 d, and 5.8 d) where SEDs have been empirically analysed. Filled circles indicate detections (uncertainties are smaller than the corresponding symbol sizes), which are connected with each other through a segment, and upside down triangles indicate 3σ upper limits.

In SAGA, the best-fit solution is calculated through the maximisation of a likelihood function, using a Gaussian error model, which is described in L14. The Bayesian approach adopted for the broadband modelling in SAGA is performed through the Python EMCEE package[16] (Foreman-Mackey et al. 2013), based on the Markov chain Monte Carlo (MCMC) analysis; this tool allows the user to estimate uncertainties and correlations between the model parameters, and is particularly useful in high-dimensional problems like that presented here. These parameters are constrained through the definition of prior distributions that encode preliminary and general information. SAGA considers (1) uniform priors for the parameters that describe the exponential terms on the flux densities (A_V) and the power-law indices (p and the injection index m), and (2) Jeffreys priors (Jeffreys 1946), for the parameters that span different orders of magnitude ($E_{K,\mathrm{iso}}$, n_0, A_*, ϵ_e, ϵ_B and t_j). ϵ_e and ϵ_B are currently believed to be of the order of a few percent to tens of percent by energy (Sironi et al. 2013); as generally they do not exceed their equipartition values of 1/3 (e.g. L14)[17], the priors for these parameters are truncated at an upper bound of 1/3. These parameters are constrained through the parameter space derived from accurate modelling of the broadband GRB afterglows (e.g., Schulze et al. 2011; Laskar et al. 2013, 2016a; Santana et al. 2014; Perley et al. 2014; Sironi et al. 2015), and are reported in Table 1.

SAGA has been successfully tested on the broadband data of the afterglows of GRB 120521C, GRB 090423, and GRB 050904, where the results obtained with SAGA are consistent with those reported in the literature (especially in L14 who make use of a similar approach for the characterisation of the GRB afterglow) within $\lesssim 2\sigma$. We report a more detailed description – test phase included – of this Python package in a specific technical note (Marongiu & Guidorzi 2021).

[16] https://emcee.readthedocs.io/en/stable/

[17] This consists in the equal distribution of the internal energy among the magnetic field, the accelerated electrons, and the baryons (protons/neutrons).

4. Results

4.1. Preliminary SED analysis

From the multi-frequency light curves (from radio to X-rays) displayed in Fig. 1, we extract SEDs at four time intervals (centred to 0.8, 1.7, 2.7, and 5.8 d), characterised by a richness of broadband data.

To investigate the relation between radio and optical/X-rays, we linearly (in a log–log plot) interpolated data (Fig. 2, red points) at those epochs, where needed.

The high-energy side of the SEDs (Fig. 2) is well-fitted by a power law with a mean value of $\beta_{he} = -1.09 \pm 0.04$[18], corresponding to a photon index $\Gamma = 1 - \beta_{he} = 2.09 \pm 0.04$, compatible with Γ_X obtained from XRT data (Sect. 2.1). This constrains the behaviour of the break frequencies (especially ν_c and ν_m), as well as the possible jet break, the time evolution of the blastwave, and the kind of environment (ISM vs. wind).

4.2. Optical/X-ray data set: $\nu_m - \nu_c$ location, CBM density profile, and jet break

As we can see in Fig. 3, the optical/X-ray fluxes decay with temporal index $\alpha_{he} \sim -1.25$ up to ~0.1 d, followed by a plateau (more pronounced in the optical data) in the temporal range ~0.1–0.8 d ($\alpha_{X,ei} \sim -1$), possibly suggesting energy injection (Sect. 5.1); after the plateau, the flux decay steepens to $\alpha_{he} \sim -1.8$ and can be interpreted in terms of a jet break (Sect. 4.3.2).

In the context of the standard afterglow model, the absence of any break frequencies between optical and X-ray domains suggests that ν_m and ν_c must lie either below or above the optical/X-ray frequencies $\nu_{\mathrm{opt},X}$ at the first epoch of observations $t_{\mathrm{obs},0}$ (~10^{-3} d). In the following, we explore the different possibilities:

Fast cooling regime. $\nu_{\mathrm{opt},X} < \nu_c < \nu_m$ is incompatible with this regime because the optical/X-ray spectra are expected to show only positive values of β ($1/3 \lesssim \beta \lesssim 2$ for any possible spectrum). Moreover, $\nu_c < \nu_{\mathrm{opt},X} < \nu_m$ is incompatible with

[18] This value was obtained whilst neglecting (only in this specific case) the data in the range 10^{15}–10^{16} Hz, heavily affected by dust extinction.

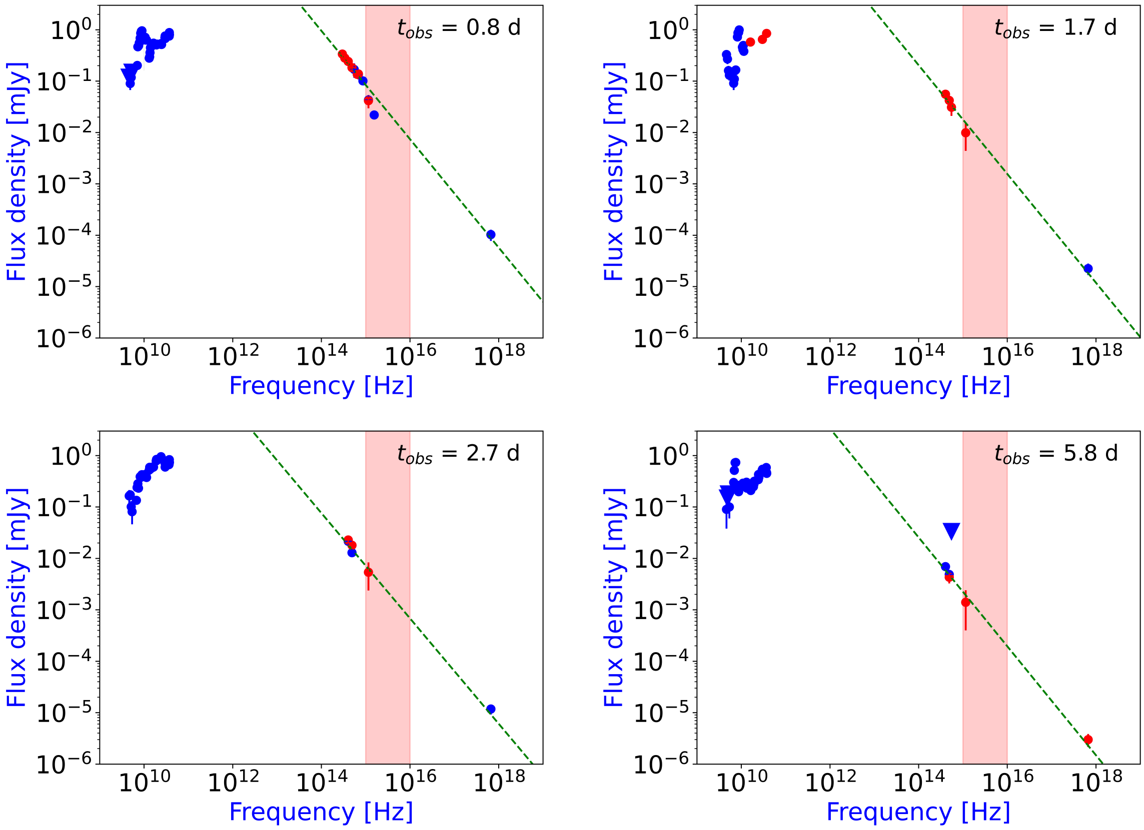

Fig. 2. Broadband SEDs of GRB 160131A at 0.8 d (*top left*), 1.7 d (*top right*), 2.7 d (*bottom left*), and 5.8 d (*bottom right*). Blue (red) points are measured (linearly interpolated in a log-log plot) data. These SEDs display radio peaks (at 0.8 d, 1.7 d, and 5.8 d) and dust extinction (red shaded regions, especially at 0.8 d). The green dashed line shows the resulting modelling of the high-energy data (optical/X-ray). Filled circles indicate detections, and upside-down triangles indicate 3σ upper limits.

this regime because the optical/X-ray spectra are expected to show $\beta \sim -0.5$ instead of the observed $\beta_{he} = -1.08$. Finally, the case where $\nu_c < \nu_m < \nu_{\mathrm{opt},X}$ is compatible with the fast-cooling regime because, following the indices α and β calculated for different spectral regimes in GS02, it requires an electron energy index of $p = -2\beta_{he} \sim 2.18$ and a decay rate of $\alpha = (2-3p)/4 \sim -1.14$ (regardless of the CBM), compatible with α_{he}; this suggests that ν_m is just below optical frequencies at $t_{\mathrm{obs},0}$.

Slow cooling regime. $\nu_{\mathrm{opt},X} < \nu_m < \nu_c$ is incompatible with this regime because the optical/X-ray spectra are expected to show only positive values of β ($1/3 \lesssim \beta \lesssim 2$ for any possible spectrum). Moreover, $\nu_m < \nu_{\mathrm{opt},X} < \nu_c$ is incompatible with this regime because it requires $p = 1-2\beta_{he} \sim 3.18$ and $\alpha \sim -1.64$ for an ISM-like CBM ($\alpha \sim -2.14$ for a wind-like CBM) in GS02, which is too steep for real light curves. Finally, the case where $\nu_m < \nu_c < \nu_{\mathrm{opt},X}$ is compatible with the slow-cooling regime, because it requires $p = -2\beta_{he} \sim 2.18$ and $\alpha = (2-3p)/4 \sim -1.14$ (the same regime as the fast-cooling case), suggesting that ν_m is well below optical frequencies at $t_{\mathrm{obs},0}$.

This picture constrains ν_m and ν_c below $\nu_{\mathrm{opt}} = 3 \times 10^{14}$ Hz at $t_{\mathrm{obs},0}$. Moreover, the absence of any break in these light curves until ~0.1 d (after which energy injection and jet break occur) suggests a decreasing evolution of ν_c, which favours an ISM-like CBM over a wind-like CBM in the standard afterglow model.

From the upper limit on ν_{opt} and using the temporal scaling for both ν_m ($t^{-3/2}$) and ν_c ($t^{-1/2}$ for ISM), we constrain the passage of ν_m and ν_c in the radio frequencies. The passage of ν_m is constrained in *Ka*-band at $t_{\mathrm{obs}} < 2.1$ d, in *K*-band at $t_{\mathrm{obs}} < 2.8$ d, in *Ku*-band at $t_{\mathrm{obs}} < 3.6$ d, in *X*-band at $t_{\mathrm{obs}} < 4.7$ d, and in *C*-band at $t_{\mathrm{obs}} < 6.7$ d. Moreover, ν_c is expected to cross the radio domain at late-time (*Ku*-band at $t_{\mathrm{obs}} < 4 \times 10^5$ d), and therefore be virtually unobservable.

Assuming the classical results by Sari et al. (1999), the decay of the light curve after the break ($t_j \sim 1$ d) is $-p$ for $\nu_m < \nu < \nu_c$ and $\nu > \nu_c$ (corresponding to our picture). This post-jet decay ($\alpha_{\mathrm{post},j} = -p \sim -2.2$) is steeper than expected for the optical/x-ray decay ($\alpha_{he} \sim -1.8$), and hence we assume a milder jet break model (pure edge effect, Sect. 3.2), characterised by a post-jet decay $\alpha_{\mathrm{post},j} = \alpha_{\mathrm{pre},j} - (3-k)/(4-k)$ (Granot 2007): assuming ISM-like CBM (and hence $k = 0$), we obtain $\alpha_{\mathrm{post},j} = -1.25 - 0.75 = -2$, which is compatible with the observed value ($\alpha \sim -1.8$).

In summary, the optical/X-ray data suggest that (1) the CBM is preferably described by ISM, (2) the transition between fast and slow cooling regime is not constrained by optical/X-ray observations, (3) $p \sim 2.2$, (4) both ν_m and ν_c lie below $\nu_{\mathrm{opt}} = 3 \times 10^{14}$ Hz already at $t_{\mathrm{post},0}$, and (5) a milder jet break model (pure edge effect) is in accordance with the optical/X-ray data. A more accurate identification of the break frequencies requires a comprehensive data analysis within a self-consistent broadband modelling (Sect. 4.4).

4.3. Data set from the Very Large Array

We analyse both the radio SEDs at each epoch from 0.8 d to 117 d and the light curves from 4.6 GHz to 37.4 GHz.

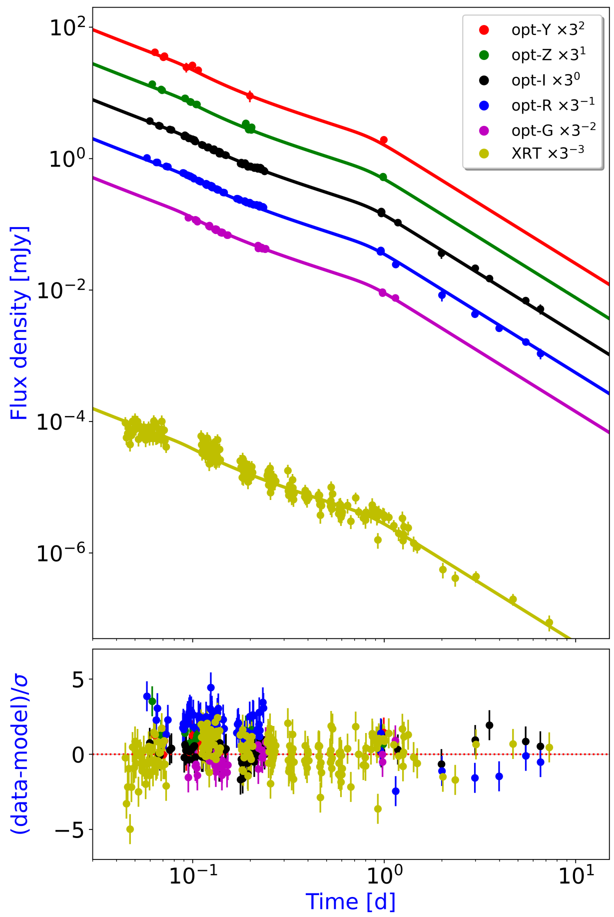

Fig. 3. Light curves for GRB 160131A of visible and X-ray data modelled with DBPL (Eq. (4)). We observe the plateau, probably ascribable to the energy injection between $\sim 10^4$ and $\sim 7\times10^4$ s ($\sim$0.1 and 0.8 d), and the achromatic break at $\sim 9\times10^4$ s ($\sim$1 d), typical of jetted emission. *Bottom panel*: residuals of the fit.

4.3.1. Radio SEDs: the $\nu_{\rm sa}$ location and the multi-component approach

One of the most impressive features in radio SEDs is the presence of spectral bumps or peaks at several epochs (Fig. 4, red circles). We preliminarily modelled these radio SEDs ignoring the peaks with either a power law or a broken power law (Fig. 4) in order to compare the resulting spectral indices with those expected from the synchrotron emission of GRB afterglows. We then analysed the radio SEDs including the whole data set in a multi-component approach (Fig. 5):

– 0.8 d radio SED. This SED shows a peak at $\sim$9 GHz and width $\Delta\nu \sim 2$ GHz (Fig. 4, top left). Neglecting this peak, this SED is described by a BPL (Eq. (3); Table 2). The constraints on ν_m described in Sect. 4.2 suggest that for this epoch $\nu_m < 150$ GHz; the comparison between the values of β shown in Table 2 and in Fig. 1 of GS02 suggests that $\nu_{\rm sa}$ crossed the radio band in the slow-cooling regime (scenario 1, $\nu_{\rm sa} < \nu_m < \nu_c$, GS02). Unfortunately, the presence of the extra-component peaking at ~ 9 GHz prevents us from better constraining $\nu_{\rm sa}$.

– 2.7 d radio SED. This SED is characterised by a broad peak at $\sim$25 GHz, which can be modelled with a BPL (Eq. (3); Fig. 4, top right; Table 2). The constraints described in Sect. 4.2 suggest that for this epoch $\nu_m < 22$ GHz. This SED is compatible with the slow-cooling regime (scenario 1, $\nu_{\rm sa} < \nu_m < \nu_c$, GS02): $\beta_{2,\rm bpl}$ in Table 2 is steeper than 1/3 for this regime, suggesting a probable proximity between $\nu_b \sim \nu_m$ and $\nu_{\rm sa}$.

– 5.8 d radio SED. This SED, characterised by a strong and narrow peak at $\sim$7 GHz, is modelled with a SPL (Eq. (2); Fig. 4, middle left; Table 2); for this epoch, $\nu_m < 7.3$ GHz (Sect. 4.2) suggests the slow-cooling regime, but the value of β is incompatible with regimes described in the standard afterglow model.

– 12.7 d radio SED. This SED, showing a peak at $\sim$7 GHz, can be modelled with a BPL (Eq. (3); Fig. 4, middle right; Table 2). At this epoch, we expect that $\nu_m < 2.3$ GHz (Sect. 4.2), and so this behaviour is compatible with the slow-cooling regime (scenario 2 of GS02, $\nu_m < \nu_{\rm sa} < \nu_c$), where $\nu_{\rm sa} = \nu_b, \beta_{1,\rm bpl} = 2.5$, and $\beta_{2,\rm bpl} = (1-p)/2$ (suggesting $p = 2.04 \pm 0.10$).

– 44.8 d radio SED. This SED is similar to the 12.7 d one, except that it is dimmer. It can be modelled with a BPL (Eq. (3); Fig. 4, bottom; Table 2). At this epoch, it is $\nu_m < 0.35$ GHz (Sect. 4.2), and therefore this behaviour could still be compatible with the slow-cooling regime (scenario 2), although $\beta_{2,\rm bpl}$ is steeper than expected; in this scenario, $\nu_{\rm sa} = \nu_b, \beta_{1,\rm bpl} = 2.5$, and $\beta_{2,\rm bpl} = (1-p)/2$ (suggesting $p = 2.1 \pm 0.6$).

The relatively large uncertainties on flux density in the SEDs at $\nu \lesssim 6$ GHz inevitably affect the ability to constrain $\nu_{\rm sa}$. Assuming $\nu_b \sim \nu_{\rm sa}$ in the radio SEDs at 0.8 d and 12.7 d (Table 2), we obtain that $\nu_{\rm sa}$ could evolve approximately as $t^{-0.1}$, with is compatible with $\nu_{\rm sa}$ being constant over time, as expected for the ISM (GS02).

Now including the peaks in the radio SEDs, we consider the whole radio data set in a multi-component approach. In addition to the continuum associated with FS emission (Sect. 4.3.1, hereafter component A), radio SEDs suggest a further two distinct emission components (Fig. 5).

Component B appears at four epochs (0.8, 1.7, 5.8, and 25.8 d) and is characterised by a faint peak around 9 GHz (Fig. 5). We fit this component with a BPL, obtaining the results shown in Table 3.

Component C shows up in the 25.8 d radio SED, and partially appears at 1.7 d (Fig. 5), when the lack of radio data at $\lesssim$5 GHz does not allow us to resolve its peak. We fit this component with a SPL (1.7 d) and a BPL (25.8 d), obtaining the results shown in Table 3.

In the multi-component approach, we briefly focus on the radio SED at 1.7 d (Fig. 5, top right), which is well-fitted by a combination of a SPL at $\lesssim$5 GHz (a possible part of the component C) and a BPL peaking at $\sim$9 GHz (component B, Table 3). As opposed to the other SEDs, the absence of data at high frequencies prevents us from constraining component A which is associated with the FS emission of GRB afterglow. In Fig. 5 (top right), we add the component A to a BPL characterised by the same spectral indices as those seen in the 0.8 d radio SED, and a flux density of 0.1 mJy (Table 3).

In summary, the radio SEDs suggest that (1) the slow-cooling regime occurs at $t \lesssim 0.8$ d, (2) at 5.8 d the features are incompatible with the standard GRB afterglow model, (3) at 12.7 d $\nu_{\rm sa} \sim 7$ GHz, and that (4) the radio data set is composed of three spectral components (A, B, and C), of which only the first one (A) is connected with a known physical effect (the continuum associated with FS emission). We explore these components further in Sect. 5.

4.3.2. Radio light curves: evidence for a jet

Radio data help to constrain both the FS emission and the jet opening angle. In this context we analysed the radio light curves

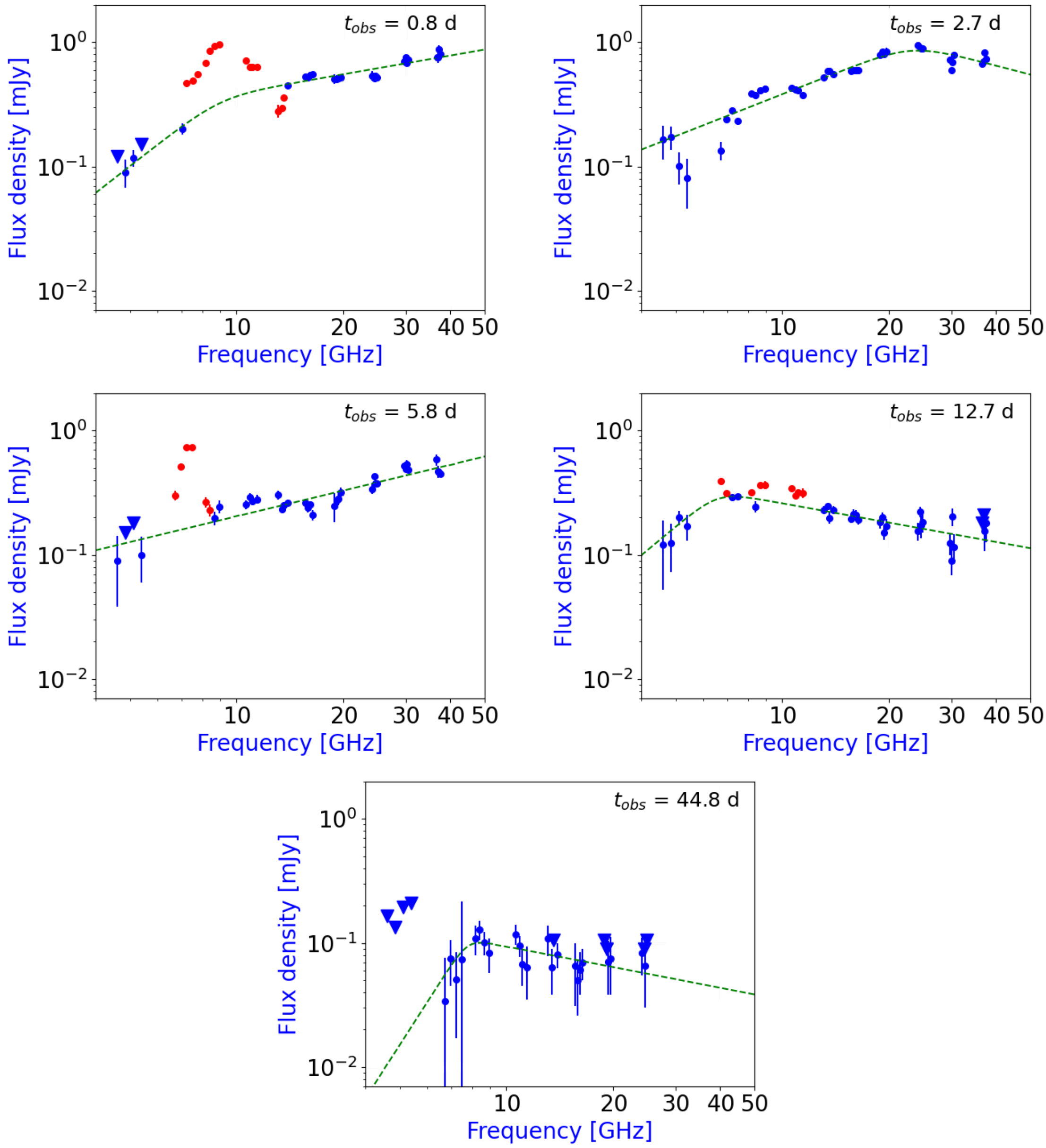

Fig. 4. Radio SEDs of GRB 160131A from 0.8 to 44.8 d. *Top left*: data together with a BPL (Eq. (3)) at 0.8 d; red points identify the bump and were ignored by the fit. *Top right*: radio SED at 2.7 d fitted with a BPL. *Middle left*: data together with an empirical SPL (Eq. (2)) at 5.8 d; red points identify the bump ~8 GHz and were ignored by the fit. *Middle right*: radio SED at 12.7 d fitted with a BPL. *Bottom*: data together with a BPL (Eq. (3)) at 44.8 d. Green dashed lines show the resulting modelling. Filled circles indicate detections, and upside-down triangles indicate 3σ upper limits.

whilst ignoring the peaks ascribed to additional components (Sect. 4.3.1) as well as data below 8 GHz because of the high variability, which is probably caused by strong ISS (Sects. 5.2 and 3.2), which prevents further constraint of the rise and decline rates.

In the standard afterglow model, a jet break arises at the time t_j when the bulk Lorentz factor Γ decreases below the inverse opening angle of the jet θ_j^{-1} and its edges become visible to an observer (Sect. 3.2). Once ν_m has crossed the observing frequency, the flux density decays steeply following a jet break. In this regime, the steepening in the radio light curves is expected to follow that of the steepening in the optical/X-ray light curves, depending on the time it takes for ν_m to cross the radio band (Laskar et al. 2015). The identification of $\nu_b \sim 23$ GHz with ν_m observed in the SED at $t_{\rm obs} = 2.7$ d (Fig. 4 and Table 2) indicates that the light curve at $\nu_{\rm obs} \sim \nu_b$ would peak at $t_{\rm obs}$. We observed this behaviour in the light curve at 24.6 GHz (Fig. 6, middle left), which is well fitted by a BPL (Eq. (3)); the best-fit results (Table 4) show that $\alpha_{2,\rm bpl}$ is also compatible with α_{he} obtained for optical/X-ray light curves (Sect. 4.2), and therefore with the passage of ν_m in the light curves of standard GRB afterglow model (Sari et al. 1998). The radio light curves above 24.6 GHz show a steep decay of the flux densities at t_b ranging between ~3 and ~5 d, compatible with jet break; modelling with BPL (Eq. (3)) shows $-0.1 \lesssim \alpha_1 \lesssim 0.1$ and $-2 \lesssim \alpha_2 \lesssim -1.6$ (Fig. 6, middle left and bottom; Table 4). At $t = t_j \sim 1$ d, as inferred from optical/X-ray light curves, ν_m lies close to $\sim 10^{11}$ GHz, which is well below the optical/X-ray domain. This is consistent

Table 2. Best-fit parameters obtained by empirically fitting the radio SEDs of GRB 160131A from 0.8 to 44.8 days after the GRB trigger (see Fig. 4).

$t_{\rm obs}$	0.8 d	2.7 d	5.8 d	12.7 d	44.8 d
Model	BPL	BPL	SPL	BPL	BPL
ν_b $^{(a)}$	8.9 ± 0.6	23.1 ± 0.5	–	6.6 ± 0.3	7.8 ± 0.3
F_b $^{(b)}$	0.32 ± 0.02	0.86 ± 0.10	–	0.32 ± 0.01	0.09 ± 0.01
β_{pl}	–	–	0.69 ± 0.04	–	–
$\beta_{1,\rm bpl}$	2.2 ± 0.4	1.13 ± 0.03	–	2.39 ± 0.34	4.46 ± 1.90
$\beta_{2,\rm bpl}$	0.50 ± 0.05	-0.75 ± 0.11	–	-0.52 ± 0.05	-0.55 ± 0.26
χ^2_r	0.79	1.60	1.27	0.74	0.88

Notes. "SPL" and "BPL" indicate a power-law (Eq. (2)) and a broken power-law model (Eq. (3)), respectively. ν_b is the break frequency and $F_{\rm b}$ the flux density at $\nu = \nu_b$; $\beta_{1,\rm bpl}$ and $\beta_{2,\rm bpl}$ are the two BPL spectral indices, while β_{pl} is the SPL index. The reduced chi square is denoted with χ^2_r. $^{(a)}$In units of GHz. $^{(b)}$In units of mJy.

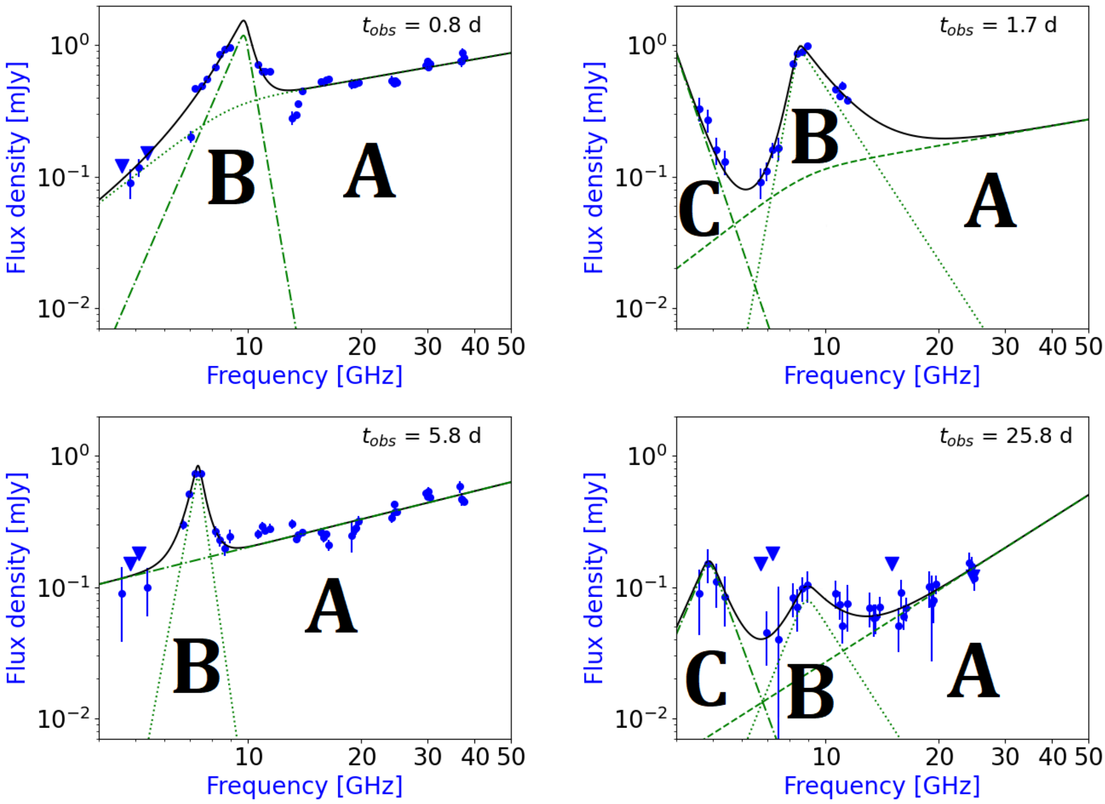

Fig. 5. Radio SEDs of GRB 160131A from 0.8 to 25.8 d in a multi-component approach. *Top left*: data together with the sum of two BPLs at 0.8 d. *Top right*: radio data at 1.7 d together with the sum of a SPL and two BPLs. *Bottom left*: data together with the sum of a SPL and a BPL at 5.8 d. *Bottom right*: radio SED at 25.8 d fitted with the sum of a SPL and two BPLs. Black lines show the resulting modelling, and green dash-dotted or dotted lines indicate each component. Filled circles indicate detections, and upside-down triangles indicate 3σ upper limits.

with the steep decline observed around the same epoch in these bands.

For completeness, we obtained further information about break frequencies of synchrotron emission from the decreasing temporal decay indices α in the light curves between 8 GHz and 24.6 GHz. In particular, the value $\alpha \sim -0.6$ (Table 4) obtained by modelling the light curves between 8 GHz and 14 GHz (Fig. 6, top left and top right) with a SPL (Eq. (2)) suggests that –in agreement with what was inferred from the high-energy data analysis (Sect. 4.2)– (1) ν_c crosses these frequencies after 45 d and (2) the passage of ν_m occurs at $t \lesssim 3$ d (Sari et al. 1998). Furthermore, the decreasing temporal indices in the light curves between 14 GHz and 24.6 GHz, evolving from ~ -0.8 at 14 GHz to ~ -1.2 at 24 GHz, are suggestive of the passage of ν_c in these light curves above ~120 d, and the passage of ν_m at these observing frequencies is very close to 3 d (Sari et al. 1998).

4.4. Physical approach: modelling with SAGA

The complexity of the broadband spectral and temporal properties, in particular the spectral radio peaks (Fig. 2), means that an iterative analysis (optical, optical/X-ray, optical/X-ray/radio) is necessary to probe the physical characteristics of the afterglow of GRB 160131A, and that the broadband model of GRB afterglow needs to be overseen in order to determine when it starts losing validity. We considered in this analysis a jetted

Table 3. Parameters for empirical fits to radio SEDs of GRB 160131A from 0.8 to 25.8 d in a multi-component approach (see Fig. 5).

t_{obs}	0.8 d	1.7 d	5.8 d	25.8 d
N_{comp}	2	3	2	3
Type	–	SPL (C?)	SPL (A?)	SPL (A)
β_{pl}	–	-9.9 ± 0.3	0.68 [(c)]	1.8 ± 0.4
Type	BPL (A)	BPL (A)	BPL (B)	BPL (C)
ν_{peak} [(a)]	8.9 [(c)]	8.9 [(c)]	7.4 ± 0.2	4.9 ± 0.1
F_{peak} [(b)]	0.32 [(c)]	0.1 [(c)]	0.68 ± 0.07	0.15 ± 0.01
$\beta_{1,bpl}$	2.2 [(c)]	2.2 [(c)]	15.5 ± 1.3	6.8 ± 0.2
$\beta_{2,bpl}$	0.5 [(c)]	0.5 [(c)]	-19.9 ± 2.0	-7.8 ± 0.2
Type	BPL (B)	BPL (B)	–	BPL (B)
ν_{peak} [(a)]	9.8 ± 0.5	8.5 ± 0.2	–	8.9 ± 0.5
F_{peak} [(b)]	1.2 ± 0.5	0.9 ± 0.1	–	0.08 ± 0.01
$\beta_{1,bpl}$	6.6 ± 0.3	15.8 ± 1.3	–	7.1 ± 1.2
$\beta_{2,bpl}$	-16.8 ± 1.8	-4.4 ± 0.2	–	-4.4 ± 1.2
χ_r^2	1.8	1.03	1.7	1.1

Notes. The letter in parentheses in the "Type" rows indicates the associated component. See the caption of Table 2 for a full description of the fit parameters. [(a)]In units of GHz. [(b)]In units of mJy. [(c)]Fixed.

(edge-regime) FS emission with dust extinction and energy injection in an ISM-like CBM; we also considered the ISS effect, which is typical of the radio domain, following the procedure described in Misra et al. (2021). The modelling ignored the data at $t_{obs} < T_{90} = 4 \times 10^{-3}$ d, where the prompt emission has not yet subsided.

From the analysis reported in Sects. 4.2 and 4.3, we adopted the following values as starting points for the micro-physics parameters (Sect. 3.2 and Table 1): $p = 2.2$, $\epsilon_B = 0.01$, $n_0 = 1$ cm^{-3}, $E_{k,\mathrm{iso},52} = 50$, $A_V = 0.1$, $t_j = 1$ d, and $m = 0.2$. Moreover, according to a method that has been used in the past to constrain ϵ_e through the identification of the radio peaks (observed in the radio light curves) connected with the passage of ν_m (Beniamini & van der Horst 2017), we used the peak (with a flux density $F \sim 0.9$ mJy) observed in the 24.6 GHz light curve at $t_{obs} \sim 3$ d (Sect. 4.3.2) to estimate $\epsilon_e \sim 0.1$ as a starting point.

4.4.1. From optical to X-rays

The iterative process of modelling from 3×10^{14} to 6.6×10^{17} Hz shows a good best-fit model ($\chi_r^2 \sim 1$; see results in the first two columns of Table 5), as displayed in the broadband light curves (Fig. 7 for optical frequencies, and Fig. 8 for optical/X-ray domain).

Our results (Table 5) show that the spectrum is in the fast-cooling regime until $t_{trans} \sim 0.02$ d and the NR regime occurs at ~300 d; the cooling due to IC scattering is negligible because of the very low Compton y-parameter (0.02).

SAGA also estimates the behaviour of the synchrotron break frequency over time (Fig. 9). With reference to the lines of reasoning put forward in Sect. 4.2 ($\beta_{he} = -1.09$ suggests that ν_m and ν_c must lie in the same spectral regime below $\nu_{opt,X}$ at $t_{obs,0} \sim= 10^{-3}$ d), the temporal evolution of ν_c and ν_m is in accordance with SAGA results (Fig. 9). On the other hand, with reference to the arguments proposed in Sect. 4.3.2 (radio SEDs suggest that $\nu_{sa} \sim 7$ GHz until $t_{obs} \sim 13$ d), the temporal evolution of ν_{sa} (Fig. 9) is incompatible with SAGA results ($\nu_{sa} \sim 100$ GHz at $t_{obs} \sim 13$ d), which is due to the lack of radio data in the optical/X-ray analysis.

For completeness, Fig. 10 shows the light curves in the UVOIR/X-rays domain at four observing frequencies (i'-filter, top left; g'-filter, top right; UV/uvw1-filter, bottom left; and X-ray frequency, bottom right), and Fig. 11 shows all the radio data (dashed lines, not included in this part of the modelling) with the predicted SEDs in this domain obtained from modelling the optical/X-ray data; these data do not match the high-energy sample, as we show and discuss in the following section.

4.4.2. From radio to X-ray frequencies

The radio/mm data set from 0.6 to 92.5 GHz does not include the data points affected by the bumps (Sect. 4.3), because the best-fit model with the whole radio data set was very poor ($\chi_r^2 > 30$). To verify the stability and robustness of the best-fit solution, we repeated the analysis assuming three different starting values for p (2.1, 2.4, 2.9); we obtained $p \sim 2$, which is lower than that estimated from the high-energy approach (Sect. 4.2), but is compatible with the analysis of the radio SEDs in the empirical approach (Sect. 4.3.1). The poor modelling of these three analyses ($\chi_r^2 > 20$) led us to consider a fixed value for p (2.2, according to the high-energy approach; Sect. 4.2) as a compromise.

Unsurprisingly, the best-fit model has a very high χ_r^2 (~10; Table 5, third column). This is indicative of the problems faced by the standard GRB afterglow model, which are common in cases where a rich data set at low frequencies is available (Fig. 12).

Our results (Table 5, third column) show that the jet break time of 0.9 d translates into a jet opening angle $\theta_j \sim 8$ degrees, $t_{trans} \sim 9 \times 10^{-5}$ d, and the NR regime occurs at ~120 d. Moreover, Fig. 12 shows that the model is only suitable for radio (except for $\nu \lesssim 10$ GHz) domains, and is only partially suited to X-ray frequencies and is poorly suited to the optical band. This behaviour suggests that other radiation mechanisms are responsible for the afterglow emission for GRB 160131A. As in the case of the analysis of optical/X-ray data (Sect. 4.4.1), the Compton y-parameter is 0.02, indicating that cooling due to IC scattering is negligible. The temporal evolution of the cooling frequency ν_c (Fig. 13) suggests that it lies above the X-rays (as opposed to ν_{sa} and ν_m), in contrast with the behaviour expected from empirical considerations based on the optical/X-ray spectra (Sect. 4.2).

5. Discussion

The addition of radio data set in the afterglow modelling considerably complicates the broadband analysis, challenging the standard GRB afterglow model.

We point out three problematic features at radio frequencies:

1. The presence of the same rather constant peak at ~8 GHz in SEDs up to ~25 d, whose width $\Delta\nu/\nu$ evolves from ~0.5 at 1.7 d to ~0.1 at ~25 d, with a temporary disappearance at ~2.7 d (Fig. 4).

2. The SED at 5.8 d evolves with $\beta \sim 0.7$ (Table 2 and Fig. 4), a value which is incompatible with slow cooling regimes for FS emission (Sect. 4.2).

3. Flux densities at low frequencies ($\lesssim$7 GHz) seem to be constant over time (Figs. 4 and 5).

Our results suggest that radio data cannot be fully accounted for alongside the optical/X-ray data within the framework of the standard GRB afterglow model. This is not unprecedented: for example, Kangas & Fruchter (2021) reported a lack of detectable jet breaks in the radio light curves of a sample of 15 GRB

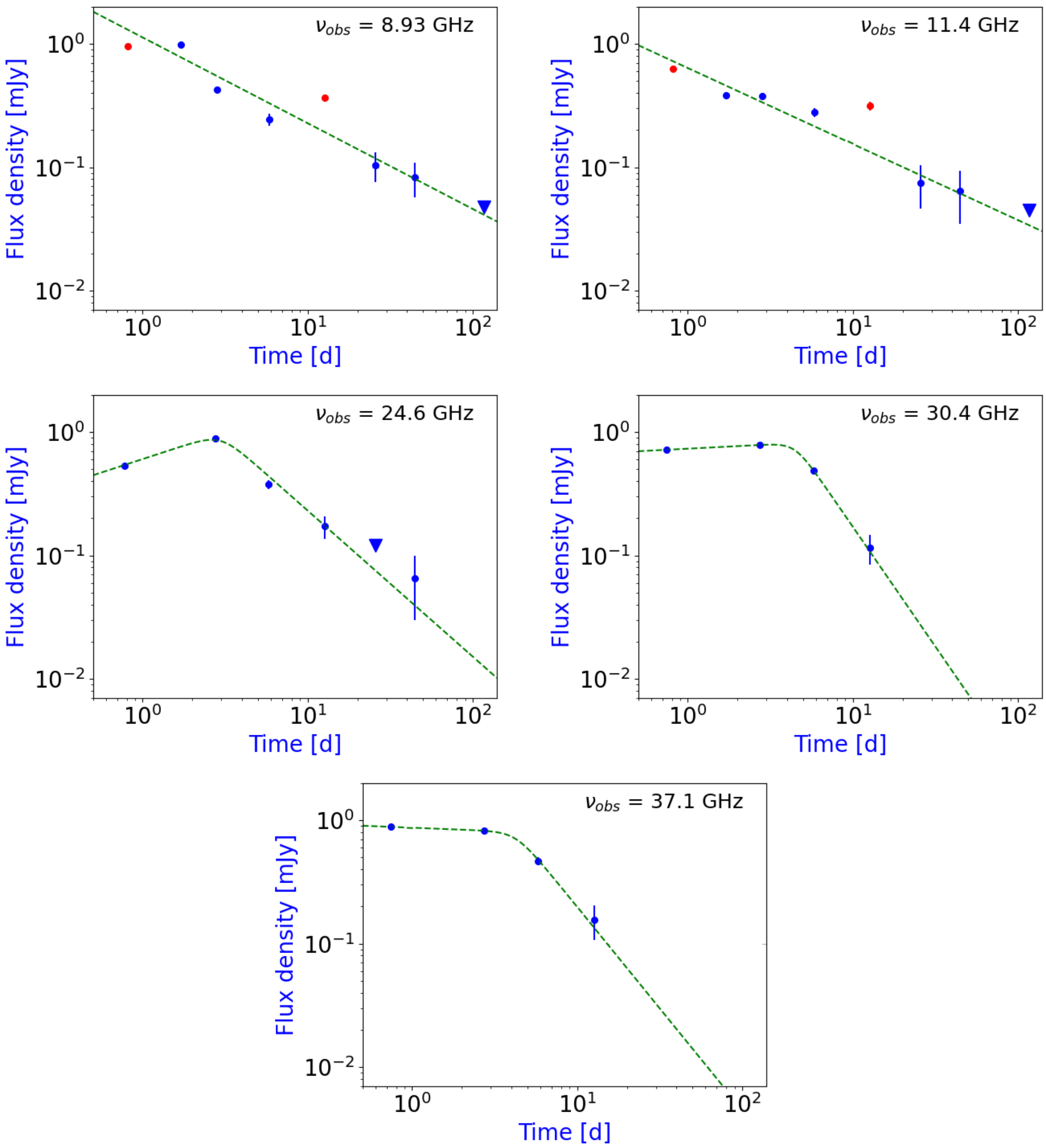

Fig. 6. Radio light curves of GRB 160131A in the range 9 – 37 GHz. 8.93 GHz (*top left*) and 11.4 GHz (*top right*) fitted with a SPL (Eq. 2); the other light curves (24.6 GHz, *middle left*; 30.4 GHz, *middle right*; 37.1 GHz, *bottom*) are fitted with a BPL (Eq. (3)). Blue filled circles indicate detections, and upside-down triangles indicate 3σ upper limits; red circles indicate the ignored points corresponding to the peaks observed in radio SEDs (Fig. 4), and green lines show the resulting model.

Table 4. Parameters for empirical fits to VLA radio light curves of GRB 160131A from 4.6 to 37.4 GHz (see Fig. 6).

ν_{obs} [a]	8.93	11.4	24.6	30.4	37.1
Model	SPL	SPL	BPL	BPL	BPL
t_b [b]	–	–	2.96 ± 0.04	4.47 ± 0.14	4.16 ± 0.11
F_b [c]	–	–	0.85 ± 0.13	0.71 ± 0.05	0.71 ± 0.07
α_{pl}	-0.64 ± 0.04	-0.62 ± 0.02	–	–	–
$\alpha_{1,bpl}$	–	–	0.44 ± 0.05	0.07 [d]	−0.05 [d]
$\alpha_{2,bpl}$	–	–	-1.18 ± 0.02	-1.93 ± 0.23	-1.59 ± 0.13
χ^2_r	1.8	1.3	1.1	0.99	1.02

Notes. t_b indicates the break time corresponding to the flux density F_b, $\alpha_{1,bpl}$ and $\alpha_{2,bpl}$ indicate the temporal decay indices for a broken power law, and α_{pl} indicates the temporal decay index for a power law. See the caption of Table 2 for a full description of the other fit parameters. [a]In units of GHz. [b]In units of days. [c]In units of mJy. [d]Fixed.

Table 5. Summary statistics from MCMC analysis obtained with SAGA applied to the visible and UV data of GRB 160131A for a model based on a jetted (edge-regime) FS emission with optical absorption and energy injection, in an ISM-like CBM.

Parameter	Unit	UVOIR	UVOIR/X-ray	Radio/X
p	–	$2.20^{+0.07}_{-0.04}$	$2.14^{+0.02}_{-0.01}$	2.20 [(a)]
ϵ_e	–	$(1.1 \pm 0.2) \times 10^{-2}$	$(1.3^{+0.3}_{-0.2}) \times 10^{-2}$	$(3.4^{+0.5}_{-0.2}) \times 10^{-2}$
ϵ_B	–	$(1.5^{+1.2}_{-0.9}) \times 10^{-1}$	$(9.3^{+9.0}_{-5.1}) \times 10^{-2}$	$(1.5 \pm 0.3) \times 10^{-3}$
n_0	cm^{-3}	$8.4^{+20.5}_{-5.9}$	$10.7^{+12.8}_{-6.4}$	$(3.6^{+2.7}_{-0.8}) \times 10^{1}$
E_{52}	10^{52} erg	$(4.4^{+1.1}_{-0.8}) \times 10$	$(4.9^{+0.9}_{-0.8}) \times 10$	$(1.2^{+0.1}_{-0.2}) \times 10$
A_v	mag	$(1.1^{+0.5}_{-0.6}) \times 10^{-1}$	$(1.8 \pm 0.4) \times 10^{-1}$	0.2 ± 0.1
t_j	d	$0.9^{+0.2}_{-0.1}$	$0.82^{+0.03}_{-0.02}$	0.9 ± 0.1
θ_j	deg	$5.6^{+0.9}_{-0.8}$	$5.6^{+0.6}_{-0.7}$	$7.7^{+0.7}_{-0.3}$
t_{NR}	d	$(3.0^{+0.9}_{-0.8}) \times 10^{2}$	$(2.7^{+1.1}_{-0.7}) \times 10^{2}$	$(1.2^{+0.1}_{-0.3}) \times 10^{2}$
$t_{b,0}$	d	$(1.99^{+0.03}_{-0.07}) \times 10^{-1}$	$(2.09 \pm 0.01) \times 10^{-1}$	$(2.10^{+0.01}_{-0.03}) \times 10^{-1}$
m	–	0.181 ± 0.002	0.120 ± 0.002	$(5.03^{+0.05}_{-0.02}) \times 10^{-2}$
ν_m [(b)]	Hz	4.2×10^{11}	3.0×10^{11}	1.7×10^{11}
ν_c [(b)]	Hz	1.8×10^{12}	3.1×10^{12}	5.9×10^{14}
ν_{sa} [(b)]	Hz	4.0×10^{11}	3.4×10^{11}	1.5×10^{11}
ν_{ac} [(b)]	Hz	1.4×10^{12}	2.3×10^{12}	2.9×10^{12}
$t_{\rm trans,51}$	d	5.6×10^{-2}	1.8×10^{-2}	9.2×10^{-5}
$t_{\rm trans,12}$	d	0.8	0.5	1.3
χ^2_r	–	1.22	0.97	10.97

Notes. $t_{\rm trans,51}$ and $t_{\rm trans,12}$ indicate the transition time between FS spectral regimes (5 → 1 and 1 → 2, respectively) as described in GS02; χ^2_r indicates the reduced chi-squared of the best-fit model. [(a)]Fixed. [(b)]Measured at $t_{\rm obs} = 1$ d.

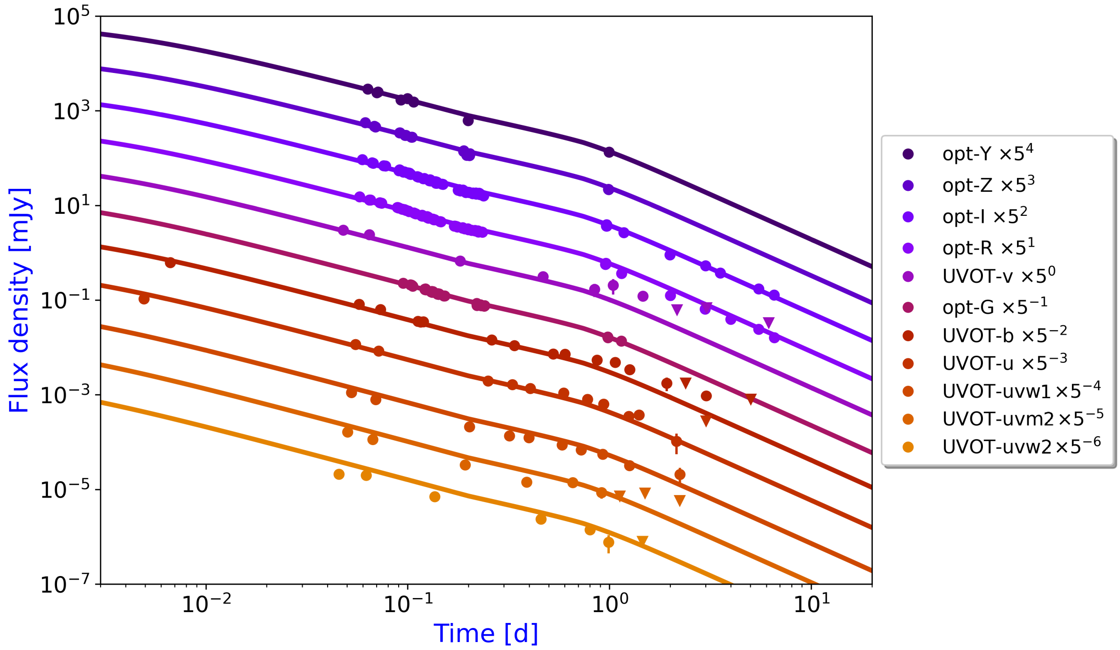

Fig. 7. Broadband modelling (UVOIR frequencies; Table 5, first column) of GRB 160131A for a FS model with a ISM-like CBM (GS02); we considered in this analysis a jetted (edge-regime) emission with dust extinction and energy injection. Filled circles indicate detections, and downward triangles indicate 3σ upper limits.

afterglows, whereas X-rays seem to support them. However, we underline that these latter authors (1) considered only one spectral regime (5-1-2) of afterglow emission in GS02, (2) assumed the sideways expansion for jetted emission, and (3) ignored any observed rise period of the light curve and any early features attributed to flares, plateau, or RS in the literature. They interpret the long-lasting single power-law decline of the radio emission in terms of a two-component jet.

There are other possible assumptions that might not necessarily hold true for the afterglow of GRB 160131A: (1) the constant micro-physics parameters, in light of the evidence of the temporal evolution of the micro-physics parameters in the afterglow of GRB 190114C (Misra et al. 2021), (2) a unique CBM, as in the case of evidence of the transition from a wind-like to ISM-like CBM in the afterglow of GRB 140423A (Li et al. 2020), and (3) a uniform jet model, in light of the evidence of other

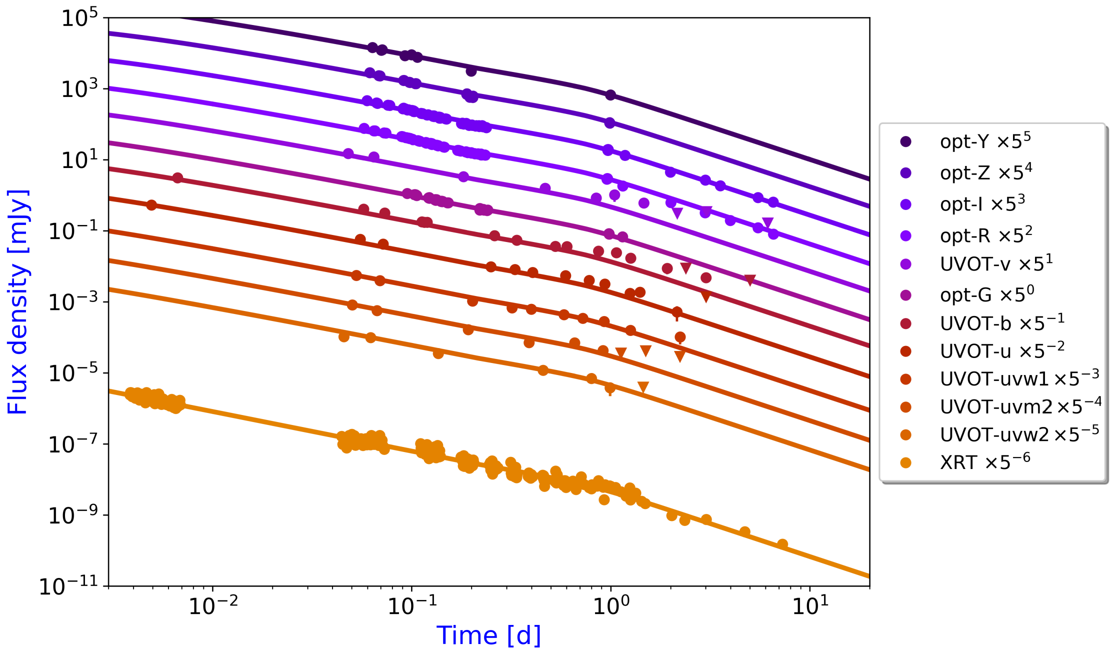

Fig. 8. Broadband modelling (from optical to X-ray frequencies; Table 5, second column) of GRB 160131A. See the caption of Fig. 7 for a full description of the modelling. Filled circles indicate detections, and downward triangles indicate 3σ upper limits.

jet models used to interpret the broadband data for several GRB afterglows, such as the structured jet model (e.g. De Colle et al. 2012; Granot et al. 2018; Alexander et al. 2018; Coughlin & Begelman 2020), a two-component jet (e.g. Berger et al. 2003; Peng et al. 2005; Racusin et al. 2008; Liu & Wang 2011; Holland et al. 2012) and other more complex regimes (e.g. Huang et al. 2004; Wu et al. 2005; Granot et al. 2018). In recent years, growing evidence has been found in favour of the structured jet[19], as in the case of the GRB 170817A associated to GW 170817 (Alexander et al. 2018).

5.1. Energy injection

A flattening in the optical/X-ray light curves prior to 0.8 d of GRB 160131A could demand energy injection. Nothing can be inferred in this regard from radio data, which were taken starting from ~1 d.

In the energy injection approach (Sect. 3.2), the inferred value $p \sim 2.2$ (Sect. 4) suggests $\nu_c < \nu_X$, where the flux density is $F_{\nu > \nu_c} \propto E_{k,\mathrm{iso},52}^{(2+p)/4} t^{(2-3p)/4}$ (GS02); in this regime we obtain $F_{\nu > \nu_c} \propto E_{k,\mathrm{iso},52}^{1.1} t^{-1.3}$. The temporal evolution of the injected energy is parameterised as $E \propto t^m$, and hence $F_{\nu > \nu_c} \propto t^{1.1m-1.3}$. Fitting the X-ray light curve with a power law from ~0.2 d to ~0.8 d, which roughly corresponds to the flattening, we obtain $\alpha_{X,ei} = -1.0 \pm 0.2$; apparently, this temporal decay index does not require that an energy injection effect being added in the modelling, but the addition of the UVOIR data set in the broadband modelling necessarily invokes this effect. In the energy injection approach, the value of $\alpha_{X,ei}$ implies $m = 0.27 \pm 0.20$, or, equivalently, $q = 1 - m = 0.73 \pm 0.20$. This conclusion is perfectly compatible with our optical/X-ray modelling (Sect. 4.4.1 and Table 5, first and second column), where we adopted the energy injection approach (Sect. 3.2); in particular, we obtained an increasing $E_{k,\mathrm{iso},52}$ from $\sim 4.2 \times 10^{53}$ erg to $\sim 4.9 \times 10^{53}$ erg (Fig. 14). A similar energy injection process was discussed for GRB 100418A, for which $m \sim 0.7$ was found (Marshall et al. 2011; Laskar et al. 2015).

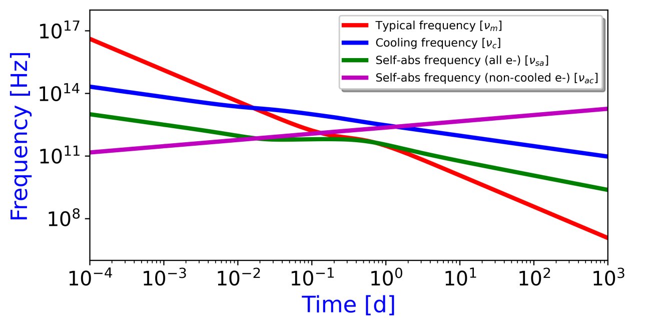

Fig. 9. Temporal evolution of the synchrotron break frequencies for afterglow emission of GRB 160131A, based on analysis of UVOIR/X-ray data (Table 5, second column). See the caption of Fig. 7 for a full description of the modelling. The self-absorption frequency produced by noncooled electrons ν_{ac} makes sense only in fast-cooling regime ($\lesssim$0.02 d).

As we can see in Fig. 3, the X-ray light curve shows a less pronounced flattening with respect to optical light curves. This unusual light curve was also observed with GRB 090102 (Gendre et al. 2010), where the optical flattening could then be interpreted as (1) a change of the CBM (e.g. Ramirez-Ruiz et al. 2001; Chevalier et al. 2004), and (2) a normal fireball expanding in an ISM, with a RS component (the lack of radio data does not corroborate this assumption). Another similar feature is present in GRB 060908 (Covino et al. 2010), where it is possible to model the optical and X-ray afterglows independently, but the multi-frequency spectral and temporal data challenge available theoretical scenarios. The broadband modelling of the afterglow of the ultra-long duration GRB 111209A (Kann et al. 2018) shows a strong chromatic rebrightening in the optical domain,

[19] Recently, the open-source Python package AFTERGLOWPY became available for on-the-fly computation of structured jet afterglows with arbitrary viewing angle (Ryan et al. 2020).

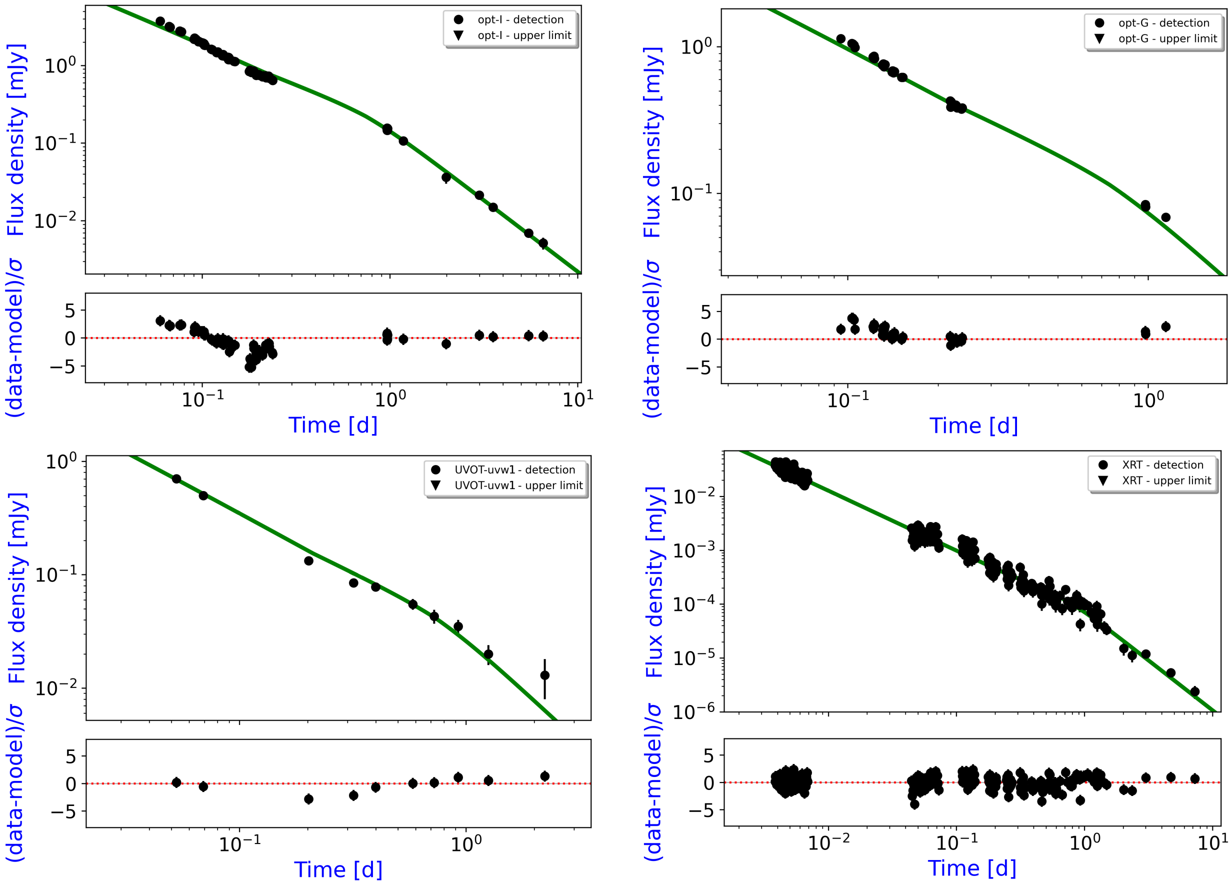

Fig. 10. Light curves of GRB 160131A in the UVOIR/X-rays domain at i'-filter (4.03×10^{14}, *top left*), g'-filter (6.47×10^{14}, *top right*), UV/uvw1-filter (1.15×10^{15}, *bottom left*), and X-ray frequency (6.65×10^{17}, *bottom right*), referred to the broadband modelling from optical to X-ray frequencies (Table 5, second column), displayed in Fig. 8. The bottom panel of each light curve corresponds to the residuals of the fit. See the caption of Fig. 7 for a full description of the modelling. Filled circles indicate detections, upside down triangles indicate 3σ upper limits, and green lines show the resulting model.

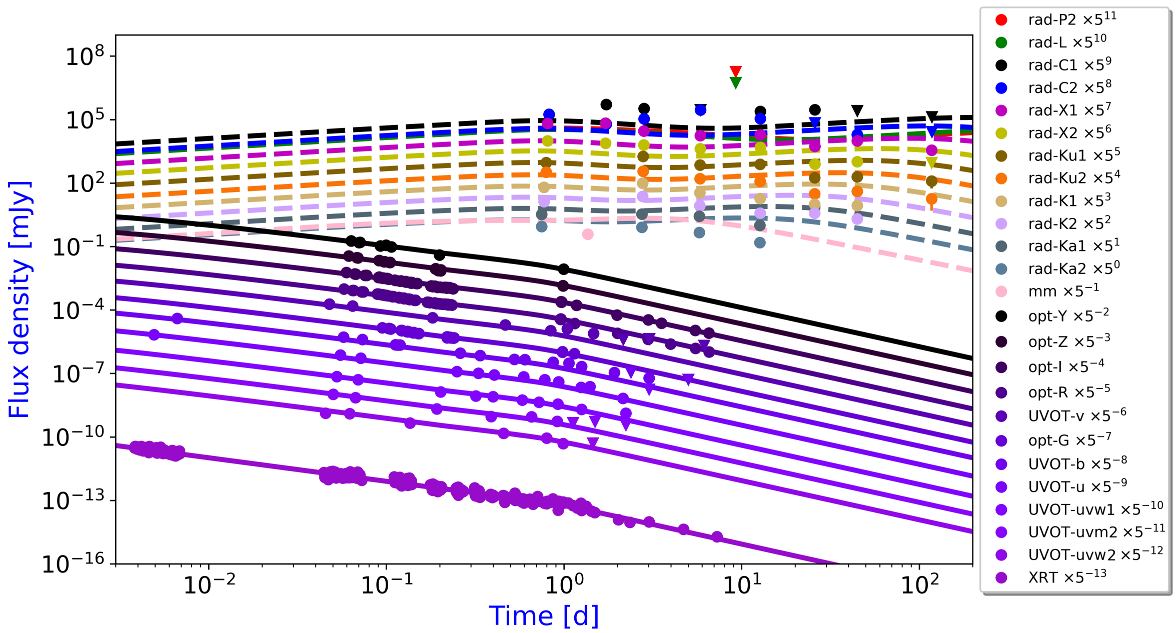

Fig. 11. Broadband modelling (from optical to X-ray frequencies; Table 5, second column) of GRB 160131A. See the caption of Fig. 7 for a full description of the modelling. Filled circles indicate detections, and downward triangles indicate 3σ upper limits. For completeness we include all the radio data (dashed lines, not modelled in this approach) and relative light curves (derived from optical/X-ray modelling).

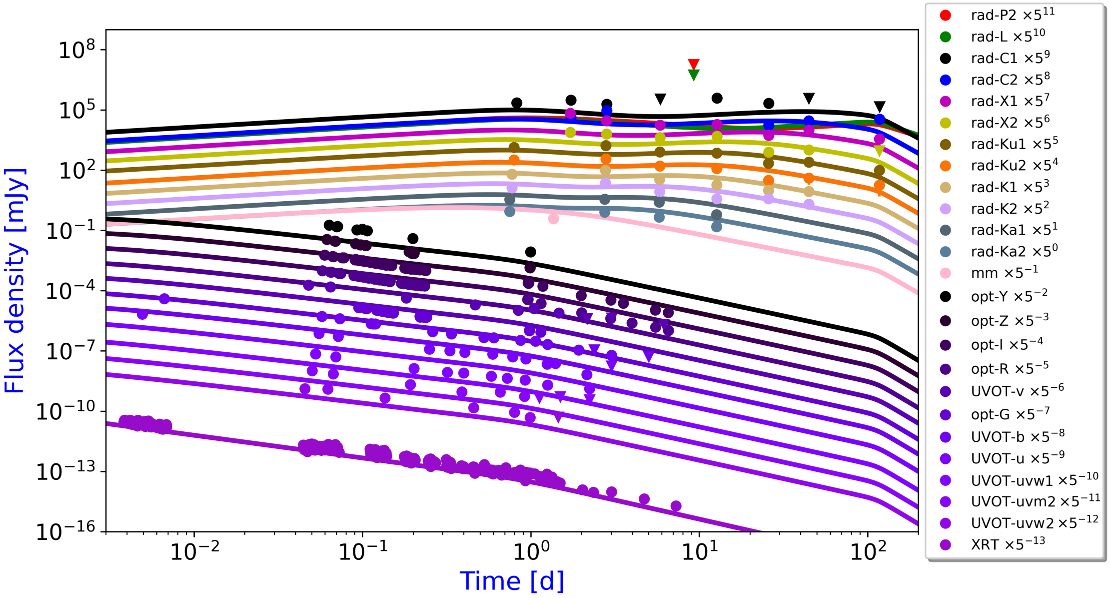

Fig. 12. Broadband modelling of GRB 160131A from radio to X-ray frequencies (Table 5, third column). See the caption of Fig. 7 for a full description of the modelling. Filled circles indicate detections, and downward triangles indicate 3σ upper limits.

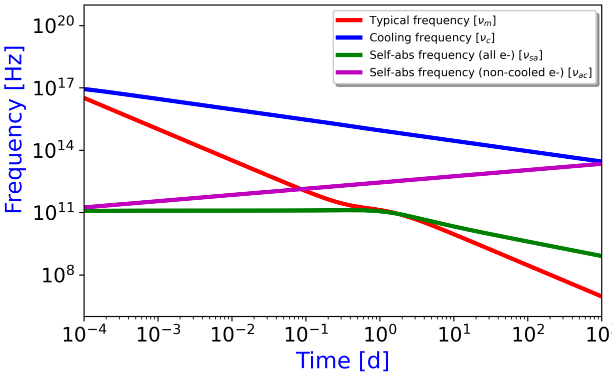

Fig. 13. Temporal evolution of the synchrotron break frequencies for afterglow emission of GRB 160131A based on analysis of broadband data (from radio to X-ray frequencies; Table 5, third column). See the caption of Fig. 7 for a full description of the modelling. The self-absorption frequency produced by non-cooled electrons ν_{ac} only makes sense in the fast-cooling regime ($\lesssim 9 \times 10^{-5}$ d).

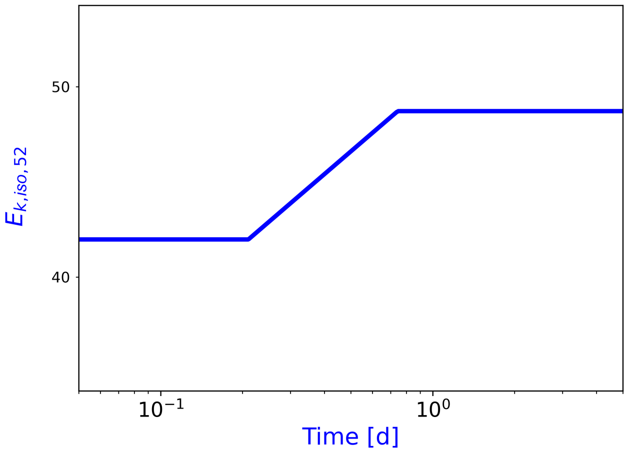

Fig. 14. Isotropic equivalent kinetic energy $E_{k,\mathrm{iso},52}$ (in units of 10^{52} erg) as a function of time, as determined from modelling of the optical/X-ray data set (Table 5, second column).

which is modelled with a two-component jet; the late afterglow also shows several smaller, achromatic rebrightenings, which are likely to be energy injections.

5.2. The possible role of ISS in the multi-component radio SEDs

The evidence of the multi-component SEDs at radio frequencies (A, B, and C; Sect. 4.3.1) suggests further radiation mechanisms for the GRB afterglow in addition to the continuum associated with FS emission.

The presence of peaks in radio SEDs had already been observed in other sources, and the main candidate to explain this pronounced radio variability is the ISS (or other extreme scattering effects); in particular, the VLA SED at ~2 d of GRB 130925A (Horesh et al. 2015) shows a peak at ~8 GHz, with $\Delta\nu/\nu \sim 0.7$, compatible with our values ($\Delta\nu/\nu \sim 0.1 - 0.5$, as observed in Sect. 5). Horesh et al. (2015) suggest that these peaks are well modelled with the ISS emission model in which the emission originates from either mono-energetic electrons or an electron population with an unusually steep power-law energy distribution. Moreover, thanks to a simple modelling of the radio data set with SAGA, we obtained SEDs (Fig. 15) and light curves (Fig. 16) that are well modelled with the expected variability due to the ISS effect (red shaded regions).

Another interpretation for this radio excess at early times is that it should have been ascribable to the presence of a RS in addition to a FS (e.g. Gomboc et al. 2008; Melandri et al. 2010; Japelj et al. 2014; Alexander et al. 2017; Laskar et al. 2018a), because (1) the RS emission is expected to peak at lower frequencies than the FS, and (2) the RS spectrum is expected to cut off steeply above the RS cooling frequency (Kobayashi & Sari 2000). A recent study (Laskar et al. 2019b) showed for the first time that within a SED it is possible to disentangle the contributions of RS and FS in the radio band. Moreover, the first case of a SED instantaneously and clearly decomposed into RS and

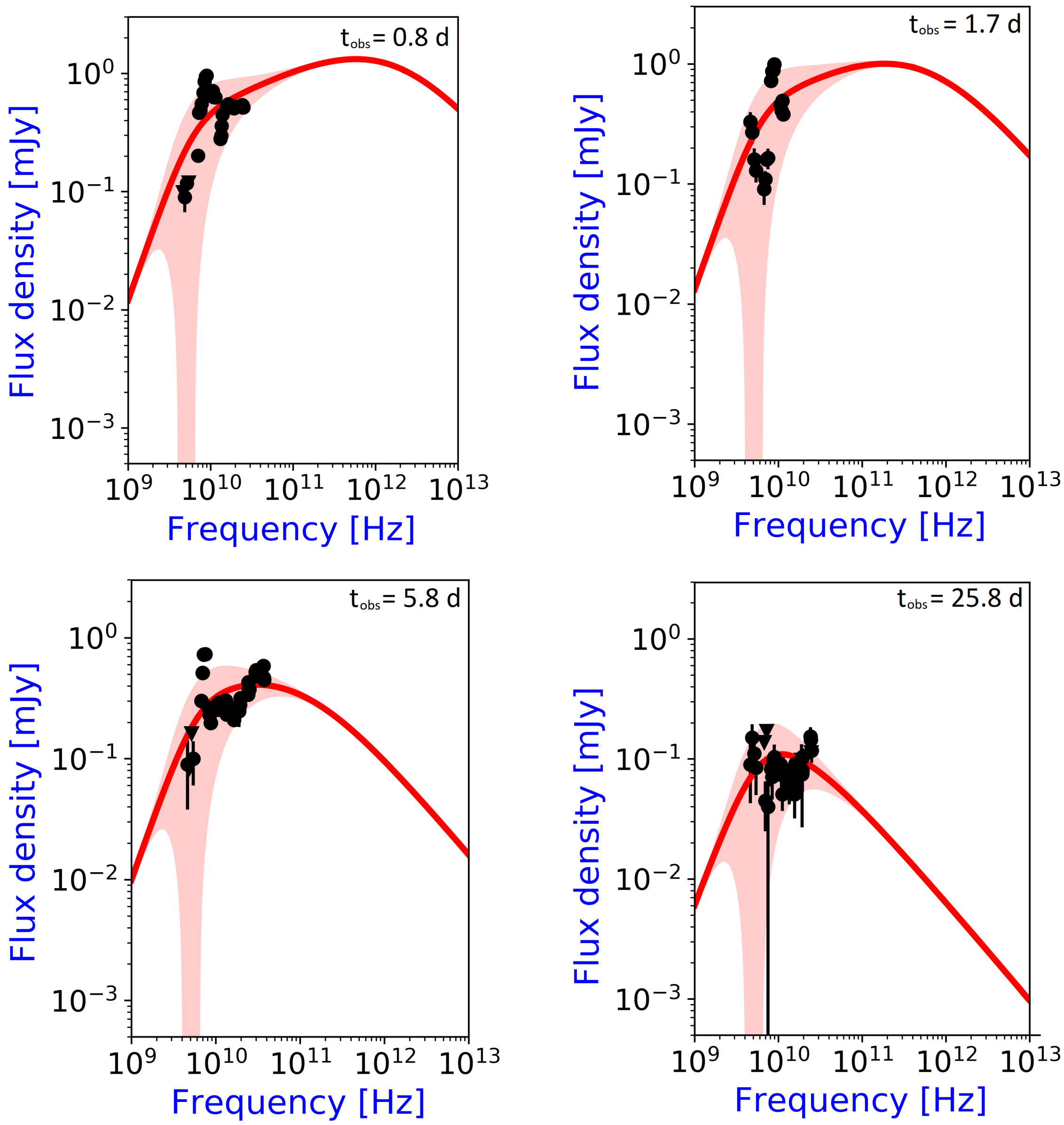

Fig. 15. Radio SEDs of GRB 160131A at 0.8 d (*top left*), 1.7 d (*top right*), 5.8 d (*bottom left*), and 25.8 d (*bottom right*), obtained through a radio modelling for a FS model in ISM; we considered a jetted (edge-regime) emission with ISS effect. Filled circles indicate detections, and upside down triangles indicate 3σ upper limits; the red shaded regions represent the expected variability due to ISS effect, obtained through the prescription described in Misra et al. (2021).

FS components (GRB 181201A, Laskar et al. 2018b) suggests that an early-time radio peak is consistent with emission from a refreshed RS produced by the violent collision of two shells with different Lorentz factors emitted at different times. Nevertheless, the peak at lower frequency bands observed in the radio SEDs of Laskar et al. (2019b), which is characterised by $\Delta\nu/\nu \sim 3$, is much broader than what we find ($\Delta\nu/\nu \sim 0.1$–0.5, as observed in Sect. 5), calling for something else that comes into play in addition to the RS prescription. This incompatibility is strengthened by the lower limit on n_0 estimated with SAGA ($n_0 \gtrsim 5$ cm^{-3}) and the strong observed correlation –highlighted in several analyses (e.g. GRB 160509A in Laskar et al. 2016a, GRB 161219B in Laskar et al. 2018a, and GRB 181201A in Laskar et al. 2019b)– between broadband detections of RS emission and CBM characterised by low densities (typically $n_0 \lesssim 10^{-2}$ cm^{-3} in ISM-like CBM, and $A_* \lesssim 10^{-2}$ in wind-like CBM). In hindsight, these features could have possibly been observed in more sparse radio data sets from past GRBs as well, and erroneously interpreted as evidence of a RS.

We further rule out the presence of RS emission by analysing these peaks in the radio SEDs according to the prescription taken up by Laskar et al. (2018b). These authors assume $\nu_{c,rs}$ to be located near each observed radio spectral peak in order to compute a conservative lower limit to the optical light curve[20]. At radio frequencies, the first spectral peak takes place at $F \approx 0.9$ Jy in X-band ($\sim$ 9 GHz) at 0.8 d (Fig. 4); following the

[20] Once the RS has crossed the ejecta (timescale of days), the flux above $\nu_{c,rs}$ declines rapidly because no electron is newly accelerated within the ejecta.

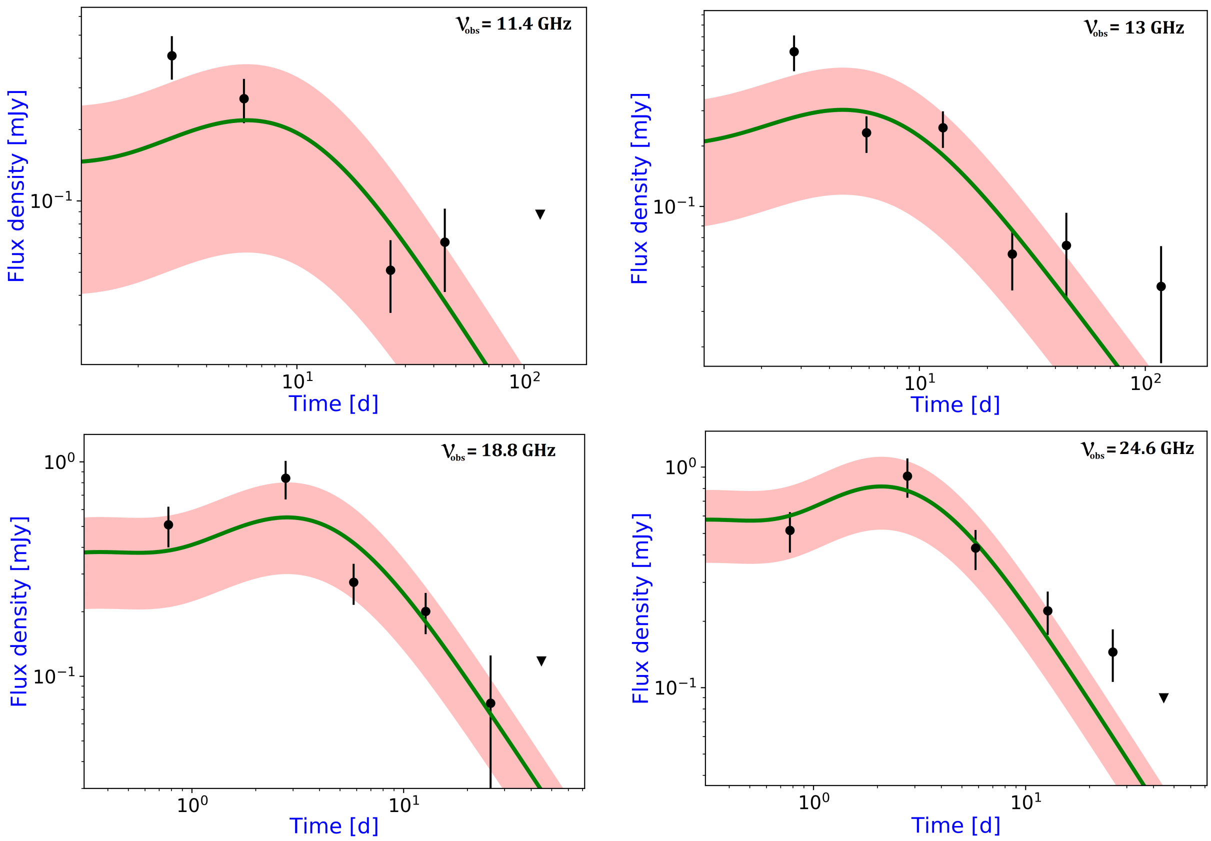

Fig. 16. Radio light curves of GRB 160131A at 11.4 GHz (*top left*), 13 GHz (*top right*), 18.8 GHz (*bottom left*), and 24.6 GHz (*bottom right*), obtained through a radio modelling (from radio to X-ray frequencies) for a FS model in ISM; we considered a jetted (edge-regime) emission with ISS effect, dust extinction and energy injection. Filled circles indicate detections, and upside-down triangles indicate 3σ upper limits; the red shaded regions represent the expected variability due to the ISS effect obtained through the prescription described in Misra et al. (2021).

reasoning behind the evolution of $\nu_{c,rs}$, we assume $\nu_{c,rs} \approx 9$ GHz and $F_{\nu,pk} \approx 0.9$ Jy at this epoch.

– In the relativistic RS regime, the Y-band ($\sim 3 \times 10^{14}$ Hz) would be crossed by a relativistic RS (ISM) at $t_{pk} \sim 8.5 \times 10^{-4}$ d with $F_{\nu,pk} \sim 730$ Jy ($t_{pk} \sim 3.1 \times 10^{-3}$ d and $F_{\nu,pk} \sim 465$ Jy for wind). Unfortunately, there are no optical data at those epochs, and therefore we scale $F_{\nu,pk}$ at t_{pk} knowing that the observed Y-band light curve evolves as $\sim t^{-1.25}$ (Sect. 4.2), obtaining $F_{\nu,pk} \sim 920$ Jy for ISM-like CBM ($F_{\nu,pk} \sim 180$ Jy at $\sim 3.1 \times 10^{-3}$ d for wind-like CBM), which is incompatible with the relativistic RS regime.

– In the Newtonian RS approach, for the same spectral peak we obtain the passage of $\nu_{c,rs}$ in Y-band (1) in the range $\approx(1.7 - 0.5) \times 10^{-3}$ d (corresponding to $F_{\nu,pk} \sim 450 - 728$ Jy) for an ISM-like CBM, and (2) in the range $\approx(8.6 - 1.7) \times 10^{-3}$ d (corresponding to $F_{\nu,pk} \sim 260 - 450$ Jy) for a wind-like CBM. In this case, there are also no optical data at those epochs to verify this assumption; the observed Y-band light curve evolves as ~ -1.25, resulting in $F_{\nu,pk} \sim 390$–1930 Jy for an ISM-like CBM ($F_{\nu,pk} \sim 50$–390 Jy for wind-like CBM); this behaviour seems to be compatible with the predicted Y-band light curve.

The radio peak clearly observed in the 1.7 d SED at the same frequency (Fig. 5, top right) is incompatible with the temporal evolution of $\nu_{c,rs}$ for RS emission because, considering the observed peak at $\sim$9 GHz in the 0.8 d-radio SED, at 1.7 d we would observe $\nu_{c,rs} \sim 3$ GHz in an ISM-like CBM ($\nu_{c,rs} \sim 2$ GHz in wind-like CBM); this suggests that the RS is unlikely to play a dominant role in radio data for GRB 160131A.

Other possible explanations for the radio spectral bumps could be (1) a two-component jet, one in which the optical/X-ray emission arises from a narrower, faster jet than that producing the radio observations (i.e. Peng et al. 2005; Racusin et al. 2008; Holland et al. 2012), or (2) the presence of a population of thermal electrons not accelerated by the FS passage into a relativistic power-law distribution (Eichler & Waxman 2005), and characterised by a much lower Lorentz factor than the minimum Lorentz factor of the shock-accelerated electrons ('cold electron model'; Ressler & Laskar 2017).

6. Conclusions

We present our results on the broadband modelling of the afterglow of GRB 160131A, whose observations span from $\sim$330 s to $\sim$160 d post explosion at 26 frequencies from 6×10^8 Hz to 7×10^{17} Hz.

In the data modelling we consider a jetted (edge-regime) FS emission with energy injection, the ISS effect, dust extinction, and absorption effects in ISM-like CBM. Our analysis of the UVOIR/X-ray data alone leads us to the following results: $p \sim 2.2$, $\epsilon_e \sim 0.01$, $\epsilon_B \sim 0.1$, $n_0 \gtrsim 10$ cm^{-3}, $E_{K,\rm iso} \gtrsim 5 \times 10^{53}$ erg, $A_V \sim 0.2$ mag, and $t_j \sim 0.9$ d. The constraint on t_j leads to an estimate of the jet half opening angle of $\theta_j \sim 6°$, corresponding to a beaming-corrected kinetic energy of the explosion $E_K = E_{K,\rm iso}(1 - \cos\theta_j) \gtrsim 3 \times 10^{51}$ erg, in agreement with the typical values of long GRBs (Figs. 21 and 22 of Laskar et al. 2015). The spectrum is in fast cooling until $\sim$0.02 d, the non-relativistic regime sets in at $\sim$100 d, and the energy injection is characterised by $m \sim 0.15$. The radio data set –which in this case is particularly rich– shows the presence of spectral bumps in several SEDs, which are incompatible with a simple standard GRB afterglow model and probably ascribable to either ISS (or other extreme scattering effects) or a more complex multi-component structure. This incompatibility is corroborated by the broadband modelling from radio to high energies, where the model works well for the radio domain (except for $\nu \lesssim 10$ GHz), but not quite as well at X-ray frequencies, and poorly for the optical band. Our conclusions challenge the standard GRB afterglow model; moreover, these results highlight the as-yet poorly understood physics, especially when a rich data set (from radio to high-energy domain) – as in the case of GRB 160131A – is included in the modelling.

Future broadband follow-up studies of GRB afterglows, particularly at radio frequencies with the latest and forthcoming generation facilities –especially in interferometric mode– such as the Very Large Baseline Array (VLBA[21]), LOw Frequency ARray (LOFAR, van Haarlem et al. 2013) or the next generation Square Kilometer Array (SKA; Johnston et al. 2008), are essential in order to reach an exhaustive comprehension of the GRB afterglow physics, particularly within the modern era of multi-messenger astronomy.

Acknowledgements. We thank the anonymous referee for helping us improve the paper. Support for this work was provided by Università degli Studi di Ferrara through grant FIR 2018 "A Broad-band study of Cosmic Gamma-Ray Burst Prompt and Afterglow Emission" (PI Guidorzi). M. Marongiu acknowledges financial support from the Italian Ministry of University and Research – Project Proposal CIR01_00010, and the University of Ferrara for the financial support of his PhD scholarship (during the data analysis and the interpretation of the results). M. Marongiu is very grateful to R. Martone for useful conversations about GRB science; moreover, M. Marongiu thanks P. Bergamini and G. Angora for the useful discussion about Python programming language and data analysis. A. Gomboc acknowledges the financial support from the Slovenian Research Agency (grants P1-0031, I0-0033, J1-8136, J1-2460) and networking support by the COST Actions CA16104 GWverse and CA16214 PHAROS. N. Jordana and C.G. Mundell acknowledge financial support from Mr Jim Sherwin and Mrs Hiroko Sherwin. D. Kopac acknowledges the financial support from the Slovenian Research Agency (research core funding No. P1-0188). The National Radio Astronomy Observatory is a facility of the National Science Foundation operated under cooperative agreement by Associated Universities, Inc..

References

Abbott, B. P., Abbott, R., Abbott, T. D., et al. 2017, ApJ, 848, L12
Aksulu, M. D., Wijers, R. A. M. J., van Eerten, H. J., & van der Horst, A. J. 2020, MNRAS, 497, 4672
Alexander, K. D., Laskar, T., Berger, E., et al. 2017, ApJ, 848, 69
Alexander, K. D., Margutti, R., Blanchard, P. K., et al. 2018, ApJ, 863, L18
Ayache, E. H., van Eerten, H. J., & Eardley, R. W. 2022, MNRAS, 510, 1315
Beniamini, P., & van der Horst, A. J. 2017, MNRAS, 472, 3161
Berger, E., Kulkarni, S. R., Pooley, G., et al. 2003, Nature, 426, 154
Björnsson, C.-I., & Fransson, C. 2004, ApJ, 605, 823
Breeveld, A. A., Landsman, W., Holland, S. T., et al. 2011, in Gamma Ray Bursts 2010, eds. J. E. McEnery, J. L. Racusin, & N. Gehrels, AIP Conf. Ser., 1358, 373
Brown, P. J., Holland, S. T., Immler, S., et al. 2009, AJ, 137, 4517
Brown, T. M., Baliber, N., Bianco, F. B., et al. 2013, PASP, 125, 1031
Cannizzo, J. K., Gehrels, N., & Vishniac, E. T. 2004, ApJ, 601, 380
Castro-Tirado, A. J., Bremer, M., McBreen, S., et al. 2007, A&A, 475, 101
Chandra, P., & Frail, D. A. 2012, ApJ, 746, 156
Chandra, P., & Nayana, A. J. 2016a, GRB Coordinates Network, 19009, 1
Chandra, P., & Nayana, A. J. 2016b, GRB Coordinates Network, 19010, 1
Chattopadhyay, T., Vadawale, S. V., Aarthy, E., et al. 2019, ApJ, 884, 123
Chenu, J.-Y., Navarrini, A., Bortolotti, Y., et al. 2016, IEEE Trans. Terahertz Sci. Technol., 6, 223
Chevalier, R. A., & Li, Z.-Y. 2000, ApJ, 536, 195
Chevalier, R. A., Li, Z.-Y., & Fransson, C. 2004, ApJ, 606, 369

[21] https://science.nrao.edu/facilities/vlba

Chincarini, G., Mao, J., Margutti, R., et al. 2010, MNRAS, 406, 2113
Corsi, A., Piro, L., Kuulkers, E., et al. 2005, A&A, 438, 829
Coughlin, E. R., & Begelman, M. C. 2020, MNRAS, 499, 3158
Covino, S., Campana, S., Conciatore, M. L., et al. 2010, A&A, 521, A53
Cucchiara, A., Veres, P., Corsi, A., et al. 2015, ApJ, 812, 122
Cummings, J. R., Barthelmy, S. D., Gehrels, N., et al. 2016, GRB Coordinates Network, 18959, 1
Daigne, F., & Mochkovitch, R. 2000, A&A, 358, 1157
De Colle, F., Granot, J., López-Cámara, D., & Ramirez-Ruiz, E. 2012, ApJ, 746, 122
de Ugarte Postigo, A., Thoene, C. C., & Sanchez-Ramirez, R. 2016a, GRB Coordinates Network, 18966, 1
de Ugarte Postigo, A., Schulze, S., Bremer, M., & Martin, S. 2016b, GRB Coordinates Network, 18976, 1
Eichler, D., & Waxman, E. 2005, ApJ, 627, 861
Evans, P. A., Beardmore, A. P., Page, K. L., et al. 2009, MNRAS, 397, 1177
Foreman-Mackey, D., Hogg, D. W., Lang, D., & Goodman, J. 2013, PASP, 125, 306
Frail, D. A., Kulkarni, S. R., Nicastro, L., Feroci, M., & Taylor, G. B. 1997, Nature, 389, 261
Frail, D. A., Waxman, E., & Kulkarni, S. R. 2000a, ApJ, 537, 191
Frail, D. A., Berger, E., Galama, T., et al. 2000b, ApJ, 538, L129
Frail, D. A., Kulkarni, S. R., Sari, R., et al. 2001, ApJ, 562, L55
Frail, D. A., Cameron, P. B., Kasliwal, M., et al. 2006, ApJ, 646, L99
Frail, D. A., Yost, S. A., Berger, E., et al. 2003, ApJ, 590, 992
Fukugita, M., Ichikawa, T., Gunn, J. E., et al. 1996, AJ, 111, 1748
Gao, H., & Mészáros, P. 2015, ApJ, 802, 90
Gao, H., Lei, W.-H., Zou, Y.-C., Wu, X.-F., & Zhang, B. 2013a, New Astron. Rev., 57, 141
Gao, H., Lei, W.-H., Wu, X.-F., & Zhang, B. 2013b, MNRAS, 435, 2520
Gehrels, N., Chincarini, G., Giommi, P., et al. 2004, ApJ, 611, 1005
Gendre, B., Corsi, A., & Piro, L. 2006, A&A, 455, 803
Gendre, B., Klotz, A., Palazzi, E., et al. 2010, MNRAS, 405, 2372
Gomboc, A., Kobayashi, S., Guidorzi, C., et al. 2008, ApJ, 687, 443
Goodman, J. 1997, New Astron., 2, 449
Goodman, J., & Narayan, R. 2006, ApJ, 636, 510
Granot, J. 2007, Rev. Mex. Astron. Astrofis. Conf. Ser., 27, 140
Granot, J., & Königl, A. 2003, ApJ, 594, L83
Granot, J., & Kumar, P. 2006, MNRAS, 366, L13
Granot, J., & Piran, T. 2012, MNRAS, 421, 570
Granot, J., & Sari, R. 2002, ApJ, 568, 820
Granot, J., & van der Horst, A. J. 2014, PASA, 31, 8
Granot, J., Miller, M., Piran, T., Suen, W. M., & Hughes, P. A. 2001, in Gamma-ray Bursts in the Afterglow Era, eds. E. Costa, F. Frontera, & J. Hjorth, 312
Granot, J., De Colle, F., & Ramirez-Ruiz, E. 2018, MNRAS, 481, 2711
Guidorzi, C., Monfardini, A., Gomboc, A., et al. 2006, PASP, 118, 288
Guidorzi, C., Dichiara, S., & Amati, L. 2016, A&A, 589, A98
Gupta, Y., Kale, H., Nayak, S., et al. 2017, Current Science, 113, 707
Hascoët, R., Daigne, F., Mochkovitch, R., & Vennin, V. 2012, MNRAS, 421, 525
Heyl, J. S., & Perna, R. 2003, ApJ, 586, L13
Högbom, J. A. 1974, A&AS, 15, 417
Holland, S. T., De Pasquale, M., Mao, J., et al. 2012, ApJ, 745, 41
Horesh, A., Cenko, S. B., Perley, D. A., et al. 2015, ApJ, 812, 86
Huang, Y. F., Wu, X. F., Dai, Z. G., Ma, H. T., & Lu, T. 2004, ApJ, 605, 300
Jakobsson, P., Frail, D. A., Fox, D. B., et al. 2005, ApJ, 629, 45
Japelj, J., Kopač, D., Kobayashi, S., et al. 2014, ApJ, 785, 84
Jeffreys, H. 1946, Proc. R. Soc. London Ser. A, 186, 453
Johnston, S., Taylor, R., Bailes, M., et al. 2008, Exp. Astron., 22, 151
Jordana-Mitjans, N., Mundell, C. G., Kobayashi, S., et al. 2020, ApJ, 892, 97
Kangas, T., & Fruchter, A. S. 2021, ApJ, 911, 14
Kann, D. A., Schady, P., Olivares, E. F., et al. 2018, A&A, 617, A122
Kapahi, V. K., & Ananthakrishnan, S. 1995, Bull. Astron. Soc. India, 23, 265
Klotz, A., Gendre, B., Stratta, G., et al. 2008, A&A, 483, 847
Kobayashi, S., & Sari, R. 2000, ApJ, 542, 819
Kobayashi, S., & Zhang, B. 2003, ApJ, 582, L75
Kobayashi, S., & Zhang, B. 2007, ApJ, 655, 973
Kobayashi, S., Piran, T., & Sari, R. 1999, ApJ, 513, 669
Kopač, D., Mundell, C. G., Kobayashi, S., et al. 2015, ApJ, 806, 179
Kumar, P., & Granot, J. 2003, ApJ, 591, 1075
Laskar, T. 2016, GRB Coordinates Network, 18978, 1
Laskar, T., Berger, E., Zauderer, B. A., et al. 2013, ApJ, 776, 119
Laskar, T., Berger, E., Tanvir, N., et al. 2014, ApJ, 781, 1
Laskar, T., Berger, E., Margutti, R., et al. 2015, ApJ, 814, 1
Laskar, T., Alexander, K. D., Berger, E., et al. 2016a, ApJ, 833, 88
Laskar, T., Alexander, K. D., & Berger, E. 2016b, GRB Coordinates Network, 18977, 1
Laskar, T., Alexander, K. D., Berger, E., et al. 2018a, ApJ, 862, 94
Laskar, T., Berger, E., Margutti, R., et al. 2018b, ApJ, 859, 134

Laskar, T., Alexander, K. D., Gill, R., et al. 2019a, ApJ, 878, L26
Laskar, T., van Eerten, H., Schady, P., et al. 2019b, ApJ, 884, 121
Lazzati, D. 2002, MNRAS, 337, 1426
Leventis, K., van Eerten, H. J., Meliani, Z., & Wijers, R. A. M. J. 2012, MNRAS, 427, 1329
Leventis, K., van der Horst, A. J., van Eerten, H. J., & Wijers, R. A. M. J. 2013, MNRAS, 431, 1026
Li, L., Wang, X.-G., Zheng, W., et al. 2020, ApJ, 900, 176
Liang, E., Zhang, B., Virgili, F., & Dai, Z. G. 2007, ApJ, 662, 1111
Liu, R.-Y., & Wang, X.-Y. 2011, ApJ, 730, 1
Livio, M., & Waxman, E. 2000, ApJ, 538, 187
Madau, P. 1995, ApJ, 441, 18
Magic, C., Acciari, V. A., et al. 2019, Nature, 575, 459
Malesani, D., D'Elia, V., D'Avanzo, P., et al. 2016, GRB Coordinates Network, 18965, 1
Margutti, R., Genet, F., Granot, J., et al. 2010a, MNRAS, 402, 46
Margutti, R., Guidorzi, C., Chincarini, G., et al. 2010b, MNRAS, 406, 2149
Marongiu, M., & Guidorzi, C. 2021, A Python Approach for GRB Afterglow Analysis: sAGa (Software for AfterGlow Analysis), Tech. Rep. 99, OA Cagliari
Marongiu, M., Pellizzoni, A., Egron, E., et al. 2020, Exp. Astron., 49, 159
Marquette, J. B. 2018, Statistics for Astrophysics: Bayesian Methodology
Marshall, F. E., Antonelli, L. A., Burrows, D. N., et al. 2011, ApJ, 727, 132
Mazaeva, E., Pozanenko, A., & Minaev, P. 2018, Int. J Mod. Phys. D, 27, 1844012
McMullin, J. P., Waters, B., Schiebel, D., Young, W., & Golap, K. 2007, in Astronomical Data Analysis Software and Systems XVI, eds. R. A. Shaw, F. Hill, & D. J. Bell, ASP Conf. Ser., 376, 127
Melandri, A., Kobayashi, S., Mundell, C. G., et al. 2010, ApJ, 723, 1331
Mészáros, P. 2006, Rep. Prog. Phys., 69, 2259
Meszaros, P., & Rees, M. J. 1997, ApJ, 476, 232
Mészáros, P., & Rees, M. J. 1999, MNRAS, 306, L39
Misra, K., Bhattacharya, D., Sahu, D. K., et al. 2007, A&A, 464, 903
Misra, K., Resmi, L., Kann, D. A., et al. 2021, MNRAS, 504, 5685
Mooley, K. P., Fender, R. P., Staley, T. D., et al. 2016, GRB Coordinates Network, 19206, 1
Morrison, R., & McCammon, D. 1983, ApJ, 270, 119
Mundell, C. G., Melandri, A., Guidorzi, C., et al. 2007, ApJ, 660, 489
Nakar, E., Piran, T., & Waxman, E. 2003, JCAP, 2003, 005
Nousek, J. A., Kouveliotou, C., Grupe, D., et al. 2006, ApJ, 642, 389
Page, K. L., & Barthelmy, S. D. 2016, GRB Coordinates Network, 18951, 1
Panaitescu, A., & Kumar, P. 2002, ApJ, 571, 779
Panaitescu, A., Meszaros, P., & Rees, M. J. 1998, ApJ, 503, 314
Pei, Y. C. 1992, ApJ, 395, 130
Peng, F., Königl, A., & Granot, J. 2005, ApJ, 626, 966
Perley, D. A., Cenko, S. B., Corsi, A., et al. 2014, ApJ, 781, 37
Piran, T. 1999, Phys. Rep., 314, 575
Piran, T. 2004, Rev. Mod. Phys., 76, 1143
Planck Collaboration VI. 2020, A&A, 641, A6
Racusin, J. L., Karpov, S. V., Sokolowski, M., et al. 2008, Nature, 455, 183
Ramirez-Ruiz, E., Merloni, A., & Rees, M. J. 2001, MNRAS, 324, 1147
Rees, M. J., & Meszaros, P. 1992, MNRAS, 258, 41P
Resmi, L., Misra, K., Jóhannesson, G., et al. 2012, MNRAS, 427, 288
Ressler, S. M., & Laskar, T. 2017, ApJ, 845, 150
Rhoads, J. E. 1999, ApJ, 525, 737
Rhodes, L., van der Horst, A. J., Fender, R., et al. 2020, MNRAS, 496, 3326
Rickett, B. J. 1990, ARA&A, 28, 561
Roming, P. W. A., Kennedy, T. E., Mason, K. O., et al. 2005, Space Sci. Rev., 120, 95
Ryan, G., van Eerten, H., Piro, L., & Troja, E. 2020, ApJ, 896, 166
Santana, R., Barniol Duran, R., & Kumar, P. 2014, ApJ, 785, 29
Sari, R. 1999, ApJ, 524, L43
Sari, R. 2006, in Relativistic Jets: The Common Physics of AGN, Microquasars, and Gamma-Ray Bursts, eds. P. A. Hughes, & J. N. Bregman, AIP, Conf. Ser., 856, 33
Sari, R., & Esin, A. A. 2001, ApJ, 548, 787
Sari, R., & Piran, T. 1999, ApJ, 520, 641
Sari, R., Piran, T., & Narayan, R. 1998, ApJ, 497, L17
Sari, R., Piran, T., & Halpern, J. P. 1999, ApJ, 519, L17
Schlafly, E. F., & Finkbeiner, D. P. 2011, ApJ, 737, 103
Schulze, S., Klose, S., Björnsson, G., et al. 2011, A&A, 526, A23
Sharma, S. 2017, ARA&A, 55, 213
Sironi, L., Spitkovsky, A., & Arons, J. 2013, ApJ, 771, 54
Sironi, L., Keshet, U., & Lemoine, M. 2015, Space Sci. Rev., 191, 519
Starling, R. L. C., Rol, E., van der Horst, A. J., et al. 2009, MNRAS, 400, 90
Steele, I. A., Smith, R. J., Rees, P. C., et al. 2004, in Ground-based Telescopes, ed. J. M. Oschmann, Jr., Proc. SPIE, 5489, 679
Swarup, G. 1990, Indian J. Radio Space Phys., 19, 493
Thompson, A. R., Clark, B. G., Wade, C. M., & Napier, P. J. 1980, ApJS, 44, 151
Tonry, J. L., Stubbs, C. W., Lykke, K. R., et al. 2012, ApJ, 750, 99
Tsvetkova, A., Golenetskii, S., Aptekar, R., et al. 2016, GRB Coordinates Network, 18974, 1
van der Horst, A. J., Levan, A. J., Pooley, G. G., et al. 2015, MNRAS, 446, 4116
van Eerten, H. 2014, MNRAS, 442, 3495
van Eerten, H. 2018, Int. J. Modern Phys. D, 27, 1842002
van Eerten, H., Zhang, W., & MacFadyen, A. 2010a, ApJ, 722, 235
van Eerten, H. J., Leventis, K., Meliani, Z., Wijers, R. A. M. J., & Keppens, R. 2010b, MNRAS, 403, 300
van Eerten, H., van der Horst, A., & MacFadyen, A. 2012, ApJ, 749, 44
van Haarlem, M. P., Wise, M. W., Gunst, A. W., et al. 2013, A&A, 556, A2
Veres, P., Corsi, A., Frail, D. A., Cenko, S. B., & Perley, D. A. 2015, ApJ, 810, 31
Walker, M. A. 1998, MNRAS, 294, 307
Wang, X.-G., Zhang, B., Liang, E.-W., et al. 2018, ApJ, 859, 160
Waxman, E. 1997, ApJ, 491, L19
Waxman, E. 2003, Nature, 423, 388
Wijers, R. A. M. J., Rees, M. J., & Meszaros, P. 1997, MNRAS, 288, L51
Willingale, R., Starling, R. L. C., Beardmore, A. P., Tanvir, N. R., & O'Brien, P. T. 2013, MNRAS, 431, 394
Woosley, S. E., & Bloom, J. S. 2006, ARA&A, 44, 507
Wu, X. F., Dai, Z. G., Huang, Y. F., & Lu, T. 2005, MNRAS, 357, 1197
Wygoda, N., Waxman, E., & Frail, D. A. 2011, ApJ, 738, L23
Zauderer, B. A., Berger, E., Margutti, R., et al. 2013, ApJ, 767, 161
Zhang, B. 2019, The Physics of Gamma-Ray Bursts (Cambridge University Press)
Zhang, W., & MacFadyen, A. 2009, ApJ, 698, 1261
Zhang, B., & Mészáros, P. 2002, ApJ, 566, 712
Zhang, B., Fan, Y. Z., Dyks, J., et al. 2006, ApJ, 642, 354
Zhang, B., Liang, E., Page, K. L., et al. 2007, ApJ, 655, 989
Zhang, H., Christie, I. M., Petropoulou, M., Rueda-Becerril, J. M., & Giannios, D. 2020, MNRAS, 496, 974
Zwart, J. T. L., Barker, R. W., Biddulph, P., et al. 2008, MNRAS, 391, 1545

Appendix A: Additional tables

Table A.1. Swift XRT observations of GRB 160131A.

$t - t_0$ (days)	Flux density (mJy)	Uncertainty (mJy)	Frequency (Hz)
3.83×10^{-3}	3.78×10^{-2}	5.63×10^{-3}	6.65×10^{17}
3.85×10^{-3}	4.40×10^{-2}	6.55×10^{-3}	6.65×10^{17}
3.87×10^{-3}	4.39×10^{-2}	6.69×10^{-3}	6.65×10^{17}
3.89×10^{-3}	3.98×10^{-2}	6.34×10^{-3}	6.65×10^{17}
3.91×10^{-3}	3.77×10^{-2}	5.62×10^{-3}	6.65×10^{17}
3.94×10^{-3}	3.36×10^{-2}	5.35×10^{-3}	6.65×10^{17}
3.96×10^{-3}	4.20×10^{-2}	6.26×10^{-3}	6.65×10^{17}
3.98×10^{-3}	3.75×10^{-2}	5.59×10^{-3}	6.65×10^{17}
4.00×10^{-3}	3.66×10^{-2}	5.58×10^{-3}	6.65×10^{17}
4.02×10^{-3}	3.60×10^{-2}	5.61×10^{-3}	6.65×10^{17}
4.04×10^{-3}	3.97×10^{-2}	6.18×10^{-3}	6.65×10^{17}
4.07×10^{-3}	3.44×10^{-2}	5.13×10^{-3}	6.65×10^{17}
4.09×10^{-3}	3.07×10^{-2}	4.68×10^{-3}	6.65×10^{17}
4.11×10^{-3}	4.09×10^{-2}	6.36×10^{-3}	6.65×10^{17}
4.14×10^{-3}	3.44×10^{-2}	5.13×10^{-3}	6.65×10^{17}
4.16×10^{-3}	3.27×10^{-2}	4.98×10^{-3}	6.65×10^{17}
4.18×10^{-3}	4.34×10^{-2}	6.47×10^{-3}	6.65×10^{17}
4.20×10^{-3}	3.28×10^{-2}	4.83×10^{-3}	6.65×10^{17}
4.23×10^{-3}	3.69×10^{-2}	5.50×10^{-3}	6.65×10^{17}
4.25×10^{-3}	3.38×10^{-2}	5.15×10^{-3}	6.65×10^{17}
4.28×10^{-3}	2.72×10^{-2}	4.14×10^{-3}	6.65×10^{17}
4.31×10^{-3}	3.00×10^{-2}	4.47×10^{-3}	6.65×10^{17}
4.34×10^{-3}	2.99×10^{-2}	4.55×10^{-3}	6.65×10^{17}
4.36×10^{-3}	3.51×10^{-2}	5.47×10^{-3}	6.65×10^{17}
4.38×10^{-3}	3.95×10^{-2}	6.02×10^{-3}	6.65×10^{17}
4.41×10^{-3}	3.40×10^{-2}	5.06×10^{-3}	6.65×10^{17}
4.43×10^{-3}	3.45×10^{-2}	5.15×10^{-3}	6.65×10^{17}
4.46×10^{-3}	2.80×10^{-2}	4.17×10^{-3}	6.65×10^{17}
4.48×10^{-3}	3.07×10^{-2}	4.79×10^{-3}	6.65×10^{17}
4.51×10^{-3}	3.35×10^{-2}	5.00×10^{-3}	6.65×10^{17}
4.53×10^{-3}	3.24×10^{-2}	4.83×10^{-3}	6.65×10^{17}
4.56×10^{-3}	3.06×10^{-2}	4.57×10^{-3}	6.65×10^{17}
4.59×10^{-3}	2.28×10^{-2}	3.79×10^{-3}	6.65×10^{17}
4.62×10^{-3}	3.33×10^{-2}	4.96×10^{-3}	6.65×10^{17}
4.64×10^{-3}	4.41×10^{-2}	6.58×10^{-3}	6.65×10^{17}
4.66×10^{-3}	3.69×10^{-2}	5.88×10^{-3}	6.65×10^{17}
4.69×10^{-3}	3.22×10^{-2}	4.80×10^{-3}	6.65×10^{17}
4.71×10^{-3}	2.67×10^{-2}	4.07×10^{-3}	6.65×10^{17}
4.74×10^{-3}	3.81×10^{-2}	5.69×10^{-3}	6.65×10^{17}
4.76×10^{-3}	2.89×10^{-2}	4.41×10^{-3}	6.65×10^{17}
4.79×10^{-3}	3.62×10^{-2}	5.33×10^{-3}	6.65×10^{17}
4.82×10^{-3}	2.61×10^{-2}	4.06×10^{-3}	6.65×10^{17}
4.85×10^{-3}	2.88×10^{-2}	4.29×10^{-3}	6.65×10^{17}
4.87×10^{-3}	3.35×10^{-2}	4.99×10^{-3}	6.65×10^{17}
4.90×10^{-3}	2.87×10^{-2}	4.38×10^{-3}	6.65×10^{17}
4.93×10^{-3}	3.15×10^{-2}	4.90×10^{-3}	6.65×10^{17}
4.96×10^{-3}	2.53×10^{-2}	3.77×10^{-3}	6.65×10^{17}
4.99×10^{-3}	2.50×10^{-2}	3.89×10^{-3}	6.65×10^{17}
5.02×10^{-3}	2.39×10^{-2}	3.56×10^{-3}	6.65×10^{17}

Notes. $t - t_0$ indicates the epoch of observation, where t_0 is the GRB explosion date (57418.3476 MJD). Flux densities refers to an energy of 2.75 keV (6.65×10^{17} Hz).

Table A.1. continued.

$t - t_0$ (days)	Flux density (mJy)	Uncertainty (mJy)	Frequency (Hz)
5.05×10^{-3}	3.18×10^{-2}	4.74×10^{-3}	6.65×10^{17}
5.07×10^{-3}	3.85×10^{-2}	5.74×10^{-3}	6.65×10^{17}
5.10×10^{-3}	3.78×10^{-2}	5.75×10^{-3}	6.65×10^{17}
5.13×10^{-3}	2.16×10^{-2}	3.22×10^{-3}	6.65×10^{17}
5.16×10^{-3}	3.53×10^{-2}	5.26×10^{-3}	6.65×10^{17}
5.18×10^{-3}	3.01×10^{-2}	4.48×10^{-3}	6.65×10^{17}
5.21×10^{-3}	2.35×10^{-2}	3.66×10^{-3}	6.65×10^{17}
5.24×10^{-3}	3.05×10^{-2}	4.64×10^{-3}	6.65×10^{17}
5.27×10^{-3}	3.11×10^{-2}	4.74×10^{-3}	6.65×10^{17}
5.30×10^{-3}	2.78×10^{-2}	4.32×10^{-3}	6.65×10^{17}
5.33×10^{-3}	2.26×10^{-2}	3.59×10^{-3}	6.65×10^{17}
5.36×10^{-3}	4.01×10^{-2}	6.11×10^{-3}	6.65×10^{17}
5.38×10^{-3}	2.88×10^{-2}	4.49×10^{-3}	6.65×10^{17}
5.41×10^{-3}	3.42×10^{-2}	5.20×10^{-3}	6.65×10^{17}
5.43×10^{-3}	2.46×10^{-2}	3.67×10^{-3}	6.65×10^{17}
5.47×10^{-3}	2.82×10^{-2}	4.21×10^{-3}	6.65×10^{17}
5.49×10^{-3}	2.92×10^{-2}	4.45×10^{-3}	6.65×10^{17}
5.53×10^{-3}	2.06×10^{-2}	3.07×10^{-3}	6.65×10^{17}
5.56×10^{-3}	2.63×10^{-2}	3.92×10^{-3}	6.65×10^{17}
5.60×10^{-3}	2.27×10^{-2}	3.39×10^{-3}	6.65×10^{17}
5.63×10^{-3}	2.93×10^{-2}	4.37×10^{-3}	6.65×10^{17}
5.66×10^{-3}	2.63×10^{-2}	4.10×10^{-3}	6.65×10^{17}
5.69×10^{-3}	2.65×10^{-2}	4.03×10^{-3}	6.65×10^{17}
5.72×10^{-3}	2.22×10^{-2}	3.38×10^{-3}	6.65×10^{17}
5.76×10^{-3}	2.40×10^{-2}	3.57×10^{-3}	6.65×10^{17}
5.79×10^{-3}	2.43×10^{-2}	3.63×10^{-3}	6.65×10^{17}
5.83×10^{-3}	2.39×10^{-2}	3.81×10^{-3}	6.65×10^{17}
5.86×10^{-3}	2.03×10^{-2}	3.16×10^{-3}	6.65×10^{17}
5.90×10^{-3}	2.34×10^{-2}	3.64×10^{-3}	6.65×10^{17}
5.93×10^{-3}	2.45×10^{-2}	3.66×10^{-3}	6.65×10^{17}
5.97×10^{-3}	1.98×10^{-2}	2.95×10^{-3}	6.65×10^{17}
6.01×10^{-3}	2.44×10^{-2}	3.72×10^{-3}	6.65×10^{17}
6.04×10^{-3}	2.25×10^{-2}	3.35×10^{-3}	6.65×10^{17}
6.08×10^{-3}	1.85×10^{-2}	3.16×10^{-3}	6.65×10^{17}
6.12×10^{-3}	2.46×10^{-2}	3.67×10^{-3}	6.65×10^{17}
6.15×10^{-3}	2.28×10^{-2}	3.40×10^{-3}	6.65×10^{17}
6.19×10^{-3}	2.34×10^{-2}	3.50×10^{-3}	6.65×10^{17}
6.22×10^{-3}	2.83×10^{-2}	4.21×10^{-3}	6.65×10^{17}
6.25×10^{-3}	2.42×10^{-2}	3.69×10^{-3}	6.65×10^{17}
6.29×10^{-3}	2.32×10^{-2}	3.46×10^{-3}	6.65×10^{17}
6.32×10^{-3}	2.22×10^{-2}	3.38×10^{-3}	6.65×10^{17}
6.36×10^{-3}	1.68×10^{-2}	2.86×10^{-3}	6.65×10^{17}
6.40×10^{-3}	2.58×10^{-2}	3.85×10^{-3}	6.65×10^{17}
6.44×10^{-3}	2.18×10^{-2}	3.25×10^{-3}	6.65×10^{17}
6.47×10^{-3}	2.25×10^{-2}	3.83×10^{-3}	6.65×10^{17}
6.51×10^{-3}	1.58×10^{-2}	2.43×10^{-3}	6.65×10^{17}
6.56×10^{-3}	1.89×10^{-2}	2.87×10^{-3}	6.65×10^{17}
6.60×10^{-3}	2.06×10^{-2}	3.21×10^{-3}	6.65×10^{17}
6.64×10^{-3}	2.32×10^{-2}	3.46×10^{-3}	6.65×10^{17}
6.68×10^{-3}	1.80×10^{-2}	2.75×10^{-3}	6.65×10^{17}
6.72×10^{-3}	2.37×10^{-2}	3.61×10^{-3}	6.65×10^{17}
6.76×10^{-3}	1.98×10^{-2}	3.09×10^{-3}	6.65×10^{17}
6.80×10^{-3}	2.11×10^{-2}	3.14×10^{-3}	6.65×10^{17}
6.83×10^{-3}	2.68×10^{-2}	4.09×10^{-3}	6.65×10^{17}
6.87×10^{-3}	1.99×10^{-2}	3.03×10^{-3}	6.65×10^{17}

Table A.1. continued.

$t-t_0$ (days)	Flux density (mJy)	Uncertainty (mJy)	Frequency (Hz)
4.45×10^{-2}	2.58×10^{-3}	5.67×10^{-4}	6.65×10^{17}
4.50×10^{-2}	1.54×10^{-3}	3.46×10^{-4}	6.65×10^{17}
4.57×10^{-2}	1.78×10^{-3}	3.90×10^{-4}	6.65×10^{17}
4.63×10^{-2}	2.13×10^{-3}	4.79×10^{-4}	6.65×10^{17}
4.71×10^{-2}	1.21×10^{-3}	2.68×10^{-4}	6.65×10^{17}
4.79×10^{-2}	1.67×10^{-3}	3.75×10^{-4}	6.65×10^{17}
4.85×10^{-2}	2.73×10^{-3}	5.74×10^{-4}	6.65×10^{17}
4.90×10^{-2}	2.01×10^{-3}	4.52×10^{-4}	6.65×10^{17}
4.95×10^{-2}	2.00×10^{-3}	4.50×10^{-4}	6.65×10^{17}
5.00×10^{-2}	2.93×10^{-3}	6.58×10^{-4}	6.65×10^{17}
5.05×10^{-2}	2.09×10^{-3}	4.36×10^{-4}	6.65×10^{17}
5.10×10^{-2}	2.38×10^{-3}	5.34×10^{-4}	6.65×10^{17}
5.15×10^{-2}	2.70×10^{-3}	5.91×10^{-4}	6.65×10^{17}
5.21×10^{-2}	1.45×10^{-3}	3.28×10^{-4}	6.65×10^{17}
5.27×10^{-2}	2.22×10^{-3}	4.85×10^{-4}	6.65×10^{17}
5.32×10^{-2}	2.21×10^{-3}	4.98×10^{-4}	6.65×10^{17}
5.37×10^{-2}	2.11×10^{-3}	4.62×10^{-4}	6.65×10^{17}
5.43×10^{-2}	1.74×10^{-3}	3.84×10^{-4}	6.65×10^{17}
5.50×10^{-2}	1.93×10^{-3}	4.21×10^{-4}	6.65×10^{17}
5.55×10^{-2}	2.23×10^{-3}	5.03×10^{-4}	6.65×10^{17}
5.61×10^{-2}	1.82×10^{-3}	4.08×10^{-4}	6.65×10^{17}
5.68×10^{-2}	1.42×10^{-3}	3.20×10^{-4}	6.65×10^{17}
5.75×10^{-2}	1.61×10^{-3}	3.62×10^{-4}	6.65×10^{17}
5.82×10^{-2}	1.76×10^{-3}	3.85×10^{-4}	6.65×10^{17}
5.88×10^{-2}	2.23×10^{-3}	4.76×10^{-4}	6.65×10^{17}
5.95×10^{-2}	1.49×10^{-3}	3.29×10^{-4}	6.65×10^{17}
6.01×10^{-2}	2.02×10^{-3}	4.52×10^{-4}	6.65×10^{17}
6.07×10^{-2}	2.14×10^{-3}	4.81×10^{-4}	6.65×10^{17}
6.13×10^{-2}	1.74×10^{-3}	3.81×10^{-4}	6.65×10^{17}
6.20×10^{-2}	1.49×10^{-3}	3.27×10^{-4}	6.65×10^{17}
6.26×10^{-2}	2.75×10^{-3}	6.16×10^{-4}	6.65×10^{17}
6.31×10^{-2}	1.69×10^{-3}	3.69×10^{-4}	6.65×10^{17}
6.37×10^{-2}	2.57×10^{-3}	5.79×10^{-4}	6.65×10^{17}
6.43×10^{-2}	1.53×10^{-3}	3.45×10^{-4}	6.65×10^{17}
6.50×10^{-2}	1.55×10^{-3}	3.40×10^{-4}	6.65×10^{17}
6.58×10^{-2}	1.59×10^{-3}	3.58×10^{-4}	6.65×10^{17}
6.64×10^{-2}	2.10×10^{-3}	4.61×10^{-4}	6.65×10^{17}
6.70×10^{-2}	1.75×10^{-3}	3.92×10^{-4}	6.65×10^{17}
6.76×10^{-2}	1.74×10^{-3}	3.83×10^{-4}	6.65×10^{17}
6.83×10^{-2}	1.42×10^{-3}	3.20×10^{-4}	6.65×10^{17}
6.89×10^{-2}	2.72×10^{-3}	6.14×10^{-4}	6.65×10^{17}
6.95×10^{-2}	1.92×10^{-3}	4.19×10^{-4}	6.65×10^{17}
7.01×10^{-2}	1.42×10^{-3}	3.19×10^{-4}	6.65×10^{17}
7.08×10^{-2}	2.00×10^{-3}	4.41×10^{-4}	6.65×10^{17}
7.15×10^{-2}	1.39×10^{-3}	3.05×10^{-4}	6.65×10^{17}
7.27×10^{-2}	1.11×10^{-3}	2.13×10^{-4}	6.65×10^{17}
1.11×10^{-1}	1.62×10^{-3}	3.65×10^{-4}	6.65×10^{17}
1.11×10^{-1}	1.19×10^{-3}	2.68×10^{-4}	6.65×10^{17}
1.12×10^{-1}	8.89×10^{-4}	2.01×10^{-4}	6.65×10^{17}
1.13×10^{-1}	9.68×10^{-4}	2.19×10^{-4}	6.65×10^{17}
1.13×10^{-1}	1.46×10^{-3}	3.28×10^{-4}	6.65×10^{17}
1.14×10^{-1}	1.30×10^{-3}	2.93×10^{-4}	6.65×10^{17}
1.14×10^{-1}	9.37×10^{-4}	2.06×10^{-4}	6.65×10^{17}
1.15×10^{-1}	9.77×10^{-4}	2.14×10^{-4}	6.65×10^{17}
1.16×10^{-1}	1.04×10^{-3}	2.23×10^{-4}	6.65×10^{17}

Table A.1. continued.

$t-t_0$ (days)	Flux density (mJy)	Uncertainty (mJy)	Frequency (Hz)
1.17×10^{-1}	8.08×10^{-4}	1.78×10^{-4}	6.65×10^{17}
1.17×10^{-1}	1.29×10^{-3}	2.91×10^{-4}	6.65×10^{17}
1.18×10^{-1}	9.14×10^{-4}	2.05×10^{-4}	6.65×10^{17}
1.18×10^{-1}	1.14×10^{-3}	2.56×10^{-4}	6.65×10^{17}
1.19×10^{-1}	1.51×10^{-3}	3.40×10^{-4}	6.65×10^{17}
1.20×10^{-1}	7.89×10^{-4}	1.77×10^{-4}	6.65×10^{17}
1.20×10^{-1}	9.45×10^{-4}	2.14×10^{-4}	6.65×10^{17}
1.21×10^{-1}	8.47×10^{-4}	1.91×10^{-4}	6.65×10^{17}
1.22×10^{-1}	6.14×10^{-4}	1.38×10^{-4}	6.65×10^{17}
1.23×10^{-1}	9.51×10^{-4}	2.09×10^{-4}	6.65×10^{17}
1.24×10^{-1}	8.89×10^{-4}	1.96×10^{-4}	6.65×10^{17}
1.24×10^{-1}	1.20×10^{-3}	2.71×10^{-4}	6.65×10^{17}
1.25×10^{-1}	1.04×10^{-3}	2.33×10^{-4}	6.65×10^{17}
1.26×10^{-1}	9.02×10^{-4}	2.04×10^{-4}	6.65×10^{17}
1.26×10^{-1}	1.07×10^{-3}	2.42×10^{-4}	6.65×10^{17}
1.27×10^{-1}	7.15×10^{-4}	1.61×10^{-4}	6.65×10^{17}
1.28×10^{-1}	1.03×10^{-3}	2.32×10^{-4}	6.65×10^{17}
1.29×10^{-1}	9.80×10^{-4}	2.20×10^{-4}	6.65×10^{17}
1.29×10^{-1}	8.43×10^{-4}	1.91×10^{-4}	6.65×10^{17}
1.30×10^{-1}	6.84×10^{-4}	1.53×10^{-4}	6.65×10^{17}
1.31×10^{-1}	1.33×10^{-3}	2.92×10^{-4}	6.65×10^{17}
1.31×10^{-1}	9.54×10^{-4}	2.16×10^{-4}	6.65×10^{17}
1.32×10^{-1}	6.50×10^{-4}	1.46×10^{-4}	6.65×10^{17}
1.33×10^{-1}	1.04×10^{-3}	2.29×10^{-4}	6.65×10^{17}
1.34×10^{-1}	6.90×10^{-4}	1.56×10^{-4}	6.65×10^{17}
1.35×10^{-1}	1.42×10^{-3}	3.04×10^{-4}	6.65×10^{17}
1.35×10^{-1}	7.35×10^{-4}	1.58×10^{-4}	6.65×10^{17}
1.36×10^{-1}	1.01×10^{-3}	2.22×10^{-4}	6.65×10^{17}
1.37×10^{-1}	6.91×10^{-4}	1.57×10^{-4}	6.65×10^{17}
1.38×10^{-1}	1.02×10^{-3}	2.28×10^{-4}	6.65×10^{17}
1.39×10^{-1}	7.07×10^{-4}	1.28×10^{-4}	6.65×10^{17}
1.77×10^{-1}	6.81×10^{-4}	1.53×10^{-4}	6.65×10^{17}
1.78×10^{-1}	6.84×10^{-4}	1.53×10^{-4}	6.65×10^{17}
1.79×10^{-1}	5.47×10^{-4}	1.23×10^{-4}	6.65×10^{17}
1.80×10^{-1}	5.09×10^{-4}	1.12×10^{-4}	6.65×10^{17}
1.81×10^{-1}	3.81×10^{-4}	8.60×10^{-5}	6.65×10^{17}
1.82×10^{-1}	7.39×10^{-4}	1.66×10^{-4}	6.65×10^{17}
1.84×10^{-1}	3.69×10^{-4}	8.36×10^{-5}	6.65×10^{17}
1.86×10^{-1}	4.36×10^{-4}	9.88×10^{-5}	6.65×10^{17}
1.87×10^{-1}	4.82×10^{-4}	1.09×10^{-4}	6.65×10^{17}
1.89×10^{-1}	4.80×10^{-4}	1.08×10^{-4}	6.65×10^{17}
1.90×10^{-1}	6.13×10^{-4}	1.35×10^{-4}	6.65×10^{17}
1.91×10^{-1}	4.82×10^{-4}	1.09×10^{-4}	6.65×10^{17}
1.93×10^{-1}	5.13×10^{-4}	1.16×10^{-4}	6.65×10^{17}
1.94×10^{-1}	3.27×10^{-4}	7.44×10^{-5}	6.65×10^{17}
1.96×10^{-1}	4.31×10^{-4}	9.59×10^{-5}	6.65×10^{17}
1.98×10^{-1}	5.54×10^{-4}	1.25×10^{-4}	6.65×10^{17}
1.99×10^{-1}	4.10×10^{-4}	9.27×10^{-5}	6.65×10^{17}
2.00×10^{-1}	5.25×10^{-4}	1.19×10^{-4}	6.65×10^{17}
2.02×10^{-1}	3.88×10^{-4}	8.56×10^{-5}	6.65×10^{17}
2.03×10^{-1}	5.56×10^{-4}	1.22×10^{-4}	6.65×10^{17}
2.05×10^{-1}	4.53×10^{-4}	8.24×10^{-5}	6.65×10^{17}
2.45×10^{-1}	4.07×10^{-4}	9.21×10^{-5}	6.65×10^{17}
2.46×10^{-1}	4.23×10^{-4}	9.48×10^{-5}	6.65×10^{17}
2.47×10^{-1}	4.00×10^{-4}	8.97×10^{-5}	6.65×10^{17}

Table A.1. continued.

$t-t_0$ (days)	Flux density (mJy)	Uncertainty (mJy)	Frequency (Hz)
2.48×10^{-1}	4.77×10^{-4}	1.07×10^{-4}	6.65×10^{17}
2.49×10^{-1}	2.92×10^{-4}	6.56×10^{-5}	6.65×10^{17}
2.50×10^{-1}	3.42×10^{-4}	7.70×10^{-5}	6.65×10^{17}
2.51×10^{-1}	3.83×10^{-4}	8.61×10^{-5}	6.65×10^{17}
2.52×10^{-1}	4.40×10^{-4}	9.62×10^{-5}	6.65×10^{17}
2.53×10^{-1}	5.27×10^{-4}	1.19×10^{-4}	6.65×10^{17}
2.55×10^{-1}	2.24×10^{-4}	5.06×10^{-5}	6.65×10^{17}
2.56×10^{-1}	2.81×10^{-4}	6.37×10^{-5}	6.65×10^{17}
2.58×10^{-1}	3.89×10^{-4}	8.82×10^{-5}	6.65×10^{17}
2.59×10^{-1}	3.40×10^{-4}	8.15×10^{-5}	6.65×10^{17}
2.61×10^{-1}	2.86×10^{-4}	7.29×10^{-5}	6.65×10^{17}
2.63×10^{-1}	2.97×10^{-4}	6.89×10^{-5}	6.65×10^{17}
2.64×10^{-1}	3.89×10^{-4}	8.94×10^{-5}	6.65×10^{17}
2.66×10^{-1}	3.11×10^{-4}	6.93×10^{-5}	6.65×10^{17}
2.69×10^{-1}	3.19×10^{-4}	7.42×10^{-5}	6.65×10^{17}
2.71×10^{-1}	3.35×10^{-4}	5.73×10^{-5}	6.65×10^{17}
3.14×10^{-1}	4.85×10^{-4}	1.09×10^{-4}	6.65×10^{17}
3.15×10^{-1}	2.38×10^{-4}	5.33×10^{-5}	6.65×10^{17}
3.17×10^{-1}	2.04×10^{-4}	4.61×10^{-5}	6.65×10^{17}
3.19×10^{-1}	2.11×10^{-4}	4.75×10^{-5}	6.65×10^{17}
3.21×10^{-1}	2.91×10^{-4}	6.56×10^{-5}	6.65×10^{17}
3.23×10^{-1}	2.18×10^{-4}	4.93×10^{-5}	6.65×10^{17}
3.25×10^{-1}	2.35×10^{-4}	5.31×10^{-5}	6.65×10^{17}
3.27×10^{-1}	2.35×10^{-4}	5.32×10^{-5}	6.65×10^{17}
3.29×10^{-1}	1.88×10^{-4}	4.32×10^{-5}	6.65×10^{17}
3.31×10^{-1}	2.54×10^{-4}	5.79×10^{-5}	6.65×10^{17}
3.32×10^{-1}	3.51×10^{-4}	7.92×10^{-5}	6.65×10^{17}
3.34×10^{-1}	2.65×10^{-4}	5.77×10^{-5}	6.65×10^{17}
3.36×10^{-1}	1.76×10^{-4}	4.05×10^{-5}	6.65×10^{17}
3.38×10^{-1}	2.18×10^{-4}	4.50×10^{-5}	6.65×10^{17}
3.84×10^{-1}	1.95×10^{-4}	4.27×10^{-5}	6.65×10^{17}
3.87×10^{-1}	2.42×10^{-4}	5.29×10^{-5}	6.65×10^{17}
3.90×10^{-1}	1.84×10^{-4}	4.04×10^{-5}	6.65×10^{17}
3.92×10^{-1}	1.89×10^{-4}	4.28×10^{-5}	6.65×10^{17}
3.95×10^{-1}	1.71×10^{-4}	3.90×10^{-5}	6.65×10^{17}
3.98×10^{-1}	2.16×10^{-4}	4.87×10^{-5}	6.65×10^{17}
4.01×10^{-1}	2.06×10^{-4}	4.66×10^{-5}	6.65×10^{17}
4.04×10^{-1}	1.87×10^{-4}	3.70×10^{-5}	6.65×10^{17}
4.53×10^{-1}	2.05×10^{-4}	4.64×10^{-5}	6.65×10^{17}
4.55×10^{-1}	2.09×10^{-4}	4.70×10^{-5}	6.65×10^{17}
4.57×10^{-1}	1.75×10^{-4}	3.86×10^{-5}	6.65×10^{17}
4.59×10^{-1}	2.04×10^{-4}	4.49×10^{-5}	6.65×10^{17}
4.61×10^{-1}	1.48×10^{-4}	3.72×10^{-5}	6.65×10^{17}
4.64×10^{-1}	1.02×10^{-4}	2.64×10^{-5}	6.65×10^{17}
4.67×10^{-1}	1.57×10^{-4}	3.53×10^{-5}	6.65×10^{17}
4.70×10^{-1}	1.42×10^{-4}	2.72×10^{-5}	6.65×10^{17}
5.22×10^{-1}	1.61×10^{-4}	3.62×10^{-5}	6.65×10^{17}
5.24×10^{-1}	1.39×10^{-4}	3.63×10^{-5}	6.65×10^{17}
5.26×10^{-1}	1.68×10^{-4}	3.80×10^{-5}	6.65×10^{17}
5.28×10^{-1}	2.72×10^{-4}	6.10×10^{-5}	6.65×10^{17}
5.30×10^{-1}	1.43×10^{-4}	3.73×10^{-5}	6.65×10^{17}
5.32×10^{-1}	1.26×10^{-4}	3.18×10^{-5}	6.65×10^{17}

Table A.1. continued.

$t-t_0$ (days)	Flux density (mJy)	Uncertainty (mJy)	Frequency (Hz)
5.34×10^{-1}	1.46×10^{-4}	3.68×10^{-5}	6.65×10^{17}
5.37×10^{-1}	2.14×10^{-4}	3.52×10^{-5}	6.65×10^{17}
5.78×10^{-1}	1.07×10^{-4}	2.80×10^{-5}	6.65×10^{17}
5.80×10^{-1}	1.24×10^{-4}	3.27×10^{-5}	6.65×10^{17}
5.83×10^{-1}	1.46×10^{-4}	3.49×10^{-5}	6.65×10^{17}
5.85×10^{-1}	1.43×10^{-4}	3.72×10^{-5}	6.65×10^{17}
5.87×10^{-1}	1.03×10^{-4}	2.70×10^{-5}	6.65×10^{17}
5.90×10^{-1}	1.47×10^{-4}	3.83×10^{-5}	6.65×10^{17}
5.92×10^{-1}	1.40×10^{-4}	3.43×10^{-5}	6.65×10^{17}
5.95×10^{-1}	9.46×10^{-5}	2.47×10^{-5}	6.65×10^{17}
5.98×10^{-1}	1.37×10^{-4}	3.17×10^{-5}	6.65×10^{17}
6.01×10^{-1}	1.03×10^{-4}	2.63×10^{-5}	6.65×10^{17}
6.04×10^{-1}	1.13×10^{-4}	2.68×10^{-5}	6.65×10^{17}
6.43×10^{-1}	1.43×10^{-4}	3.55×10^{-5}	6.65×10^{17}
6.69×10^{-1}	8.23×10^{-5}	1.97×10^{-5}	6.65×10^{17}
7.10×10^{-1}	1.87×10^{-4}	3.76×10^{-5}	6.65×10^{17}
7.35×10^{-1}	1.13×10^{-4}	2.12×10^{-5}	6.65×10^{17}
7.78×10^{-1}	9.22×10^{-5}	1.98×10^{-5}	6.65×10^{17}
7.96×10^{-1}	9.82×10^{-5}	2.56×10^{-5}	6.65×10^{17}
7.99×10^{-1}	8.58×10^{-5}	2.24×10^{-5}	6.65×10^{17}
8.03×10^{-1}	1.13×10^{-4}	2.49×10^{-5}	6.65×10^{17}
8.53×10^{-1}	1.03×10^{-4}	2.71×10^{-5}	6.65×10^{17}
8.66×10^{-1}	1.45×10^{-4}	3.82×10^{-5}	6.65×10^{17}
8.69×10^{-1}	1.29×10^{-4}	3.07×10^{-5}	6.65×10^{17}
9.10×10^{-1}	1.11×10^{-4}	2.89×10^{-5}	6.65×10^{17}
9.12×10^{-1}	1.11×10^{-4}	2.91×10^{-5}	6.65×10^{17}
9.15×10^{-1}	9.59×10^{-5}	2.51×10^{-5}	6.65×10^{17}
9.18×10^{-1}	1.01×10^{-4}	2.64×10^{-5}	6.65×10^{17}
9.21×10^{-1}	1.09×10^{-4}	2.84×10^{-5}	6.65×10^{17}
9.26×10^{-1}	4.28×10^{-5}	1.14×10^{-5}	6.65×10^{17}
9.30×10^{-1}	1.04×10^{-4}	2.74×10^{-5}	6.65×10^{17}
9.33×10^{-1}	1.05×10^{-4}	2.75×10^{-5}	6.65×10^{17}
9.36×10^{-1}	1.13×10^{-4}	2.86×10^{-5}	6.65×10^{17}
9.86×10^{-1}	1.04×10^{-4}	2.73×10^{-5}	6.65×10^{17}
9.99×10^{-1}	1.02×10^{-4}	2.66×10^{-5}	6.65×10^{17}
1.00	9.42×10^{-5}	2.30×10^{-5}	6.65×10^{17}
1.06	9.43×10^{-5}	1.87×10^{-5}	6.65×10^{17}
1.12	7.07×10^{-5}	1.46×10^{-5}	6.65×10^{17}
1.19	5.40×10^{-5}	1.29×10^{-5}	6.65×10^{17}
1.24	9.14×10^{-5}	2.38×10^{-5}	6.65×10^{17}
1.25	5.04×10^{-5}	1.32×10^{-5}	6.65×10^{17}
1.25	4.16×10^{-5}	1.09×10^{-5}	6.65×10^{17}
1.26	5.18×10^{-5}	1.35×10^{-5}	6.65×10^{17}
1.27	6.78×10^{-5}	1.57×10^{-5}	6.65×10^{17}
1.33	6.54×10^{-5}	1.56×10^{-5}	6.65×10^{17}
1.43	3.81×10^{-5}	1.00×10^{-5}	6.65×10^{17}
1.49	3.32×10^{-5}	6.54×10^{-6}	6.65×10^{17}
2.02	1.51×10^{-5}	4.06×10^{-6}	6.65×10^{17}
2.35	1.12×10^{-5}	2.91×10^{-6}	6.65×10^{17}
3.01	1.19×10^{-5}	2.40×10^{-6}	6.65×10^{17}
4.71	5.35×10^{-6}	1.10×10^{-6}	6.65×10^{17}
7.27	2.39×10^{-6}	6.52×10^{-7}	6.65×10^{17}

Table A.2. Swift XRT Observations of GRB 160131A.

$t-t_0$ (days)	Flux density (mJy)	Uncertainty (mJy)	Filter	Frequency (Hz)
0.093	1.191	0.054	g’	6.47×10^{14}
0.094	1.180	0.053	g’	6.47×10^{14}
0.094	1.170	0.053	g’	6.47×10^{14}
0.095	1.138	0.051	g’	6.47×10^{14}
0.103	1.057	0.029	g’	6.47×10^{14}
0.104	1.047	0.029	g’	6.47×10^{14}
0.105	1.028	0.028	g’	6.47×10^{14}
0.106	0.991	0.036	g’	6.47×10^{14}
0.121	0.855	0.031	g’	6.47×10^{14}
0.122	0.840	0.030	g’	6.47×10^{14}
0.122	0.863	0.031	g’	6.47×10^{14}
0.123	0.832	0.023	g’	6.47×10^{14}
0.130	0.752	0.034	g’	6.47×10^{14}
0.131	0.759	0.021	g’	6.47×10^{14}
0.131	0.752	0.034	g’	6.47×10^{14}
0.131	0.766	0.021	g’	6.47×10^{14}
0.131	0.752	0.027	g’	6.47×10^{14}
0.132	0.731	0.026	g’	6.47×10^{14}
0.132	0.752	0.020	g’	6.47×10^{14}
0.133	0.759	0.021	g’	6.47×10^{14}
0.140	0.673	0.036	g’	6.47×10^{14}
0.141	0.686	0.019	g’	6.47×10^{14}
0.141	0.686	0.025	g’	6.47×10^{14}
0.142	0.667	0.018	g’	6.47×10^{14}
0.142	0.673	0.018	g’	6.47×10^{14}
0.143	0.679	0.019	g’	6.47×10^{14}
0.151	0.619	0.017	g’	6.47×10^{14}
0.153	0.619	0.017	g’	6.47×10^{14}
0.219	0.429	0.027	g’	6.47×10^{14}
0.220	0.387	0.024	g’	6.47×10^{14}
0.221	0.421	0.030	g’	6.47×10^{14}
0.229	0.402	0.029	g’	6.47×10^{14}
0.229	0.398	0.021	g’	6.47×10^{14}
0.230	0.387	0.017	g’	6.47×10^{14}
0.231	0.384	0.021	g’	6.47×10^{14}
0.239	0.377	0.017	g’	6.47×10^{14}
0.241	0.384	0.014	g’	6.47×10^{14}
0.979	0.084	0.006	g’	6.47×10^{14}
0.980	0.081	0.006	g’	6.47×10^{14}
1.143	0.069	0.004	g’	6.47×10^{14}
0.053	4.169	0.188	i’	4.03×10^{14}
0.053	4.169	0.151	i’	4.03×10^{14}
0.059	3.802	0.171	i’	4.03×10^{14}
0.060	3.733	0.168	i’	4.03×10^{14}
0.066	3.192	0.144	i’	4.03×10^{14}
0.067	3.133	0.141	i’	4.03×10^{14}
0.076	2.780	0.125	i’	4.03×10^{14}
0.077	2.729	0.123	i’	4.03×10^{14}
0.090	2.188	0.118	i’	4.03×10^{14}
0.091	2.270	0.122	i’	4.03×10^{14}
0.091	2.229	0.100	i’	4.03×10^{14}

Notes. $t-t_0$ indicates the epoch of observation, where t_0 is the GRB explosion date (57418.3476 MJD). Flux densities refers to an energy of 2.75 keV (6.65×10^{17} Hz).

Table A.2. continued.

$t-t_0$ (days)	Flux density (mJy)	Uncertainty (mJy)	Filter	Frequency (Hz)
0.092	2.188	0.118	i’	4.03×10^{14}
0.093	2.188	0.137	i’	4.03×10^{14}
0.095	2.032	0.074	i’	4.03×10^{14}
0.096	2.051	0.092	i’	4.03×10^{14}
0.099	1.977	0.106	i’	4.03×10^{14}
0.100	1.959	0.105	i’	4.03×10^{14}
0.101	1.941	0.104	i’	4.03×10^{14}
0.102	1.923	0.103	i’	4.03×10^{14}
0.102	1.837	0.066	i’	4.03×10^{14}
0.103	1.820	0.066	i’	4.03×10^{14}
0.111	1.629	0.073	i’	4.03×10^{14}
0.113	1.600	0.058	i’	4.03×10^{14}
0.119	1.472	0.066	i’	4.03×10^{14}
0.120	1.472	0.079	i’	4.03×10^{14}
0.121	1.500	0.094	i’	4.03×10^{14}
0.127	1.380	0.062	i’	4.03×10^{14}
0.128	1.343	0.072	i’	4.03×10^{14}
0.128	1.380	0.074	i’	4.03×10^{14}
0.129	1.393	0.087	i’	4.03×10^{14}
0.129	1.368	0.074	i’	4.03×10^{14}
0.129	1.393	0.087	i’	4.03×10^{14}
0.130	1.331	0.060	i’	4.03×10^{14}
0.130	1.343	0.084	i’	4.03×10^{14}
0.137	1.282	0.069	i’	4.03×10^{14}
0.137	1.259	0.079	i’	4.03×10^{14}
0.138	1.271	0.068	i’	4.03×10^{14}
0.138	1.191	0.043	i’	4.03×10^{14}
0.139	1.247	0.067	i’	4.03×10^{14}
0.139	1.191	0.043	i’	4.03×10^{14}
0.148	1.138	0.061	i’	4.03×10^{14}
0.149	1.127	0.061	i’	4.03×10^{14}
0.178	0.840	0.030	i’	4.03×10^{14}
0.179	0.871	0.032	i’	4.03×10^{14}
0.181	0.855	0.031	i’	4.03×10^{14}
0.182	0.817	0.030	i’	4.03×10^{14}
0.184	0.840	0.030	i’	4.03×10^{14}
0.188	0.855	0.068	i’	4.03×10^{14}
0.188	0.817	0.065	i’	4.03×10^{14}
0.193	0.780	0.049	i’	4.03×10^{14}
0.194	0.752	0.040	i’	4.03×10^{14}
0.200	0.766	0.048	i’	4.03×10^{14}
0.201	0.752	0.053	i’	4.03×10^{14}
0.209	0.718	0.039	i’	4.03×10^{14}
0.211	0.738	0.040	i’	4.03×10^{14}
0.217	0.738	0.052	i’	4.03×10^{14}
0.218	0.724	0.064	i’	4.03×10^{14}
0.219	0.698	0.056	i’	4.03×10^{14}
0.225	0.731	0.052	i’	4.03×10^{14}
0.226	0.711	0.051	i’	4.03×10^{14}
0.227	0.718	0.057	i’	4.03×10^{14}
0.228	0.686	0.055	i’	4.03×10^{14}
0.236	0.655	0.035	i’	4.03×10^{14}
0.237	0.643	0.035	i’	4.03×10^{14}
0.963	0.156	0.008	i’	4.03×10^{14}

Table A.2. continued.

$t - t_0$ (days)	Flux density (mJy)	Uncertainty (mJy)	Filter	Frequency (Hz)
0.965	0.147	0.008	i’	4.03×10^{14}
0.966	0.157	0.008	i’	4.03×10^{14}
0.968	0.147	0.009	i’	4.03×10^{14}
0.969	0.154	0.010	i’	4.03×10^{14}
1.178	0.107	0.008	i’	4.03×10^{14}
1.989	0.036	0.006	i’	4.03×10^{14}
2.986	0.021	0.002	i’	4.03×10^{14}
3.543	0.015	0.000	i’	4.03×10^{14}
5.477	0.007	0.001	i’	4.03×10^{14}
6.543	0.005	0.001	i’	4.03×10^{14}
0.052	3.373	0.062	r’	4.90×10^{14}
0.052	3.373	0.062	r’	4.90×10^{14}
0.057	3.076	0.084	r’	4.90×10^{14}
0.058	3.076	0.056	r’	4.90×10^{14}
0.065	2.630	0.048	r’	4.90×10^{14}
0.065	2.630	0.048	r’	4.90×10^{14}
0.073	2.291	0.062	r’	4.90×10^{14}
0.074	2.249	0.041	r’	4.90×10^{14}
0.089	1.820	0.050	r’	4.90×10^{14}
0.089	1.820	0.050	r’	4.90×10^{14}
0.090	1.787	0.049	r’	4.90×10^{14}
0.090	1.787	0.049	r’	4.90×10^{14}
0.093	1.691	0.031	r’	4.90×10^{14}
0.094	1.675	0.031	r’	4.90×10^{14}
0.096	1.644	0.030	r’	4.90×10^{14}
0.097	1.629	0.030	r’	4.90×10^{14}
0.097	1.600	0.029	r’	4.90×10^{14}
0.098	1.585	0.029	r’	4.90×10^{14}
0.101	1.528	0.028	r’	4.90×10^{14}
0.101	1.486	0.027	r’	4.90×10^{14}
0.107	1.393	0.025	r’	4.90×10^{14}
0.108	1.368	0.025	r’	4.90×10^{14}
0.109	1.355	0.025	r’	4.90×10^{14}
0.110	1.343	0.025	r’	4.90×10^{14}
0.117	1.213	0.033	r’	4.90×10^{14}
0.118	1.247	0.034	r’	4.90×10^{14}
0.118	1.191	0.032	r’	4.90×10^{14}
0.119	1.225	0.033	r’	4.90×10^{14}
0.124	1.148	0.021	r’	4.90×10^{14}
0.124	1.170	0.021	r’	4.90×10^{14}
0.125	1.107	0.020	r’	4.90×10^{14}
0.126	1.148	0.031	r’	4.90×10^{14}
0.126	1.107	0.020	r’	4.90×10^{14}
0.126	1.086	0.030	r’	4.90×10^{14}
0.127	1.097	0.030	r’	4.90×10^{14}
0.127	1.097	0.040	r’	4.90×10^{14}
0.133	1.038	0.028	r’	4.90×10^{14}
0.134	1.028	0.028	r’	4.90×10^{14}
0.134	1.019	0.019	r’	4.90×10^{14}
0.135	1.009	0.018	r’	4.90×10^{14}
0.135	1.000	0.018	r’	4.90×10^{14}

Table A.2. continued.

$t - t_0$ (days)	Flux density (mJy)	Uncertainty (mJy)	Filter	Frequency (Hz)
0.136	1.009	0.018	r’	4.90×10^{14}
0.144	0.921	0.017	r’	4.90×10^{14}
0.146	0.912	0.025	r’	4.90×10^{14}
0.170	0.738	0.013	r’	4.90×10^{14}
0.171	0.738	0.013	r’	4.90×10^{14}
0.173	0.731	0.013	r’	4.90×10^{14}
0.174	0.718	0.013	r’	4.90×10^{14}
0.176	0.705	0.013	r’	4.90×10^{14}
0.187	0.667	0.024	r’	4.90×10^{14}
0.187	0.679	0.031	r’	4.90×10^{14}
0.191	0.643	0.018	r’	4.90×10^{14}
0.192	0.649	0.018	r’	4.90×10^{14}
0.199	0.643	0.018	r’	4.90×10^{14}
0.199	0.619	0.017	r’	4.90×10^{14}
0.206	0.603	0.011	r’	4.90×10^{14}
0.208	0.597	0.011	r’	4.90×10^{14}
0.215	0.597	0.032	r’	4.90×10^{14}
0.216	0.586	0.026	r’	4.90×10^{14}
0.216	0.586	0.026	r’	4.90×10^{14}
0.217	0.586	0.026	r’	4.90×10^{14}
0.222	0.570	0.021	r’	4.90×10^{14}
0.222	0.586	0.021	r’	4.90×10^{14}
0.223	0.555	0.025	r’	4.90×10^{14}
0.224	0.555	0.020	r’	4.90×10^{14}
0.232	0.555	0.015	r’	4.90×10^{14}
0.234	0.545	0.015	r’	4.90×10^{14}
0.955	0.115	0.005	r’	4.90×10^{14}
0.957	0.118	0.005	r’	4.90×10^{14}
0.958	0.118	0.005	r’	4.90×10^{14}
0.960	0.120	0.005	r’	4.90×10^{14}
0.961	0.118	0.005	r’	4.90×10^{14}
1.147	0.074	0.004	r’	4.90×10^{14}
2.000	0.025	0.005	r’	4.90×10^{14}
2.976	0.013	0.001	r’	4.90×10^{14}
3.982	0.008	0.001	r’	4.90×10^{14}
5.488	0.005	0.000	r’	4.90×10^{14}
6.554	0.003	0.001	r’	4.90×10^{14}
0.055	5.445	0.293	Y	2.98×10^{14}
0.056	5.598	0.301	Y	2.98×10^{14}
0.063	4.614	0.208	Y	2.98×10^{14}
0.063	4.613	0.208	Y	2.98×10^{14}
0.070	3.873	0.208	Y	2.98×10^{14}
0.071	4.018	0.216	Y	2.98×10^{14}
0.092	2.729	0.459	Y	2.98×10^{14}
0.100	2.911	0.328	Y	2.98×10^{14}
0.107	2.466	0.278	Y	2.98×10^{14}
0.199	1.000	0.198	Y	2.98×10^{14}
0.995	0.215	0.024	Y	2.98×10^{14}
0.054	4.966	0.180	z’	3.37×10^{14}
0.055	4.921	0.178	z’	3.37×10^{14}
0.061	4.447	0.121	z’	3.37×10^{14}

Table A.2. continued.

$t - t_0$ (days)	Flux density (mJy)	Uncertainty (mJy)	Filter	Frequency (Hz)
0.061	4.529	0.123	z’	$3.37{\times}10^{14}$
0.068	3.767	0.103	z’	$3.37{\times}10^{14}$
0.069	3.665	0.100	z’	$3.37{\times}10^{14}$
0.091	2.754	0.124	z’	$3.37{\times}10^{14}$
0.091	2.754	0.124	z’	$3.37{\times}10^{14}$
0.097	2.444	0.110	z’	$3.37{\times}10^{14}$
0.098	2.421	0.130	z’	$3.37{\times}10^{14}$
0.104	2.229	0.100	z’	$3.37{\times}10^{14}$
0.105	2.229	0.100	z’	$3.37{\times}10^{14}$
0.189	1.117	0.126	z’	$3.37{\times}10^{14}$
0.189	1.148	0.111	z’	$3.37{\times}10^{14}$
0.195	0.973	0.077	z’	$3.37{\times}10^{14}$
0.196	0.921	0.057	z’	$3.37{\times}10^{14}$
0.202	0.912	0.065	z’	$3.37{\times}10^{14}$
0.203	1.000	0.062	z’	$3.37{\times}10^{14}$
0.986	0.177	0.011	z’	$3.37{\times}10^{14}$
0.988	0.174	0.012	z’	$3.37{\times}10^{14}$
0.007	15.626	0.563	B-UVOT	$6.83{\times}10^{14}$
0.057	2.045	0.058	B-UVOT	$6.83{\times}10^{14}$
0.073	1.596	0.078	B-UVOT	$6.83{\times}10^{14}$
0.112	0.895	0.035	B-UVOT	$6.83{\times}10^{14}$
0.116	0.867	0.031	B-UVOT	$6.83{\times}10^{14}$
0.119	0.873	0.030	B-UVOT	$6.83{\times}10^{14}$
0.260	0.364	0.012	B-UVOT	$6.83{\times}10^{14}$
0.337	0.275	0.016	B-UVOT	$6.83{\times}10^{14}$
0.526	0.183	0.009	B-UVOT	$6.83{\times}10^{14}$
0.601	0.181	0.011	B-UVOT	$6.83{\times}10^{14}$
0.868	0.135	0.010	B-UVOT	$6.83{\times}10^{14}$
1.067	0.121	0.010	B-UVOT	$6.83{\times}10^{14}$
1.257	0.085	0.008	B-UVOT	$6.83{\times}10^{14}$
1.922	0.044	0.014	B-UVOT	$6.83{\times}10^{14}$
2.380	< 0.045	-	B-UVOT	$6.83{\times}10^{14}$
3.010	0.024	0.005	B-UVOT	$6.83{\times}10^{14}$
5.001	< 0.020	-	B-UVOT	$6.83{\times}10^{14}$
0.005	13.366	0.371	U-UVOT	$8.66{\times}10^{14}$
0.055	1.450	0.050	B-UVOT	$8.66{\times}10^{14}$
0.072	1.058	0.039	B-UVOT	$8.66{\times}10^{14}$
0.250	0.245	0.010	B-UVOT	$8.66{\times}10^{14}$
0.330	0.205	0.008	B-UVOT	$8.66{\times}10^{14}$
0.405	0.170	0.015	B-UVOT	$8.66{\times}10^{14}$
0.592	0.137	0.007	B-UVOT	$8.66{\times}10^{14}$
0.778	0.101	0.011	B-UVOT	$8.66{\times}10^{14}$

Table A.2. continued.

$t - t_0$ (days)	Flux density (mJy)	Uncertainty (mJy)	Filter	Frequency (Hz)
0.934	0.080	0.006	B-UVOT	$8.66{\times}10^{14}$
1.247	0.044	0.006	B-UVOT	$8.66{\times}10^{14}$
1.400	0.047	0.006	B-UVOT	$8.66{\times}10^{14}$
2.148	0.013	0.006	B-UVOT	$8.66{\times}10^{14}$
3.007	< 0.035	-	B-UVOT	$8.66{\times}10^{14}$
0.050	0.513	0.036	UVM2-UVOT	$1.34{\times}10^{15}$
0.067	0.355	0.030	UVM2-UVOT	$1.34{\times}10^{15}$
0.192	0.104	0.009	UVM2-UVOT	$1.34{\times}10^{15}$
0.388	0.045	0.007	UVM2-UVOT	$1.34{\times}10^{15}$
0.657	0.044	0.008	UVM2-UVOT	$1.34{\times}10^{15}$
0.914	0.027	0.007	UVM2-UVOT	$1.34{\times}10^{15}$
1.123	< 0.023	-	UVM2-UVOT	$1.34{\times}10^{15}$
1.495	< 0.026	-	UVM2-UVOT	$1.34{\times}10^{15}$
2.226	< 0.018	-	UVM2-UVOT	$1.34{\times}10^{15}$
0.053	0.703	0.039	UVW1-UVOT	$1.15{\times}10^{15}$
0.069	0.500	0.031	UVW1-UVOT	$1.15{\times}10^{15}$
0.202	0.133	0.009	UVW1-UVOT	$1.15{\times}10^{15}$
0.319	0.085	0.007	UVW1-UVOT	$1.15{\times}10^{15}$
0.399	0.078	0.006	UVW1-UVOT	$1.15{\times}10^{15}$
0.582	0.055	0.006	UVW1-UVOT	$1.15{\times}10^{15}$
0.724	0.043	0.006	UVW1-UVOT	$1.15{\times}10^{15}$
0.924	0.035	0.005	UVW1-UVOT	$1.15{\times}10^{15}$
1.255	0.020	0.004	UVW1-UVOT	$1.15{\times}10^{15}$
2.230	0.013	0.005	UVW1-UVOT	$1.15{\times}10^{15}$
0.046	0.330	0.024	UVW2-UVOT	$1.56{\times}10^{15}$
0.062	0.311	0.022	UVW2-UVOT	$1.56{\times}10^{15}$
0.136	0.111	0.008	UVW2-UVOT	$1.56{\times}10^{15}$
0.457	0.037	0.005	UVW2-UVOT	$1.56{\times}10^{15}$
0.800	0.022	0.004	UVW2-UVOT	$1.56{\times}10^{15}$
0.990	0.012	0.005	UVW2-UVOT	$1.56{\times}10^{15}$
1.454	< 0.013	-	UVW2-UVOT	$1.56{\times}10^{15}$
0.048	3.025	0.112	V-UVOT	$5.49{\times}10^{14}$
0.065	2.427	0.094	V-UVOT	$5.49{\times}10^{14}$
0.182	0.676	0.031	V-UVOT	$5.49{\times}10^{14}$
0.467	0.315	0.020	V-UVOT	$5.49{\times}10^{14}$
0.843	0.169	0.053	V-UVOT	$5.49{\times}10^{14}$
1.043	0.206	0.074	V-UVOT	$5.49{\times}10^{14}$
1.464	0.122	0.016	V-UVOT	$5.49{\times}10^{14}$
2.156	< 0.063	-	V-UVOT	$5.49{\times}10^{14}$
3.018	< 0.070	-	V-UVOT	$5.49{\times}10^{14}$
6.142	< 0.033	-	V-UVOT	$5.49{\times}10^{14}$

Table A.3. Radio and millimetre observations of GRB 160131A.

$t - t_0$ (days)	Flux density[a] (mJy)	Uncertainty (mJy)	Frequency (Hz)	Instrument	Reference
1.360	1.940	0.070	9.25×10^{10}	NOEMA	1
9.262	< 0.570	-	1.28×10^{9}	GMRT	2
9.262	< 0.382	-	6.10×10^{8}	GMRT	2
10.430	< 0.105	-	1.42×10^{9}	GMRT	3
24.5	< 0.150	-	1.5×10^{10}	AMI-LA	4
34.5	< 0.210	-	1.5×10^{10}	AMI-LA	4
0.825	< 0.120	-	4.62×10^{9}	VLA	This work
0.825	0.090	0.023	4.87×10^{9}	VLA	This work
0.825	0.118	0.019	5.13×10^{9}	VLA	This work
0.825	< 0.150	-	5.38×10^{9}	VLA	This work
0.825	0.202	0.022	7.02×10^{9}	VLA	This work
0.825	0.467	0.020	7.23×10^{9}	VLA	This work
0.825	0.489	0.019	7.53×10^{9}	VLA	This work
0.825	0.555	0.023	7.78×10^{9}	VLA	This work
0.809	0.687	0.025	8.17×10^{9}	VLA	This work
0.809	0.857	0.023	8.42×10^{9}	VLA	This work
0.809	0.937	0.031	8.68×10^{9}	VLA	This work
0.809	0.958	0.031	8.93×10^{9}	VLA	This work
0.809	0.714	0.024	1.06×10^{10}	VLA	This work
0.809	0.631	0.025	1.09×10^{10}	VLA	This work
0.809	0.632	0.033	1.11×10^{10}	VLA	This work
0.809	0.630	0.031	1.14×10^{10}	VLA	This work
0.793	0.280	0.034	1.31×10^{10}	VLA	This work
0.793	0.298	0.016	1.34×10^{10}	VLA	This work
0.793	0.360	0.019	1.36×10^{10}	VLA	This work
0.793	0.447	0.025	1.39×10^{10}	VLA	This work
0.793	0.528	0.029	1.56×10^{10}	VLA	This work
0.793	0.525	0.024	1.59×10^{10}	VLA	This work
0.793	0.545	0.032	1.61×10^{10}	VLA	This work
0.793	0.551	0.025	1.64×10^{10}	VLA	This work
0.773	0.510	0.047	1.88×10^{10}	VLA	This work
0.773	0.509	0.039	1.91×10^{10}	VLA	This work
0.773	0.515	0.034	1.93×10^{10}	VLA	This work
0.773	0.525	0.028	1.96×10^{10}	VLA	This work
0.773	0.540	0.047	2.41×10^{10}	VLA	This work
0.773	0.517	0.030	2.44×10^{10}	VLA	This work
0.773	0.535	0.030	2.46×10^{10}	VLA	This work
0.773	0.518	0.036	2.49×10^{10}	VLA	This work
0.747	0.705	0.041	2.96×10^{10}	VLA	This work
0.747	0.758	0.036	2.99×10^{10}	VLA	This work
0.747	0.678	0.044	3.01×10^{10}	VLA	This work
0.747	0.725	0.044	3.04×10^{10}	VLA	This work
0.747	0.760	0.049	3.67×10^{10}	VLA	This work
0.747	0.756	0.075	3.69×10^{10}	VLA	This work
0.747	0.885	0.057	3.71×10^{10}	VLA	This work
0.747	0.805	0.051	3.74×10^{10}	VLA	This work
1.726	0.330	0.068	4.62×10^{9}	VLA	This work
1.726	0.270	0.055	4.87×10^{9}	VLA	This work
1.726	0.160	0.038	5.13×10^{9}	VLA	This work
1.726	0.130	0.027	5.38×10^{9}	VLA	This work
1.726	0.091	0.024	6.72×10^{9}	VLA	This work
1.726	0.110	0.018	6.97×10^{9}	VLA	This work
1.726	0.160	0.021	7.23×10^{9}	VLA	This work
1.726	0.165	0.032	7.48×10^{9}	VLA	This work

Table A.3. continued.

$t - t_0$ (days)	Flux density[a] (mJy)	Uncertainty (mJy)	Frequency (Hz)	Instrument	Reference
1.713	0.725	0.033	8.17×10^{9}	VLA	This work
1.713	0.870	0.029	8.42×10^{9}	VLA	This work
1.713	0.890	0.030	8.68×10^{9}	VLA	This work
1.713	0.995	0.030	8.93×10^{9}	VLA	This work
1.713	0.460	0.028	1.06×10^{10}	VLA	This work
1.713	0.412	0.028	1.09×10^{10}	VLA	This work
1.713	0.495	0.031	1.11×10^{10}	VLA	This work
1.713	0.382	0.026	1.14×10^{10}	VLA	This work
2.819	0.164	0.050	4.62×10^{9}	VLA	This work
2.819	0.173	0.036	4.87×10^{9}	VLA	This work
2.819	0.101	0.029	5.13×10^{9}	VLA	This work
2.819	0.081	0.035	5.38×10^{9}	VLA	This work
2.819	0.135	0.023	6.72×10^{9}	VLA	This work
2.819	0.240	0.015	6.97×10^{9}	VLA	This work
2.819	0.283	0.019	7.23×10^{9}	VLA	This work
2.819	0.232	0.016	7.48×10^{9}	VLA	This work
2.810	0.388	0.022	8.17×10^{9}	VLA	This work
2.810	0.375	0.018	8.42×10^{9}	VLA	This work
2.810	0.410	0.020	8.68×10^{9}	VLA	This work
2.810	0.425	0.022	8.93×10^{9}	VLA	This work
2.810	0.430	0.026	1.06×10^{10}	VLA	This work
2.810	0.415	0.022	1.09×10^{10}	VLA	This work
2.810	0.410	0.023	1.11×10^{10}	VLA	This work
2.810	0.376	0.023	1.14×10^{10}	VLA	This work
2.767	0.790	0.038	1.88×10^{10}	VLA	This work
2.767	0.840	0.036	1.91×10^{10}	VLA	This work
2.767	0.805	0.032	1.93×10^{10}	VLA	This work
2.767	0.847	0.065	1.96×10^{10}	VLA	This work
2.788	0.522	0.023	1.31×10^{10}	VLA	This work
2.788	0.591	0.020	1.34×10^{10}	VLA	This work
2.788	0.585	0.017	1.36×10^{10}	VLA	This work
2.788	0.550	0.017	1.39×10^{10}	VLA	This work
2.788	0.585	0.024	1.56×10^{10}	VLA	This work
2.788	0.600	0.020	1.59×10^{10}	VLA	This work
2.788	0.597	0.018	1.61×10^{10}	VLA	This work
2.788	0.598	0.022	1.64×10^{10}	VLA	This work
2.767	0.954	0.036	2.41×10^{10}	VLA	This work
2.767	0.910	0.030	2.44×10^{10}	VLA	This work
2.767	0.895	0.032	2.46×10^{10}	VLA	This work
2.767	0.890	0.036	2.49×10^{10}	VLA	This work
2.741	0.727	0.039	2.96×10^{10}	VLA	This work
2.741	0.598	0.036	2.99×10^{10}	VLA	This work
2.741	0.691	0.036	3.01×10^{10}	VLA	This work
2.741	0.790	0.038	3.04×10^{10}	VLA	This work
2.741	0.668	0.046	3.66×10^{10}	VLA	This work
2.741	0.700	0.043	3.69×10^{10}	VLA	This work
2.741	0.831	0.033	3.71×10^{10}	VLA	This work
2.741	0.740	0.058	3.74×10^{10}	VLA	This work
5.857	0.090	0.052	4.62×10^{9}	VLA	This work
5.857	< 0.150	-	4.87×10^{9}	VLA	This work
5.857	< 0.180	-	5.13×10^{9}	VLA	This work
5.857	0.100	0.040	5.38×10^{9}	VLA	This work
5.857	0.301	0.025	6.72×10^{9}	VLA	This work
5.857	0.515	0.017	6.97×10^{9}	VLA	This work
5.857	0.730	0.024	7.23×10^{9}	VLA	This work

Table A.3. continued.

$t - t_0$ (days)	Flux density[a] (mJy)	Uncertainty (mJy)	Frequency (Hz)	Instrument	Reference
5.857	0.735	0.031	7.48×10^{9}	VLA	This work
5.842	0.265	0.026	8.17×10^{9}	VLA	This work
5.842	0.230	0.025	8.42×10^{9}	VLA	This work
5.842	0.198	0.024	8.68×10^{9}	VLA	This work
5.842	0.245	0.028	8.93×10^{9}	VLA	This work
5.842	0.255	0.021	1.06×10^{10}	VLA	This work
5.842	0.291	0.024	1.09×10^{10}	VLA	This work
5.842	0.270	0.019	1.11×10^{10}	VLA	This work
5.842	0.280	0.023	1.14×10^{10}	VLA	This work
5.806	0.248	0.065	1.88×10^{10}	VLA	This work
5.806	0.275	0.023	1.91×10^{10}	VLA	This work
5.806	0.281	0.030	1.93×10^{10}	VLA	This work
5.806	0.317	0.029	1.96×10^{10}	VLA	This work
5.826	0.303	0.026	1.31×10^{10}	VLA	This work
5.826	0.233	0.013	1.34×10^{10}	VLA	This work
5.826	0.250	0.015	1.36×10^{10}	VLA	This work
5.826	0.263	0.017	1.39×10^{10}	VLA	This work
5.826	0.264	0.020	1.56×10^{10}	VLA	This work
5.826	0.240	0.019	1.59×10^{10}	VLA	This work
5.826	0.253	0.013	1.61×10^{10}	VLA	This work
5.826	0.210	0.020	1.64×10^{10}	VLA	This work
5.806	0.340	0.032	2.41×10^{10}	VLA	This work
5.806	0.430	0.023	2.44×10^{10}	VLA	This work
5.806	0.378	0.031	2.46×10^{10}	VLA	This work
5.806	0.375	0.022	2.49×10^{10}	VLA	This work
5.780	0.523	0.032	2.96×10^{10}	VLA	This work
5.780	0.490	0.029	2.99×10^{10}	VLA	This work
5.780	0.541	0.036	3.01×10^{10}	VLA	This work
5.780	0.485	0.030	3.04×10^{10}	VLA	This work
5.780	0.585	0.061	3.66×10^{10}	VLA	This work
5.780	0.468	0.051	3.69×10^{10}	VLA	This work
5.780	0.466	0.034	3.71×10^{10}	VLA	This work
5.780	0.451	0.036	3.74×10^{10}	VLA	This work
12.740	0.120	0.068	4.62×10^{9}	VLA	This work
12.740	0.125	0.052	4.87×10^{9}	VLA	This work
12.740	0.200	0.026	5.13×10^{9}	VLA	This work
12.740	0.170	0.040	5.38×10^{9}	VLA	This work
12.740	0.390	0.020	6.72×10^{9}	VLA	This work
12.740	0.315	0.013	6.97×10^{9}	VLA	This work
12.740	0.290	0.015	7.23×10^{9}	VLA	This work
12.740	0.295	0.014	7.48×10^{9}	VLA	This work
12.725	0.320	0.014	8.17×10^{9}	VLA	This work
12.725	0.245	0.025	8.42×10^{9}	VLA	This work
12.725	0.362	0.017	8.68×10^{9}	VLA	This work
12.725	0.365	0.025	8.93×10^{9}	VLA	This work
12.725	0.342	0.019	1.06×10^{10}	VLA	This work
12.725	0.299	0.020	1.09×10^{10}	VLA	This work
12.725	0.318	0.022	1.11×10^{10}	VLA	This work
12.725	0.315	0.026	1.14×10^{10}	VLA	This work
12.709	0.230	0.017	1.31×10^{10}	VLA	This work
12.709	0.247	0.013	1.34×10^{10}	VLA	This work
12.709	0.199	0.022	1.36×10^{10}	VLA	This work
12.709	0.230	0.018	1.39×10^{10}	VLA	This work
12.709	0.195	0.015	1.56×10^{10}	VLA	This work

Table A.3. continued.

$t - t_0$ (days)	Flux density[a] (mJy)	Uncertainty (mJy)	Frequency (Hz)	Instrument	Reference
12.709	0.214	0.018	$1.59{\times}10^{10}$	VLA	This work
12.709	0.211	0.019	$1.61{\times}10^{10}$	VLA	This work
12.709	0.192	0.016	$1.64{\times}10^{10}$	VLA	This work
12.689	0.155	0.025	$2.41{\times}10^{10}$	VLA	This work
12.689	0.223	0.022	$2.44{\times}10^{10}$	VLA	This work
12.689	0.172	0.035	$2.46{\times}10^{10}$	VLA	This work
12.689	0.183	0.032	$2.49{\times}10^{10}$	VLA	This work
12.689	0.183	0.021	$1.88{\times}10^{10}$	VLA	This work
12.689	0.201	0.017	$1.91{\times}10^{10}$	VLA	This work
12.689	0.150	0.018	$1.93{\times}10^{10}$	VLA	This work
12.689	0.169	0.025	$1.96{\times}10^{10}$	VLA	This work
12.662	< 0.180	-	$3.66{\times}10^{10}$	VLA	This work
12.662	< 0.210	-	$3.69{\times}10^{10}$	VLA	This work
12.662	0.155	0.048	$3.71{\times}10^{10}$	VLA	This work
12.662	0.180	0.054	$3.74{\times}10^{10}$	VLA	This work
12.662	0.124	0.024	$2.96{\times}10^{10}$	VLA	This work
12.662	0.090	0.022	$2.99{\times}10^{10}$	VLA	This work
12.662	0.203	0.033	$3.01{\times}10^{10}$	VLA	This work
12.662	0.115	0.031	$3.04{\times}10^{10}$	VLA	This work
25.813	0.090	0.047	$4.62{\times}10^{9}$	VLA	This work
25.813	0.151	0.044	$4.87{\times}10^{9}$	VLA	This work
25.813	0.111	0.041	$5.13{\times}10^{9}$	VLA	This work
25.813	0.085	0.035	$5.38{\times}10^{9}$	VLA	This work
25.813	< 0.150	-	$6.72{\times}10^{9}$	VLA	This work
25.813	0.045	0.020	$6.97{\times}10^{9}$	VLA	This work
25.813	< 0.180	-	$7.23{\times}10^{9}$	VLA	This work
25.813	0.040	0.061	$7.48{\times}10^{9}$	VLA	This work
25.798	0.083	0.024	$8.17{\times}10^{9}$	VLA	This work
25.798	0.071	0.025	$8.42{\times}10^{9}$	VLA	This work
25.798	0.098	0.021	$8.68{\times}10^{9}$	VLA	This work
25.798	0.104	0.028	$8.93{\times}10^{9}$	VLA	This work
25.798	0.090	0.022	$1.06{\times}10^{10}$	VLA	This work
25.798	0.074	0.018	$1.09{\times}10^{10}$	VLA	This work
25.798	0.051	0.014	$1.11{\times}10^{10}$	VLA	This work
25.798	0.075	0.029	$1.14{\times}10^{10}$	VLA	This work
25.782	0.070	0.021	$1.31{\times}10^{10}$	VLA	This work
25.782	0.058	0.016	$1.34{\times}10^{10}$	VLA	This work
25.782	0.059	0.015	$1.36{\times}10^{10}$	VLA	This work
25.782	0.071	0.013	$1.39{\times}10^{10}$	VLA	This work
25.782	0.051	0.019	$1.56{\times}10^{10}$	VLA	This work
25.782	0.091	0.022	$1.59{\times}10^{10}$	VLA	This work
25.782	0.060	0.013	$1.61{\times}10^{10}$	VLA	This work
25.782	0.069	0.014	$1.64{\times}10^{10}$	VLA	This work
25.761	0.101	0.032	$1.88{\times}10^{10}$	VLA	This work
25.761	0.075	0.048	$1.91{\times}10^{10}$	VLA	This work
25.761	0.080	0.027	$1.93{\times}10^{10}$	VLA	This work
25.761	0.105	0.017	$1.96{\times}10^{10}$	VLA	This work
25.761	0.154	0.030	$2.41{\times}10^{10}$	VLA	This work
25.761	0.145	0.026	$2.44{\times}10^{10}$	VLA	This work
25.761	< 0.120	-	$2.46{\times}10^{10}$	VLA	This work
25.761	0.118	0.025	$2.49{\times}10^{10}$	VLA	This work
44.767	< 0.165	-	$4.62{\times}10^{9}$	VLA	This work
44.767	< 0.135	-	$4.87{\times}10^{9}$	VLA	This work
44.767	< 0.195	-	$5.13{\times}10^{9}$	VLA	This work
44.767	< 0.210	-	$5.38{\times}10^{9}$	VLA	This work

Table A.3. continued.

$t - t_0$ (days)	Flux density[a] (mJy)	Uncertainty (mJy)	Frequency (Hz)	Instrument	Reference
44.767	0.034	0.042	6.72×10^{9}	VLA	This work
44.767	0.075	0.030	6.97×10^{9}	VLA	This work
44.767	0.051	0.034	7.23×10^{9}	VLA	This work
44.767	0.074	0.141	7.48×10^{9}	VLA	This work
44.751	0.109	0.029	8.17×10^{9}	VLA	This work
44.751	0.129	0.023	8.42×10^{9}	VLA	This work
44.751	0.101	0.022	8.68×10^{9}	VLA	This work
44.751	0.083	0.026	8.93×10^{9}	VLA	This work
44.751	0.118	0.022	1.06×10^{10}	VLA	This work
44.751	0.095	0.018	1.09×10^{10}	VLA	This work
44.751	0.067	0.022	1.11×10^{10}	VLA	This work
44.751	0.064	0.029	1.14×10^{10}	VLA	This work
44.734	0.108	0.030	1.31×10^{10}	VLA	This work
44.734	0.064	0.026	1.34×10^{10}	VLA	This work
44.734	< 0.105	-	1.36×10^{10}	VLA	This work
44.734	0.081	0.018	1.39×10^{10}	VLA	This work
44.734	0.065	0.034	1.56×10^{10}	VLA	This work
44.734	0.050	0.024	1.59×10^{10}	VLA	This work
44.734	0.061	0.023	1.61×10^{10}	VLA	This work
44.734	0.070	0.020	1.64×10^{10}	VLA	This work
44.711	0.083	0.028	2.41×10^{10}	VLA	This work
44.711	< 0.090	-	2.44×10^{10}	VLA	This work
44.711	0.065	0.035	2.46×10^{10}	VLA	This work
44.711	< 0.105	-	2.49×10^{10}	VLA	This work
44.711	< 0.105	-	1.88×10^{10}	VLA	This work
44.711	< 0.090	-	1.91×10^{10}	VLA	This work
44.711	0.071	0.033	1.93×10^{10}	VLA	This work
44.711	0.075	0.037	1.96×10^{10}	VLA	This work
117.499	< 0.099	-	4.62×10^{9}	VLA	This work
117.499	< 0.069	-	4.87×10^{9}	VLA	This work
117.499	< 0.075	-	5.13×10^{9}	VLA	This work
117.499	< 0.075	-	5.38×10^{9}	VLA	This work
117.499	< 0.060	-	6.72×10^{9}	VLA	This work
117.499	0.090	0.014	6.97×10^{9}	VLA	This work
117.499	< 0.069	-	7.23×10^{9}	VLA	This work
117.499	< 0.060	-	7.48×10^{9}	VLA	This work
117.478	< 0.072	-	8.17×10^{9}	VLA	This work
117.478	0.046	0.018	8.42×10^{9}	VLA	This work
117.478	< 0.105	-	8.68×10^{9}	VLA	This work
117.478	< 0.048	-	8.93×10^{9}	VLA	This work
117.478	< 0.105	-	1.06×10^{10}	VLA	This work
117.478	< 0.060	-	1.09×10^{10}	VLA	This work
117.478	< 0.060	-	1.11×10^{10}	VLA	This work
117.478	< 0.045	-	1.14×10^{10}	VLA	This work
117.455	< 0.075	-	1.31×10^{10}	VLA	This work

Table A.3. continued.

$t - t_0$ (days)	Flux density[a] (mJy)	Uncertainty (mJy)	Frequency (Hz)	Instrument	Reference
117.455	0.040	0.022	1.34×10^{10}	VLA	This work
117.455	< 0.075	-	1.36×10^{10}	VLA	This work
117.455	0.032	0.020	1.39×10^{10}	VLA	This work
117.455	0.029	0.021	1.56×10^{10}	VLA	This work
117.455	< 0.045	-	1.59×10^{10}	VLA	This work
117.455	< 0.075	-	1.61×10^{10}	VLA	This work
117.455	< 0.060	-	1.64×10^{10}	VLA	This work

Notes. $t - t_0$ indicates the epoch of observation, where t_0 is the GRB explosion date (57418.3476 MJD). All upper limits are at 3σ. (1) GCN 18976 (de Ugarte Postigo et al. 2016b); (2) GCN 19009 (Chandra & Nayana 2016a); (3) GCN 19010 (Chandra & Nayana 2016b); (4) GCN 19206 (Mooley et al. 2016).